Universidad de Huelva

Departamento de Ciencias de la Tierra

Seismotectonics and lithospheric-scale strain partitioning in relation to complex plate convergence settings

Memoria para optar al grado de doctor
presentada por:

David Amador Luna

Fecha de lectura: 11 de junio de 2025

Bajo la dirección de los doctores:

Carlos Fernández Rodríguez

Francisco Manuel Alonso Chaves

Huelva, 2025

SEISMOTECTONICS AND LITHOSPHERIC-SCALE STRAIN PARTITIONING IN RELATION TO COMPLEX PLATE CONVERGENCE SETTINGS

SISMOTECTÓNICA Y PARTICIÓN DE LA DEFORMACIÓN A ESCALA LITOSFÉRICA EN RELACIÓN CON CONTEXTOS COMPLEJOS DE CONVERGENCIA DE PLACAS

David Amador Luna

TESIS DOCTORAL. HUELVA, 2025

Universidad de Huelva

Departamento de Ciencias de la Tierra

SEISMOTECTONICS AND LITHOSPHERIC-SCALE STRAIN PARTITIONING IN RELATION TO COMPLEX PLATE CONVERGENCE SETTINGS

SISMOTECTÓNICA Y PARTICIÓN DE LA DEFORMACIÓN A ESCALA LITOSFÉRICA EN RELACIÓN CON CONTEXTOS COMPLEJOS DE CONVERGENCIA DE PLACAS

MEMORIA PARA OPTAR AL GRADO DE DOCTOR EN CIENCIAS DE LA TIERRA, DENTRO DEL PROGRAMA OFICIAL DE DOCTORADO EN CIENCIA Y TECNOLOGÍA INDUSTRIAL Y AMBIENTAL.

David Amador Luna

BAJO LA DIRECCIÓN DE:

Dr. Carlos Fernández Rodríguez

Dr. Francisco Manuel Alonso Chaves

Huelva, 2025

This doctoral thesis has been funded through the “Estrategia Política de Investigación y Transferencia” (EPIT) of the University of Huelva, aimed at promoting the recruitment of early-career researchers (EPIT20/00832).

Esta tesis doctoral ha sido financiada gracias a la «Estrategia Política de Investigación y Transferencia» (EPIT) de la Universidad de Huelva para la promoción de la contratación de personal investigador novel (EPIT20/00832)

“It must have appeared almost as improbable to the earlier geologists, that the laws of earthquakes should one day throw light on the origin of mountains, as it must to the first astronomers, that the fall of an apple should assist in explaining the motions of the moon”.

CHARLES LYELL.

BRITISH GEOLOGIST AND FOUNDER OF MODERN GEOLOGY.

"There are facts that can only be explained by the existence of certain invisible (blind) faults. Faults that our eyes cannot see because they do not surface. In that sense, faults are like God."

FRANCISCO M. ALONSO-CHAVES.

GEOLOGIST FROM LANJARÓN.

Acknowledgments

As expected, a doctoral thesis is far from being a bed of roses—it's more like a thorny path until you find that long-awaited rose. Or perhaps it's more like a roller coaster, where you must endure a slow and grueling climb before enjoying the thrilling descent. Like any good roller coaster, the final stretch, just before reaching the end, often holds the best moment of the ride, when you finally see the fruits of the tree you planted years ago. This thesis is undoubtedly one of those fruits, nurtured not only during the five (or rather six) years it took to complete, but also during the 30 years of learning that shaped me.

This thesis is especially dedicated to my very first teachers, who guided me through these 30 years of education. Most importantly, it is dedicated to my parents (José Manuel and Mª Ángeles) and my brother (Víctor), who accompanied me throughout this journey (and every journey before it). They helped me push the cart up the steep inclines of this roller coaster, even though they didn't enjoy the exhilarating descents as much as I did. I owe them for making me who I am, for giving me my values and ambitions, for standing by me during my hardest moments, for laughing with me, and, of course, for sheltering, caring for, and feeding me throughout these 30 years—which, like the good parasite I am, I have no intention of leaving behind anytime soon.

To my brother: my best friend, my partner in adventures, my study buddy, and even my roommate, even when he moved to Madrid to live on his own. When I needed a retreat, he welcomed me into his home. If I managed to finish this thesis, you will finish yours too—and in better shape than I did. Stay strong, good luck, and enjoy the ride.

Continuing with the roller coaster analogy, riding alone is never the same as riding with others. That's why I also want to thank my supervisors for their guidance and support—both academic and emotional. This thesis would have been impossible without you.

Thank you, Francis, for awakening my love for geology since that fateful day we met in high school. It was written in the destiny pages that my doctoral thesis would be under your mentorship. You inspired me to see our planet not as something static and inert, but as something alive and constantly moving.

Thank you, Carlos, for making humility your hallmark. You are a great teacher, an outstanding researcher, an exceptional supervisor, and, above all, a great person. Your creative teaching methods—using toy trucks to explain accretionary prisms or spinning

bits of paper to illustrate Euler poles—sparked some of the best classes I've ever taught, using books as makeshift folds and measuring axes with a ruler.

I also want to express my gratitude to my unofficial supervisors:

To Albert Macau, for his invaluable help, insightful comments, and guidance on using passive seismic equipment and, of course, with this thesis. Thank you for always responding to my emails, no matter the time or day. To Manu Díaz Azpiroz, for including me in scientific fieldwork campaigns and lending us the equipment essential for this work. To Elisa Buforn, for her advice on seismology; without her guidance, the EAFZ article would never have been accepted or published. To the members of the Internal Geodynamics Department at UCM, for their advice and for welcoming me during my research stay. And, of course, to Alberto González Díez, for countless reasons: for hosting me at the University of Cantabria with open arms, for guiding me in the applications of passive seismology, for helping me with GIS tools, for inviting me to submit a paper in Remote Sensing, and for providing feedback on the article that ultimately resulted in a publication so well-received that it was published free of charge.

I also want to thank the organizations AFAD, KOERI, IGN, and IGME and Anthony Lomax for their efforts in collecting seismic and geological data. Special thanks to the University of Huelva for funding this work through the Estrategia Política de Investigación y Transferencia (EPIT) for predoctoral contract (EPIT20/00832), without which this thesis would not have been possible.

I extend my gratitude to the anonymous reviewers, whose feedback significantly improved the manuscript and emphasized the importance of publishing the article.

To my friends: thank you for making the hard times more bearable. To Luis Collantes and Rafa León, my colleagues and companions, for advising and helping me with my thesis while simultaneously working on yours. For being companions at conferences and presentations, over beers and feasts across Spain. Your companionship and support throughout this shared journey have been invaluable. Thank you so much for your help, doctors. To Raquel Molina, Paula Sanz, Cristina Escalante, and Cristina Urbano, for acting as unofficial therapists. To Miguel Ángel Cordero, my lifelong friend and durum buddy. To those who joined me in the field despite having their own matters to attend to: Cristóbal Cantero, José Ramírez (Cuadri), Joaquín Rodríguez (Quino), and especially Dani Cruzado, my brother-in-arms, who not only joined me in the lonely fields but also

walked alongside me during the solitary paths of despair—him with his studies and I with this thesis. To the rest of my friends: Fernando Hervás, Chema Fuentes, Gema Enríquez, Sandra Burgada and José Manuel Amador (a.k.a. my father from other family). Thank you all.

Finally, to the students I've taught since 2020: thank you for reminding me that admitting you don't know something—and promising to find the answer—is not a weakness but a sign that their questions matter. Thank you for the nickname "David the Wise", even though I'm far from deserving it.

To my uncles, cousins, and my entire family: thank you for putting up with me, even though half the time you have no idea what I do or talk about.

Thank you all. This thesis is as much yours as it is mine.

RESUMEN

RESUMEN

Los contextos complejos de convergencia de placas se caracterizan por la interacción de distintos tipos de fallas activas (normales, inversas y de desgarre) o, a una escala mayor, por la confluencia de diversas placas tectónicas. Estos escenarios generan regiones de alta complejidad sismotectónica, en las que, en algunos casos, se presentan núcleos de alta densidad de población o proximidad a zonas industriales. Por ello, resulta fundamental el estudio y la elaboración de mapas de riesgo sísmico más precisos.

Uno de los avances clave de esta investigación es el uso de *big data* sísmico para el desarrollo de un nuevo método de análisis denominado "método de las lonchas". Este método permite delimitar niveles sismogenéticos (“lonchas”) a partir de los cuales se generan mapas de densidad (*kernel*), facilitando la construcción de modelos tridimensionales de estructuras sísmicamente activas.

Aprovechando la relevancia de los terremotos ocurridos en Turquía y Siria en 2023, se puso a prueba esta metodología aplicándola a dos conjuntos de datos sísmicos: un primer conjunto sin procesar y otro conformado por terremotos relocalizados de alta fiabilidad. En ambos casos, se aplicó el mismo procedimiento, obteniendo interpretaciones coincidentes y demostrando la eficacia del método. El uso del método kernel actuó como filtro, permitiendo obtener resultados equiparables.

El análisis en la Zona de Falla del Este de Anatolia permitió identificar cinco lonchas, generando una imagen tridimensional de la falla. Se detectaron zonas previamente inactivas que se reactivaron tras los eventos sísmicos de 2023, así como una estructura en forma de palma a lo largo de la falla principal. Se identificaron diferencias en el comportamiento sismotectónico a lo largo de la falla, diferenciando entre regiones transtensivas al sur y oeste, una zona transpresiva al norte y un segmento central de desgarre puro. La falla Nurdagi-Pazarcik, previamente considerada una *splay fault*, fue reinterpretada no como una rama secundaria, sino como parte del brazo oriental de la falla principal, convergiendo en profundidad con la denominada *main fault*. También se realizó un estudio cinemático y la elaboración de perfiles reológicos para explicar la segmentación de la falla en el marco de la tectónica de placas y la distribución sísmica en profundidad.

Este mismo método se aplicó a la cuenca de Granada, una región con una alta actividad sísmica histórica y múltiples enjambres sísmicos recientes, destacando tres entre 2020 y

2022. Se identificaron cuatro lonchas con patrones de sismicidad orientados NW-SE y NE-SW. En profundidad, estos patrones parecen converger en un despegue basal a 10-15 km de profundidad, con un ligero buzamiento hacia el WSW. Esta estructura se asocia con un régimen extensional vinculado a la convergencia entre Nubia y Eurasia. A partir de los núcleos de densidad, se identificaron fallas de alto y bajo ángulo que convergen en dicho despegue, sugiriendo un desplazamiento predominante hacia el SSW. Este *detachment* parece truncarse al este por una estructura con orientación N-S y buzamiento al sur en la Sierra de Loja, y al oeste por una falla NW-SE en el extremo oriental de la cuenca. La orientación estimada de los núcleos de densidad coincide con la prolongación del límite entre las zonas interna y externa de las Béticas.

En la segunda parte de la tesis, se evaluó la eficacia del método *Horizontal-to-Vertical Spectral Ratio* en el estudio del basamento de la cuenca del Guadalquivir. Se realizaron mediciones de ruido sísmico en el extremo occidental de la cuenca, lo que permitió desarrollar una nueva relación empírica para la zona (h=80.16$\cdot f_0^{-1.48}$). Esta relación permitió estimar la profundidad del basamento mecánico, reconstruir la paleotopografía tortoniense y detectar fracturas que condicionan la morfología actual del terreno.

Se determinó que el basamento mecánico presenta una tendencia paralela al contacto basamento-cobertera, con una inclinación de 1-3º hacia el sureste y rupturas de pendiente coincidentes con los cursos fluviales. Se detectaron ligeras discrepancias entre los sondeos mecánicos y las estimaciones de este método, probablemente debido a la presencia de unidades mecánicamente duras, como las calcarenitas de Niebla.

El modelo resultante sugiere una configuración de *horst* y *graben*, donde los altos estructurales corresponden a zonas elevadas (como los Cabezos de Huelva) y las depresiones a áreas de marisma.

Estos avances abren nuevas oportunidades de investigación en otros contextos tectónicos, con aplicaciones potenciales en estudios de riesgo sísmico, planificación territorial y evaluación de la evolución tectónica en orógenos activos

ABSTRACT

ABSTRACT

Complex plate convergence contexts are characterized by the interaction of various types of active faults (normal, reverse, and strike-slip) or, on a larger scale, by the convergence of different tectonic plates. These scenarios create regions of high seismic-tectonic complexity, some of which are located near densely populated areas or industrial zones. Thus, it is essential to study and develop more precise seismic hazard maps.

One of the key advances of this research is the use of seismic big data for the development of a new analytical method known as the "slice method." This method allows for the delimitation of seismogenic levels ("slices"), from which density maps (kernel) are generated, facilitating the construction of three-dimensional models of seismically active structures.

Taking advantage of the significance of the 2023 earthquakes in Turkey and Syria, this methodology was tested by applying it to two seismic datasets: one unprocessed and the other consisting of highly reliable relocated earthquakes. In both cases, the same procedure was applied, yielding consistent interpretations and demonstrating the method's effectiveness. The use of the kernel method acted as a filter, allowing for comparable results.

Analysis of the East Anatolian Fault Zone identified five slices, generating a three-dimensional image of the fault. Previously inactive areas were reactivated after the 2023 seismic events, and a palm-like structure was observed along the main fault. Moreover, differences in seismic-tectonic behavior were identified along the fault, distinguishing transtensional regions to the south and west, a transpressive zone to the north, and a central strike-slip segment. The Nurdagi-Pazarcik fault, previously considered a splay fault, was reinterpreted not as a secondary branch but as part of the eastern arm of the main fault, converging at depth with the so-called main fault. A kinematic study and the development of rheological profiles were also conducted to explain the fault segmentation within the framework of plate tectonics and the seismic distribution at depth.

This method was also applied to the Granada Basin, a region with a history of significant seismic activity and multiple recent seismic swarms, including three notable events between 2020 and 2022. Four slices with NW-SE and NE-SW seismicity patterns were identified. At depth, these patterns appear to converge in a basal detachment at 10-15 km depth, with a slight dip toward the WSW. This structure is associated with an extensional

regime linked to the convergence between the Nubian and Eurasian plates. From the density cores, high- and low-angle faults converging at the detachment were identified, suggesting a predominant displacement toward the SSW. This detachment appears to be truncated in the east by a north-south oriented structure with a southward dip in the Sierra de Loja and in the west by an NW-SE fault at the eastern end of the basin. The estimated orientation of the density cores matches the extension of the boundary between the internal and external zones of the Betics.

In the second part of the thesis, the effectiveness of the Horizontal-to-Vertical Spectral Ratio method was evaluated for studying the basement of the Guadalquivir Basin. Seismic noise measurements were taken in the western end of the basin, which enabled the development of a new empirical relationship for the region (h=80.16$\cdot f_0^{-1.48}$). This relationship allowed for the estimation of the mechanical basement depth, reconstruction of the Tortonian paleotopography, and detection of fractures that influence the current terrain morphology.

The results determined that the mechanical basement trends parallel to the basement-cover contact, with a 1-3º dip toward the southeast and slope breaks coincident with river courses. Minor discrepancies were found between mechanical boreholes and the estimates from this method, likely due to the presence of mechanically hard units, such as the Niebla calcarenites.

The resulting model suggests a horst-and-graben configuration, where the structural highs correspond to elevated zones (such as the Cabezos de Huelva) and the depressions correspond to marshland areas.

These advances open new research opportunities in other tectonic contexts, with potential applications in seismic risk studies, territorial planning, and the evaluation of tectonic evolution in active orogens.

INDEX

FIGURE INDEX

TABLE INDEX

INTRODUCTION

1. INTRODUCTION

1.1. Preface

Seismotectonics is a geological discipline that integrates seismological, geodetic, and geological knowledge to study seismic activity and its association with the structures responsible for earthquakes. This integrative approach is essential for analyzing contemporary tectonics, as many surface structures can be correlated with active subsurface structures (Keller & Pinter, 1996). However, not all seismicity can be directly associated with visible surface structures. While geology provides tools such as fault mapping and analysis, seismology contributes insights into the spatial and temporal distribution of earthquakes, focal mechanisms, and slip rates. These tools have played a pivotal role in the development and evolution of global tectonics (Lay & Wallace, 1995). In this context, seismology still constitutes one of the fundamental pillars for investigating lithospheric structures (Vera et al., 2004).

Although earthquakes have captivated human interest since ancient civilizations—when explanations from classical Greece and China often extended beyond divine punishment— modern seismology has a history of just over a century (Agnew, 2002). Since its inception, plate tectonic theory has provided deeper insight into geological phenomena. However, it remains a young science, constrained by the brevity of the instrumental seismic record, which dates back to the early 20th century. Open questions persist, such as the relationship between tectonics and intraplate volcanism, the asymmetric distribution of plate sizes, the existence of plate tectonics on other planets, and the onset of the subduction process (e.g., Foulger & Natland, 2003; Kious & Tilling, 1996; Stern, 2004). Until recently, debates surrounded the primary drivers of plate dynamics, including asthenosphere drag versus slab pull–ridge push (e.g., Kious & Tilling, 1996; Lithgow-Bertelloni, 2014).

A three-dimensional understanding of seismogenic structures would enable a more detailed comprehension of tectonic processes and allow for precise parameterization of seismic phenomena. This would not only facilitate the identification of active faults or fault segments but also enable the assessment of high-risk seismic zones, the quantification of seismic hazards, effective planning and mitigation strategies, the development of more accurate short-term risk models, and the modeling of complex tectonic contexts.

Complex contexts are defined as scenarios where multiple tectonic phenomena converge, such as the interaction of strike-slip, thrust, and extensional faults in restricted areas or zones of interaction between multiple tectonic plates (e.g., triple junctions). Examples of such areas include the Anatolia-Syria boundary and the Iberia-Africa boundary, both of which are the focus of this thesis.

This thesis employs passive seismic techniques and instrumental seismic records to obtain a three-dimensional view of the lithosphere. Additionally, a novel method based on the depth distribution of seismicity and kernel density estimation (KDE), referred to as the "slice method," was developed to delineate seismogenic levels and evaluate seismic hazard in three dimensions from earthquake big data, yielding results comparable to those from high-precision seismic catalogs.

The method was initially applied to the Türkiye-Syria region as a case study due to recent seismic events. On February 23, 2023, a magnitude 7.8 earthquake struck southeastern Türkiye near the Syrian border. Hours later, a second major earthquake (M7.5) impacted the region, both ranking as the largest earthquakes recorded in the area in the past 100 years, alongside the Erzincan (1939, M7.8) and Izmit (1999, M7.6) events (USGS, 2023). This rich seismic record allowed validation of the accuracy and utility of the new method using both unfiltered and relocated databases (sections 5.1 and 5.2).

Subsequently, the method was applied to the Granada basin, one of the most seismically active areas of the Iberian Peninsula, located within the Betic Cordillera, part of the Gibraltar Arc (section 5.3). Between December 2020 and August 2021, a seismic swarm comprising over 2,000 shallow earthquakes with maximum magnitude of 4.4 occurred in Santa Fe, northwest of Granada, followed by another swarm in August 2021 (Lozano et al., 2022). The results obtained from the Granada basin study (section 5.3) were complemented by additional applications in other areas of the Gibraltar Arc, such as Al Hoceima and Seville-Cádiz, as well as in contexts like the Azores-Gibraltar Fault or the La Palma eruption. These studies are still in the preliminary stages but have yielded promising results so far.

Finally, the forebulge area—the elevated zone behind a depression, formed by the flexing of the lithosphere due to the weight of the orogenic formation at the opposite end—of the Betic foreland basin was analyzed to examine the morphology of the underlying basement and the structures shaping the relief using passive seismic techniques (section 5.4). This

analysis began as part of the ALERTES-RIM project (Early Earthquake Warning: Regional and In-Situ System for the Ibero-Maghrebian Region), funded by the Spanish Ministry of Science and Innovation ("Ministerio de ciencia e innovación") and coordinated by various institutions, including the Complutense University of Madrid ("Universidad Complutense de Madrid", UCM), the Royal Naval Observatory ("Real Observatorio de la Armada", ROA), and the Cartographic and Geological Institute of Catalonia ("Institut Cartogràphic i Geològic de Catalunya", ICGC). The project primary objective was to develop an early earthquake warning system for the region, encompassing earthquakes affecting Portugal, Spain, Morocco, and Algeria.

As part of the project, several field campaigns were conducted to measure the seismic response in the city of Huelva, in which the doctoral candidate David Amador Luna actively participated. As a result, a seismic microzonation of the city was achieved, with results documented in the works of Alonso-Chaves et al. (2020b), Macau et al. (2016), and ICGC (2016). These initial studies were later expanded and complemented by the doctoral candidate, with this dissertation being one of the main outcomes derived from the project.

Additionally, although beyond the main thematic scope of this thesis, other outcomes from the analysis include a paleotopographic study inferred through passive seismic techniques on Vaguada de Las Llamas in Santander, presented at the 2023 Hispano-Portuguese Assembly of Geodesy and Geophysics ("Asamblea Hispano-Portuguesa de Geodesia y Geofísica", AHPGG) in Toledo, as well as a qualitative classification of double peaks and their correlation with mechanical differences within the sediments of the Guadalquivir basin. This latter work will be presented in June 2025 at the 38th International Meeting of Sedimentology in Huelva.

1.2. General geographical setting of the study areas

1.2.1. South-East Türkiye and northwest Syria

The East Anatolian Fault Zone is a major sinistral transform fault trending in a northeast direction, delineating the boundary between the Anatolian and Arabian plates. To the south, it connects with the Cyprus Arc and the Dead Sea Fault, while to the north it merges with the North Anatolian Fault. The triple junction located in the southern region marks

the convergence of the Anatolian, Arabian, and African plates, situated near the border between Türkiye and Syria (see **Figure *1***).

This region was the site of the devastating 2023 Türkiye-Syria earthquakes. The first earthquake, with a magnitude of 7.8, occurred between the towns of Gaziantep and Kahramanmaraş, followed by a second event of magnitude 7.5 approximately 30 km to the north, only a few hours later (see **Figure *1***). The provinces most affected in Türkiye included Gaziantep, Adıyaman, Kahramanmaraş, Osmaniye, Malatya, and Hatay, while in Syria, the regions of Aleppo and Latakia suffered significant impacts. These earthquakes are considered among the deadliest in Türkiye since the 1939 Erzincan earthquake and in Syria since the 1822 Aleppo event, making them the deadliest globally since the 2010 Haiti earthquake (USGS, 2023).

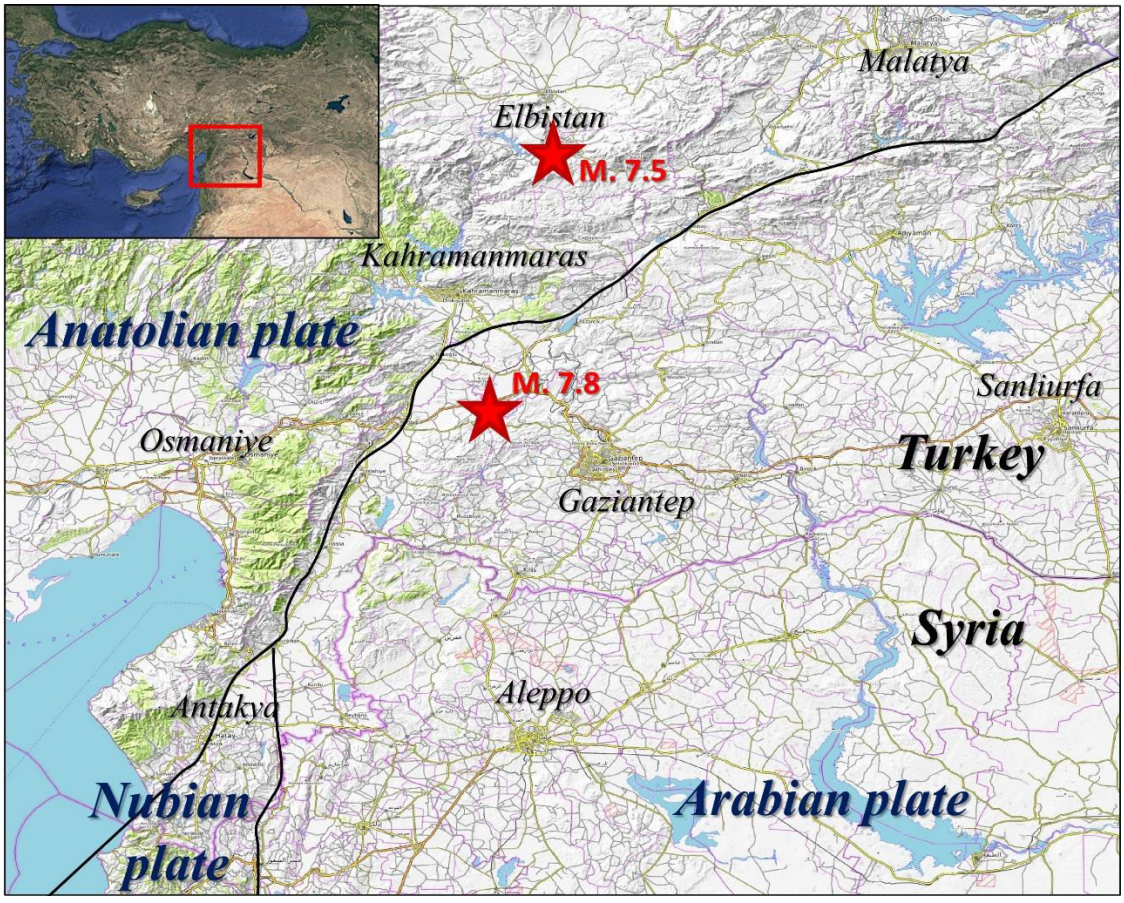

Figure 1. Figure illustrating the location of the study area. The approximate boundaries of the three major tectonic plates are depicted (black lines), along with the Türkiye-Syria border (purple line) and the approximate epicenters of the two main earthquakes.

The southwestern region of the East Anatolian Fault Zone is characterized by densely populated urban centers, each with a population exceeding one million inhabitants. This area serves as one of Türkiye most significant industrial hubs and is renowned for its

agricultural output, particularly pistachio cultivation, which underpins the production of its iconic baklava desserts. Additionally, the region is notable for its traditional carpet manufacturing industry.

From a geographical perspective, the region displays two markedly distinct landscapes. Southeast of the fault, the terrain is predominantly flat, with an average elevation of approximately 500 meters above sea level. In contrast, the northwestern area features rugged topography, with elevations exceeding 1,000 meters. The central part of the fault is characterized by extensive elongated plains that run parallel to the fault trace.

Southwest of the fault lies a broad gulf known as the Gulf of Iskenderun, which has a roughly rectangular morphology elongated in a NE-SW direction, running parallel to the primary fault structure.

The study area is located approximately between 36° and 39° longitude and 36° and 38° latitude.

This region is of particular interest due to its high seismic activity, its location on a tectonic plate boundary, the proximity of a triple plate junction, and its densely populated urban and industrial centers. Ensuring adequate seismic monitoring in such areas is essential for the development of accurate hazard maps.

Given the abundance of geological, seismological, and geophysical data related to the activity of the East Anatolian Fault Zone (EAFZ) and the contemporary relevance of seismic events in the region, this area was deemed particularly suitable for testing the "slice method" (Amador Luna et al., 2024a, subsection 5.1). This study compared two seismic datasets: one comprising highly reliable, relocated, and filtered data from Lomax (2023), and the other consisting of unfiltered raw data from AFAD (Disaster and Emergency Management Authority of Türkiye). The objective was to evaluate the utility of the slicing method and to identify critical factors in estimating kernel density (KDE).

Additionally, applying this technique enabled the visualization of the three-dimensional architecture of seismicity along this fault segment. The fault was further subdivided into distinct zones, with analyses conducted on the kinematics, structure, and rheology of each zone. These findings could contribute to the development of three-dimensional seismic

hazard maps, complementing existing two-dimensional models and enhance the geological understanding of the region.

1.2.2. Granada basin

The Granada basin, located in the southeastern Iberian Peninsula, is one of the Cenozoic basins forming part of the so-called Intramontane Betic Depression. This depression comprises a series of intermontane sedimentary basins situated in the central depressed areas of the Betic Cordillera. The basin exhibits an elongated, approximately rectangular shape oriented ENE-WSW and is composed of deposits resulting from the erosion and dismantling of the adjacent mountain ranges.

The basin spans the Granada Plain covering an area of approximately 2,000 km². It includes municipalities such as Granada, Albolote, Santa Fe, Atarfe, Pinos-Puente, Alhama de Granada, Huétor-Tájar, and Las Gabias, among others. Many of these localities have populations exceeding 10,000 inhabitants, with Granada city itself hosting over 200,000 residents.

The basin is bounded by Sierra Nevada to the east (brown in **Figure *2***), Sierra de Guajares, Sierra Tejeda and Sierra Almijarra to the south (purple colors), Sierra de Alhama and Sierra de Loja to the west (dark blue), and the Subbetic Zone to the north (greenish-blue colors). Some of these mountain ranges reach elevations exceeding 2,000 meters, such as Sierra Nevada and Sierra Tejeda.

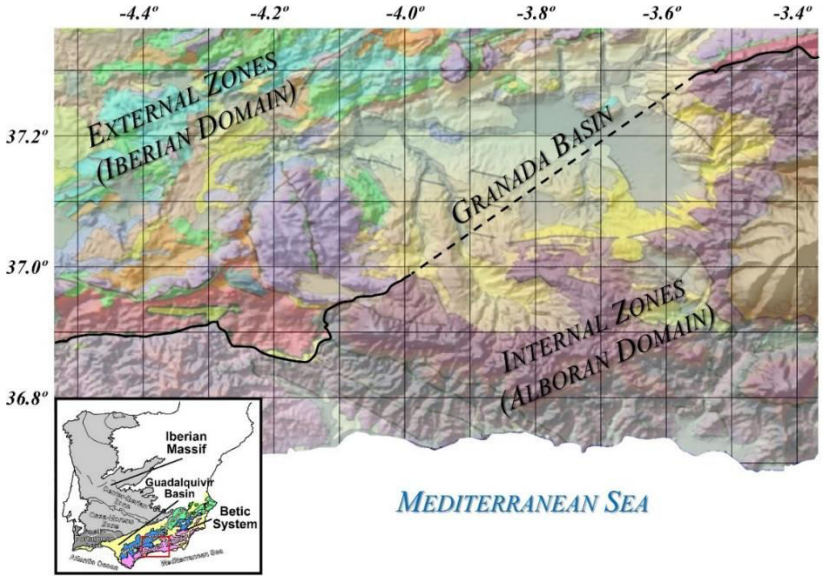

Figure 2. Geological map overlaid on a digital elevation model (DEM) to highlight the relief and main geological units of the area. The lower-left corner shows the location of the Granada basin in relation to the Iberian Peninsula,

emphasizing the three major domains of the southern region (Iberian Massif, Guadalquivir basin, and Betic Cordillera). The red rectangle highlights the detailed view area. Brown and purple shades represent the internal zones of the Betic Cordillera, while yellow and gray tones depict the Neogene-Quaternary sediments of the Granada basin. The northwestern sector shows materials of the External Zones of the Betic Cordillera, primarily in shades of blue, green, and orange. The Flysch Units of the Campo de Gibraltar are shown in red. The boundary between the Internal and External Zones of the Betics is represented by a solid black line, while the inferred position and orientation of this boundary beneath the basin sediments are depicted by a dashed line.

The Genil River, a major tributary of the Guadalquivir River, flows westward (E-W) across approximately 65 km of the study area. Originating at an altitude exceeding 2700 meters in the Sierra Nevada, at the confluence of the Guarnón, Valdeinfierno, Vacares and Real streams, on the northern slope of the Veleta and Mulhacen rivers. It traverses the Granada basin, passing through Granada city and exiting through Loja, where it forms a significant gorge. The Genil is the second longest river in Andalusia, after the Guadalquivir, and one of the longest rivers in the Iberian Peninsula. Beyond the basin, it flows through parts of Córdoba before joining the southern margin of the Guadalquivir. Several reservoirs along its course provide water to southern Granada, and the river is also renowned for its suitability for rafting.

The study area is situated approximately between the meridian of Sierra Nevada to the east and the western limits near Loja. It spans the latitude of Pinos Puente to the north and extends southward to the Mediterranean. Geographically, it is bounded by coordinates -3.5° to -4.4° longitude and 36.7° to 37.3° latitude.

The study area is of significant interest due to its high seismic activity. Over recent years, at least three seismic swarms have been recorded: December 2020–August 2021 (with over 3,000 earthquakes), August 2021 (exceeding 100 earthquakes), and October 2022 (more than 500 events). This makes the region one of the most seismically active zones within the Iberian Peninsula.

A total of more than 6,000 unfiltered earthquakes have been analyzed, extracted from the seismic catalog of the Spanish National Geographic Institute ("Instituto Geográfico nacional", IGN) spanning from 1997 to the end of 2023. Additionally, approximately 100 focal mechanisms and over 30 fault measurements from the Sierra Elvira region (Atarfe) have been examined. This comprehensive dataset aims to identify the principal active structures affecting the Granada basin, define their three-dimensional morphology, and refine the boundary between the underlying Internal and External Zones, concealed by Neogene sediments.

1.2.3. Western End of Guadalquivir basin

The third study area is situated in the western part of the Iberian Peninsula, within the Guadalquivir basin, specifically at its westernmost end near the river's mouth.

The Guadalquivir basin is a subtriangular basin oriented approximately N070ºE located between the Betic Cordillera and Sierra Morena (Iberian Massif). Through it flows the Guadalquivir River, originating at Cañada de las Fuentes at an altitude of around 1390 m (between the Cazorla and Segura Mountain ranges, in the province of Jaén) and emptying into the Atlantic Ocean at Sanlúcar de Barrameda in Cádiz. The river's margins exhibit markedly different characteristics. While tributaries on the southern margin have longer courses—such as the Genil, the longest tributary in Spain—and predominantly flow SE-NW from the Betics, those on the northern margin, from the Guadalimar in Jaén to the Guadiamar in Seville, are influenced by the orientation of the geological features of the Iberian Massif. These western tributaries display poorly articulated networks with a primary NE-SW or N-S orientation (Cano, 2004; 2016; see **Figure *3*A**).

In the western part of the basin, rivers exhibit a unique behavior: they abruptly change their orientation to an approximately N-S direction, contrasting with the gentle slope of the surrounding terrain to the southeast. The Guadalquivir River itself flows approximately ENE-WSW, parallel to the boundary between these two domains, until reaching Seville province at the western end of the basin. Here, it abruptly turns southward, assuming an almost N-S direction until it discharges into the Gulf of Cádiz (see **Figure 3A** and **B**). From this point—between the meridians of Aznalcóllar and Villamanrique de la Condesa—the western margin of the river features no major tributaries, with most being short first-order streams. In contrast, the eastern tributaries exhibit longer courses and more hierarchical drainage networks (see again **Figure *3***). The slope of the river margins in this segment is notably asymmetric, with the eastern margin having a gradient below 5%, while the western margin exceeds 30%.

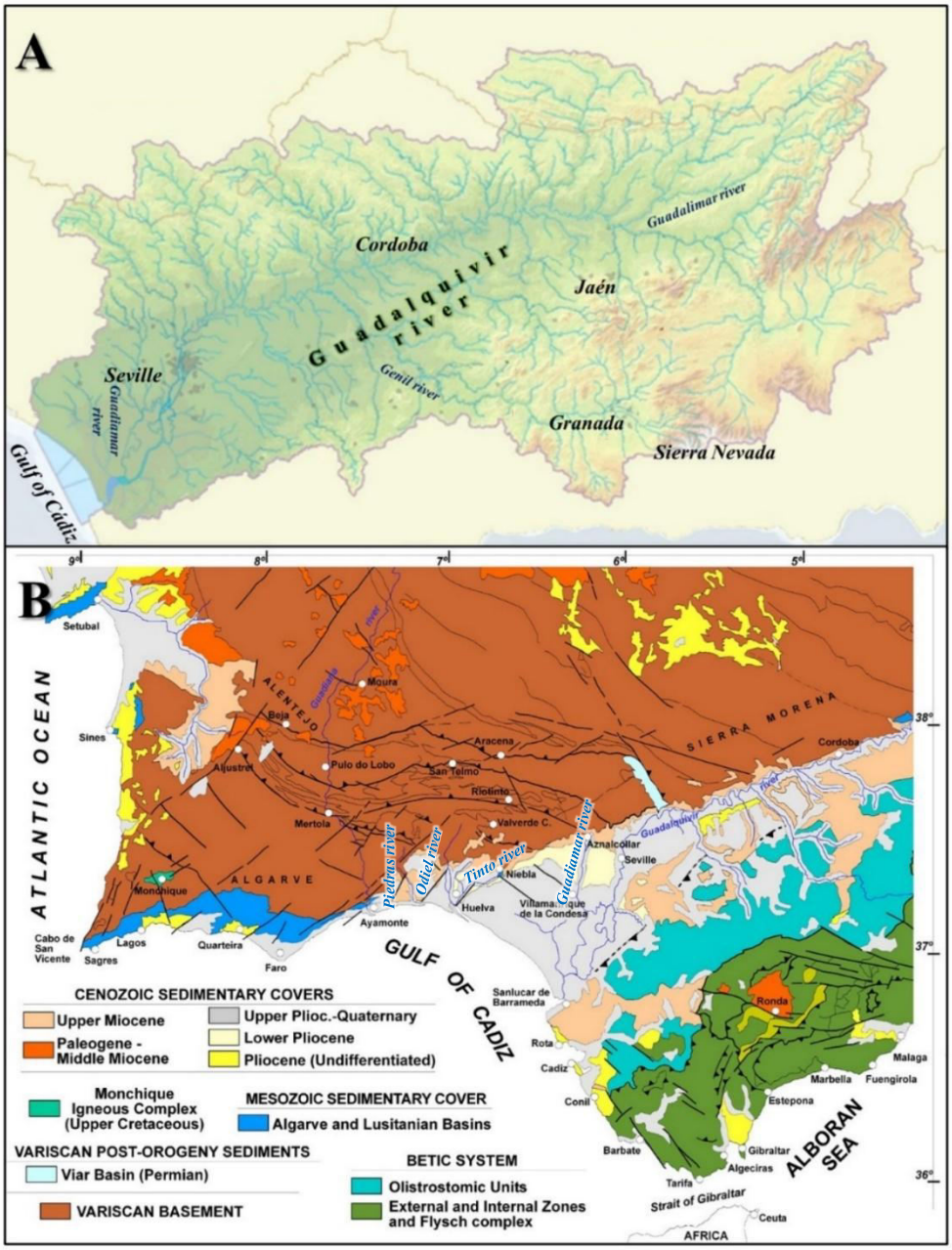

Figure 3. A. Map of the Guadalquivir River Basin District highlighting the main rivers mentioned in the text and the principal cities (modified from Plan Hidrológico Nacional, 2015). B. Geological map of the southwestern Iberian Peninsula showing the three major domains: Sierra Morena (Iberian Massif), the Guadalquivir basin, and the orogenic front of the Betic System. Faults within the basin, represented by simple lines, are inferred based on morphological features; however, no fault plane has been expliecitly identified (modified from Alonso-Chaves, 2020a).

The Guadiamar River, a tributary of the Guadalquivir, exhibits a similar pattern. Spanning approximately 80 km, the river originates at 300 meters above sea level and initially flows NW-SE from the Sierra de Aracena (Huelva). Near Aznalcóllar (Seville), it reorients to a NNE-SSW direction. In this segment, its western margin is characterized by a well-developed hierarchical drainage network, whereas the eastern margin consists of smaller, less-ordered first-order tributaries. A transverse profile of the river along this transect

reveals significant asymmetry in slope gradients, with the eastern margin exceeding 30% compared to the western margin, which is generally below 10%.

A similar situation is observed in the Tinto, Odiel, and Piedras rivers, which are located further west within the Guadalquivir basin in Huelva province. Such rivers drain directly into the Atlantic Ocean.

The Tinto River, non-tributary to the Guadalquivir, is globally renowned for its reddish waters caused by the sulfide-rich materials it traverses, which contribute iron and other metals. Flowing entirely within Huelva province for approximately 100 km, it empties into the "Ría de Huelva", where it converges with the Odiel River. The Tinto course is relatively sinuous until, a few kilometers northeast of Huelva city, it aligns in a pronounced N045ºE direction before meeting the Odiel in the estuary. The slope of its margins is highly contrasting, with the eastern margin being steep (exceeding 30%) and the western margin, where extensive marshes develop, having gradients below 5%.

The Odiel River originates in Sierra de Aracena at approximately 660 meters above sea level, also within Huelva province. It flows for in an approximately NW-SE direction until the reservoir of "Embalse del Sancho" on the north of Gibraleón, where it changes to a N-S direction. Near the Tinto-Odiel estuary, the river becomes confined between contrasting reliefs on either margin, with elevations exceeding 20 meters on the western margin and over 50 meters on the eastern margin ("los cabezos de Huelva"). The slope is gentler on the western side (exceeding 10%) but more abrupt on the eastern side (locally exceeding 50%). Adjacent to these reliefs lies an expansive marshland more than 4 km wide (the protected natural area of "Marismas del Odiel"), with gradients below 1%.

Finally, the Piedras River, a smaller system spanning just 40 km, originates at approximately 350 meters above sea level. It flows through three distinct segments: an initial NE-SW course leading to the Piedras Reservoir, followed by a NW-SE direction near Lepe, and a final NNE-SSW segment as it approaches its estuary. The river significant sediment load has formed prominent E-W-aligned coastal spits, which redirect its final course. The margins of the Piedras River share similarities with those of the Odiel, exhibiting contrasting reliefs with elevations exceeding 20 meters and slopes locally steeper than 30%, never dropping below 10%. In contrast, extensive marshlands, over 1 km wide with gradients below 1%, dominate the surrounding lowlands.

In the Ayamonte area the Guadiana River, with a north-south orientation, represents the southernmost end of the Guadalquivir basin and the limit of the investigated area.

The study area is situated in the southwesternmost part of the Guadalquivir basin, extending from the town of Aznalcóllar in the northeast to the city of Ayamonte in the southwest. This area encompasses the southern region of Huelva province and a portion of the southwestern region of Seville province, located between coordinates: 37.10º and 37.50º latitude, and -7.4º and -6.18º longitude. Passive seismic techniques were employed in this region to identify and model the basal structure of the basin, specifically its mechanical basement, which underlies the sedimentary deposits. These sediments conceal the subsurface structures that influence the present-day topography. While the overall study area encompasses a quadrangular region, the sampling efforts were confined to a triangular section covering the southern and southeastern sectors of the area, corresponding to the distal margin of the basin. A total of 319 passive seismic sampling points were strategically distributed across this section.

Due to restricted access to protected areas, such as the Odiel Marshes Natural Area (Huelva) and the Guadiamar Green Corridor (Seville), where vehicle entry and access to certain zones were limited, efforts were undertaken to maintain a sufficiently dense sampling grid to mitigate potential data gaps. Additional challenges arose from intense agricultural, industrial, and urban land use, which further constrained access to specific sites. As a result, sampling efforts were adapted to focus on public areas, including forest roads, walking paths, and other accessible locations.

1.3. Motivation and objectives.

As previously mentioned, plate convergence zones with complex tectonic interactions pose significant challenges to the geological understanding of these regions. Developing methodologies that enable three-dimensional visualization of these areas is essential, not only for advancing geological, geophysical, and seismological knowledge but also for improving the accuracy of seismic hazard and risk maps. In this regard, the hipothesis of this thesis is the development of methodologies for the three-dimensional reconstruction and analysis of complex areas.

The selected areas of study, the Eastern Anatolian Fault Zone (EAFZ) and the Granada basin, are characterized by high seismic activity and their proximity to densely populated

and industrialized regions. These areas provide a unique opportunity to test a novel technique for three-dimensional visualization using seismic records. Enhancing the quality and scope of seismic catalogs will further refine this technique and improve the resolution of the internal structure of these and similar regions. This methodology has potential applicability in analogous settings, such as the Azores-Gibraltar Fault Zone, the San Andreas Fault, and other regions with triple junctions. At the moment, techniques such as described here (the slice method) have begun to be explored in these areas. By validating this approach in highly complex tectonic contexts, it could also be extended to areas with less complexity to investigate active structures that influence regional dynamics.

Moreover, studying the forebulge zone of an active orogen —the elevated zone formed by the flexing of the lithosphere due to the weight of the orogene at the opposite end, such as the southwestern margin of the Guadalquivir basin, offers an opportunity to analyze how deformation partitioning in areas distant from the orogenic front explains surface features. These include the orientation of river courses and topographical reliefs, whose fault planes are often obscured by lithological conditions. By utilizing passive techniques, such as the H/V spectral ratio, seismic microzonation maps can be generated to determine the soil fundamental soil frequency and calculate the depth to the bedrock. This information can be used to produce three-dimensional maps of the sedimentary basin floor quickly and efficiently. These maps facilitate the identification of structures affecting both the basin's basement and overlying sediments, which, in turn, influence surface geomorphology.

Furthermore, this technique is currently being tested for detecting mechanical variations within sedimentary deposits to estimate the thickness of individual sedimentary layers. This approach has broad applications in industry, engineering, and construction. Additionally, it can be extended to other contexts with similar conditions, such as zones of intensely faulted regions or greisen within granitic rocks, to determine the thickness of altered zones. This versatility underscores the technique potential to contribute significantly to understanding the mechanical and structural properties of various geological settings, including areas with loose sediments overlaying a rocky basement.

This methodology demonstrates a significant leap forward in three-dimensional seismic and geological analysis, with potential implications for both scientific research and practical applications in hazard assessment, civil engineering, and resource exploration.

In this context, the objectives outlined within the framework of this doctoral thesis are as follows:

1) To analyze the seismic series that occurred along the Eastern Anatolian Fault Zone (EAFZ) in 2023 and identify the active segments during the event.
2) To examine the historical and instrumental seismic records of the Gibraltar Arc, with a specific focus on the Granada basin as one of the most seismically active areas in the region, delineating currently active structures and attempting to define the boundary between the internal and external zones beneath the basin.
3) To investigate the western sector of the Guadalquivir basin, particularly its northern margin in contact with the Variscan basement, in order to determine the morphology of the underlying basin using passive seismic techniques.

To achieve these objectives, several partial goals were established. Initially (objectives 1 and 2), these include:

- Comparison of two seismic catalogs: one unfiltered catalog containing a substantial volume of raw data where the Kernel Density Estimation (KDE) method will be applied, and another catalog that has been filtered and relocated to evaluate the efficiency of the filtering process.
- Identification of distinct seismogenic levels: levels with differentiated mechanical behavior in each studied region (EAFZ and Granada basin), enabling the creation of kernel density maps for each level.
- Three-dimensional identification of seismic structures and gaps: features affecting the various seismogenic levels.
- Comparison of density maps with other geological and tectonic data, including surface geology, plate kinematics, rheological profiles, focal mechanisms (from the literature), and surface fault data, either extracted from bibliographic sources or measured directly in the field (in the case of the Granada basin).
- Development of an applicable methodology for similar (or different) tectonic contexts.

Subsequently, the secondary goals focus on the western end of the Guadalquivir basin (objective 3):

- Collection of seismic noise samples: along the western margin of the basin, from Ayamonte to Aznalcóllar.

- To evaluate the applicability of the H/V Spectral Ratio to the Guadalquivir basin materials.
- Determination of the soil fundamental frequency at each sampling point and estimation of the depth to the bedrock.
- Identification of response types correlated with distinct structures: potentially associated with variations in geological conditions.
- Analysis of structural trends: identifying features that affect both the basement and sediments within the basin, shaping the landscape.
- Development of a three-dimensional model: of the southwestern edge of the Guadalquivir basin.

1.4. Thesis Structure

This doctoral thesis, written primarily in English and, in accordance with the regulations of the University of Huelva, begins with a general summary of its content, available in both Spanish and English. This is followed by this introductory chapter explaining the concept of seismotectonics, the relevance of its study, and its inherent limitations, followed by a brief presentation of the methods to be used for subsurface investigation. Subsequently, a section that briefly addresses the history of seismology, both globally and in Spain (seismological framework).

After establishing the historical-seismological framework, a general explanation of the methodology employed throughout this work is provided. Subsequently, a chapter is dedicated to the geology of the various study areas (East Anatolian Fault Zone in Türkiye and the Gibraltar Arc and Guadalquivir basin in Spain). The core of the research consists of individual subsections based on the articles derived from this study – whether published, submitted, or still under preparation. Each of these sections follows a standardized structure: abstract, introduction, geological settings, methodology, results and interpretation, discussion, and conclusions. While this arrangement may result in some conceptual redundancy between chapters, it ensures that each section can be read and understood independently.

The content of the subsections is as follows:

1. Kernel Density Estimation for the Interpretation of Seismic Big Data in Tectonics using QGIS: The Türkiye-Syria Earthquakes (2023)

This part applies and compares the use of Kernel Density Estimation (KDE) in the study of the 2023 Türkiye-Syria earthquake, utilizing raw data and interpretations derived from the analysis of a high-precision, reliable seismic dataset. The purpose is to present the "slice method" and demonstrate its utility and potential applications in other contexts, such as the Granada basin, which will be discussed later.

2. Kinematic Analysis of the Central and Southwestern Parts of the East Anatolian Fault Zone

This chapter presents interpretations derived exclusively from filtered, high-precision data. The East Anatolian Fault Zone is divided into six segments, and the three-dimensional distribution of earthquakes is analyzed in relation to local geological structures and the physical properties of the lithosphere. Additionally, a three-dimensional interpretation of the structural complexity along the eastern margin of Anatolia is provided.

3. Analysis of the recent seismicity at the Internal-External Zones Boundary of the Betic System in the Granada basin Using the Slice Method

This segment demonstrates the application of the previously presented slice method to recent, unfiltered seismic records at the boundary between the internal and external zones of the Betic mountain range beneath the Granada basin. The three-dimensional seismic distribution is presented, along with a potential interpretation of the active subsurface structures causing this activity, hidden beneath the basin.

4. Three-Dimensional Architecture of Foreland Basins from Seismic Noise Recording: Tectonic Implications for the Western End of the Guadalquivir basin

This chapter presents the interpretations resulting from the application of the H/V method to the materials of the Guadalquivir basin, the foreland basin of the Betic orogen. A three-dimensional view of the bedrock hidden under the western end of this basin is provided, identifying structures that disrupt and control the geomorphology. The shape and structures affecting the basin are consistent with deformation in the forebulge zone of this orogen.

Finally, the thesis concludes with a brief chapter summarizing the general conclusions, also presented in both Spanish and English, to provide a comprehensive overview of the work conducted.

SEISMOLOGICAL FRAMEWORK

2. Seismological framework

2.1. Brief history of seismology

Seismology, a fundamental branch of seismotectonics, is a discipline that integrates applied knowledge from mathematics, physics, engineering, and geology, deriving from the analysis and interpretation of seismograms. Unlike other scientific disciplines, it is relatively young, tracing its origins back to around the 1850s. Until then, earthquakes were mainly associated with divine wrath, a belief shared in both Europe and Asia. In the latter, for example, the first seismoscope was designed by Zhang Heng around 200 BCE. His device consisted of a big vessel with eight dragon heads oriented toward the main cardinal points, each holding a ball in its mouth, which would drop into the mouth of a frog when shaken, indicating the direction of the wavefront (Yan & Hsiao, 2006, 2007; Ceccarelli, 2007; Batlló, 2014; Shearer, 2019).

In classical Greece, new explanations for earthquakes began to emerge, associating them with the four natural elements. Thales of Miletus linked them to water, while Anaximenes attributed them to the Earth itself (Udías, 2024). Others associated earthquakes with fire, interpreting them as underground explosions caused by volcanic activity, as suggested by Anaxagoras (Shearer, 2019). Democritus, on the other hand, proposed a combination of all four elements. However, the most influential theory was that of Aristotle, who, in his treatise Meteorologica (*Μετεωρολογικά*), addressed topics of the Earth, such as meteorology itself, but also the study of oceans, lakes, and rivers, minerals, comets, and, of course, earthquakes and volcanoes (Aristotelis, 1887). In Book II, Chapters VII and VIII (*Περὶ σεισμοῦ καὶ κινήσεως γῆς*, "On the shaking and movement of the Earth"), Aristotle attributed earthquakes to air trapped in underground cavities, which, when escaping as exhalations (*ἀναζυμίασις*), would shake, move, and break these cavities, generating seismic activity (Wilsdorf & Schmidt, 1981; Agnew, 2002; Udías, 2024).

It was not until the great Lisbon earthquake of 1755 that new theories began to develop. One example is Michell's (1761) hypothesis, which proposed that earthquakes were caused by the propagation of waves from a specific point ("point of origin"). By studying the earthquake's effects and wave arrival times, he even attempted to estimate the depth of the focus. However, these ideas did not lead to further research at the time (Agnew, 2002; Davison, 1921). The first seismology commission was established after the 1783 Calabria earthquake, and nearly a century later, the 1884 Andalusia earthquake led to the

creation of three new commissions: one in Spain, one in France, and another in Italy (Agnew, 2002).

It was only in the early 19th century that the theory of elastic wave propagation was formulated, describing the main types of waves traveling through solid materials. This theory, developed by scholars mathematicians and physicists such as Cauchy, Poisson, Stokes, and Rayleigh, among others, forms the foundation for understanding seismic waves and earthquakes (Shearer, 2019).

These findings were applied to seismic studies by William Hopkins in the 1840s and Robert Mallet from 1848 to the early 1860s. Hopkins published analyses on crustal deformation and seismic phenomena, observing how wave arrival times could be used to locate earthquakes—what we now call the hypocenter (Oldroyd et al., 2007).

In 1857, a major earthquake struck the city of Naples, prompting Robert Mallet to travel there. He further developed the idea that earthquakes radiate from a central point, proposing that the displacement and direction of movement of an earthquake could be calculated, and that its point of origin could be determined by tracing the waves back to their source (Agnew, 2002; Shearer, 2019). Mallet created the most comprehensive seismic catalog of his time, along with the first map of seismic and aseismic zones of the Earth (Mallet, 1858). He also studied the rotation of obelisks in Calabria, concluding that their movement was likely caused by seismic waves. Additionally, he measured wave velocities in various sediments and hard granites using artificial explosions and high-precision clocks, determining that wave velocity was higher in the latter (Oldroyd et al., 2007).

It was also during this period that the first instrument for recording wave arrival times—the seismograph—was built. Filippo Cecchi developed it in 1875 in Italy, using pendulums connected to a clock (Shearer, 2019).

Modern seismology can be dated to the late 19th century when the Japanese government invited a large number of earthquake experts to the country. Among them was John Milne, founder of the Seismological Society of Japan and considered as the father of the modern seismology, who became the world's first professor of seismology, as well as Alfred Ewing, a mechanical engineer, and Thomas Gray, a telegraph engineer. Milne applied Mallet's principles to quantitatively study all aspects of earthquakes and elastic waves. However, he demonstrated that early seismometers were not sensitive enough, leading to

the development and improvement of these instruments (Herbert-Gustar & Nott, 1980; Agnew, 2002; Batlló, 2014). With all these improvements, Ernst von Rebeur-Paschwitz added more sensitive horizontal pendulums to measure small changes in the vertical axis, helping to record the first teleseism in Potsdam, Germany, as well as an earthquake in Japan (Rebeur-Paschwitz, 1889). Both Milne and von Rebeur-Paschwitz promoted the development of a global seismic network. In the USA, the first seismograph was installed in 1897, where the 1906 San Francisco earthquake was recorded shortly after (Shearer, 2019; Agnew, 2002).

In this period, a new series of seismometers where developed Emil Wiechert introduced a seismometer with a big pendulum of 17t, with much more sensitivity (Wiechert, 1904), and the first horizontal electromagnetic seismograph was presented by the prince Boris B. Golitsyn (the Galitzin seismograph) with an electromagnetic transducer and a pendulum damping with galvanometric-photographic recording, a seismometer that generate an electric current in a coil (Galitzin, 1902; 1903; 1905; 1907). This latter stabished several stations across Russia (Walker, 1910; Shearer, 2019).

With these advancements, Ernst von Rebeur-Paschwitz introduced more sensitive horizontal pendulums to detect small vertical changes, which facilitated the recording of the first teleseism in Potsdam, Germany, from an earthquake in Japan (Rebeur-Paschwitz, 1889). Milne and von Rebeur-Paschwitz played a crucial role in promoting the development of a global seismic network. In the United States, the first seismograph was installed in 1897, and it later recorded the 1906 San Francisco earthquake (Shearer, 2019; Agnew, 2002).

With the development of a better seismic network, the identification of Earth's internal structure began to take shape. It was in 1900 when Emil Wiechert suggested that the Earth’s interior could be subdivided in two layers, a metallic core that is enclosed in a rocky mantle (Wiechert, 1896; 1897). Later, Richard Oldham described the structure of the earth by identifying a series of seismic waves, which Wiechert and van den Borne later classified using the nomenclature P, S, and L only based on their shape and arrival time not their type (Agnew, 2002; Oldham, 1899). Shortly after, in 1906, Oldham also discovered the Earth's core by noting the absence of direct P and S waves beyond 100° from the earthquake source (Oldham, 1906; 1919).

A few years later, Mohorovičić analyzed data from the Kulpa Valley earthquake in Zagreb (Croatia), and identified additional seismic phases, which he attributed to a velocity discontinuity between the crust and the mantle at a depth of approximately 54 km in Central Europe—what is now known as the Mohorovičić discontinuity (Mohorovičić, 1910). In 1911, Augustus Love mathematically deduced the existence of another type of surface wave, which was later confirmed by seismic records (Love, 1911). Then, in 1914, Beno Gutenberg estimated the depth of the Earth's fluid outer core at approximately 2,900 km (Gutenberg, 1914a, b), and in 1936, Inge Lehmann discovered the existence of a solid inner core (Lehmann, 1936).

During the 1920s, seismology began incorporating a stronger mathematical component, focusing on wave propagation within the Earth. More refined seismometers were developed, such as the Wood-Anderson seismograph, specialized in detecting horizontal movement, and electromagnetic and strain seismometers, invented by Hugo Benioff (e.g., Benioff, 1935). The Wood-Anderson seismograph, in particular, played a crucial role in transforming Southern California into a key regional seismic network.

This period also marked the beginning of the use of artificial energy sources, such as explosions, for subsurface studies. Ludger Mintrop, a student of Wiechert and the discoverer of Mintrop waves, pioneered refraction seismology. He developed a portable seismograph capable of detecting waves generated by an impact. Mintrop later founded an exploration company that applied these techniques primarily to the petroleum industry, particularly in regions such as Mexico and the United States. His work involved measuring wave velocities between two distinct media with significantly different propagation velocities (e.g., Mintrop, 1941, 1947; von Schmidt, 1938, 1939; Maecker, 1949; Glassmeier, 2020).

In 1935, Charles F. Richter and Beno Gutenberg developed the first scale that related the magnitude of an earthquake to its size (Richter, 1935; Gutenberg & Richter, 1936, 1941). This logarithmic scale assigned a numerical value to quantify the energy released by an earthquake, aiming to distinguish less frequent, higher-magnitude earthquakes from more common, smaller ones, specifically in Southern California. To achieve this, they defined a magnitude 0 earthquake as one producing a maximum horizontal displacement of 1 micron on a Wood-Anderson seismograph located 100 km from the epicenter. Due to the limitations of this instrument, the scale could not accurately measure magnitudes greater than 6.8. Today, this scale is no longer in use, having been largely replaced by the moment

magnitude scale, also logarithmic, which is based on the total energy released by an earthquake. This modern scale was introduced by Hanks & Kanamori (1979).

With the onset of the Cold War, seismology advanced further, primarily for the purpose of identifying nuclear test sources. The first nuclear explosion, in 1945, was detected seismically, and from that moment on, seismic methods were employed to locate potential nuclear threats. One example of this application was the VELA-UNIFORM program, funded by the United States, which focused on detecting underground and underwater nuclear tests and contributed to the development of the Partial Test Ban Treaty (U.S. Department of Defense, 1961).

Over the past few decades, seismology has advanced tremendously thanks to improvements in instrumentation, data analysis, and computational modelling. Large global and regional seismic networks equipped with high-precision sensors have been deployed, significantly enhancing the detection and localization of earthquakes, including those of very low magnitude. Real-time telemetry and remote sensing have further facilitated the understanding of the Earth's active regions.

Focal mechanisms, once difficult to calculate, have become a routine tool for studying tectonics and mapping seismic activity patterns, thanks to refinements in fault rupture mechanisms. Seismic activity, previously considered an isolated phenomenon, is now explained within the framework of Earth's geodynamics, making it a fundamental tool for the development of seismic hazard maps and early warning systems. Examples of such systems include ShakeAlert (USA), SASMEX (Mexico), J-ALERT (Japan), or, in a minor scale, SAST o ALERTES-RIM (Spain).

Furthermore, NASA's InSight mission placed a seismometer on Mars, which is providing valuable information on Martian seismic activity, detecting marsquakes, meteorite impacts, and vibrations generated by the planet's atmosphere. However, despite these advances, many fundamental questions remain unanswered, such as the origin of deep-focus earthquakes or the processes that initiate fault rupture in the Earth's crust (or why they stop) (Shearer, 2002). These are some of the key questions for the future of seismotectonics. After all, this discipline is still relatively young, with its origins tracing back only about 150 years.

2.2. Seismology in Spain

The earliest beginnings of seismology in Spain can be traced back to Lucius A. Séneca, a philosopher, politician, orator, and writer from Córdoba, who wrote about earthquakes in his work *Quaestiones Naturales*. This treatise primarily explores natural phenomena occurring on Earth. In Book VI, *De terrae motu*, he discusses the earthquake in Campania, which is believed to have been a precursor to the eruption of Mount Vesuvius that destroyed Pompeii and Herculaneum (Séneca, reedited in 1929,1966; Udías, 2024).

In this work, Séneca seeks to explain these natural phenomena, concluding that their cause must lie within the Earth. Ultimately, influenced by Aristotle's writings, he attributes earthquakes to air trapped inside the Earth. In Spain, until the modern era, the prevailing belief regarding the cause of earthquakes was that they were primarily the result of air (or exhalations) confined within the Earth, which, upon release, would shake and fracture the ground, generating tremors. In some cases, also influenced by the movement of celestial bodies (Udías, 2024).

It was not until the late 17th century that the possibility of earthquakes being caused by fire and trapped air expanding and seeking an escape route was presented. This explanation was briefly addressed in the work Esphera en común celeste y terráquea (Zaragoza, 1675). This idea was based on *Mundus Subterraneus* (1664) by Athanasius Kircher, in which he proposed that the Earth is composed of three channels through which air, water, and fire circulate (*aerophylacios*, *hydrophylacios*, and *pyrophylacios*, respectively) (Kircher, 1664). According to this model, the *pyrophylacios* were responsible for volcanoes, and their interaction with air would produce earthquakes.

Shortly afterward, in the early 18th century, Spanish physician Andrés Piquer, citing Nicolas Lémery, proposed that earthquakes originated from the presence of bitumen, sulfur, and flammable materials inside the Earth, which caused explosions underground (Piquer, 1745). This hypothesis was originally suggested by Martin Lister, who associated the formation of brimstone (sulfur) and flammable gases with pyrite deposits within the Earth (Lister, 1684). This theory was later expanded upon by Isaac Newton and Georges-Louis Leclerc, Comte de Buffon (Udías, 2024).

Interest in earthquakes grew significantly in 1755, when, on November 1 of that year, the Lisbon earthquake struck. The earthquake occurred 300 km southwest of Lisbon (along the Azores-Gibraltar fault) and triggered both a tsunami and a fire—likely caused by the

collapse of candles lit for All Saints' Night. In Spain, the most significant damage was reported in Cádiz and Huelva. Numerous studies and reports were published about the event (Martínez Solares, 2001; Rodríguez Domingo, 2006; Udías & López Arroyo, 2009), but one of particular note is the work of Antonio Jacobo del Barco. A priest, professor, and ecclesiastical vicar of Huelva, del Barco lived through and documented the effects of the earthquake before, during, and after its occurrence. His descriptions were so detailed that his writings allowed for the identification of earthquake damage and even the effects of different types of seismic waves (Del Barco, 1756; 1996).

Following the earthquakes of 1801 (Atarfe, Granada), 1806 (Pinos Puente, Granada), and 1829 (Torrevieja, Alicante), and especially the Great Andalusian Earthquake of 1884 (Arenas del Rey, Granada), seismic studies began to gain particular importance. For example José Ponce de León emphasized that earthquakes should be studied through science—particularly chemistry and physics—excluding any divine intervention (Ponce de León, 1806). He attributed the earthquakes in Granada to three causes: aerial (resulting from the compression of air due to the collapse of underground caverns), igneous (due to the release of energy from pyrite decomposition), and electrical (caused by underground electrical discharges igniting combustible and volatile materials). He also examined the origin of the Sierra Nevada, its composition, and the height of its two highest peaks, Veleta (3,394 m) and Mulhacén (3,478 m). Ponce de León hypothesized that the gases responsible for earthquakes formed in the Sierra Nevada and traveled to Sierra Elvira, where he located the epicenter of the 1806 earthquake (Udías, 2024).

However, a new paradigm emerged in the mid-19th century. Charles Lyell, considered the father of modern geology, also studied the dynamic processes of the Earth's crust, laying the foundation for modern geology and suggesting that earthquakes result from fractures in the Earth's crust (Lyell, 1830 or 1847, spanish version). Mallet, previously mentioned, studied the Great Naples Earthquake and demonstrated that earthquakes propagate as waves, although he still supported the explosive origin hypothesis (Mallet, 1862). Around this time, theories emerged proposing that earthquakes result from vertical movements of crustal materials, which create faults and folds due to cooling. Alexander von Humboldt argued that wave propagation was a mechanical phenomenon rather than one dependent on rock composition (von Humboldt, 1848).

Eduard Suess and his disciple Rudolf Hoernes further developed this idea by distinguishing earthquakes into volcanic and tectonic categories, with the latter attributed

to fault movements (Hoernes, 1893). This classification was solidified by James D. Dana in his book Manual of Geology (1862), where he associated earthquakes with fractures in crustal materials. Additionally, during this period, Alexis Perrey compiled what is considered the first modern Iberian seismic catalog (Perrey, 1847).

The new ideas developed in the rest of the world slowly permeated into Spain. It was during this period that significant advancements were made in the study of geology: the School of Mines of Almadén was founded (1777), geognosy (geology) began to be taught in Madrid (1799), the title of Mining Engineer was established (1857), the Royal Academy of Exact, Physical, and Natural Sciences was founded, the Commission for the Geological Map of Spain was created in 1849 to oversee the geological mapping of the country, and in 1852, the Chair of Geology and Paleontology was established at the University of Madrid (Udías, 2024).

In 1869, Juan Vilanova y Piera, after becoming the first holder of the Chair of Geology and Paleontology in Madrid and participating in the Commission for the Geological Map of Spain, published *Manual de Geología Aplicada* (1869), the first modern geology textbook written by a Spanish author (Vilanova y Piera, 1860). In this work, he discussed the propagation of seismic waves, the use of seismometers for earthquake recording, and the close relationship between earthquakes and volcanoes—both of which he explained within the framework of Earth's geodynamics. He accepted the theory that earthquakes were caused by the cooling and contraction of the Earth's crust but did not entirely dismiss the influence of underground deposits of water, steam, and other flammable gases.

As can be seen, while the rest of the world was beginning to adopt a more modern understanding of the causes of earthquakes, Spain still adhered to classical perspectives. The Andalusian Earthquake was the turning point for introducing contemporary global ideas about earthquakes into Spain. This seismic event occurred on December 25, 1884, primarily affecting the provinces of Granada and Málaga. Its impact extended beyond Spain, drawing worldwide attention and responses in the form of both financial aid and scientific studies. This was the first Spanish earthquake to be the subject of modern scientific investigation, with technical reports evaluating the damage and soil conditions (López Arroyo et al., 1981; Udías, 2024).

As mentioned earlier, one of the key responses was the organization of three commissions—one Spanish and two foreign (one French and one Italian)—which

produced modern reports on the effects and causes of the earthquake. Additionally, more contemporary studies emerged, such as those by the Cadiz-born José Macpherson and the geologist from Malaga, Domingo de Orueta y Duarte, who attributed earthquakes to geodynamic processes in the Earth's crust. They argued that earthquakes were caused by the cooling and contraction of the Earth, leading to vertical movements and the formation of crustal fractures. This perspective discarded explosive and electrical theories (Macpherson, 1885). Orueta y Duarte further asserted that earthquakes were directly related to mountain formation (Orueta y Duarte, 1885).

By the late 19th century, with the development of new seismographs, the lack of seismological stations in Spain became evident, particularly after the Andalusian Earthquake. At that time, such stations were already being installed worldwide. In Europe, one of the selected locations for seismograph implementation was the Royal Observatory of the Navy in San Fernando (Cádiz) (Udías, 2024). The first instrument installed there was a Milne horizontal pendulum, followed later by additional horizontal and vertical Milne components, which were eventually complemented by new seismographs (Boloix Carlos-Roca, 1998). A catalogue of the early Spanish seismographs was compiled by Batlló & Borrman (2000) and Batlló (2004).

Later, Jesuit scientists established 75 observatories worldwide, including the Cartuja Observatory (Granada) and Ebro in Barcelona (Udías & Stauder, 1996; Anduaga, 2004; Ammon et al., 2010).

The Geographical and Statistical Institute (*Instituto Geográfico y Estadístico*), later known as the Geographical and Cadastral Institute (*Instituto Catastral y Geográfico)*, and currently the National Geographic Institute (*Instituto Geográfico Nacional,* IGN), was founded in 1870. In 1905, it assumed responsibility for the Seismological Service. Among its functions were:

- Development and monitoring of Spain's national seismic and volcanic surveillance plan.
- Planning and management of early warning and communication systems for national seismic events.
- Participation in international seismological networks.
- Conducting studies on seismic activity and updating the national seismic hazard map.

- Preparing regulations for earthquake-resistant construction.
- Planning and managing tsunami monitoring and warning systems.
- Participating in international tsunami warning networks and conducting studies on early warning systems for tsunamis.

The IGN appointed Eduardo Mier y Miura, a military engineer and geographer, to represent Spain in the International Association of Seismology (Mier y Miura, 1910). He laid the foundations of Spain's Seismological Service and proposed the installation of six seismological stations. However, only the Toledo Seismological Service Station was successfully installed in 1909 (Payo Subiza & Gómez-Menor, 1998; Anduaga, 2004; Udías, 2013). It was followed by the stations in Almería (1911), Alicante (1914), and Málaga (1915), with modernized instrumentation, transitioning from Milne, Vicentini, and Bosch-Omori seismographs to Mainka and Wiechert models (circa 1924; Anduaga, 2004, 2009). Eventually, the network expanded to include stations in Tenerife and La Palma (Canary Islands) (Udías, 2024).

The Spanish Civil War and the subsequent postwar period led to a decline in seismological research, as reflected in the apparent decrease in recorded seismic activity during that time (Rodríguez de la Torre, 1989). However, during the Cold War, as part of nuclear test monitoring, the United States installed an array of 19 seismological stations in Toledo, later expanded to 26 stations, which were integrated into the IGN in 1996. Additionally, in 1962, under the same program, two WWSSN (World Wide Standard Seismograph Network) stations were installed in Toledo and Málaga to study seismic waves, primarily generated by nuclear tests, marking a renewed interest in seismology (e. g., Alguacil & Martín Dávila, 2003; López & Muñoz, 2003; Martínez-Solares, 2003; Peterson & Hutt, 2014).

With the development of modern seismology in Spain, influential seismologists such as Alfonso López Arroyo, director of the Málaga Observatory and deputy director of the IGN, emerged alongside Agustín Udías, a Jesuit and currently Professor Emeritus of Geophysics at the Complutense University of Madrid. They were the first to analyze the seismicity and earthquake mechanisms in the Gulf of Cádiz and Cape St. Vincent, near the location of the 1755 earthquake (Azores-Gibraltar Fault), within the context of the emerging plate tectonics theory. This research was later expanded in collaboration with

Julio Mezcua Rodríguez, professor at the Complutense University of Madrid (Udías & López Arroyo, 1972; Udías et al., 1967).

Other significant research groups include the University of Granada, where a prominent team specializing in seismology, seismotectonics, and seismic risk was established. In 1989, this group was formalized as the Andalusian Institute of Geophysics and Seismic Disaster Prevention. Additionally, the Servei Geològic de Catalunya del Institut Cartogràfic de Catalunya and the Jaume Almera Institute of Earth Sciences (CSIC), now Geo3Bcn-CSIC, have played key roles in advancing seismological research.

One of the most significant projects was the Geodynamic Project, which involved a series of seismic profiles across the Iberian Peninsula and the Balearic and Canary Islands, with the Professor Udías as the coordinator (Buforn & Udías, 2022). The project also collaborated with the Spanish Navy to conduct marine explosions for seismic studies (Udías, 1977).

Currently, the IGN operates 115 real-time seismic stations connected to the Seismic Data Reception Center within the National Seismic Information Center in Madrid. In addition, other seismic networks contribute to national monitoring, including 22 stations in Catalonia, 17 stations within the Andalusian Institute of Geophysics at the University of Granada, and 11 stations forming the Western Mediterranean network, managed by the Complutense University and the Navy Observatory. These networks also collaborate with stations from the University of Évora (Portugal) and Mohammed V University in Rabat (Morocco).

2.3. Seismological methods for the subsurface exploration

As observed in the previous sections, seismic methods have been used for the study of the Earth—particularly in structural geology and geodynamics—since the early days of modern seismology and the development of the first seismometers. The analysis of early seismic records allowed scientists to identify and model the internal structure of the planet. Since then, seismic catalogs have been periodically reviewed and expanded, continuously improving earthquake detection, particularly for low-magnitude events, and refining data accuracy in Spain and worldwide (e.g., Carreño et al., 1991a, b; Benson et al., 1992; Martínez Solares, 1992, 1995; Batlló & Bormann, 2000; Alguacil & Martín Dávila, 2003; Mezcua et al., 2004; Anduaga, 2004; Batlló, 2004; Rodríguez de la Torre, 2004; Woessner & Wiemer, 2005; Schorlemmer et al., 2010; Tormann et al., 2010, 2012;

Yan & Ben-Zion, 2010; Peterson & Hutt, 2014; González, 2017; Sanchez-Roldán et al., 2021; Lomax, 2023; Fernández-Fraile et al., 2024; Lozano et al., 2025). These advancements have led to higher-quality seismic records and increased precision in key earthquake parameters (e.g., epicenter, depth, magnitude, focal mechanism), allowing for more accurate interpretations and subsurface structural modeling.

However, as previously mentioned in the preceding subsections, maintaining an accurate seismic catalog that records seismic events worldwide is not the only way to study the Earth's internal structure. New geophysical methods have been developed for seismic prospecting, categorized into active and passive seismic methods.

Geophysical seismic prospecting methods are based on analyzing changes in the propagation velocity of various seismic waves, whether they originate naturally or artificially, from internal or external sources. Internal sources refer to seismic waves generated within the Earth, including those caused by active faults, deep explosions, mining activities, and volcanic movements. While external sources originate at the surface, such as volcanic eruptions, rockfalls and landslides, meteorite impacts, or anthropogenic explosions. Among external sources, ambient seismic noise deserves special attention. This term encompasses low-amplitude vibrations generated by both natural phenomena (e.g., wind and atmospheric agents, tides and ocean waves, root movements, and microtremors) and human activities (e.g., vehicular traffic, building construction, mining operations, pedestrian movement, and industrial activity). Seismic methods serve as effective tools for mapping geological layers or structures and identifying underlying materials.

The primary difference between active and passive seismic methods lies in the origin of the vibration source.

Active seismic methods typically rely on an external (artificial) vibration source, such as an explosion or an impact on the ground, which generates seismic waves that propagate through the subsurface. These transmitted waves—of different types (e.g., P, S, Rayleigh, and Love waves)—interact with geological layers, either reflecting or refracting due to variations in mechanical properties, before being recorded by surface receivers known as geophones.

This approach traces back to the research of Robert Mallet, where he used gunpowder cartridges as a vibration source and discovered that each material has a unique wave

propagation velocity. A table listing the average velocities of different materials and other seismic properties can be found in Christensen (1965, 1974, 1979, 1982, 1985, 1989), Christensen & Shaw (1970), Chistensen & Fountain (1975) and Christensen & Salisbury (1975).

The data acquisition process involves deploying a series of geophones at a specific distance from the seismic source. Each geophone independently records the arrival time of the seismic waves, allowing for the estimation of wave velocity. Changes in velocity indicate variations in the composition of underlying materials.

The depth reached by this method depends on: the vibration source, the length of the sensor profile, the composition of subsurface layers, and the sensitivity of the geophones. And, obviously, the distance between the power source and the location of the geophones.

Several key properties can be inferred from wave propagation velocity, including rigidity or elasticity of the soil, density and contrasts in the mechanical behavior (differences in material composition).

The main applications of active seismic methods include hydrocarbon exploration, mining, geotechnical investigations and geological hazard assessment.

Although there are many active seismic methods, the most notable ones include:

Seismic Refraction Tomography Method. This method is based on the analysis of refracted seismic waves as they pass through subsurface layers with different wave velocities. As seismic waves travel through the ground, when they encounter a layer with a higher seismic velocity, part of the wave is refracted and propagates along this discontinuity. The refracted wave later returns to the surface, where it is recorded by geophones (with a velocity different from that of the direct wave). Geophones are deployed on the surface in transects or arrays (circular, triangular, or in 2D and 3D grids), positioned at specific locations and distances.

There are multiple interpretation methods, which can be categorized into two main approaches: refractor-interface modeling approach, which defines the depth and position of refracting layers using techniques such as, Delay-time method (e.g., Pakiser and Black, 1957), or Ray-tracing method (e.g., Musset and Khan, 2000). And Three-dimensional velocity tomography using inverse methods (e.g., Kirsch, 2006; Piip, 2009).

Although this technique has been widely used, other methods have gained prominence in recent years (e.g., Piip & Efimova, 1996; Leung, 1997; Rucker, 2002; Sheehan et al., 2005; Ostrowski et al., 2016; Abbas & Abdelgowad, 2024; Hamed et al., 2024; Abdelgowad et al., 2025). The seismic refraction method is useful for determining the depth of the bedrock, exploring aquifers, and studying faults and deep structures.

Furthermore, it is especially effective for analyzing the shallow subsurface, making it a commonly used technique in geotechnical applications (Lankston, 1990).

However, in complex geological settings, seismic reflection techniques are often preferred.

Seismic Reflection Method. This method is based on recording seismic waves reflected at the interfaces between subsurface layers. As seismic waves travel through the subsurface, they encounter a contrast in seismic impedance (the product of density and wave velocity), which causes part of the wave to be reflected back to the surface. The arrival time of these reflected waves is recorded by geophones, which are deployed in an array configuration with multiple receivers, spaced equidistantly, positioned at least on one side of the seismic source.

The depth of the reflectors is determined by aligning and comparing the recorded traces, which allows for subsurface imaging and the determination of contact depths and layer geometries (Mussett and Khan, 2000).

Both compressional (P) waves and shear (S) waves can be used in this technique. However, P-waves can penetrate denser and more porous materials but provide lower resolution of the bedrock surface. While S-waves offer higher resolution (Haines and Ellefsen, 2010; Pugin et al., 2013).

Due to its high resolution, seismic reflection is widely used for oil and gas exploration, particularly for identifying structural and stratigraphic traps, aquifer mapping and geothermal studies, cavity detection and fault and fold analysis or soil stability assessments and geotechnical evaluations.

However, this method is more expensive and requires advanced data processing, including static corrections for topographic variations, noise filtering, and time-to-depth conversion (migration) (e. g., Juhlin et al., 2000; Martínez & Mendoza, 2011; Lundberg et al., 2014; Sun et al., 2022; Wang et al., 2025).

Additionally, it often requires complementary geophysical, drilling, and mapping data to enhance accuracy (Mussett & Khan, 2000).

On the other hand, passive seismic methods, rely on ambient noise (whether natural or human-induced) without the need to intentionally generate seismic waves, while active seismic reflection requires a controlled seismic source. In passive methods, seismic data is recorded by a seismometer placed in the area of interest.

The SPAC (Spatial Autocorrelation) method, first introduced by Aki (1957), the f-k method (frequency-wave number; Lacoss et al., 1969 and Capon, 1969) and the ReMi (Refraction Microtremor) method (Louie, 2001), are based on the spatial correlation of seismic noise (primarily Rayleigh waves) recorded by seismometers arranged in an array. These methods allow for the determination of shear-wave velocity and subsurface characterization. Due to their non-invasive nature, these methods have widespread application in urban environments. Their primary uses include foundation assessment, hydrogeological exploration, and regional seismic analysis (e.g., Okada & Matsushima, 1989; Miyakoshi et al., 1998; Yamamoto, 1998; Chávez-García et al., 2005, 2006; Haney et al., 2012; Eker et al., 2012; Büyüksaraç et al., 2013; Takagi et al., 2014).

Among passive seismic methods, Horizontal to Vertical Spectral Ratio (HVSR) is the most well-known. The HVSR method utilizes seismic noise signals to estimate the properties of an unconsolidated sediment layer overlying a hard basement.

By measuring the three components of seismic noise (N-S, E-W and Z), it is possible to identify the fundamental frequency at a specific location. This is done by detecting amplitude peaks in H/V (horizontal components vs vertical) vs. frequency (Hz) graphs, which indicate frequencies that are being amplified by the soil itself (f_0).

This method is particularly useful in urbanized areas, where traditional seismic methods may be difficult or impossible to implement (Benjumea et al., 2011). Additionally, it can identify multiple peaks, which may indicate multilayered systems that require further analysis (Bard et al., 2004).

The HVSR method has been extensively studied and validated as a fast and cost-effective technique (e.g., Konno & Ohmachi, 1998; Bard, 1999; Enomoto et al., 2002), proving especially useful for seismic zonation (e. g., Alfaro et al., 1997a; Cheddadi, 2001; Navarro et al., 2002, 2007, 2014; Caselles et al., 2010; Macau et al., 2016).

This technique is highly valuable as either a primary or complementary source of information for deep basement determination, sediment thickness estimation, structural recognition, glacial mapping, microzonation, and geotechnical studies, among others.

Further details on this method will be provided in the following section, as HVSR has been selected for the study of the Guadalquivir basin.

A separate mention should be made of the Multichannel Analysis of Surface Waves (MASW) method. This technique is used to obtain subsurface shear-wave velocity profiles in 1D (depth) (e. g. Park et al., 1999; Xia et al., 2002), 2D (depth and surface location) (e. g. Miller et al., 1999; Ivanov et al., 2001; Socco et al., 2010; Martínez-Pagán et al., 2012), or even 3D (e. g. Miller et al., 2003).

MASW is based on the dispersion properties of surface waves (mainly Rayleigh waves) recorded with a multichannel acquisition system (typically 24 or more channels). It utilizes low-frequency surface waves (e.g., 1–30 Hz) and is applied to shallow investigations (a few tens of meters).

This method can be implemented in both active and passive modes: active MASW, that uses a sledgehammer as an energy source (e.g., Xu et al., 2006) or passive MASW, which relies on seismic noise (e.g., Park & Miller, 2008; Dou et al., 2017). MASW can be considered a hybrid method (e. g., Park et al., 2007).

MASW is widely used in civil engineering and geophysical studies, including cavity detection (e. g., Xu & Butt, 2006; Tallavó et al., 2009), bedrock mapping (e. g. Miller et al., 1999), seismic site characterization (e. g., Kanli et al., 2006; Mahajan et al., 2007; Martínez-Pagán et al., 2014), and Poisson's ratio studies (e.g., Ivanov et al., 2000).

METHODOLOGY

3. GENERAL METHODOLOGY

3.1. Fieldwork

For both the Granada and Guadalquivir basins, multiple field campigns were conducted. The field methodology encompasses all processes related to surface geological prospecting, including literature review, virtual area assessment using IGME geological maps, orthophotos, and Google Earth, campaign planning and sampling area selection, in-situ lithological identification, sample collection, measurement of S_0 (primary layering), foliation, faults, and striations, and, in the case of passive seismic surveys, seismic noise recording.

The self-produced maps, inspired by the literature and maps provided by the IGME and analogous institutions from other regions, were created using Macromedia FreeHand MX v11.0.1.

3.2. Seismic record: The slice method.

Kernel Density Estimation (KDE) is a non-parametric method that defines a probability density function for a random variable, such as an earthquake hypocenter. By grouping these hypocenters into seismogenic layers, KDE facilitates the generation of density maps at different depths (referred to in this study as "slices"), identifying regions with high earthquake concentration. This approach enables a three-dimensional visualization of underlying active structures.

Seismic catalogs from various institutions (e.g., IGN, KOERI, AFAD, USGS) provide access to critical seismic data for the study area. These datasets allow the construction of graphs depicting the relationship between earthquake occurrence and depth (see **Figure *4***) as well as the frequency–magnitude distribution based on the Gutenberg-Richter law. This methodology enables the delineation of layers with similar seismic behavior, separated by regions of low earthquake density. Changes in seismic frequency, which typically decrease with depth, may indicate lithological transitions or, more broadly, reflect variations in the mechanical properties of crustal and lithospheric materials.

The regional physical properties of these materials, particularly their resistance, can be characterized through the analysis of the b-value in the Gutenberg-Richter law. Variations in this parameter provide insights into the mechanical behavior of geological formations and the geodynamic processes influencing seismic activity in the study area.

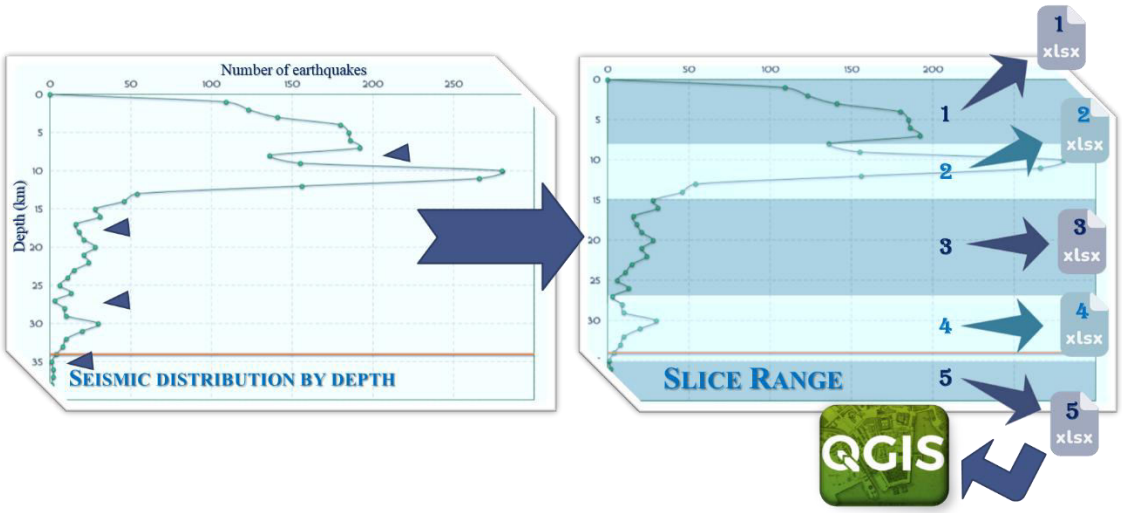

Figure 4. Graphical representation of earthquake depth distribution and the process of selecting depth ranges. The orange line in the figure represents the depth of the Mohorovičić discontinuity (Moho), as reported in the literature for this region.

Once the depth ranges are defined, seismic event data corresponding to each slice are exported as separate Excel files for subsequent processing in QGIS. These datasets must include essential parameters such as earthquake coordinates, depth, and magnitude, among others.

Particular attention must be paid to institutional datasets, as some organizations assign fixed depths to certain seismic events to expedite the computation of additional parameters. These predefined depths may lead to the artificial identification of high-density seismic zones that do not necessarily correspond to actual brittle deformation zones. In this regard, the Instituto Geográfico Nacional (IGN) provides datasets that include all relevant seismic information while marking fixed-depth values with an "f". These datasets are readily accessible for earthquakes occurring after November 1997, but not for previous events.

The exported files must be converted from XLSX format (native to Excel) to Shapefile (SHP) format, which is compatible with QGIS. Once converted, these files serve as the basis for generating heat maps or Kernel Density Estimation (KDE).

KDE is a statistical analysis technique that applies a window function to define an area of influence around each data point. The function assigns a specific weight to points within this area based on a selected kernel function, while points outside the range are assigned a value of zero. In this process, the bandwidth—which determines the influence radius of each point—must be specified. In QGIS, this parameter can be expressed in:

meters, degrees, or map units. Additionally, the kernel method must be selected, as it defines how the parameter values are distributed within the specified range.

For this study, influence radii ranging from 0.02° to 0.04° were used, depending on the study area's extent. A pixel size of 0.001° was chosen, which determines the resolution of the resulting map. The quartic kernel function, as defined by Silverman (1986) (1), was applied for KDE calculations. (see **Figure 5**).

$$K(x) = \frac{15}{16}(1 - x^2)^2 \quad (1)$$

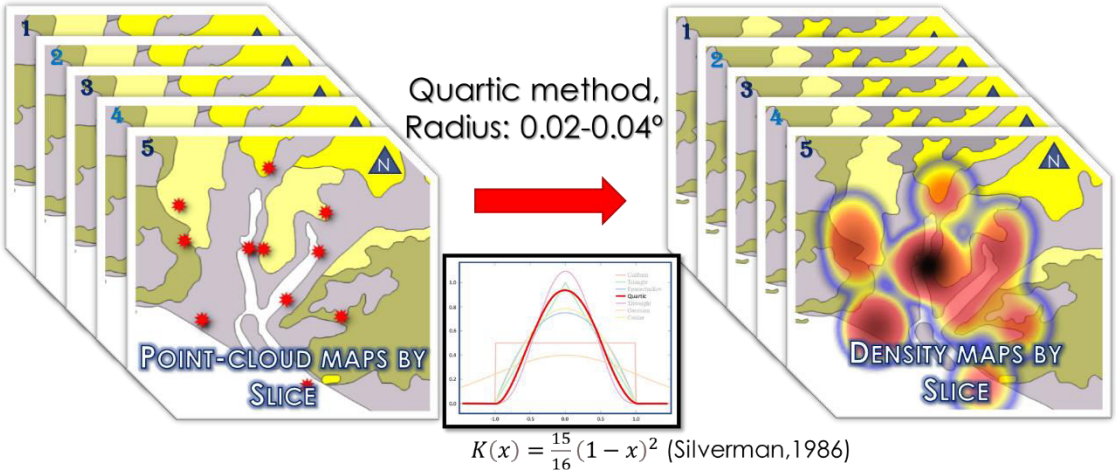

Figure 5. Schematic representation of the workflow in QGIS, including the Silverman equation, which was applied for the quartic kernel method.

The effects of variations in the different parameters are analyzed in the Results section, specifically in Subsection 5.1.

Finally, the color range is defined based on quartiles: First quartile, blue; second, yellow; third, red; and, forth, black. Since the range is continuous, intermediate colors emerge as a result of blending between adjacent quartiles.

3.3. Passive seismic: HVSR (Horizontal-to-Vertical Spectral Ratio) Method.

The HVSR (Horizontal-to-Vertical Spectral Ratio) method, also known as the H/V spectral ratio, is a passive seismic technique derived from the Nakamura method (1989). It is based on the recording of ambient seismic noise, enabling the analysis of both natural and anthropogenic ground vibrations to determine the soil fundamental frequency (f_0). This parameter is closely related to the thickness and shear-wave velocity of the sedimentary cover in a basin, following the relationship proposed by Bard (1985) (2):

$$f_0 = \frac{V_S}{4h} \quad (2)$$

Where, V_S is the shear wave velocity and h is the depth of the bedrock.

The HVSR method has proven to be a cost-effective, rapid, and highly efficient approach for delineating the geometry of a concealed bedrock surface (e.g., Ibs-von Seht & Wohlenberg, 1999; Delgado et al., 2000; Parolai et al., 2002).

Although Nakamura (1989) popularized the technique due to its simplicity, reliability, and low cost for site-effect estimation, it was originally proposed by Nogoshi & Igarashi (1970, 1971). This method calculates the ratio between the Fourier amplitude spectra of the horizontal (average of the seismic noise in N-S and E-W directions) and vertical components of seismic noise to estimate the soil fundamental frequency. Due to its simplicity, it quickly gained popularity. Lermo & Chávez-García (1993) applied this method to S-wave seismic records and developed the theoretical foundation for the numerical inversion of SV-waves. Later, Yamazaki and Ansary (2008) expanded this approach to include site characterization, terrain classification, and other applications.

Subsequently, many researchers applied this method to site-effect studies and seismic microzonation in different regions (e.g., Lermo & Chávez-García, 1993; Ansary et al., 1995; Field et al., 1995; Theodulidis & Bard, 1995; Alfaro et al., 1997b; Duval et al., 1998, 2001a, b, ; Konno & Ohmachi, 1998; Bard, 1999; Ibs-von Seht & Wohlenberg, 1999; Alfaro et al., 2001;; Fäh et al., 2001; Lebrun et al., 2001; Lombardo et al., 2001; Delgado et al., 2002; Huang et al., 2002; Parolai et al., 2002; Nguyen et al., 2004; Panou et al., 2005; Bonnefoy-Claudet et al., 2003, 2004, 2009; Castellaro & Mulargia, 2009).

Of particular note is the work of Ibs-von Seht & Wohlenberg (1999), who identified a strong correlation between the soil fundamental frequency, measured using passive seismic techniques, and the thickness of the sedimentary cover overlying bedrock.

In Europe, this method has played a key role in the SESAME project (Site EffectS Assessment using AMbient Excitations), which aimed to evaluate the reliability of H/V and array techniques for site-effect estimation and seismic risk mitigation in urban areas. The project also sought to develop guidelines for the application of this technique (Bard et al., 2004).

Currently, the HVSR method is widely used for subsurface seismic property characterization, including site classification, site-effect analysis, and velocity structure

inversion, among other applications (e.g., Atakan et al., 2004a, b; Harinarayan & Kumar, 2017; Ji et al., 2017; Macau et al., 2015; Pinzón et al., 2019; Putti & Satyam, 2020; Xu & Wang, 2021).

Specifically, in the Guadalquivir basin, the HVSR method has proven to be a particularly effective tool for studying the underlying bedrock geometry (e.g., Alonso-Chaves et al., 2019, 2020b; Amador Luna et al., 2023b, 2024b; Macau et al., 2016; ICGC, 2016), enabling the identification of structures that influence the basin's bedrock configuration and geomorphology.

The soil fundamental frequency is the frequency value (measured in Hz) at which the ground naturally tends to oscillate when subjected to external vibrations. This concept is directly linked to soil resonance, a phenomenon in which certain vibrations are amplified when the frequency of incoming waves matches the fundamental frequency of the ground.

In this context, the thicker the sediment deposit, the lower its fundamental frequency.

This technique was employed in the westernmost part of the Guadalquivir basin through 319 passive seismic sampling points distributed southeast of the boundary between the Variscan basement and the basin's sediments. The goal was to extend the data from the outcropping materials to the northwest, towards the interior of the basin to the southeast.

Seismic noise measurements were made with a SARA SL06 digitizer and a Lennartz LE 3D/5s triaxial seismometer, with a natural frequency of 0.2 Hz. Exceptionally, Lennartz LE-3D/20s, with natural frequency of 0.05 Hz were employed in areas presumed to have greater basement depths (southeastern portion of the study area).

The system also includes a GPS connected to the device to record the location and UTC time of the site. The power supply for all the instrumentation is provided by a small 12 V battery. Finally, due to the sensitivity of the device, it must be covered with a plastic shield to protect it from fluctuations caused by wind. Additionally, the equipment should be placed in locations away from any potential disturbances, such as frequent pedestrian traffic, vehicle movement, tree root motion, or vibrations generated by high-voltage towers.

The recording time is determined by the depth of the basement. For greater depths (low frequencies), longer measurement times are required. For sampling, approximately 30 minutes were recorded in the more northern areas (where the basement is closer to the

surface), and just over an hour in the southern areas (where the basement is deeper). The most common recording time was around 45-50 minutes.

Once the signal was exported to the computer, it was processed using Geopsy software (Whatelet et al., 2020), which transforms the signal from the time domain to the frequency domain, filters high frequencies, and calculates the soil fundamental frequency. This is done through the ratio of Fourier spectra of the horizontal components (average of N and E) and the vertical component (Z), resulting in a plot of H/V amplitude vs frequency (Hz) (see **Figure *6***). The detection limit for the soil fundamental frequency is set between 0.2 and 20 Hz. The peak with the lowest frequency and highest amplitude (in most cases) represents the soil fundamental frequency. The peak will have greater amplitude and narrower width the greater the mechanical contrast between the "soft" sediment cover and the underlying hard rock basement.

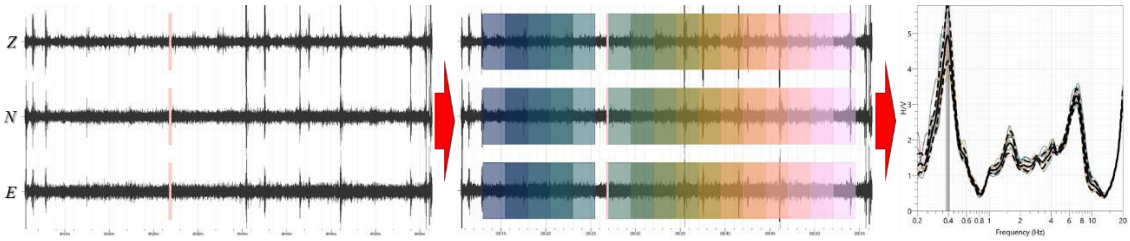

Figure 6. Illustrative diagram of the transformation performed by the Geopsy software. On the left, the seismic noise record obtained at a station for the three components (vertical, Z; horizontal, N and E). In the central zone, the number of selected windows (for the given time) used for the calculation of the Fourier spectra and transformation to the H/V vs. frequency plot. On the right, the H/V graph for the mentioned station. The extreme windows (at the beginning and end of the record) were removed due to noise introduced during the setup and dismantling of the equipment. The colored lines represent the H/V graph for each of the selected windows shown in the previous figure. Dashed lines indicate the error, while the thick black line shows the mean. The gray bands represent the f_0 and the estimated error.

The time established for the calculation windows ranges from 200 to 300 seconds, with the most frequent value being 300 seconds (larger measurement windows reduce errors due to external noise). The number of calculation windows varies between 10 and 20, with the most common value being 17 windows (a larger number of windows reduces the resulting error). It is important to maintain a balance between time and the number of measurement windows.

As shown in **Figure *6***, the H/V graph exhibits a narrow and clearly identifiable peak, with a very low determination error. This graph is representative of most stations. This enabled a clear identification of the fundamental frequency, and therefore, the depth of the bedrock.

Traditionally, this peak must have an amplitude greater than 2H/V to be considered as f_0.

As will be discussed in the corresponding subsection (5.4), the calculation of the boundary between the mechanical basement (which is not necessarily geological, as there can be hard materials different from the geological basement that act as the bedrock layer) and the sedimentary cover can be determined from the f_0 and the S-wave velocity (V_S). However, this information is not always available a priori. In such cases, empirical equations must be constructed that relate this f_0 to the depth of the basement (h). As shown below, the equation used has been refined for the Guadalquivir basin, combining data from the H/V spectral ratio method, array techniques (seismometers like the one used in this study arranged in a triangular layout with progressively increasing concentric radii), and mechanical drilling data reaching the bedrock.

Finally, the data were processed using Excel LTSC MSO (v. 16.0.1), contour maps were generated through kriging interpolation using Surfer (v. 15.6.3), and subsequently overlaid with geological data using QGIS (v. 3.32).

GEOLOGICAL SETTING

4. GEOLOGICAL SETTING

4.1. Introduction

As previously mentioned, the study areas are threefold: the Eastern Anatolian Fault Zone (EAFZ), the Granada basin, located within the Betic Cordillera, which corresponds to the northern part of the Gibraltar Arc, and the Guadalquivir basin, its associated foreland basin. The following sections will provide a brief overview of the general geology of the area, followed by a more detailed discussion of the specific study area in the results section.

4.2. The plate boundary between Anatolia and Syria

Anatolia is a peninsula surrounded by the Black Sea to the north, which represents the back-arc basin of the orogen, formed during the Cretaceous as a result of the subduction of the northern Neo-Tethys Ocean (e.g., Görür, 1988); by the Aegean Sea to the west, which formed during the Oligocene due to the N-S extension of the Hellenic Subduction Zone (e.g., Jolivet, 2001); and by the Eastern Mediterranean to the south, representing the southern branch of the Neo-Tethys, which is older than the other basins (e.g., Garfunkel, 2004).

Geologically, the entire region is mainly divided into three major tectonic domains: the Pontides, in the northern part of the area; the Anatolides-Taurides, in the central region; and the Arabian Platform, in the southeast (Ketin, 1966). These units are now separated by suture zones that correspond to ancient oceans.

The Pontides are considered part of the Laurussian block, with units similar to those in the Balkan region, the Caucasus, and Central Europe. This domain was part of the northern branch of the Neo-Tethys, which resulted in the İzmir-Ankara-Erzincan Suture (e.g., Okay & Sahintürk, 1997; Robinson et al., 1995; Topuz et al., 2007; Ustaömer et al., 2005; Ustaömer & Robertson, 1994).

The second domain, the Anatolides-Taurides, has Gondwanan affinities and is separated from the Pontides by the southern branch of the Neo-Tethys. Its contact with the Arabian Platform occurs along the Assyrian Suture, mainly represented in the Arabian region. The northern margin of the Arabian Platform is marked by Southeastern Anatolia, south of the Assyrian Suture, where the study area is located (Okay, 2008; **Figure** *7*).

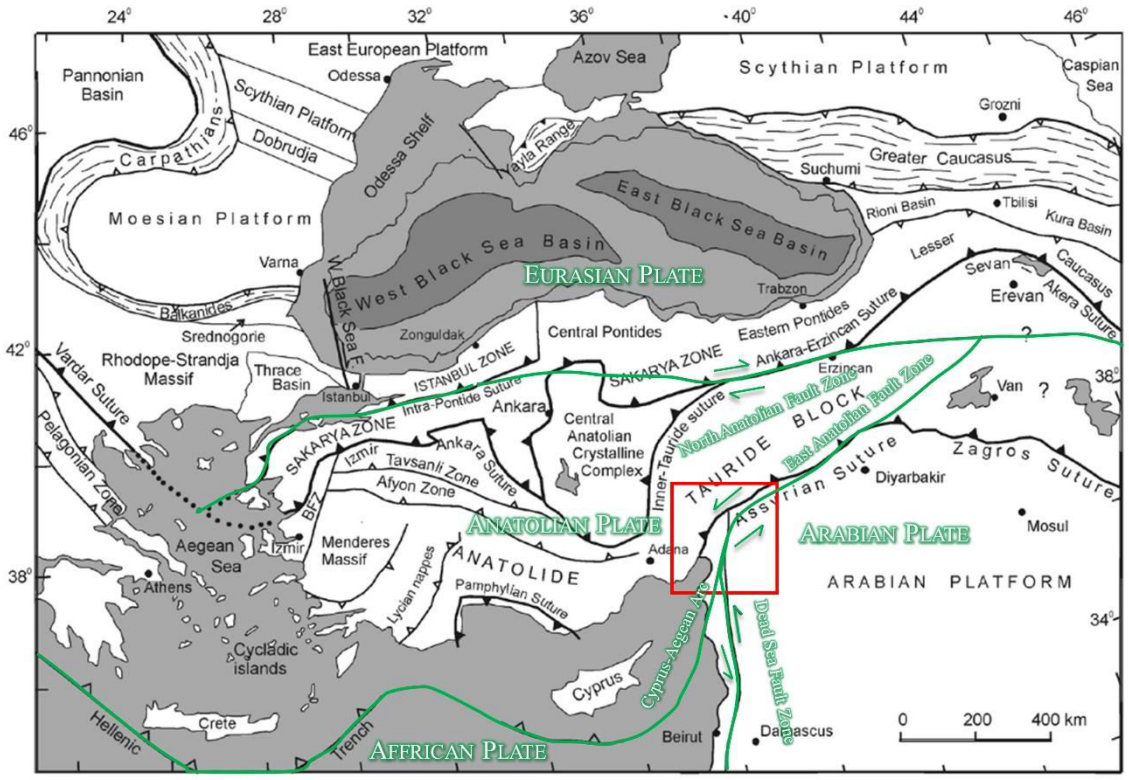

Figure 7. Simplified tectonic map of Anatolia and nearby region. The study area is highlighted in red, while approximate plate boundaries and relative movements are shown in green (Modified from Okay, 2008).

The main structure characterizing the study area is the East Anatolian Fault Zone (EAFZ), a sinistral transform fault trending NE-SW, which separates the Anatolian Plate (to the NW) from the Arabian Plate (to the SE). To the north, it is bounded by the North Anatolian Fault Zone (NAFZ), another major dextral transform fault trending E-W, which separates the Eurasian Plate (to the north) from the Anatolian Plate (to the south). To the south, it connects with the Dead Sea Fault and the Aegean-Cyprian Arc, where subduction processes occur between the Anatolian and African Plates.

This region is the result of a complex collision between the Eurasian, Anatolian, Arabian, and African Plates, leading to a highly intricate tectonic setting with several triple junction zones, mainly located in the eastern part of the peninsula, which exhibits a high seismic recurrence rate. One of these triple junctions is located very close to the epicenter of the February 2023 earthquake, at the convergence zone between the Arabian, Anatolian, and African Plates.

The morphology of Eastern Anatolia can be divided into three main areas: the Pontide Belt to the north, the Bitlis Massif in the central region and the Southeastern Anatolian Para-autochthon to the south. The Bitlis Massif represents the thrusted and metamorphosed margin of the latter (Göncüoğlu, 2010). These units are separated by a

foreland thrust and fault belt, including the Bitlis-Zagros Suture Zone and the Assyrian Suture Zone.

The exposed rock formations in the study area range from the Precambrian to the Quaternary, with a cover of Neogene-Quaternary sedimentary and volcanic rocks. The southern part of the region features a continuous sedimentary sequence from the Paleozoic to the Miocene, while the northern part is dominated by metamorphic and metasedimentary rocks of the autochthonous basement (Hall, 1976; Pearce et al., 1990).

Between the Bitlis Massif and the Arabian foreland, an ophiolitic complex has been identified, along with Late Cretaceous island arc rocks and Eocene pelagic mafic lavas, which were trapped following the continental collision (Robertson & Aktaş, 1984; Pearce et al., 1990; Yilmaz, 1993; Günay et al., 1990). The oldest rocks (Precambrian) are found in the cores of anticlines (Ketin, 1983).

The tectonic style and current morphology of the Anatolian region are influenced by the evolution of the Tethyan oceans, particularly the Neo-Tethys, which has significantly shaped the tectonic patterns of the peninsula. As this ocean closed in eastern Turkey during the Miocene, the collision between the Eurasian and Arabian plates along the Bitlis-Zagros suture gave rise to the high topographic features of southeastern Turkey, known as the Eastern Turkish High Plateau (Şengör et al., 2008).

The main local tectonic structures tend to align parallel to the East Anatolian Fault Zone (EAFZ), exhibiting faults with various orientations that correspond to strike-slip, transpressional, and transtensional tectonic settings (Duman & Emre, 2013). The EAFZ can be primarily subdivided into two main branches: the Northern Strand (Sürgü-Misis Fault System), oriented east-west, where the second major earthquake of the February 2023 seismic event occurred. And the Main Strand, oriented northeast-southwest, which marks the boundary between the Anatolian and Arabian plates. This segment of the transform fault follows a N060E direction, extending from Karlıova to Antakya, where it connects to the Cyprus Arc and the Dead Sea Fault Zone.

Near Gaziantep, the fault changes orientation to approximately north-south, which is the area where the first high-magnitude earthquake occurred. It is also important to highlight the existence of a fault considered a splay fault of the Main Strand—the Nurdağı-Pazarcık Fault (NPF)—located between Kahramanmaraş and Gaziantep. This fault runs

subparallel to the Main Strand and was the site of the initial rupture, which then rapidly propagated to the Main Strand (Okuwaki et al., 2023; Čejka et al., 2023).

4.3. Gibraltar Arc

The Iberian Peninsula is an area with significant seismic activity, particularly in the Gibraltar Arc, located to its south (**Figure *8***, left). Over 30,000 earthquakes were recorded in this area between 1370 and 2020, spanning a wide range of depths, from shallow to deep (>600 km), with some events exceeding depths of 300 km. This region marks the boundary between the Eurasian and Nubian plates, exhibiting a diffuse seismicity spread across a band approximately 300 km wide (Udías & Buforn, 1991; Galindo-Zaldivar et al., 1993).

Historically, the area has experienced high-magnitude earthquakes, as mentioned in the previous section. Using the kernel density estimation method, it is possible to highlight the regions with the highest seismic activity within this zone (**Figure *8***, right). The kernel method identifies approximately five areas of high seismic frequency, which coincide with the locations of historical large-magnitude earthquakes, such as the Granada basin, Lorca, and Al Hoceima.

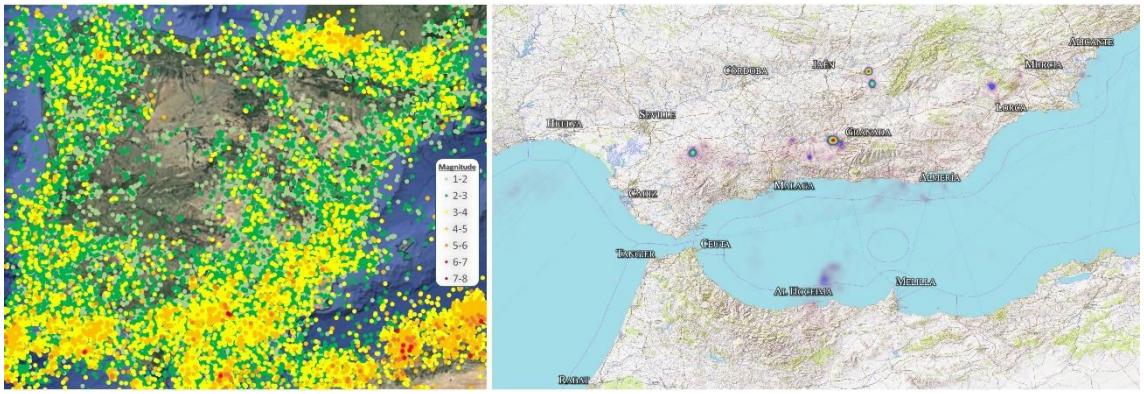

Figure 8. Left: Map of Spain showing instrumental seismicity (from 1370 to the present) as recorded in the seismic catalog of the IGN. Right: Kernel density map applied to the seismicity data from the left map, highlighting areas of higher seismic frequency over the Digital Terrain Model (DTM). Higher frequencies are represented in red, followed by green, then blue. Areas with low or no seismic activity are not represented by the kernel method. Two distinct high-frequency zones (red) can be identified in the Granada basin and the Torreperogil area (Jaén). A lower-frequency core (green) is observed southeast of Seville, along with two more diffuse blue cores in the Al Hoceima and Lorca (Murcia) regions.

The Betic-Rif orogen, also known as the Gibraltar Arc, is one of the most curved arcuate structures on the planet, formed by the collision between the Eurasian and African plates. The Betic Cordillera constitutes the northern branch of this structure, extending in a NE-SW direction. Between these mountain ranges lies the Alboran Sea, an area of thinned

continental crust located in the westernmost part of the Mediterranean. Plate motion models estimate a convergence rate of approximately 4.9 mm/year in a NW-SE direction (DeMets et al., 1994).

To the north of the Betics is the Variscan basement, the Iberian Massif, which exhibits significantly lower seismicity.

The Betic Cordillera has traditionally been divided into two zones based on petrological and structural characteristics that suggest they originally belonged to two independent plates: the Internal Zones, to the south, which are part of the Alboran Domain, and the External Zones, to the north, corresponding to the South Iberian Domain (Fallot, 1948; García-Dueñas & Balanyá, 1986; see **Figure *2***). Between these zones, flysch-type materials (the Campo de Gibraltar units) are interposed.

The Internal Zones are mainly composed of a series of superimposed metamorphic complexes: Nevado-Filábride (Egeler, 1964), Alpujárride (Van Bemmelen, 1927), and Maláguide (Blumenthal, 1927). In addition to the dorsal and predorsal units. The Rif structure is similar, although it lacks the Nevado-Filábride materials. All these complexes are primarily Paleozoic in age and mainly consist of gneisses, schists, quartzites, and marbles, as well ultramafic rocks (Ronda Peridotites). They underwent high-pressure metamorphism, estimated to be of Late Cretaceous age (Nieto et al., 1997), associated with thrusting and crustal thickening. The Maláguide Complex, which experienced lower deformation and metamorphism, also contains slates, detrital rocks, and a Mesozoic–Paleogene carbonate sequence. The contacts between these units are low-angle normal faults (e.g., Platt & Vissers, 1980; Aldaya et al., 1984, 1991; Galindo-Zaldivar et al., 1989; Jabaloy et al., 1992; García-Dueñas et al., 1992; Alonso-Chaves et al., 1993; Lonergan & Platt, 1995; Vissers et al., 1995; Alonso & Orozco, 1998; Cuevas et al., 2001; Booth-Rea et al., 2003; Ruano, 2003).

The Flysch Trough mainly consists of Cretaceous and Paleogene turbiditic rocks, which, in the western area, are thrust over the materials of the External Zones (Martín Algarra, 2022).

The External Zones are composed of Mesozoic–Tertiary materials deposited on the Variscan basement of the Iberian Massif, forming its continental margin. This domain is subdivided into: The Prebetic (Jurassic–Cretaceous deposits), Intermediate Units (Jurassic–Cretaceous deep-sea, slope, and platform deposits), and the Subbetic (Jurassic

materials where submarine volcanism developed) (García-Hernández et al., 1980, Martín Algarra, 2022).

Above these materials, numerous Neogene–Quaternary basins are present, the largest of which is the Alboran Sea, located in the Internal Zones (both in the Betics and the Rif). Other significant basins include intramontane basins in the central part of the orogen, within the so-called Intrabetic Trough—notably, the Granada basin—and foreland basins, such as the Guadalquivir basin, located to the north, at the boundary between the Iberian Massif and the Betics (Sanz de Galdeano & Vera, 1991).

The Granada basin was selected as the first test area for the slice method due to its historical relevance, distinctive geology (situated at the boundary between the Internal and External Betic Zones), and its proximity to a major population center (Granada city). The southwestern edge of the Guadalquivir basin was chosen for the H/V method to study deformation partitioning in the forebulge region of the Betic Orogen.

4.4. Granada basin

The Granada basin is located within the so-called Intrabetic Trough, a topographic depression situated at the boundary between the External and Internal Betic Zones. It runs parallel to the Betic Cordillera (NE–SW) and hosts the city of Granada (Martín Algarra, 2022). This Neogene–Quaternary basin lies at the foothills of Sierra Nevada, enclosed by mountains, and is composed of sedimentary materials ranging from the Middle Miocene to the Quaternary.

Its scientific interest lies in its notable historical and recent seismic activity, which is associated with faults that have been active since at least the Miocene (Vissers et al., 1995).

At present, the Betic Cordillera is undergoing NW–SE-oriented compressional stresses, which are accommodated by orthogonal extensional active structures (Sanz de Galdeano et al., 2012). According to Sanz de Galdeano (1983), there are three main families of active faults in the basin, oriented ENE–WSW, NW–SE, and NNE–SSW.

4.5. Guadalquivir basin

The Guadalquivir basin is a subtriangular foreland basin that extends approximately N070°E from the western foothills of the Sierra de Cazorla (Prebetic Units) to the Gulf of Cadiz, in the southwestern Iberian Peninsula. This basin represents one of the three

major geological domains in southern Iberia: The Variscan Iberian Massif to the north, the Alpine Orogen, and the Betic Cordillera to the south, with the Guadalquivir basin situated in between as the foreland basin of the latter.

The Iberian Massif, composed of Proterozoic to Carboniferous rocks, was first deformed by the Variscan Orogeny and later intruded by various granitoids before the Permian. It occupies the western Iberian Peninsula and is subdivided, from north to south, into the Cantabrian Zone, West Asturian-Leonese Zone, Galicia-Trás-os-Montes Zone, Central Iberian Zone, Ossa-Morena Zone, and South Portuguese Zone (Lotze, 1945; Julivert et al., 1972; Farias et al., 1987). Materials from the last three zones are covered by the Neogene sediments of the Guadalquivir basin. Only the South Portuguese Zone is of interest for this research.

The Ossa-Morena Zone consists of highly deformed and metamorphosed Upper Proterozoic to Carboniferous rocks, with asymmetrical folds verging towards the SW and some granite intrusions. The South Portuguese Zone, located at the southernmost margin of the orogen, comprises Devonian–Carboniferous rocks with foliation, very low to low-grade regional metamorphism, and abundant magmatism, and is affected by folding and thrusting.

The structural guideline of the Variscan base is NW-SE, so it is strongly oblique to the northern edge of the Guadalquivir basin.

The sediments of the Guadalquivir basin overlie the Variscan basement, concealing the underlying tectonic structures that influence the geomorphology of the area. The Tortonian calcarenites were deposited in a marine environment directly over the Variscan basement, followed by clay-silt and sand-silt deposits from the Tortonian to the Pliocene, and Pleistocene reddish conglomerates. The entire sequence is overlain by Quaternary fluvial, marine, and marsh deposits.

The geomorphology of the study area exhibits abrupt changes in relief and reorientations of river courses, suggesting the presence of tectonic structures shaping the landscape. As early as Viguier (1977), the existence of several faults influencing the orientation of river courses was proposed. These faults were aptly named Odiel Fault, Guadiamar Fault, and Guadalquivir Fault, all with an orientation close to N–S (see **Figure 9**)

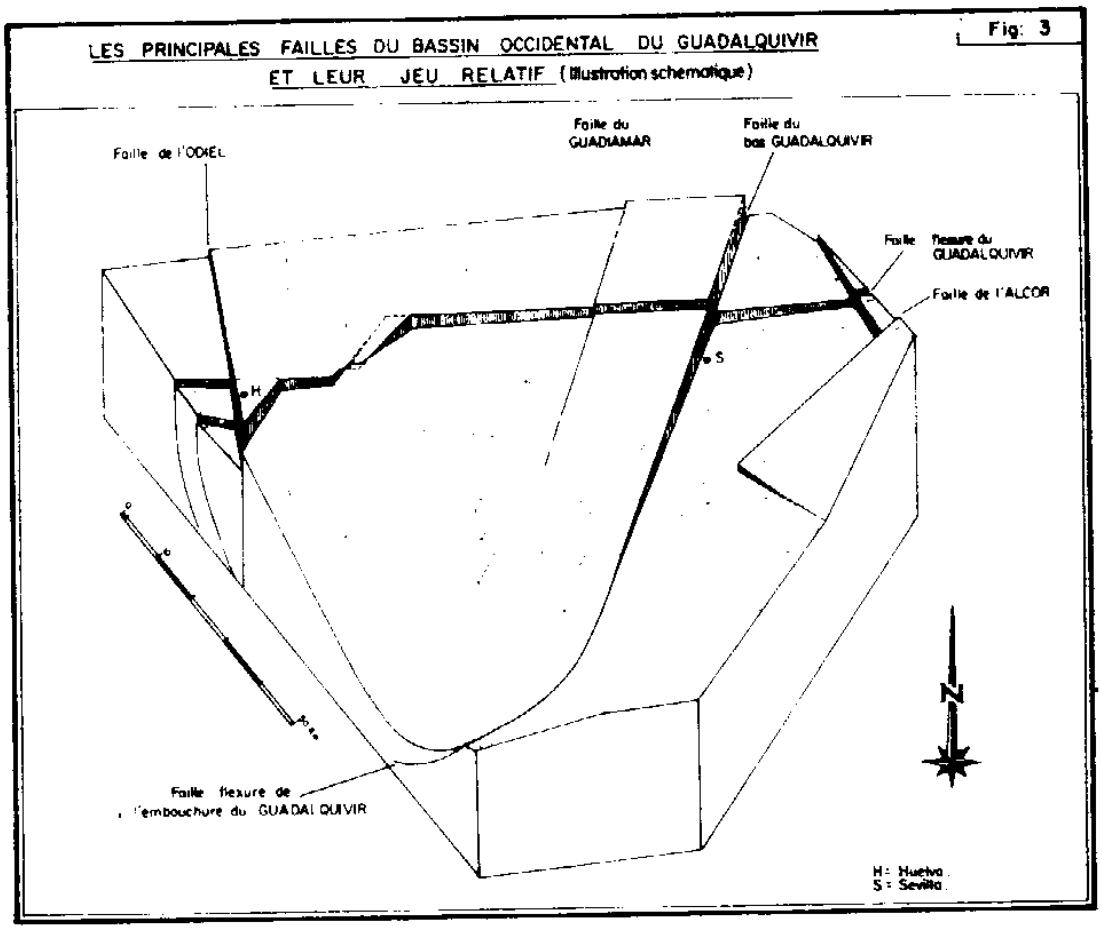

Figure 9. Main faults of the western Guadalquivir basin and their relative motion (Source: Viguier, 1977).

These structures are closely parallel to the current river courses and the structural highs, and align with the structural trends of the Variscan basement, suggesting that these structures are affecting the more modern overlying basin materials. This reactivation of structures may be consistent with the deformation caused by the convergence of Iberia and Nubia.

RESULTS

5. RESULTS

5.1. Kernel Density Estimation for the Interpretation of Seismic Big Data in Tectonics using QGIS: The Türkiye−Syria Earthquakes (2023)

This fragment is an adaptation of the published article: Amador Luna, D.; Alonso-Chaves, F. M. & Fernández, C. (2024). Kernel Density Estimation for the Interpretation of Seismic Big Data in Tectonics Using QGIS: The Türkiye−Syria Earthquakes (2023). *Remote Sensing, 16(20), 3849.* https://doi.org/10.3390/rs16203849.

5.1.1. Abstract

Numerous studies have utilized remote sensing techniques to analyze seismic data in active areas. Point density techniques, widely used in remote sensing, examine the spatial distribution of point clouds related to specific variables. Applying these techniques to complex tectonic settings, such as the East Anatolian Fault Zone, helps identify major active fractures using both surface and deep information. This study employed kernel density estimation (KDE) to compare two distinct point-cloud populations from the seismic event along the Türkiye–Syria border on 6 February 2023, providing insights into the main active orientations supporting the Global Tectonics framework. This study considered two populations of seismic foci point clouds containing over 40,000 events, recorded by the Turkish Disaster and Emergency Management Authority (AFAD) and Kandilli Observatory and Earthquake Research Institute (KOERI). These populations were divided into two datasets: crude and relocated-filtered. Kernel density analysis demonstrated that both datasets yielded similar geological interpretations. The high-density cores of both datasets perfectly matched, exhibiting identical structures consistent with geological knowledge. Areas with a minimal concentration of earthquakes at depth were also identified, separating different crustal strength levels.

5.1.2. Introduction

On 6 February 2023, highly destructive seismic events occurred in southern Türkiye and northern Syria. These earthquakes were associated with the activity of the East Anatolian Fault Zone (EAFZ), a first-order tectonic structure that constitutes the boundary between the Arabian and Anatolian plates. Interest in the tectonic, seismological, geophysical, and structural study of the EAFZ has been growing since its first definition and description

by Allen (1969) and Arpat & Saroglu (1972). Due to its relative youth (Late Pliocene, e.g., Saroglu et al., 1992; Westaway et al., 2001), the EAFZ is considered an immature (e.g.,Turkoglu et al., 2015; Güvercin et al., 2022), strongly segmented (e.g., Saroglu et al., 1992; Barka & Kadinsky-Cade, 1988; Duman & Emre, 2013) structure. It is described as a complex strike–slip-type fault, showing a complex and irregular set of structures, with abundant parallel faults, oversteps, releasing and restraining bending zones, folds, and normal or reverse faults (see, e.g., Duman & Emre, 2013 for a detailed description).

Today, there is some agreement in considering the EAFZ as weakly and heterogeneously coupled, with seismicity concentrating in the most coupled segments (e.g., Bletery et al., 2020). The exhaustive structural (e.g., Duman & Emre, 2013; Över et al., 2004a; Yilmaz et al., 2006; Aksoy et al., 2007; Köküm & Inceöz, 2018) geomorphological (e.g., Yönlü et al., 2017), geodetic (e.g., Aktug et al., 2016; Özkan et al., 2023) and geophysical (e.g., Güvercin et al., 2022; Akin, 2016; Abgarmi et al., 2017; Ozer et al., 2019; Artemieva & Shulgin, 2019) analyses carried out on the EAFZ have allowed us to achieve a general idea about the close relationship among the velocity and stress fields, the geometry of their main associated structures, the position of the seismic gaps, and the thermal and mechanical structure of the lithosphere. By using refined seismic techniques and GNSS data, rupture models of the 6 February 2023 earthquake doublet have been presented that show intermittent supershear rupture, failure of rupture barriers, and multiscale rupture growth in the complex fault network of the EAFZ (Delouis et al., 2024; Okuwaki et al., 2023).

All this abundant geological, seismological, and geophysical information on the activity of the EAFZ, obtained mainly during this century, allows us to conclude that it is a relatively well-known plate boundary. It is possible, therefore, to advance now in the seismotectonic and kinematic study of this important structure. This work focused on the central and southwestern sector of the EAFZ, the place especially affected by the February 2023 seismic event. The lateral and vertical distribution of the seismicity were analyzed using a new technique, based on kernel density estimation (KDE), to illustrate the three-dimensional architecture of the seismicity. This study compared a highly accurate dataset, obtained after months of processing, with a raw, untreated dataset by applying a new geological and seismological technique. The objective was to evaluate the feasibility of obtaining correct analyses and geological interpretations from large datasets, resulting in an immediate estimation of their parameters. This study sought to

demonstrate that when analyzed using the KDE method, a comprehensive seismic catalog with considerably high uncertainty (unfiltered, first population) can produce interpretations like those derived from a relocated catalog (second population), which provides significantly higher accuracy and reliability. This approach aims to reduce the time and resources required to achieve a preliminary approximation quickly.

An additional implication of this work is that it provides ideas on future lines of research that may contribute to improving the zoning of the seismic risk associated with the EAFZ.

5.1.3. Geological Setting

At the eastern end of the Mediterranean Sea and its adjacent regions, three tectonic plates are recognized: Anatolia, Arabia, and Nubia. Their geodynamic evolution is closely linked to their relative displacement (McKenzie, 1972; Dewey et al., 1973), with the development of suture zones implying the closure of the western Tethys (Stampfli, 2000). The majority of the Anatolian Plate is located within Türkiye and Cyprus (**Figure *10***). The North Anatolian Fault Zone (NAFZ) marks the northern boundary of this plate. It is an intracontinental transform fault, spanning 1200 km, characterized by right-lateral displacement, with relative velocities of approximately 25 mm/year (Tatar et al., 2012). To the south of Türkiye, in the Mediterranean Sea, the oceanic lithosphere of Nubia subducts northward beneath Anatolia, forming the Cyprus Arc. On the other hand, the EAFZ extends from the region around the Gulf of Iskenderun and the Hatay area to Karlıova. The EAFZ is interpreted as an intracontinental transform fault with left-lateral displacement (Arpat et al., 1972). In the easternmost part of the EAFZ, a relative displacement velocity of 10 mm/year has been observed between the Anatolian and Arabian plates. In the Türkoglu area, the displacement ranges from 1 to 4 mm/year (Aktug et al., 2016; Koç & Kaymakci, 2013; Mahmoud et al., 2013; Bayrak et al., 2015). The kinematics of the NAFZ and EAFZ help explain the westward lateral escape tectonics of the Anatolian Plate, which is related to the convergence between the Eurasian, Nubian, and Arabian plates. Geological data and geodetic displacement rates suggest that the left-lateral displacements along the EAFZ did not occur until the end of the Pliocene (Saroglu et al., 1992; Westaway et al., 2001; Allen, 2010). The proximity to the Eulerian pole between Anatolia and Arabia justifies the lateral changes in movement directions and relative displacement rates along the EAFZ (Bletely et al., 2020; Reilinger & McClusky, 2011).

The series of 1:500,000 geological maps produced by the General Directorate of Mineral Research and Exploration of Türkiye (MTA) for the EAFZ region reveal the presence of folds and faults affecting metamorphic, sedimentary, and volcanic rocks spanning different ages, from the Precambrian to the Upper Cretaceous. Overall, the predominant orientation of local tectonic structures tends to be parallel to the EAFZ, and they connect with the Cyprus Arc through the Gulf of Iskenderun. Active faults with various orientations are part of transcurrent, transpressional, and transtensional tectonic scenarios, as described in different segments of the EAFZ (e.g., Duman & Emre, 2013). Specifically, the EAFZ can be divided into two primary branches: the northern strand, consisting of the Sürgü-Misis Fault System (SMFS, approximately 350 km in length), oriented in an east–west direction; and the southern branch, which serves as the boundary between Anatolia and Arabia, known as the Main Strand. This transform fault, oriented approximately N060˚ E, extends from Karlıova to Antakya (approximately 580 km in length) and connects with the Cyprus Arc and the Dead Sea Fault Zone. Near Türkoglu (Kahramanmaras province), the tectonic structures of the Main Strand experience a sudden change in direction, which has important kinematic implications, as discussed below in this study.

It is also important to point out the Nurdagı-Pazarcık Fault (NPF), also known as the Narlıdag or Narlı Fault, located near the cities of Kahramanmaras and Gaziantep and parallel to the Main Strand of the EAFZ. This fault, oriented NNE, is considered a splay fault of the EAFZ, where the first high-magnitude earthquakes occurred before being transferred to the EAFZ (Okuwaki et al., 2023; Čejka et al., 2023).

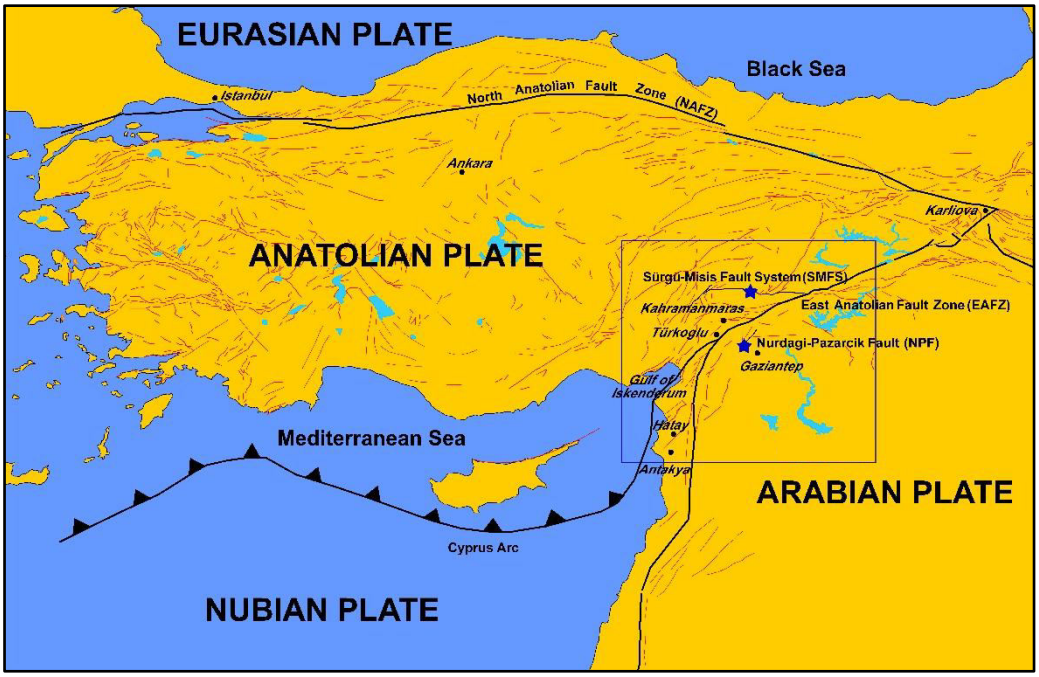

Figure 10. Tectonic map of Anatolia distinguishing the involved tectonic plates and their boundaries, as well as the location of the study area, indicated by a rectangle.

5.1.4. Methodology

5.1.4.1. Seismic Data and Catalog

The seismic data used in this study were obtained from the seismic catalog of the Earthquake Data Center System of Türkiye (TEDCS), available through the web portal of the Authority for the Management of Disasters and Emergencies (AFAD) and subsequently relocated by Lomax (2023). Additionally, data from the Kandilli Observatory and Earthquake Research Institute (KOERI) were used in this work, also relocated by Lomax (2023). The seismic record covers the period from 1 January 2023, to 31 May 2023, due to the notable improvement in the precision of location estimates by Lomax (2023) during this period. The uncertainties in the X, Y, and Z coordinates of the earthquake locations were reduced to less than 2 km. For this purpose, two datasets were compared: first, raw data from a catalog of more than 35,000 earthquakes collected by AFAD, and, second, relocated and filtered data from Lomax, comprising more than 5500 seismic events.

The study area was delimited to the southeastern part of Türkiye, specifically in the central and southwestern zones of the EAFZ. It included the vicinity of the Sürgü-Misis Fault System (SMFS) and the Main Strand segments of Erkenek, Pazarcik, and Amanos (according to the terminology of Duman & Emre, 2013), until its disappearance offshore

in the Mediterranean Sea, to the south of the Gulf of Iskenderun. The area of interest was delimited approximately by the following geographical coordinates: Lat: 35.0–39.0˚ N and Long: 35.0–40.0˚ E (**Figure *11***).

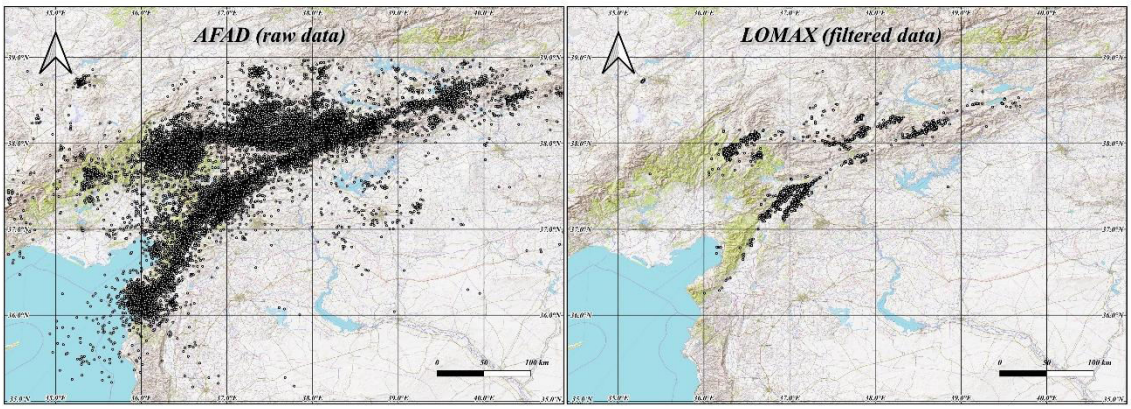

Figure 11. Point cloud maps of the central and southwestern parts of the East Anatolian Fault Zone showing the locations of seismicity of the 2023 earthquake event in Türkiye–Syria. Left: Epicenters of the earthquakes from the AFAD dataset (raw); Right: epicenters from Lomax, 2023 (relocated-filtered).

5.1.4.2. Use of Kernel Density Estimation for the Analysis of Seismicity

Geostatistics is a branch of statistics focused on the analysis and modeling of phenomena exhibiting spatial and/or temporal correlation. It deals with sets of variables where each value is associated with a specific position in space. In the context of interest, namely, seismology, the information about an earthquake is closely related to both the distance or position of its epicenter and the exact moment it occurred. Most geostatistical studies have focused on estimating expected values to create contour maps that correlate all variables of interest (Hohn, 1999; Zhang, 2011). This approach can facilitate evaluations of resources (as in mining), the distribution of contaminants (in environmental sciences), or the development of seismic microzonation and mapping of seismic risk and perceived intensities for a given area in the event of an earthquake (in seismology). The objective of geostatistics in seismology is, therefore, to predict the possible spatial distribution of a seismological property. This process can be conducted manually or with the aid of computational tools, making it a powerful resource in various disciplines such as petroleum geology, hydrogeology, meteorology, ecology, and epidemiology. Given its widespread application, geostatistical methods have been integrated into geographic information systems, such as QGIS.

In this regard, the techniques specifically noted for their use in seismology are as follows:

1. Geostatistical estimation approach. The most frequently used method is kriging, which predicts unknown values at unmeasured locations by utilizing the spatial correlation of known data points, based on a variogram model (e.g., Kyprioti & Taflanidis, 2021; Schenková et al., 2007; de Rubeis, et al., 2005). Cokriging, which is an extension of kriging, simultaneously estimates multiple correlated variables (covariates) at unmeasured locations by incorporating information from secondary variables to improve the accuracy of estimates (e.g., Han et al., 2018). And, based on the interpolation, inverse distance weighting (IDW) estimates unknown values at unmeasured locations by giving greater weight to nearby points based on the inverse of their distances (e.g., Kim et al., 2022, Scudero et al., 2021).

2. Machine learning methods are integrated with geostatistical methods to analyze and model spatial data, enhancing the prediction of spatial phenomena and improving resource estimation by using historical data and complex spatial relationships. A series of application examples in seismology are reviewed in Jia & Zhou (2024). The most known methods are the neural networking (e.g., Petrescu & Moldovan, 2022; Bilal et al., 2023), logic or decision trees and random forest (e.g., Kaviris et al., 2023; Jang et al., 2023; Llácer et al., 2020), and the support vector machine (SVM) (e.g., Asaly et al., 2022; Tang et al., 2019).

3. Density-based methods (e.g., Al-Ahmadi et al., 2014; Moustafa et al., 2024). These include point density analysis, which is a clustering algorithm that identifies groups (clusters) of closely packed points (events) based on their local density, enabling the detection of significant areas of activity while effectively handling noise and outliers. Kernel density estimation (KDE) methods estimate the probability density function of seismic events by placing a smooth kernel over each data point and adding them to create a continuous surface, allowing for the visualization of event concentrations and patterns without making strict assumptions about the data distribution.

4. Less commonly used methods include stochastic simulation, probabilistic analysis, and spatial–temporal analysis (e.g., Alavi et al., 2024; Torcal et al., 1999). All these techniques are complementary rather than mutually exclusive. Many of the cited studies have combined various methods depending on the desired analysis or applied hybrid methods combining them in phases to produce the maps.

There are numerous techniques applicable in seismology, but they differ significantly in terms of computational complexity, precision, flexibility, ease of interpretation, and response times. Estimation techniques, while offering high precision and ease of interpretation, tend to have low flexibility and long computation times, requiring large datasets and considerable processing. In contrast, machine learning methods, despite their high computational costs and complex results, provide high precision and flexibility. Density-based methods (e.g., KDE), on the other hand, appear to offer a balanced solution, with moderate computational costs, good precision, flexibility, and shorter response times, making them the most stable and convenient alternative. This is, therefore, the option presented in this study.

Kernel density estimation (KDE) is a non-parametric method that allows defining a probability density function of a given random variable (e.g., Weglarczik, 2018). In cases with insufficient information, or where it is impossible to assume the distribution shape (as with the spatial distribution of seismic events), a non-parametric estimation is commonly used. To accomplish this, techniques are used to estimate the distribution or relationship between variables without imposing a specific form (e.g., Wasserman, 2006). Among the techniques used in this work, kernel smoothing stands out, focused on the proximity and relationship among data points, such as the spatial location of earthquakes in a specific area. The kernel acts as a smoothing function placed on each data point, and its shape determines the contribution of that point to its neighborhood. The influence radius of each point, known as the bandwidth, can be defined according to the interest of the study. Combining all the contributions from each of the given points, an estimate of the probability density of a kernel is obtained.

The KDE method has been largely unused in seismology, but, nowadays, the increasing quality and density of seismic networks have made it more viable. This rise in the number of seismic catalogs allows for the application of such techniques in seismology due to the vast amount of recorded seismic events (Lasocki, 2021). More common is the application of KDE techniques for generating seismic hazard maps (e.g., Woo, 1996; Ramanna & Dodagoudar, 2012; Catita et al., 2019; Dilig & San Juan, 2019). In the study area, this technique was used to generate maps to analyze the distribution of earthquakes with magnitudes greater than three (Karaburun & Demirci, 2016), but there is no example of its application for increasing geological knowledge.

This study proposes a new technique for geological and seismological analysis by applying the KDE method to the spatial distribution of seismic foci in any study area, previously grouped by different layers, related to seismogenic levels (**Figure *12***). By analyzing the relationship between the number of earthquakes and the depth of their hypocenters, different seismogenic layers can be identified.

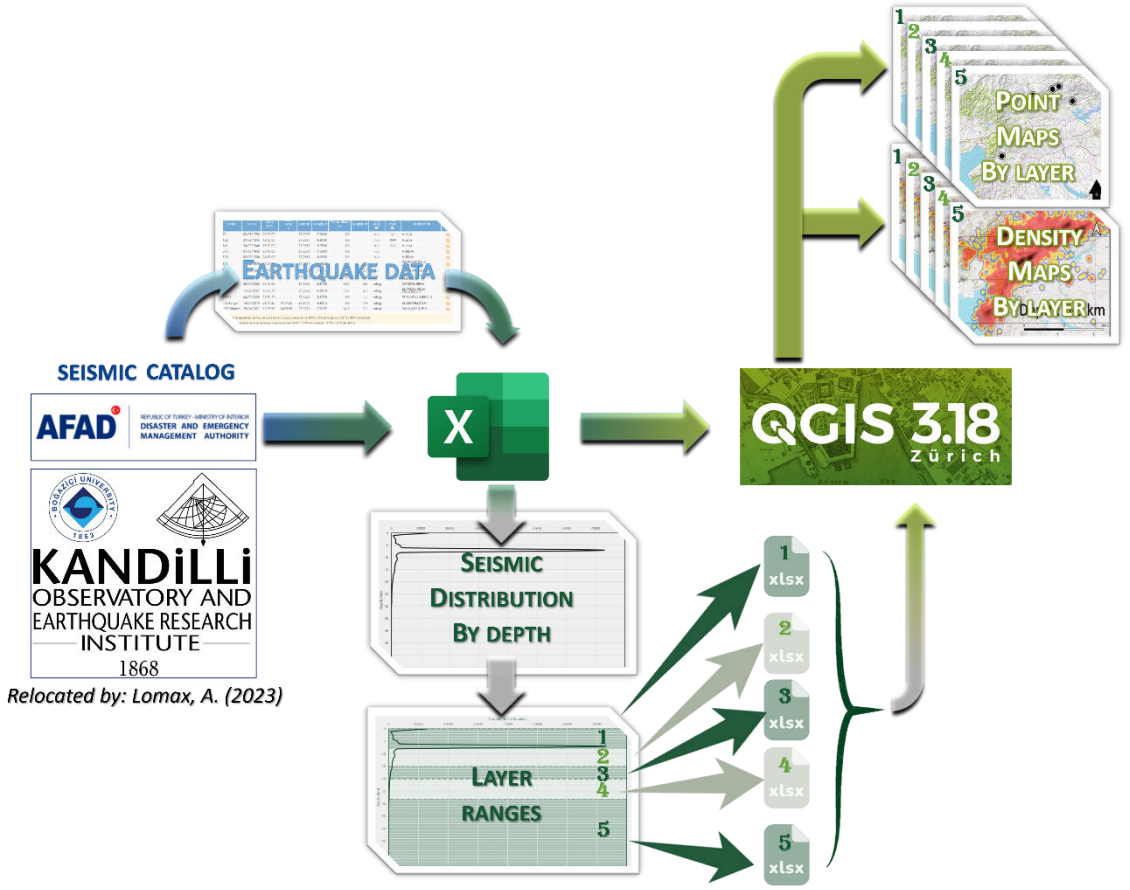

Figure 12. Descriptive summary of the process to elaborate the maps. Flowchart to explain data processing. The initial data are from seismic data sources (including relocation by Lomax, 2023). These data are then processed with Microsoft Excel LTSC MSO (v. 16.0.1) to identify different layers (numbers 1 to 5) or seismogenic levels with depth. Finally, the different point clouds are processed with QGIS (v. 3.18) to obtain point clouds and kernel density maps for each seismic layer.

Regional seismicity data were analyzed to generate graphs representing the distribution of earthquakes as a function of depth and the frequency–magnitude distribution (Gutenberg-Richter law; Gutenberg & Richter, 1944; 1956). Those analyses allowed the identification of layers (represented by a relatively high frequency of earthquakes) with similar seismic behavior delimited by low seismicity zones. It is well known that seismic frequency varies with depth, and these variations can indicate changes in lithological composition, among other factors, and may be due to differences in the mechanical behavior of distinct levels of the lithosphere (crust and mantle).

Once the depth range of the different layers was delimited, an Excel file was obtained for each one containing all the relevant information, such as the earthquake coordinates, depth, and magnitude. The AFAD dataset, in which the focal depth is fixed or predetermined (typically around 7 km in this zone), was also included for comparison with the filtered point cloud (dataset of Lomax, 2023) and their effects on the interpretations. Fixed depths are commonly used in seismic catalogs to expedite the calculation processes for certain parameters but can lead to misinterpretation of geological and seismological data. Evaluating these effects and whether this new technique helped to minimize them were also addressed in this work.

The next step was to process the information of each seismic layer through appropriate software that allows kernel analysis, QGIS (v. 3.18) in this case. Once the Excel files were imported into QGIS, they were converted to a shapefile format for their processing. Heatmaps or KDE maps can be created using a specific kernel method. In statistical analysis, as it was mentioned previously, the term kernel refers to a window function that sets a radius of influence around a given position for the measured parameter. When an element falls within that radius, its value is defined by a specific function, while for those outside this radius, its value is zero. The bandwidth must be specified and expressed in meters, degrees, or map units in QGIS. In this study, considering the size of the working area, a bandwidth of 0.05˚ was used. To achieve higher resolution, a pixel size of 0.001˚ was selected.

The choice of a 0.05˚ bandwidth was determined based on the study area, which covered approximately 250,000 km^2, resulting in a buffering influence area of 34.90 km^2, along with the spatial distribution of more than 5500 recorded seismic events. This value provided an optimal balance between spatial detail and the smoothing necessary to capture coherent seismic patterns in such an extensive region. A smaller bandwidth would be good for smaller study areas or a greater number of seismic events. For the parameters in this study, a smaller bandwidth would have increased the local resolution but introduced noise in areas with lower event density. Conversely, a larger bandwidth would have excessively smoothed the seismic distribution patterns, reducing the ability to identify key geological structures. Therefore, the 0.05˚ value enabled capturing both the global trends and regional details of seismicity in the study area. **Figure *13*** illustrates the effect of bandwidth on the resulting kernel maps.

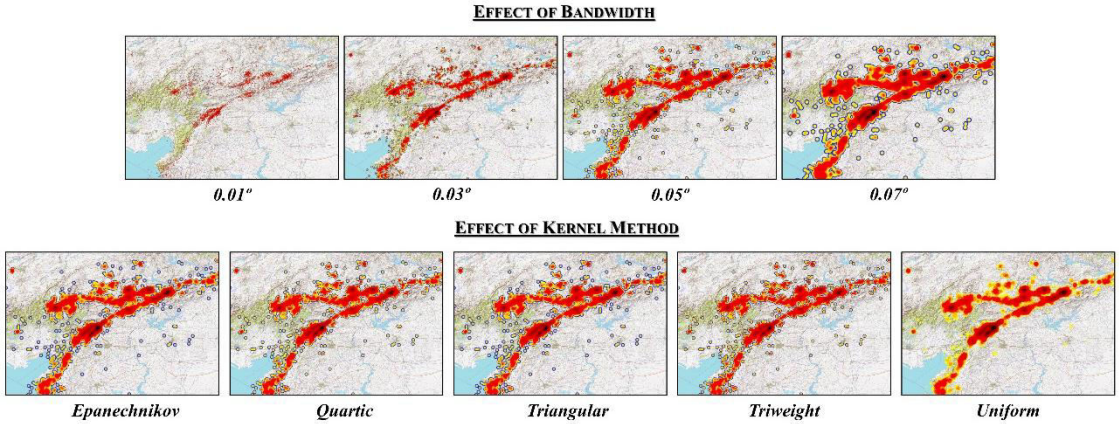

Figure 13. Evaluation of the impact on seismic density distribution due to changes in bandwidth (upper part of the figure) and the kernel method employed (lower part of the figure). As shown, lower bandwidth values generate more detailed results but introduce greater noise, while higher values emphasize regional patterns at the expense of local details. The kernel method determines the influence of a value on its surroundings, as illustrated by the functions shown in **Figure 14**. The choice of kernel function shows minimal differences (except for the uniform method) compared to the impact of bandwidth variations.

Also, a weighting function for the determination of the parameter value should be chosen. A quartic kernel function, *K(x)*, was employed. This quartic method is based on the fourth-degree polynomial (Silverman, 1986):

$$K(x) = \frac{15}{16}(1 - x^2)^2 \tag{1}$$

where x is the bounded support, closely related to the bandwidth, always within a value between −1 and 1. The function is 0 for values of x outside the support.

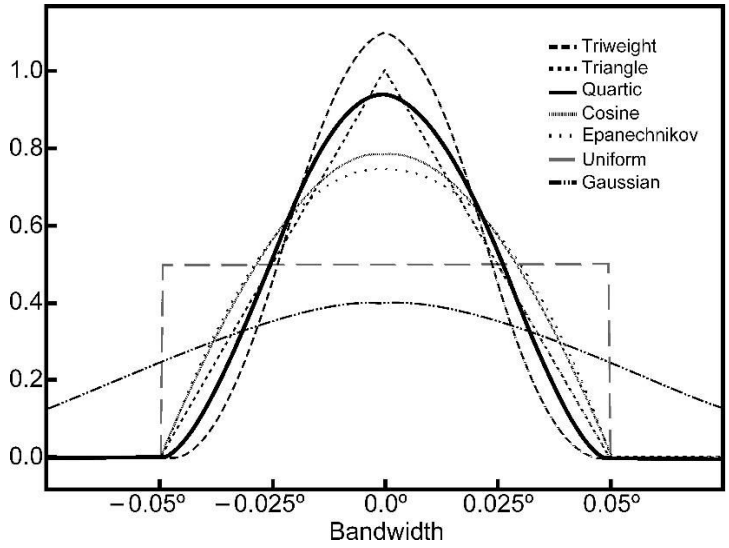

Figure 14. Examples of kernel functions. The geometry of the graphs corresponding to various kernel functions *K(x)* illustrates the influence of the data on their surroundings (taking values between 0 and 1 on the vertical axis) versus the radius of influence (horizontal axis), expressed in degrees. All curves are normalized to the same unit area.

In QGIS, several kernel functions are available by default, including quartic, triweight, uniform, Epanechnikov, and triangular functions. All these kernel functions (and other

examples) are illustrated in **Figure *14***. For this study, the quartic function was selected due to its ability to provide an optimal balance between smoothing and spatial accuracy.

Unlike the triweight function, which decreases more rapidly towards the edges, the quartic function offers a smoother transition, allowing for better detection of heterogeneously distributed patterns. The uniform function, by assigning equal weight to all points within the bandwidth, is not suitable for capturing the gradual variation in data. In contrast, the Epanechnikov function provides similar smoothing to the quartic function but has a reduced ability to detect subtle variations. Finally, the triangular function tends to overly prioritize nearby points, which could exclude the influence of distant yet relevant seismic events. Thus, the quartic function ensures an optimal balance in seismic density analysis, highlighting values closer to the center while maintaining smoother behavior than other kernel functions, such as the triweight function, which decays more rapidly towards the edges. However, it is important to note that the differences between kernel functions are minimal compared to the significant impact that bandwidth variations have on the results (see **Figure *13***).

Finally, color delineation based on quartiles is established. The first quartile is represented in blue (indicating higher data dispersion), the second in yellow, the third in red, and the fourth in black (indicating the nuclei of high seismic density). Since the range is continuous, there may be intermediate color combinations resulting from the blending of these primary colors.

5.1.4.3. Profiles along the EAFZ

Two profiles were made along the studied fault trace (Main Strand of the EAFZ, approximately oriented N060˚ E) showing the depth distribution of the hypocenters of the recorded earthquakes: one for raw data and one for relocated-filtered data. QGIS was used to establish influence radii for the points considered in the profiles. Most of the earthquakes associated with the main fault system were identified within a distance that never exceeded 20 km from the trace of the main fault (e.g., Türkoglu et al., 2015; Bulut et al., 2012). Therefore, a buffer with a radius of 0.2˚ was selected, considering the data points included within that influence radius and excluding those outside it. Additionally, the kernel quartic method with a bandwidth of 2 (in units of the map, which was equivalent to a bandwidth of around 1 km, an area of influence of around 3 km^2) was used for this specific case, due to the dimension and scale of the profiles, with a total area of

15,000 km^2. Note that the relationship between the total surface and the area of influence of the kernel quartic method was of the same order of magnitude in profiles and maps.

5.1.5. Results and Interpretations

5.1.5.1. Seismic Distribution by Depth and Delimited Layers

The analysis of the distribution of seismicity with depth allows the identification of the layers that exhibit differentiated seismic behavior. These layers were defined by the main trend and delimited, as described previously, by low-seismicity zones represented by minima in the seismic frequency. **Figure *15*** compares the distribution of the seismicity with depth for the two datasets (AFAD and Lomax, 2023). The gray range in both cases represents the limits of the point cloud, which includes all the data recorded. The seismicity in the area shows the typical distribution, with most earthquakes concentrated in the shallower layers and progressively decreasing with depth (see also, e.g., Bulut et al., 2012; Dolmaz et al., 2008; Balkan & Erkan, 2019).

Seismicity is practically absent in the lower part of the lithosphere; in both cases, there is virtually no seismicity below 20 km (only a few very isolated hypocenters). Likewise, four minima in earthquake concentration are recognized, located at depths of 4.9, 8.8, 14.5, and 18.7 km for the AFAD data (raw data) and at depths of 4.8, 7.9, 14.9, and 18.9 km for the filtered data of Lomax (2023). These minima indicate the presence of zones of lower seismicity and, therefore, constitute contacts between layers with distinct mechanical behavior. Filtered data processing estimated a hypocentral error of less than 2 km, but the minima in the raw data are included within a ±1 km range (orange band, **Figure *15***) from the minima in the filtered data. Thus, the raw and filtered data minima align very well, indicating that both datasets recognize the same minima (and maxima) within a relatively small error range.

Areas with high seismic recurrence indicate zones of interest for studying and recognizing brittle seismogenic structures. The seismicity density within the seismically active layers does not exactly coincide between the two datasets, with the absolute maximum occurring at an approximately 7 km depth in the raw data (AFAD) and around an 11 km depth in the filtered data (Lomax). As described earlier, 7 km is the predetermined depth for data processing in AFAD and could account for this maximum. However, the filtered data also show a minor peak at an approximately 8 km depth. In this case, the raw data display a

smaller peak coinciding with the maximum observed in the filtered data. Although 7 km is a predefined depth for calculations, the observed correlation with the filtered data suggests the presence of a genuine seismically active layer around this depth.

In this way, five layers were distinguished: In the case of raw data: Layer I, from 0.0 to 4.9 km; Layer II, from 4.9 to 8.8 km; Layer III, from 8.8 to 14.5 km; Layer IV, from 14.5 to 18.7 km; and Layer V, including the deeper data points below 18.7 km. In the case of filtered data: Layer I, from 0.0 to 4.8 km; Layer II, from 4.8 to 7.9 km; Layer III, from 7.9 to 14.9 km; Layer IV, from 14.9 to 18.9 km; and finally, Layer V, below 18.9 km.

Although the differences between the depths of the boundaries of the layers defined by raw (AFAD) and filtered (Lomax) data are smaller than the error in determining the depth of the earthquakes—up to 2 km for the filtered data—there is a significant variation in the density of earthquakes for each layer in both datasets, as indicated above (**Figure *15***), which are analyzed in more detail below.

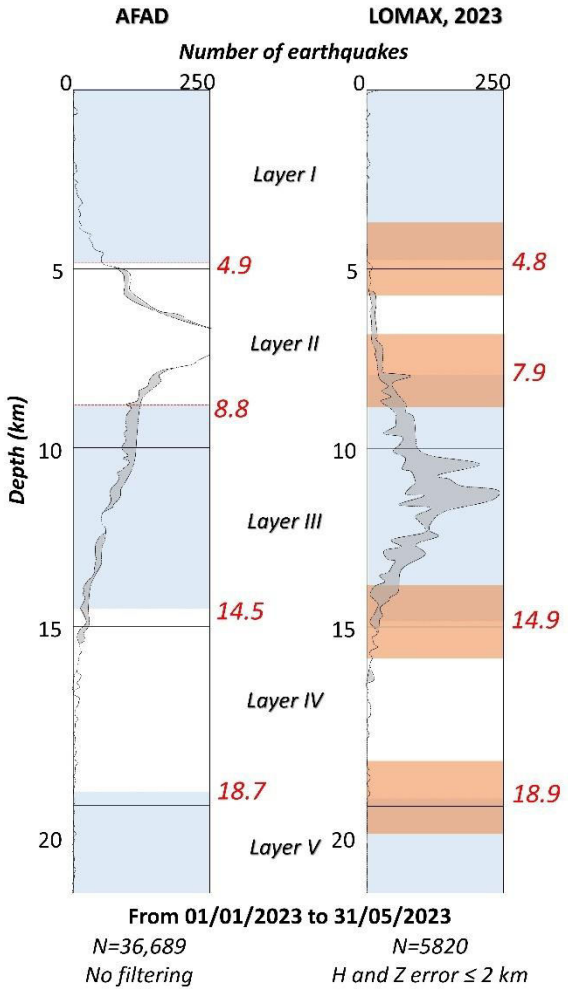

Figure 15. Comparison of the depth distribution of seismicity (number of earthquakes vs. depth). Left: Non-filtered data from the Disaster and Emergency Management Authority (AFAD) dataset. Right: Relocated and filtered data from

Lomax (2023). Layers separated by zones with minimum earthquake frequency are highlighted in alternating blue and white bands (Layers I–V). For raw data: Layer I (0.0–4.9 km), Layer II (4.9–8.8 km), Layer III (8.8–14.5 km), Layer IV (14.5–18.7 km), and Layer V (below 18.7 km). For filtered data: Layer I (0.0–4.8 km), Layer II (4.8–7.9 km), Layer III (7.9–14.9 km), Layer IV (14.9–18.9 km), and Layer V (below 18.9 km). An orange ±1 km range (less than the uncertainty in the location, ±2 km, by Lomax, 2023) is used to illustrate the statistical concordance of the layers observed in both datasets.

5.1.5.2. Seismic Distribution by Depth and Delimited Layers

All registered data points are represented in **Figure *11***, showing the distribution of earthquake foci over a digital terrain model. As can be seen, the dispersion of the data is greater in the case of raw data, as expected, but they show a more continuous trace than the filtered data. However, the main morphology of the point clouds shows the same tendency for both datasets. In both cases, the point lineations coincide with the traces of the Main Strand of the EAFZ and the SMFS. The nuclei of historically high frequencies of earthquakes, where recent events also generate more aftershocks and larger magnitudes, were recognized in both datasets. These maps show that most of the seismicity is concentrated in the northwest of the study area (over the Anatolian plate) and is virtually absent in the southeast (over the Arabian plate).

Point cloud maps are also represented for each layer (I to V) identified previously. A comparison of these maps is shown in **Figure *16***. Although the difference in the number of data points between the two datasets varies by an order of magnitude, the patterns are consistent. In both cases, the data points are concentrated in the upper layers, and their number decreases progressively in the lower layers. Seismicity is very scarce, virtually absent, at depths greater than 18.9 km for filtered data and 18.7 km for raw data. The unfiltered data show the non-existent connection between the MSFZ and the Main Strand of the EAFZ in most layers (maybe except in Layer II), whereas the filtered data suggest this same interpretation but less clearly. The 3D configuration of the data points may describe the morphology of the boundary between the Arabian and Anatolian plates. The analysis of the 3D disposition of the maps in both cases reveals that earthquakes are consistently distributed along the traces of the EAFZ and SMFS, describing structures with significant verticality from the surface downward.

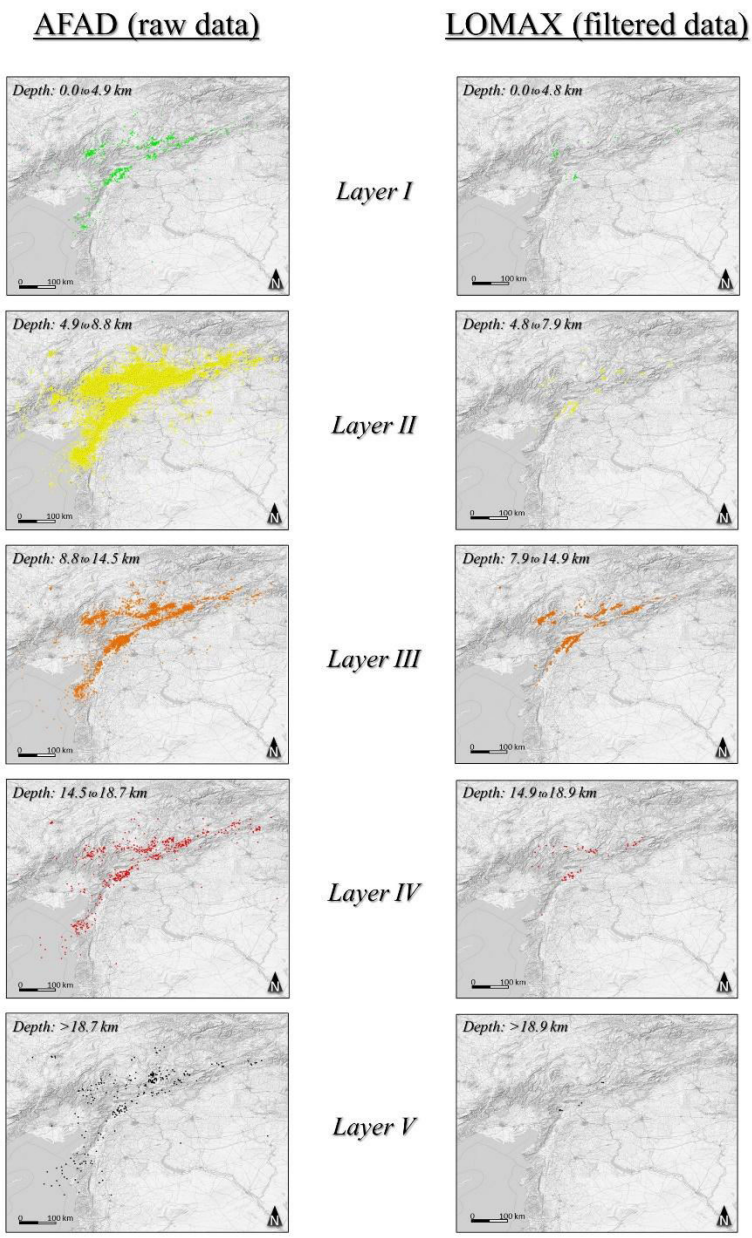

Figure 16. Comparison of point cloud maps for the central and southwestern parts of the EAFZ, represented at different depth ranges (seismological layers) identified by the seismic distribution profile, Layers I to V (**Figure 14**). Left: AFAD (raw data). Right: Lomax, 2023 (relocated-filtered data). Each color was selected to facilitate comparison and to represent the increasing depth (shallower in green and greater depths in black). The figures present scatter plots of seismic points, which display the raw locations of seismic events without any statistical treatment. A stacked view of the maps is shown in Appendix A (**Figure A1**).

5.1.5.3. Kernel Density Maps by Layer

Kernel maps were generated for each layer (**Figure *17***), applying the process described in the Methodology Section. This statistical approach allowed for analyzing the density of the seismic events over the defined area. This method smooths the data, highlighting regions with higher concentrations of seismic activity and providing a more informative representation of the underlying patterns. The black (or red) nuclei, representing higher

frequency zones of points, show a very similar tendency in both datasets (note the 'number 7'-like form of the density nuclei). As observed in the point cloud maps, the raw data exhibit a more continuous trace, whereas the filtered data only show discontinuous nuclei aligned along the Main Strand of the EAFZ and MSFZ. Similarly, the data points appear to concentrate approximately along the trace of the faults in the outer layers, converging at deeper layers into narrower high-density nuclei. This pattern is more evident in the raw data, with surface nuclei being more extensive (e.g., in Layer II) relative to the more concentrated nuclei at depth (Layers III to V). The black nuclei in Layer II of the raw data exhibit similar forms to the kernel density map of Layer II for filtered data, also aligned with the fault traces recognized at the surface. It can be suggested that the kernel maps reproduce a similar filtering function as the relocation of data points.

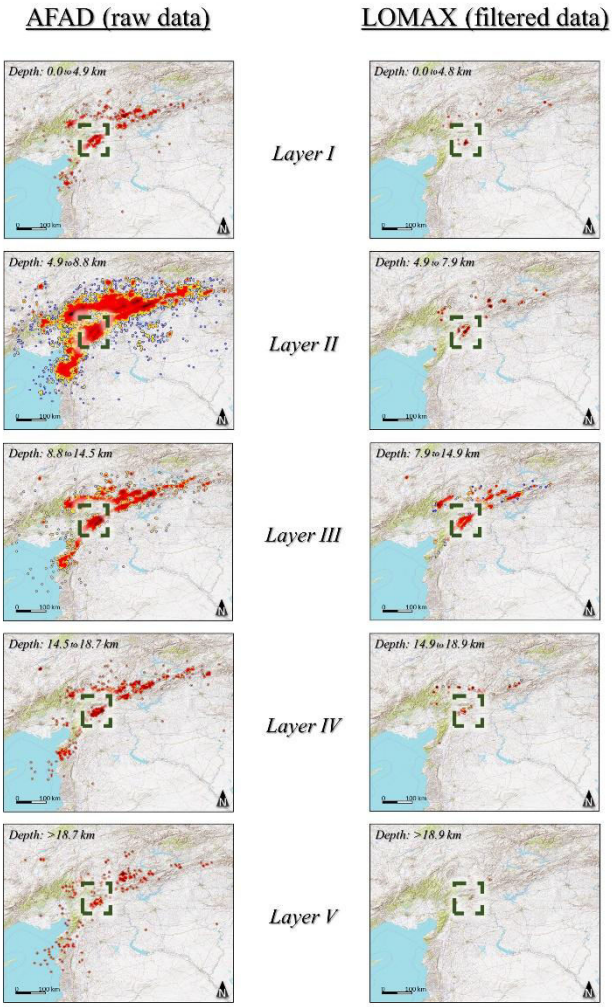

Figure 17. Comparison of kernel density maps of seismicity density for the central and southwestern parts of the East Anatolian Fault Zone (EAFZ), represented at different depth ranges (seismological layers) identified by the seismic distribution profile, Layers I to V (**Figure 14**). Left: AFAD (raw data). Right: Lomax, 2023 (relocated-filtered data). It illustrates the same seismic data from Figure 6 but applying KDE, a statistical approach, to highlight the patterns and greater frequency of earthquakes (in black). The area where the converging nuclei from upper to lower layers are easily

identifiable is highlighted by a rectangle. This is approximately the same area used to create the detailed map in **Figure 18**. A stacked view of the maps is shown in Appendix A (**Figure A2**).

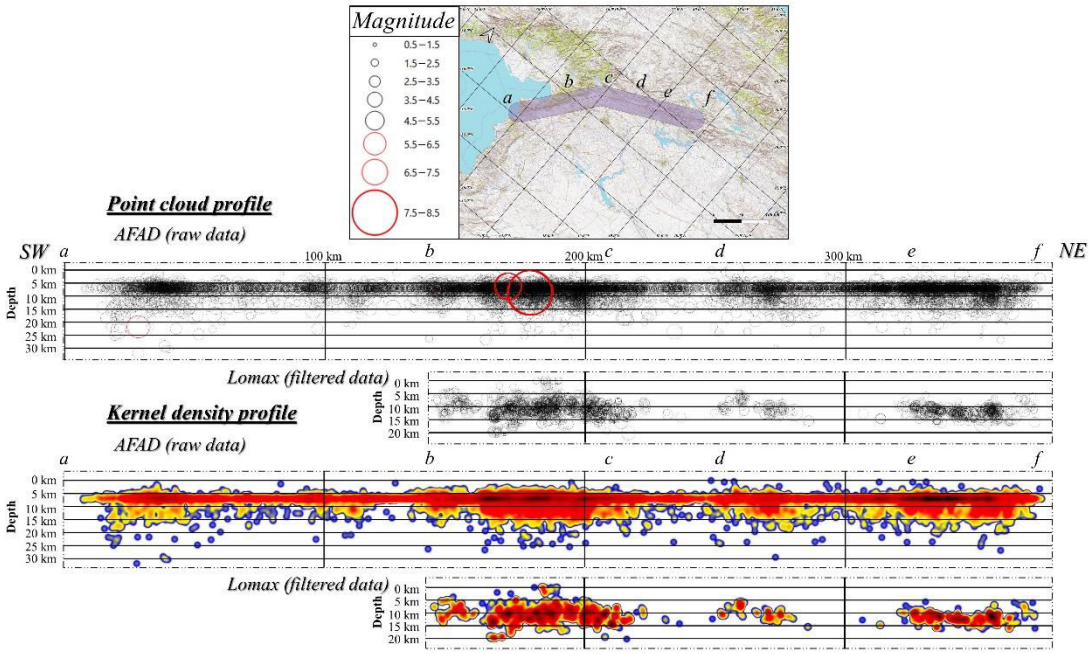

Figure 18. Seismicity profiles along the Main Strand of the EAFZ oriented approximately N60° E. Upper image: The location of the profile and the buffer used to select the seismic foci. Center of the figure: Point cloud of earthquakes at different depths, differentiated by magnitude. Upper: Raw data (AFAD); Lower: filtered data (Lomax, 2023). At the bottom of the figure: Kernel density profiles. Upper: Raw data; Lower: filtered data. Different points are marked with letters both on the profiles and on the map to accurately locate the black loci.

The main difference between the datasets can be observed in the southwest of the study area: while the raw data show a relatively high concentration of data at depth (Layers III to V), probably resulting from the interaction of the EAFZ with the subduction in the Cyprus arc, the filtered data have no recorded points in this region. The raw data allow for a more complete delineation of the plate boundaries.

The kernel density maps allow for the clear definition of a disconnection between the density nuclei belonging to the Main Strand of the EAFZ and those that are part of the SMFS. In this regard, density maps enable the delimitation of different segments within the fault zone.

By examining the maps in more detail, the area where the first major earthquakes in Türkiye occurred (highlighted with dashed rectangles in **Figure *17***), both maps (AFAD: raw data and Lomax, 2023: filtered data) reveal that the density cores in the upper layers correspond to the Main Strand of the EAFZ and the NPF traces. These two cores converge at depth into a single elongated nucleus parallel to the direction of the EAFZ. This three-dimensional geometry of the seismicity distribution suggests large, elongated funnels resembling fan or palm-tree structures in two-dimensional sections.

5.1.5.4. Seismicity profiles

The seismicity profiles along the EAFZ are presented in **Figure *18***. The profiles in the center of the figure show the magnitude of the earthquakes, while the profiles at the bottom use the kernel density method. As described earlier, seismicity in the southwest of the study area is not represented in the filtered data due to the extremely rigorous filtering process.

Four black nuclei are recognized in the raw data, three of which coincide in the horizontal coordinate with the high-density nuclei shown in the filtered data. Seismicity is distributed up to a depth of around 20 km along the transect. Particularly in the raw data, it can be observed that below this depth, the deeper foci are located approximately above the vertical of the kernel maxima. The greatest-magnitude earthquakes coincide with the high-density cores in both datasets, despite some of these earthquakes not being included in the filtered data.

The major limitation observed in the raw data profile is the notable elongated structure at a depth of 7 km due to the fixed depth of the data. However, this does not prevent the identification of the true morphology of the nuclei.

5.1.6. Discussion

5.1.6.1. Seismicity and Geology of the EAFZ

A close correlation between the point clouds from both datasets and the geological characteristics of the study area is evident (**Figure *19***). All data points are directly associated with both the Main Strand and the SMFS of the EAFZ, aligning parallel to specific geological formations. In the southwestern part of the Main Strand, the epicenter point clouds are concentrated over Quaternary deposits and ophiolites. This ophiolitic boundary between Anatolia and Arabia is distinctly delineated by the earthquakes that occurred during the February 2023 event. On the other hand, in the SMFS, point clouds tend to align predominantly with the boundaries of elongated blocks made up of metamorphic rocks of various ages, ranging from Precambrian to Cretaceous. It is worth noting that, despite the proximity to active faults, virtually no seismic activity is recorded in the volcanic and sedimentary rock formations of the Paleozoic era, both to the north and south of the study area, as well as in the plutonic formations located in the northeast.

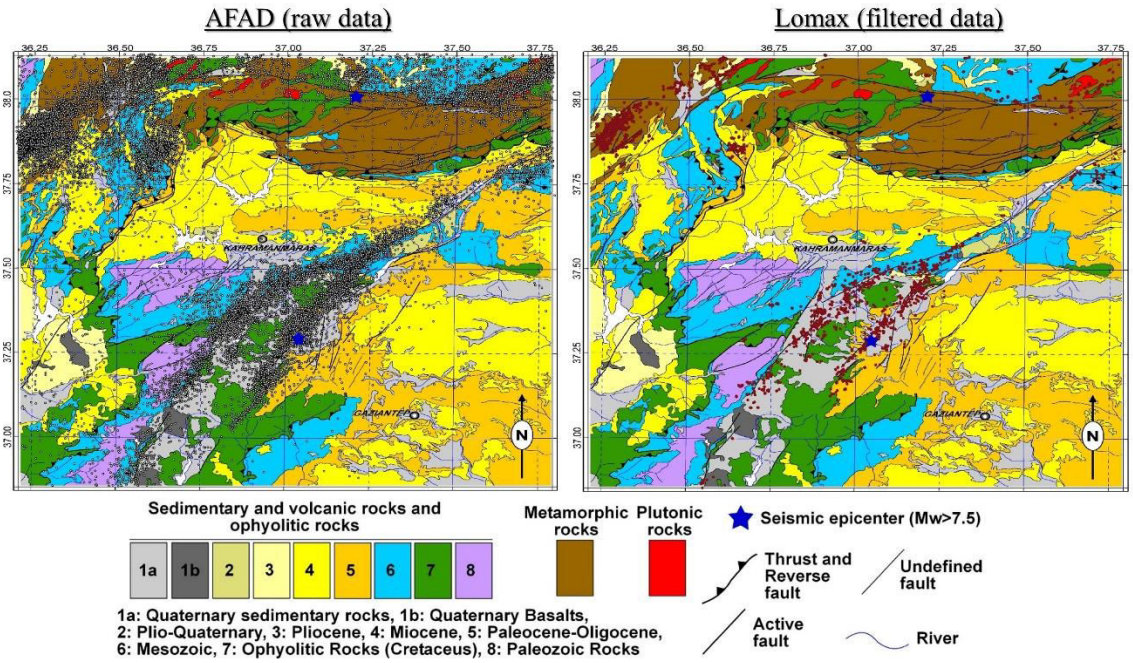

Figure 19. Detailed geological map of the surroundings of the major earthquakes, with epicenters from both datasets: AFAD (raw dataset, black dots) on the left and Lomax (2023) (relocated-filtered, red dots) on the right.

It is intriguing to note that despite the historical susceptibility of the city of Malatya to earthquakes, there was no increase in seismic activity in its vicinity during the February 2023 event. This phenomenon may be attributed to a decoupling effect along the EAFZ to the northeast and southwest of Malatya (SMFS and Main Strand of the EAFZ, respectively), as also shown by the kernel density maps (**Figure *17***).

The distribution of seismicity at depth appears to indicate the presence of extensive highly dipping to subvertical fractures converging at depth along the trace of the EAFZ (e.g., Dolmaz et al., 2008). While at the surface, the structure spans a relatively broad area, at depths exceeding 15 km, all epicenters are located along a distinct single fault or core of high seismicity (see also, e.g., Dolmaz et al., 2008; Balkan & Erkan, 2019). Güvercin et al. (2022) deduced a dip towards the N for this high-seismicity core between at least, 7 and 20 km deep. This palm-shaped arrangement (**Figure *17***) that extends towards the surface distinctly resembles the structures observed in smaller-scale strike–slip faults in various regions around the world (e.g., Harding & Lowell, 1979; Sylvester, 1988).

5.1.6.2. Evaluation of the Method and Comparison of AFAD and Lomax Datasets Maps

This new method allows for the comparison of the seismic distribution graphs of the two datasets (AFAD and Lomax, 2023). The depth distribution of seismicity shows similar behavior, with most earthquakes occurring in shallower layers and decreasing in

frequency at greater depths. The seismicity in both cases is scarce and virtually non-existent below 20 km. This distribution coincides with that observed in other transform fault contexts, such as the San Andreas Fault, where seismicity is effectively absent below 23 km (Smith-Konter et al., 2011; Zeng et al., 2022). The upper layers accommodate deformation by activating fault structures that concentrate all the seismicity, while below 20 km, this deformation might occur by non-seismogenic creep.

The recognition of minima in earthquake concentration, which indicate lower seismicity zones and changes in the mechanical behavior of materials, also allows for the definition of the five layers related to the seismogenic levels that coincide in both data sources within a ±1 km range. Filtered data processing estimated a hypocentral error of less than 2 km, but the minima in the raw data fall within a narrower range. The strong agreement between the two catalogs —raw and relocated data— in the depth distribution of seismicity, despite this being the variable with the highest uncertainty in the calculations of seismic parameters, fosters optimism regarding the interpretations derived from the maps.

According to the kernel maps generated for the two datasets, both show similar high-frequency zones with a distinctive 'number 7'-like shape in plan view. This form aligns well with the trace of the Main Strand of the EAFZ and SMFS activated during this seismological event. The raw data display a more continuous density pattern, while the filtered data show discontinuous high-density nuclei. However, the KDE maps of the Lomax (2023) dataset are consistent with the black nuclei observed in the AFAD data.

In both cases, the kernel maps reveal 3D seismically active structures that resemble large, elongated funnels or palm-tree formations. This method enables the characterization of the three-dimensional architecture of large-scale structures, which are comparable with the geometry of smaller-scale structures observed in other regions, as described previously.

Additionally, the seismicity profiles along the Main Strand of the EAFZ show significant agreement between the two datasets, indicating large vertical structures that converge at the vertical of the black nuclei. These structures are consistent with the interpretations derived from the kernel maps.

Concerning advantages and disadvantages, unfiltered data allow for quick access and processing. They facilitate the analysis of a larger volume of data, providing a more

comprehensive view of seismic activity, including smaller earthquakes that might be lost after filtering. Additionally, the data have lower processing costs and are easier to automate, enabling the application of statistical analyses and subsequent filtering.

On the other hand, the cons include high uncertainty in both the location and magnitude of events, a higher presence of noise and anomalies due to erroneous data that require additional cleaning and filtering, and a greater difficulty in identifying patterns, critical zones, or trends due to the higher dispersion of the data. However, all these issues can be minimized through an effective filtering process (as, for example, KDE does).

In contrast, relocated data ensure higher precision and reliability, as well as a significant reduction in noise due to rigorous cleaning, and allow for the accurate identification of patterns, even migration, fault activity, and risk zones, with great confidence.

However, the data require a long processing time (ranging from days to months) to produce a catalog with fewer earthquakes, are more difficult to automate, frequently need human intervention for calculation, cannot be obtained in real time, and potentially exclude relevant events (such as precursors or aftershocks) either due to filtering or because their magnitudes fall below the threshold required for precise calculation.

This technique must be applied considering a series of assumptions and limitations:

1. Fundamentals and limitations of the kernel technique: One of the primary limitations of all KDE methods is that they produce an image-based representation of seismic data, which requires expert interpretation. Another limitation of this new technique is the determination of the depth range of the layers based on the seismicity distribution, which should ideally be performed by an expert.

2. Regarding scale, data volume, type of kernel method, and bandwidth, a large amount of seismic data is required, and the bandwidth must be selected based on this data volume and the scale of the study area. Larger areas or lower data volumes necessitate greater bandwidths. Additionally, the kernel method should be chosen according to the study's objectives, but, generally, kernel methods that emphasize values closer together are preferable.

Despite all of these limitations, this new technique is useful and should be considered in future studies according to the next contexts:

1. Theoretical frameworks: This method could be applied in numerous contexts, such as fracture theory, which models the distribution of seismic events concerning geological faults and fracture structures. It can also be utilized in fault instability theory to evaluate patterns that may predict future fault behavior and in seismic risk assessment models to identify areas with high densities of seismic occurrences. Additionally, it aids in spatial analysis in geology by examining the distribution of geological features and their relationship with seismic activity. This technique is beneficial in fluid dynamics within faults, as it helps visualize how fluid pressure correlates with seismic events. Moreover, it can be applied in plate tectonics theory to analyze the interaction between tectonic processes and seismic activity, as well as in wave propagation models and studies of seismic precursors. Of course, this innovative technique can be utilized across various depth layers recognized in any planetary area.

2. Geological contexts: This method was applied in complex environments, such as this major transform boundary (Anatolian-Arabian plate boundary), but it can also be utilized in various other settings, including subduction zones, mid-ocean ridges, or volcanic areas.

To summarize, both the filtered dataset and the unfiltered dataset led to similar interpretations when the KDE method was applied. Since the uncertainty in earthquake locations is usually random, a high concentration of earthquakes determined from nonrelocated data should be found in a position close to the nucleus identified from the relocated data, which is what was observed in the case analyzed in this work. The KDE functions proved to be useful treatments and can be considered as a sort of initial, graphical, fast relocation process, accelerating both the treatment and interpretation of data. This approach enhances geological and seismological knowledge and improves earthquake preparedness, prevention, coordination, and rapid response.

5.1.7. Conclusions

Two populations of seismic foci point clouds from the seismic series that occurred in Türkiye and Syria during 2023, containing over 60,000 events, were analyzed. The datasets included raw data recorded by the Turkish Disaster and Emergency Management Authority (AFAD) and relocated and filtered data from Lomax (2023). A new technique was employed to compare these datasets. Analyzing the seismic distribution with depth allowed for the identification of minimal-frequency earthquake levels that separate distinct seismically active layers associated with the mechanical behavior of the materials.

This new technique allows the differentiation of seismogenic levels on which the kernel is applied to recognize the geometry of deep three-dimensional structures. Five seismic layers were defined for both raw and filtered data, with slight variations in depth boundaries: for the raw data: Layer I (0.0–4.9 km), Layer II (4.9–8.8 km), Layer III (8.8–14.5 km), Layer IV (14.5–18.7 km), and Layer V (below 18.7 km); for filtered data: Layer I (0.0–4.8 km), Layer II (4.8–7.9 km), Layer III (7.9–14.9 km), Layer IV (14.9–18.9 km), and Layer V (below 18.9 km).

Both datasets align closely with the Main Strand of the EAFZ and the SMFS, with high-frequency earthquake nuclei recognized in both. The raw data suggest a lack of connection between SMFS and the Main Strand of the EAFZ in most layers.

Kernel density analysis demonstrated that both datasets yield similar geological interpretations. In the southwestern Main Strand, epicenters are concentrated over Quaternary deposits and ophiolites, marked by the February 2023 earthquakes. In contrast, the SMFS aligns with the boundaries of elongated metamorphic blocks from the Precambrian to the Cretaceous. Despite proximity to active faults, seismic activity is notably absent in Paleozoic volcanic and sedimentary formations and northeastern plutonic formations.

The seismicity at depth reveals extensive, highly dipping to subvertical fractures converging along the EAFZ. While surface structures span a broad area, deeper seismicity is concentrated along a distinct fault core. This core, dipping northward between a 7 and 20 km depth, resembles the palm-shaped structures seen in strike-slip faults globally.

Seismicity profiles reveal four high-density nuclei for raw data, with three of them coinciding in horizontal coordinates with those of filtered data. Seismicity is observed up to about a 20 km depth, with high-magnitude earthquakes corresponding to density cores in both datasets. Despite limitations like the 7 km depth structure in the raw data (an artifact due to routine depth attribution of the used catalog of non-relocated data), the profiles effectively highlight the true morphology of seismicity distribution.

Overall, this study demonstrates that a comprehensive seismic catalog with significantly higher uncertainty (such as AFAD database) yields similar interpretations when analyzed using KDE compared to a relocated catalog (such as the Lomax database). This proves to be an effective tool for rapid seismic data treatment, a certain degree of filtering is inherently achieved using KDE (simulating relocation), and interpretation. It would be

ideal to work with these relocated data with very high precision and reliability whenever available, but this is not always possible. While relocated catalogs are ideal for more precise and well-defined studies, unfiltered data can lead to similar interpretations with a significantly shorter response time. While the first type of catalog can be processed almost instantly or within a few hours after the earthquake occurs, the second type requires a more extensive effort and longer processing times (days or even months). This technique, despite its limitations, provides more information relative to other methods in a short time. It can help to better define a three-dimensional seismic hazards, critical zones, segment faults, and segments that have been active but are currently inactive.

To evaluate the accuracy of the interpretations resulting from the analysis of the unfiltered catalog, this study included two forms of validation: an internal validation, which was performed by comparing two populations, one of which has high reliability and certainty (section 4.1.6.2); and an external validation, achieved through coherence with regional geological knowledge (section 4.1.6.1). Based on these validations and the low deviation from the optimal (represented by the control population), it is concluded that the procedure is valid for comparing these two populations, which is further corroborated by its alignment with independent sources, such as geological data. Moreover, the results are fully supported by additional sources, such as geomorphology or geophysics, which also converge on the same observations.

To conclude, this method enhances geological and seismological understanding, thereby contributing to improved earthquake preparedness and response in the event of a major earthquake. We propose that this technique could be a routine method used in seismic centers due to its versatility, agility, and ease of use. This technique, combined with a tectonic and rheological study of any portion of the lithosphere, is key for defining the different seismotectonic levels in that zone. This could lead to the generation of a catalog of slices or layers for each section of the Earth, like how we currently perform seismic zoning for crustal resistance in plan view, but now vertically within the lithosphere.

5.2. Kinematic analysis of the central and southwestern parts of the East Anatolian Fault zone

This fragment is an adaptation of the submitted article: Amador Luna, D.; Alonso-Chaves, F. M. & Fernández, C. (2024). Kinematic analysis of the central and southwestern parts of the East Anatolian Fault zone. Tectonophysics. Available at SSRN: https://ssrn.com/abstract=5056410 or http://dx.doi.org/10.2139/ssrn.5056410

5.2.1. Abstract

This study investigates the distribution of seismicity associated with the February 2023 seismic events in the East Anatolian Fault Zone (EAFZ) and examines its relationship with the structural features of the region, as well as with the kinematic and rheological characteristics of the lithosphere. The EAFZ was spatially divided into six zones or lateral segments across the study area. For each segment, a transpression/transtension model was applied based on the predicted relative movements between the Arabian and Anatolian plates. Results demonstrate substantial agreement with measurements of the *P* and *T* axes derived from focal mechanisms, and with the main stress orientations obtained by other researchers through fault-slip inversion analysis. Additionally, average lithospheric strength profiles were developed, whose comparison with seismicity data, alongside the other findings of this study, provides deeper insights into the complexities underlying the seismic behavior in the East Anatolian Fault Zone.

5.2.2. Introduction

In the early morning of February 6, 2023, a magnitude 7.8 earthquake shook southeastern Turkey and northwestern Syria. The epicenter was located just a few kilometers west of Gaziantep, along the East Anatolian Fault Zone (EAFZ), and quickly reached an "extreme" intensity across the region. By midday, a second magnitude 7.7 earthquake struck north of the initial epicenter, on the Sürgü-Misis Fault System (SMFS), —an east-west fault close to the EAFZ and sometimes considered its Northern Strand. Thousands of aftershocks followed these two major earthquakes, some with significant magnitudes.

The EAFZ is one of the largest transform plate boundaries globally, accommodating the movement between the Arabian, Anatolian and African plates. This complex interaction results in a left-lateral strike-slip boundary, with the Arabian plate moving northward and

the Anatolian plate moving westward. The EAFZ is bounded to the north by the transform boundary of the North Anatolian Fault Zone and to the south by the subductive Hellenic Arc (McClusky et al., 2000; McKenzie, 1972, 1978; Şengör & Yilmaz, 1981). However, there is considerable debate regarding the precise location of the triple junction where these three tectonic plates meet: some researchers place it near Hatay, while others suggest Türkoğlu (e.g., Gong et al., 2024; Mahmoud, 2012; Mahmoud et al., 2013; Meghraoui, M., 2011; Özkan et al., 2023; Yıldız et al., 2020).

Although this region represents a well-studied plate boundary, several aspects of its three-dimensional architecture warrant further investigation. This study examines the structural characteristics of the EAFZ, comparing its architecture with its geological and complex structural features. The relative motion between the Arabian and Anatolian plates is analyzed to infer the expected kinematic regimes of various sectors along the fault. These findings are contrasted with focal mechanism analyses of recent earthquakes and fault-slip inversion data reported by other researchers. Additionally, an average rheological profile of the lithosphere affected by the EAFZ is presented, exploring its relationship with the vertical distribution of seismicity. Gaining deeper insights into the intricate interplay between seismicity, kinematics, structure, and rheology along the EAFZ provides a foundation for improved modeling of its seismic behavior.

5.2.3. Geological setting

At the eastern edge of the Mediterranean Sea and nearby areas, three distinct tectonic plates are identified: the Anatolian, Arabian, and African plates (see **Figure *20***). The geometry and kinematics of these tectonic plates have evolved in a highly complex manner from the Mesozoic to the present day, and this remains a subject of debate within the scientific community (e.g., Dercourt et al., 1986; 1993; Ricou, 1994; Jolivet et al., 2003; Barrier & Vrielynck, 2008; Stampfli & Hochard, 2009; Menant et al., 2016). A significant aspect of this evolution is the formation of different sutures and the transposition of fragments of Mesozoic oceanic lithosphere within the EAFZ region, as depicted in a series of 1:500,000 geological maps produced by the General Directorate of Mineral Research and Exploration of Türkiye (MTA).

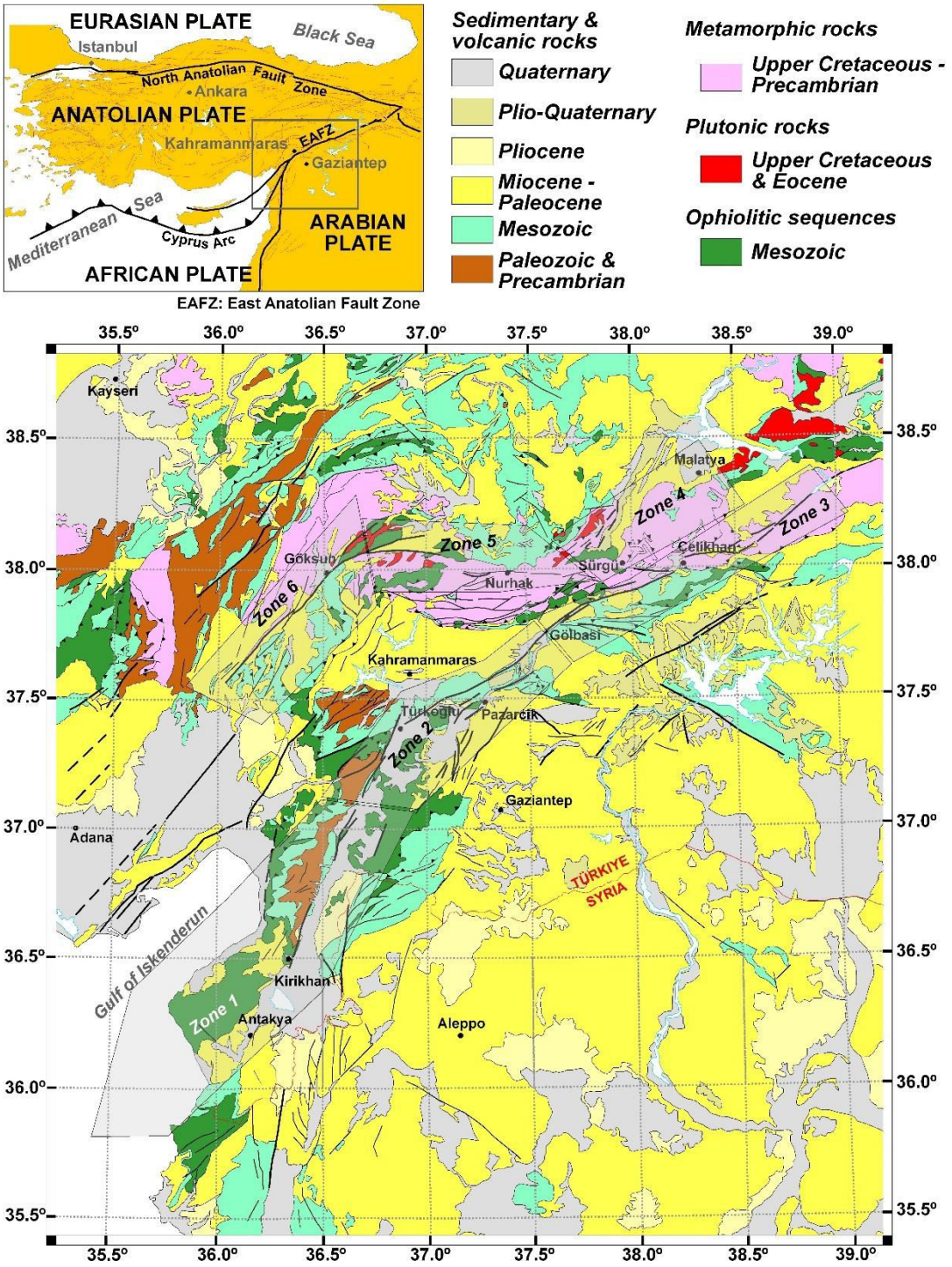

Figure 20. Geological map of the central and southwestern sections of the EAFZ, showing the boundaries between the various studied zones. In the upper left corner, a tectonic map of Anatolia outlines the relevant tectonic plates and their boundaries, as well as the location of the study area (highlighted by rectangle).

The EAFZ is a left-lateral transform boundary oriented approximately N060ºE, spanning roughly 700 km in length. Numerous studies have explored the segmentation of this EAFZ (e.g., Arpat & Şaroğlu, 1972, 1975; Hempton et al., 1981; Muehlberger & Gordon, 1987; Barka & Kadinsky-Cade, 1988; Herece & Akay, 1992; Westaway, 1994; Herece, 2008). This study adopts the classification by Duman & Emre (2013).

Only those segments activated by the 2023 seismic event, all located south of Malatya, are considered here. Along the Main Strand of the EAFZ, and from northeast to southwest, these are the Pütürge and Erkenek segments (zone 3 in **Figure *20*** and **Figure *21*b**), the Pazarcık segment, including the Narli or Nurdağı−Pazarcık Fault (zone 2, **Figure *20*** and **Figure *21*b**), and the Amanos segment (zone 1, **Figure *20*** and **Figure *21*b**).

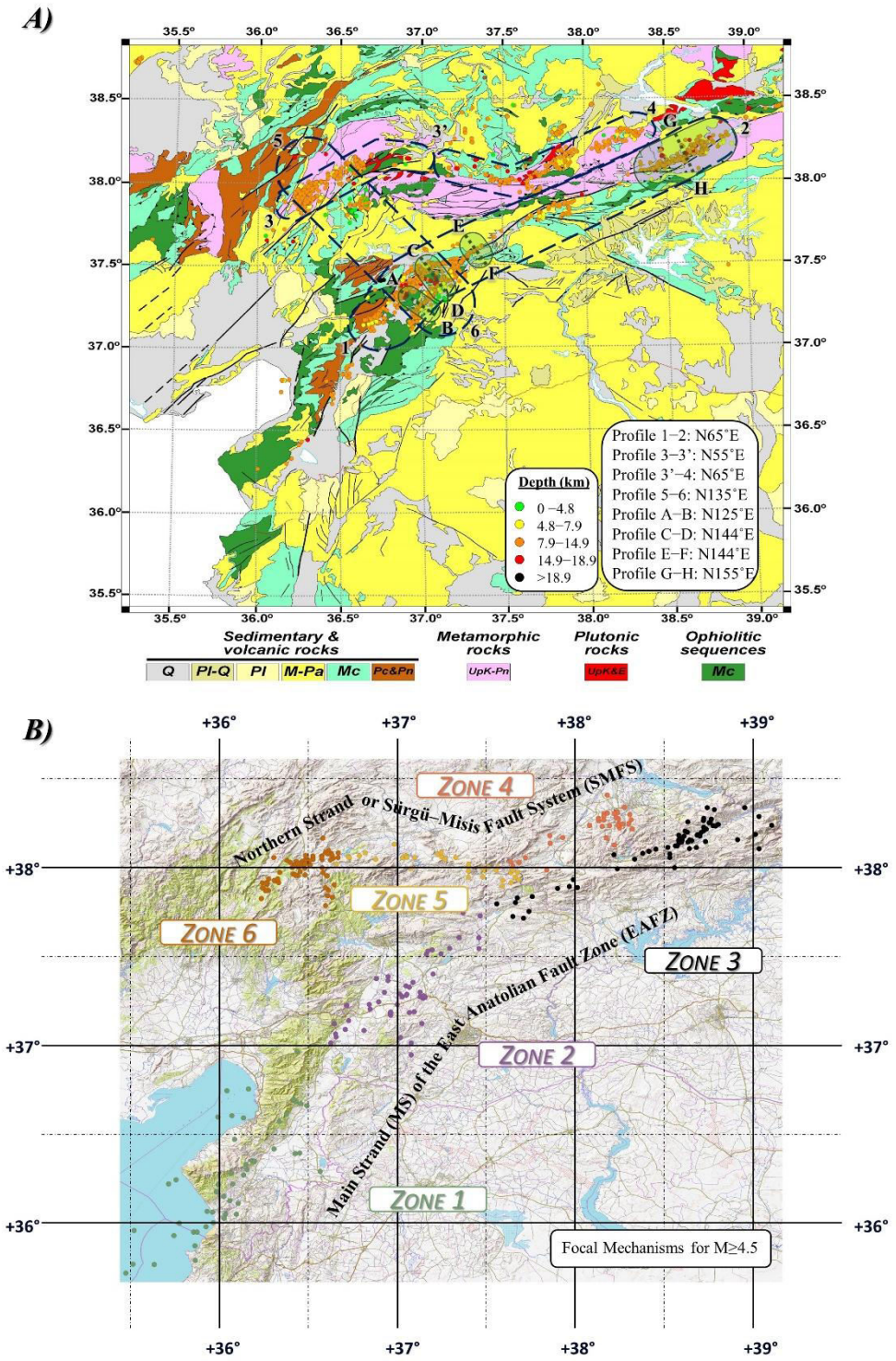

Figure 21. A seismicity map overlaid on a geological map of the southwestern part of the EAFZ, also displaying the profiles analyzed in this study. In the lower right rectangle, the average orientation used for profile representation is

shown. Additionally, the color scale applied to indicate the depth of hypocenters across the studied depth ranges is included: green for depths between 0-4.8 km, yellow for 4.8-7.9 km, orange for 7.9-14.9 km, red for 14.9-18.9 km, and black for depths exceeding 18.9 km. B. Epicenter locations of the focal mechanisms used in this study, displayed over a digital terrain map. The focal mechanisms were filtered for a magnitude greater than 4.5 and sourced from the AFAD, GCMT, KOERI, and USGS catalogs, and compiled by Över et al. (2023). Focal mechanisms are color-coded to represent each of the delineated zones: green for zone 1, purple for zone 2, and black for zone 3, all within the Main Strand of the EAFZ; orange for zone 4, yellow for zone 5, and brown for zone 6, included within the SMFS.

The Pütürge segment extends from Lake Hazar to Çelikhan, intersecting with the Sürgü-Misis Fault System. This segment has an orientation of N060ºE and measures 96 km in length, cutting through Precambrian and Cretaceous metamorphic and ophiolitic rocks.

To the southwest of the Pütürge Segment is the Erkenek Segment, which continues to the Gölbaşı District with an orientation of N075ºE and a length of 62 km. This segment crosscut predominantly Tertiary and Quaternary sedimentary rocks, with a minor presence of Mesozoic rocks. The Pazarcık segment, extends through similar rock formations until reaching a large depression near Türkoğlu, characterized by Cretaceous ophiolitic rocks and Quaternary sediments. This area is where the initial major earthquake of February 2023 and subsequent aftershocks occurred. The Pazarcık segment is oriented N060ºE spanning 82 km. From this point, a secondary branch emerges, running approximately parallel, known as the Narli or Nurdağı-Pazarcık Fault, considered by Čejka et al. (2023), Karabulut et al. (2023), and Okuwaki et al. (2023) as a splay fault. The NPF is the structure where the first earthquake occurred, rapidly transferring stress to the Main Strand of the EAFZ (Čejka et al., 2023; Karabulut et al., 2023; Okuwaki et al., 2023). The final zone along the Main Strand of the EAFZ is the Amanos segment, which begins at Türkoğlu and ends in Kırıkhan, near Antakya (Hatay District), with a length of 112 km and an orientation of N035ºE. Here, the outcropping geology is primarily Precambrian and Paleozoic rocks, as well as ophiolites, Mesozoic, Tertiary, and Quaternary rocks.

Similarly, all segments of the northern strand, or Sürgü-Misis Fault System (SMFS; zones 4, 5, and 6, **Figure *20*** and **Figure *21*b**), cross similar rock types to the Pütürge segment, with a minor presence of Cretaceous and Eocene plutonic rocks. The Sürgü segment of the SMFS is east-west oriented. It begins between Sürgü and Çelikhan and terminates in the surroundings of Nurhak. This segment measures 55 km in length, and continues along the Çardak Fault, where the second major earthquake occurred in February 2023. The Çardak segment maintains the east-west orientation until the Göksun area, shows a length of 85 km, and is considered highly intricate due to the Nurhak fault complexity where the Çardak and Sürgü segments intersect with the Malatya Fault. The final segment, the

Savrun Fault (zone 6, **Figure *20*** and **Figure *21*b**), is N050E striking and extends for 60 km.

5.2.4. Methodology

5.2.4.1. Seismic data and catalog

The seismic data used in this study were obtained from the relocated dataset by Lomax (2023), incorporating data from the Kandilli Observatory and Earthquake Research Institute (KOERI), and the Disaster and Emergency Management Authority (AFAD) catalogs. The filtering process reduced uncertainties in the hypocentral coordinates of the earthquakes to less than 2 km. In total, a catalog of approximately 5,800 earthquakes was used.

Focal mechanism data for earthquakes in Türkiye were also sourced from the AFAD and KOERI catalogs, as well as from the Global Centroid Moment Tensor Catalog (GCMT) (Dziewonski et al., 1981; Ekström et al., 2012), and the United States Geological Survey (USGS), as compiled by Över et al. (2023).

5.2.4.2. Seismic data and catalog

The slice method employed in this study is described in detail by Amador Luna et al. (2024a) (section 5.1.4). This method enables the definition of different layers, corresponding to seismogenic levels, through the analysis of earthquake frequency as a function of hypocenter depth.

Changes in seismic frequency, may indicate variations in lithological composition, among other factors, and reflect differences in mechanical behavior across lithospheric levels. Furthermore, analysis of the Gutenberg-Richter law's b-value (Gutenberg & Richter, 1944; 1945) enables the characterization of the physical properties of regional materials. When density curves of the number of seismic foci with depth are available, distinct maxima can be identified, separated by minima. Each interval between successive minima, corresponding to a layer with increased seismic density, is referred to as a "seismic slice" in this work. The regional seismicity of the study area was analyzed to delimit different layers or seismic slices.

Data for each depth interval were processed independently to generate a distribution map for each slice. Kernel Density Estimation (KDE) analysis was applied to each slice using

the following parameters: a bandwidth of 0.05º (or 0.02º for detailed maps), a pixel size of 0.001º, and the quartic kernel method (see Amador Luna et al., 2024a, or section 5.1.4.2 for a detailed explanation of the values chosen for these parameters).

The color scheme is defined based on quartiles: blue represents the first quartile (indicating greater dispersion), yellow corresponds to the second, red to the third, and black signifies the fourth quartile (indicating areas of high seismic density concentration).

The seismic frequency with depth was examined using Excel LTSC MSO (v. 16.0.1), which was also used to extract data from each slice. Maps were generated using QGIS (v. 3.32).

5.2.4.3. Profiles of seismicity along and across the EAFZ

Three longitudinal seismicity distribution profiles were conducted on the southwestern part of the EAFZ: One along the Main Strand, approximately oriented N065ºE (Profile *1-2* in **Figure *21*a**), and two along the SMFS, oriented N055ºE (Profile *3-3'*) and N065ºE (Profile *3'-4*) from east to west, respectively. Additionally, a larger transversal profile (Profile *5-6*) was carried out, approximately orthogonal to the two previous fault traces (N135ºE). Four additional detailed transversal profiles were also conducted, oriented approximately orthogonal to the fault trace (N125-155ºE). Three of these transversal profiles intersect the central section of the Main Strand (Profiles *A-B*, *C-D* and *E-F*, **Figure *21*a**), while the fourth crosses the northern part (Profile *G-H*). The objective is to illustrate the three-dimensional structure and variations in the fault's geometry along and across its trace.

QGIS was employed to define the influence radii for the earthquakes included in the profiles. Most seismic events linked to the main fault system were identified within a maximum distance of 20 km (e.g., Bulut et al., 2012; Türkoğlu et al., 2015). Consequently, a buffer zone of less than a 0.2° radius was established around each segment, with the largest buffer encompassing the area between the two strands, designed to include earthquakes within this zone while excluding those beyond it. Additionally, the quartic kernel density estimation method was applied, using a bandwidth of 1º (see again Amador Luna et al., 2024a, or section 5.1.4.3, for more details on the choice of the relevant parameter values used for the kernel method).

5.2.4.4. Strength profile

The strength of the lithosphere of the studied zone can be modeled with the concept of strength envelope (e.g., Ranalli & Murphy, 1987), in which the strength of the lithosphere at a given depth is taken as the minimum of the brittle and plastic strengths. In this sense, it is necessary to previously determine the thermal structure of the lithosphere by estimating a geotherm. To this end, the lithosphere affected by the EAFZ has been divided into several compositional layers according to the crustal architecture suggested by Ozer et al (2019) and Yilmaz (2021). In this sense, Ogden & Bastow (2022) suggested that the deformation associated with the EAFZ mainly affected crust from the Anatolian plate (see also Lyberis et al., 1992, and Hüsing et al., 2009). However, Delph et al. (2024) have shown the presence of an underthrusting lithosphere mantle from the Arabian plate below the EAFZ. The following average thicknesses have been taken here for each layer, from top to bottom: upper crust, sediments, sedimentary and metamorphic rocks (8 km); middle crust, felsic rocks, mainly granulitic (12 km); lower crust, mafic rocks (15 km); and an indeterminate thickness for the lithosphere mantle. The depth of Moho is here taken to be 30 km, according to the average depths for the EAFZ provided by Delph et al. (2024), and references therein; see also Dolmaz et al., 2008; Akin, 2016; Abgarmi et al., 2017; Artemieva & Shulgin, 2019; Ozer et al., 2019; and Yilmaz, 2021). The depth to the lithosphere-asthenosphere boundary (LAB) can vary from 60 km (Oruç et al., 2019) to 105 km (Yilmaz, 2021), but recent thermo-barometric estimations from primitive melts led to Delph et al. (2024) to propose a depth of around 71 km in the studied area. The temperature profile in each crustal layer, assuming constant heat production, can be approximated by the following equation (e.g., Tejero & Ruiz, 2002; Turcotte & Schubert, 2014):

$$T_z = T_s + \frac{F}{k}z - \frac{H}{2k}z^2, \qquad (2)$$

where T_s is the temperature at the top of each layer (here, 293 K have been considered for the top of layer 1), F is the heat flow at the top of the layer (here, two extreme values of 70 mW m^{-2} and 90 mW m^{-2} have been selected for the surface heat flow according to the determinations by Bektaş et al., 2007, and Artemieva & Shulgin, 2019), k and H are the thermal conductivity and the heat production rate per unit mass of the layer, respectively, and z is the depth from the top of the layer. The chosen values of the relevant parameters to construct the geotherm are shown in **Table 1**. From the Moho to the LAB the

geothermal gradient is assumed to be linear up to a temperature of 1398 ºC at the LAB (Delph et al., 2024).

The variation with depth of both the frictional and plastic strengths must be determined at each layer to obtain the strength envelope. The brittle frictional failure criterion can be stated in terms of maximum stress difference as (e.g., Ranalli & Murphy, 1987; Ranalli, 1995):

$$(\sigma_1 - \sigma_3)_{brittle} = \beta \rho g z (1 - \lambda) \quad (3)$$

where ρ is the density, g the acceleration due to gravity (9.8 m s^{-2}), z is the depth, β is a factor depending on the tectonic regime (for a friction coefficient of 0.75, β is of 1.2 for strike-slip, which is the regime prevailing today in the studied area), and λ is the ratio of pore fluid pressure to lithostatic pressure. Here, two distinct values of the hydrostatic pore pressure (λ) have been considered at all depths ($\lambda \approx 0$ and 0.37), a common procedure in this type of studies (e.g., Tejero & Ruiz, 2002; Bos & Spiers, 2002). Values of $\lambda \approx 0.37$ are of particular interest in the EAFZ, where geological and geophysical studies have highlighted the importance of high fluid contents or high degree of interconnection deep in the crust of the EAFZ (e.g., Türkoğlu et al., 2015). Plastic strength is approached by the Dorn equation (e.g., Ranalli, 1995):

$$(\sigma_1 - \sigma_3)_{plastic} = \left(\frac{\dot{e}}{A}\right)^{1/n} exp\left(\frac{Q}{nRT}\right) \quad (4)$$

where $\dot{e}$ is the strain rate, R is the gas constant, T is temperature, A is a material constant, n is the stress exponent, and Q the creep activation energy. The chosen values for the distinct compositional layers are shown in Table 1.

A strain rate of $2.2 \cdot 10^{-15}$ s^{-1} has been considered. Strain rate determinations for East Anatolia and the EAFZ range from $2 \cdot 10^{-14}$ s^{-1} to $4.4 \cdot 10^{-16}$ s^{-1} (e.g., Kiratzi, 1993; Bektaş et al., 2007; Aktug et al., 2016; Simão et al., 2016; Güvercin et al., 2022). A reasonable value of $2.2 \cdot 10^{-15}$ s^{-1} has been considered here from the geophysical, geological and geodetic analysis of Simão et al. (2016) and Güvercin et al. (2022) for the EAFZ. Nevertheless, Delph et al. (2024) have also considered faster values of $1 \cdot 10^{-12}$ s^{-1} according to geological information. The effect on the rheological profile of faster or slower strain rates is discussed later in this work.

Table 1. Relevant parameters for the estimation of the thermal and mechanical structure of the studied zone.

Layer	Unit	Lithology	Depth (km)	Density (ρ) kg m^{-3}	Thermal parameters		Creep parameters		
					Thermal conductivity (k) W m^{-1} K^{-1}	Heat production (H) µW m^{-3}	Material constant (A) MPa^{-n} s^{-1}	Stress exponent (n)	Activation energy (Q) kJ mol^{-1}
1	Upper crust	Sediments, sedimentary and metamorphic rocks	0-8	2700 [1]	2.59 [3]	2.93 [4]	10 [5] 1.1x10^{-22} [6]	2 [5] 4 [6]	200 [5] 233 [6]
2	Middle crust	Felsic granulites	8-20	2760 [1]	4.54 [3]	1.10 [4]	8.0x10^{-3} [7]	3.1 [7]	243 [7]
3	Lower crust	Mafic rocks	20-35	2880 [1]	1.40 [3]	0.37 [4]	2.0x10^{-4} [8] 6.3x10^{-2} [9]	3.4 [8] 3.1 [9]	200 [8] 276 [9]
4	Lithosphere mantle	Peridotites	>35	3320 [2]	4.20 [3]	0.002 [4]	2.5x10^{4} [10] 2.0x10^{3} [11]	3.5 [10] 4.0 [11]	532 [10] 471 [11]

[1] Yilmaz (2021); [2] Oruç et al. (2017); [3] Balkan et al. (2017); [4] Maden et al. (2015); [5] calcite rocks, Renner et al. (2002); [6] "wet" quartzite, Memiş et al. (2020); [7] Ranalli (1997); [8] "dry" diabase, Shelton & Tullis (1981); [9] "wet" diabase, Caristan (1982); [10] "dry" peridotite", Ranalli (1997); [11] "wet" peridotite, Ranalli (1997).

5.2.4.5. Focal mechanisms and PT axes

As stated in Section 5.2.4.1, focal mechanism data were sourced from the AFAD, GCMT, KOERI, and USGS catalogs, and compiled by Över et al. (2023). This catalog covers the entire instrumental historical record for the area (from 1977) through to the end of December 2023. To evaluate primary fault orientations and principal stress directions, only earthquakes with magnitudes greater than 4.5 were included, resulting in a dataset of approximately 400 focal mechanisms. Using these data, distribution maps of focal mechanisms were created for each recognized seismic slice and compared with the kernel density maps to establish correlations between observed structures and resulting deformation patterns. A statistical analysis of these focal mechanisms was conducted by differentiating six seismic zones (see **Figure *20*** and **Figure *21*b**), which, as stated above, only partly coincide with the segments outlined by Duman & Emre (2013). As in the profiles, selected focal mechanisms were restricted to a 0.2º radius of influence.

The seismic moment tensor calculation was performed for each focal mechanism using FaultKin software (version 8.1, Marrett & Allmendinger, 1990; Allmendinger et al., 2012). This software calculates seismic inversion based on the focal mechanisms and associated seismic data, enabling estimation of the principal axes (*P* and *T* axes; principal axes of the incremental strain tensor for fault displacement) for each earthquake. These axes were subsequently represented in stereographic projections and analyzed statistically, yielding an average orientation of the *P* and *T* axes for each analyzed zone.

5.2.4.6. Plate kinematics

The orientation of the relative velocity vector between the Anatolian and Arabian plates has been obtained at specific points of the EAFZ. With this information it is possible to evaluate, from larger-scale kinematic data, the context of local deformation in which the seismicity associated with the EAFZ activity develops. In this work, the Arabian Plate has been considered fixed and the relative rotation of Anatolia (AN) relative to Arabia (AR) has been calculated ($_{AR}ROT_{AN}$) at selected points close to the EAFZ. For this, the present-day Euler pole and relative angular velocity of $_{AN}ROT_{AR}$ given by Viltres et al. (2022, their Table 1), mainly based on geodetic measurements, has been used. Computation of $_{AR}ROT_{AN}$ only requires changing the sign of the angular velocity modulus. Conventional matrix algebra techniques applied to finite plate rotations (e.g.,

Cox & Hart, 1986) allow us to calculate the orientation and magnitude of the linear relative velocity vectors at any chosen point on the "mobile" plate (Anatolia). The 6 zones into which the EAFZ has been separated generally coincide with areas of contrasting orientation and/or kinematics. In each zone, a point located on the Anatolian plate in an approximately central position of the zone has been selected. The coordinates of those points, as well as the orientation of the relative linear velocity vector of Anatolia with respect to Arabia are shown in **Table 2**.

Table 2. Kinematic data of the distinct segments of the EAFZ studied in this work.

Zone	$\lambda^{(1)}$	$\phi^{(2)}$	Strike $^{(3)}$	$_{AR}V_{AN}{}^{(4)}$	$\alpha^{(5)}$	$W_k{}^{(6)}$	$X^{(7)}$	$Y^{(8)}$	$Z^{(9)}$
1	36.59°	36.42°	~ 010°	238°	~ -48°	0.41	079°/00°	169°/00°	-/90°
			~ 035°		~ -23°	0.76	091°/00°	001°/00°	-/90°
2	37.55°	37.26°	~ 048°	244°	~ -16°	0.87	101°/00°	-/90°	011°/00°
			~ 070°		~ +06°	0.98	111°/00°	-/90°	021°/00°
3	37.87°	37.97°	~ 050°	248°	~ -18°	0.84	104°/00°	-/90°	014°/00°
			~ 085°		~ +17°	0.85	121°/00°	-/90°	031°/00°
4	37.98°	38.12°	~ 065°	249°	~ -04°	0.99	110°/00°	-/90°	020°/00°
			~ 075°		~ +06°	0.98	116°/00°	-/90°	026°/00°
5	38.02°	37.24°	~ 055°	245°	~ -10°	0.94	104°/00°	-/90°	014°/00°
			~ 102°		~ +37°	0.55	-/90°	128°/00°	038°/00°
6	38.04°	36.64°	~ 025°	243°	~ -38°	0.54	089°/00°	179°/00°	-/90°
			~ 055°		~ -08°	0.96	103°/00°	-/90°	013°/00°

(1) latitude (λ, North) and (2) longitude (ϕ, East) of points of the Anatolian plate located in central positions of each zone; (3) Average range of fault strikes at each zone, according to the maps by Duman & Emre (2013); (4) trend of the velocity vector of Anatolia relative to Arabia (rotation pole from Viltres et al., 2022); (5) angle of oblique divergence (negative) o convergence (positive) between the blocks limited by the distinct segments of the EAFZ for each zone; (6) estimation of the range of possible values of the kinematic vorticity number W_k (Truesdell, 1953) for each zone; (7) to (9) trend and plunge of the principal axes ($X \geq Y \geq Z$) of the infinitesimal strain ellipsoid calculated for each zone from a standard model of monoclinic transtension/transtension (e.g., Fossen & Tikoff, 1993).

5.2.4.7. Transpression and transtension kinematics

The angle formed by the relative movement vector of the fault blocks with respect to the orientation of its boundaries (angle α) is an important element to establish the predominant kinematic type of the fault (e.g., Fossen & Tikoff, 1998). Once the orientation of the relative velocity vector of Anatolia with respect to Arabia has been determined at the different points of the EAFZ, as indicated above, it is compared with the strike of the main structures in each area. For this, the exhaustive cartographic-structural work of Duman & Emre (2013) has been taken as a reference, from which it is possible to obtain the average orientation of the main structures of the EAFZ in the different areas considered in this work (Table 2).

Angle α is calculated at each point, indicating whether it is a purely transcurrent structure ($\alpha = 0^o$), or implies oblique convergence ($\alpha > 0^o$) or oblique divergence ($\alpha < 0^o$). The cases of pure convergence or divergence ($\alpha = \pm 90^o$) are not verified in any EAFZ segments. Oblique tectonics, and transpression and transtension kinematic types have been previously identified on seismic, geodetic, and structural grounds for distinct segments of the EAFZ (e.g., Taymaz et al., 1991; Lyberis et al., 1992; Över et al., 2004a, b; Yilmaz et al., 2006; Güvercin et al., 2022; Özkan et al., 2023). Assuming, for simplicity, a model of steady-state, monoclinic transpression/transtension (in the sense of Passchier, 1998), the kinematic vorticity number (Wk, Truesdell, 1953) of the deformation zone can be computed from angle α according to:

$$W_k = (4\tan^2\alpha + 1)^{-1/2} \quad (5)$$

This expression is derived from the equations of Tikoff & Fossen (1993), Fossen & Tikoff (1998), and Fernández & Díaz Azpiroz (2009). Once the vorticity has been determined, the monoclinic transpression/transtension equations (e.g., Tikoff & Fossen, 1993) can be used to obtain the orientation of the principal axes of both infinitesimal and finite deformation ($X \geq Y \geq Z$). The principal axes of deformation control the orientation, relative to the boundaries of the fault zone, of the main types of minor structures associated with the main fault (folds, reverse, normal, and strike-slip faults). Finally, the predictions of the kinematic model are compared with the orientation of the different structures, that of the main axes of deformation obtained from the analysis of focal mechanisms, and that of the principal stress axes derived from fault-slip inversion procedures.

5.2.5. Results

5.2.5.1. Seismological data (kernels, profiles, slices)

The seismic record for the studied region of the EAFZ indicates a monthly average of approximately 550 earthquakes, based on AFAD data since 2013. However, after the significant seismic event in February 2023, activity surged dramatically, exceeding 10,000 recorded earthquakes within that month alone—averaging over 500 earthquakes daily. Since then, seismicity has shown a declining trend, suggesting a gradual return toward equilibrium.

The depth-based distribution of earthquake occurrences (**Figure *22***), used to define distinct seismological slices, is derived from the relocated catalog by Lomax (2023), which was filtered to include seismic events with an *H* and *Z* location error of less than 2 km. This distribution illustrates a typical seismic pattern, where most earthquakes are concentrated in the upper crust, with a gradual decrease in occurrence as depth increases (see also Dolmaz et al., 2008; Bulut et al., 2012; Balkan & Erkan, 2019). Notably, seismicity is virtually absent in the deeper portions of the lithosphere. Four depth intervals of minimal earthquake concentration are identified at 4.8, 7.9, 14.9, and 18.9 km, suggesting zones of lower strength that serve as boundaries separating slices with differing mechanical behavior (**Figure *22***). Accordingly, five seismological slices are distinguished: slice I from 0.0 to 4.8 km; slice II from 4.8 to 7.9 km; slice III from 7.9 to 14.9 km; slice IV from 14.9 to 18.9 km; and slice V, encompassing seismicity at depths greater than 18.9 km.

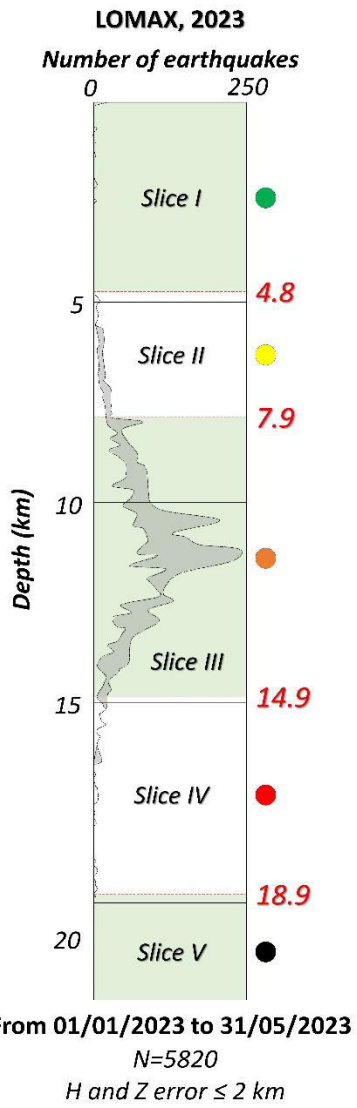

Figure 22. Seismic Depth distribution (number of earthquakes vs. depth in km) for the central and southwestern parts of the EAFZ and adjacent areas (same as contained in **Figure 15**). The catalog used for this analysis is the relocated catalog by Lomax (2023), filtered to include only events with horizontal and vertical location errors (*H* and *Z*) lower than 2 km. It should be mentioned that the Lomax catalog covers the period from January 1st to May 31st, 2023, so the maps only represent seismic activity during this timeframe. Green boxes highlight relatively high-seismicity slices (labelled I to V) separated by weakness bands (low earthquake count), indicated in red. Colored circles denote the color scheme used for each slice in the accompanying map.

Kernel maps have been generated for each slice (**Figure *23***, right). Despite the strict filtering applied, discernible patterns emerge. Seismic activity is mainly concentrated along the fault trace of the Main Strand. Notably, the SMFS, which had been nearly inactive before 2023, appears reactivated after the February 2023 seismic event, now exhibiting intense activity. Depth-wise, the SMFS and the Main Strand maintain large, elongate density maxima down to approximately 18.9 km. At depth, the structure becomes fragmented, showing only isolated nuclei along both strands of the EAFZ. The seismic nuclei exhibit greater lateral spread at shallow depths, progressively narrowing both longitudinally and transversely depth increases, aligning in a funnel-like structure.

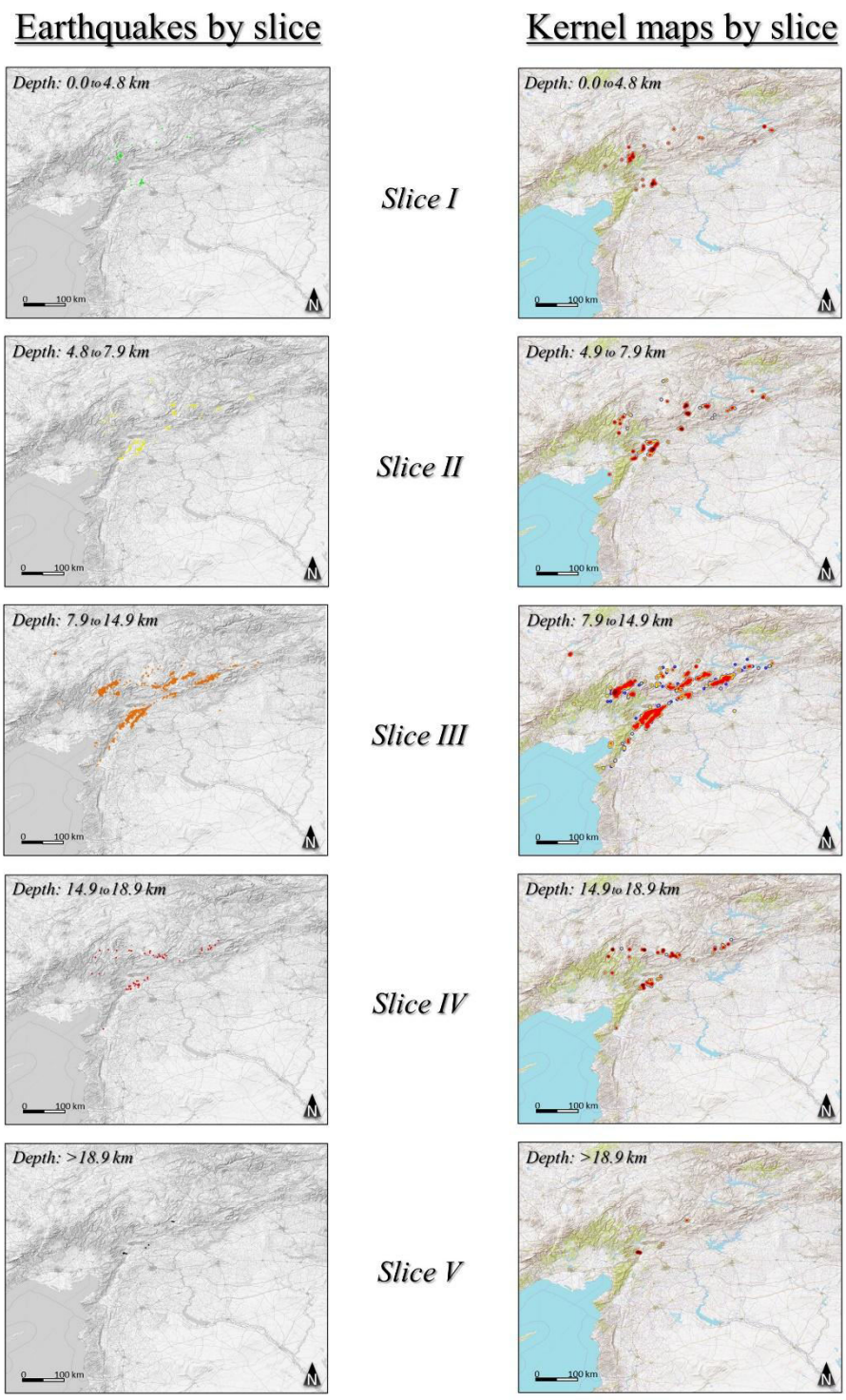

Figure 23. Comparison of earthquake locations and kernel density maps for the central and southwestern parts of the EAFZ, represented at different depth ranges (seismological slices) identified by the seismic distribution profile, Slices I to V (**Figure 22**) (same as contained in **Figure 16** and **Figure 17**). On the left: earthquake locations by slice, with colors chosen to enhance clarity and to represent increasing depth, ranging from green for shallower depths to black for greater depths, as shown in **Figure 22**. On the right: kernel density maps by slice. Black (and red) areas indicate high-density seismicity.

Figure *24* and **Figure *25*** display the earthquake distribution along various profiles. As seen in **Figure *22*** and **Figure *23***, seismicity is relatively uniform down to a depth of

approximately 20 km along profiles parallel and transverse to the SMFS and Main Strand, with most seismic events concentrated between 5 and 15 km depth. At greater depths, the deepest foci are roughly aligned vertically with the kernel maxima (from **Figure *23***). The large-scale three-dimensional geometry of the seismic distribution resembles a series of funnel-like structures, which in two-dimensional cross-sections appear like fan or palm-tree geometries (dashed black lines in **Figure *24***).

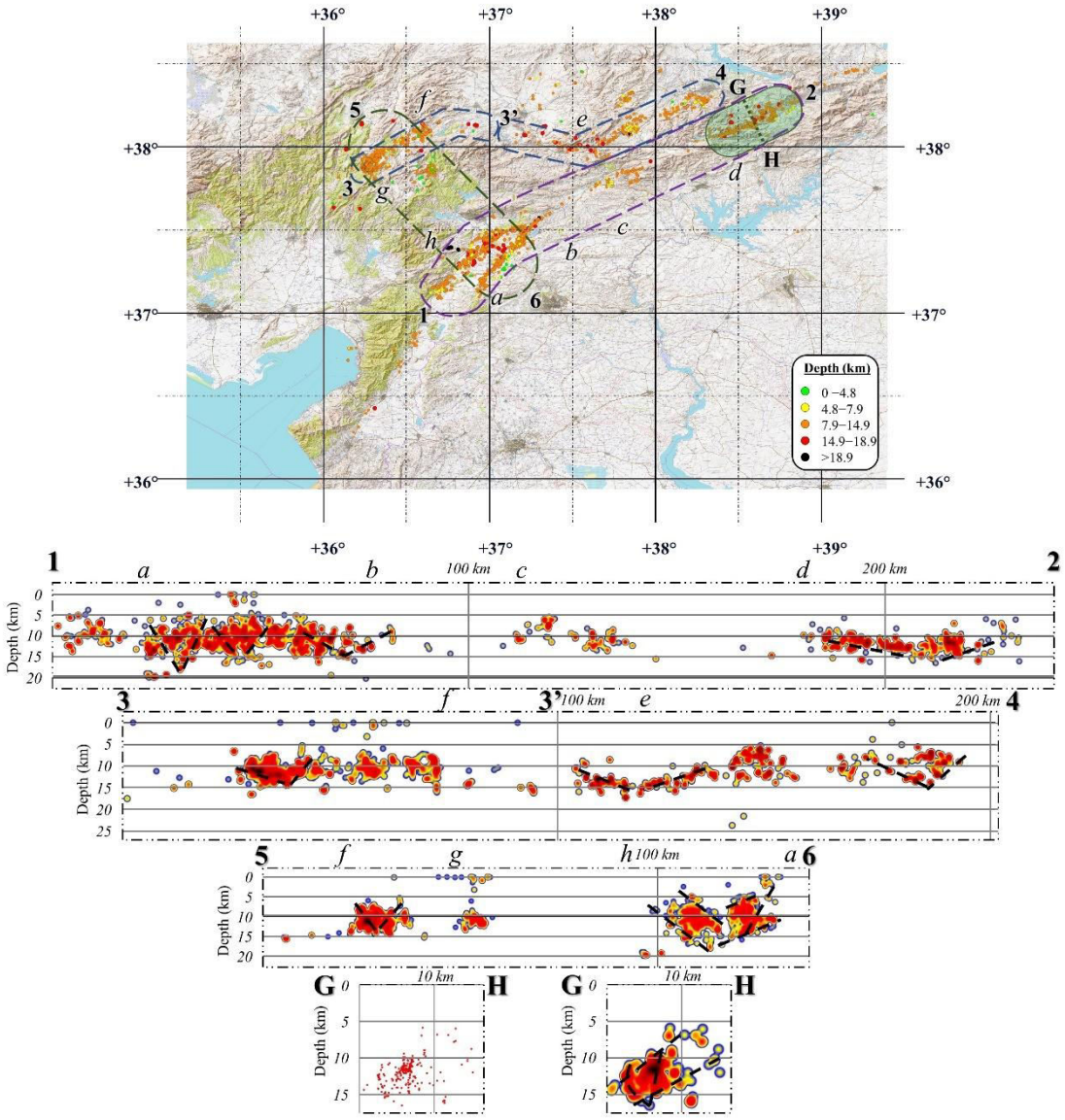

Figure 24. Seismicity profiles along and across the EAFZ: along the fault: *1-2* (Main Strand), *3-3'-4* (Northern Strand); and across: *5-6* (intersecting both the Main Strand and northern strand) and *G-H* (northern part of the Main Strand only). The earthquakes represented correspond to a band about 20 km wide around each profile. For the first three profiles, only kernel density profiles are represented, while for the last one, *G-H*, both point-cloud and kernel density maps are shown. Different points are marked with letters on both the profiles and the map to accurately locate the black loci. The dashed black lines mark possible alignments of kernel density maxima in the profiles.

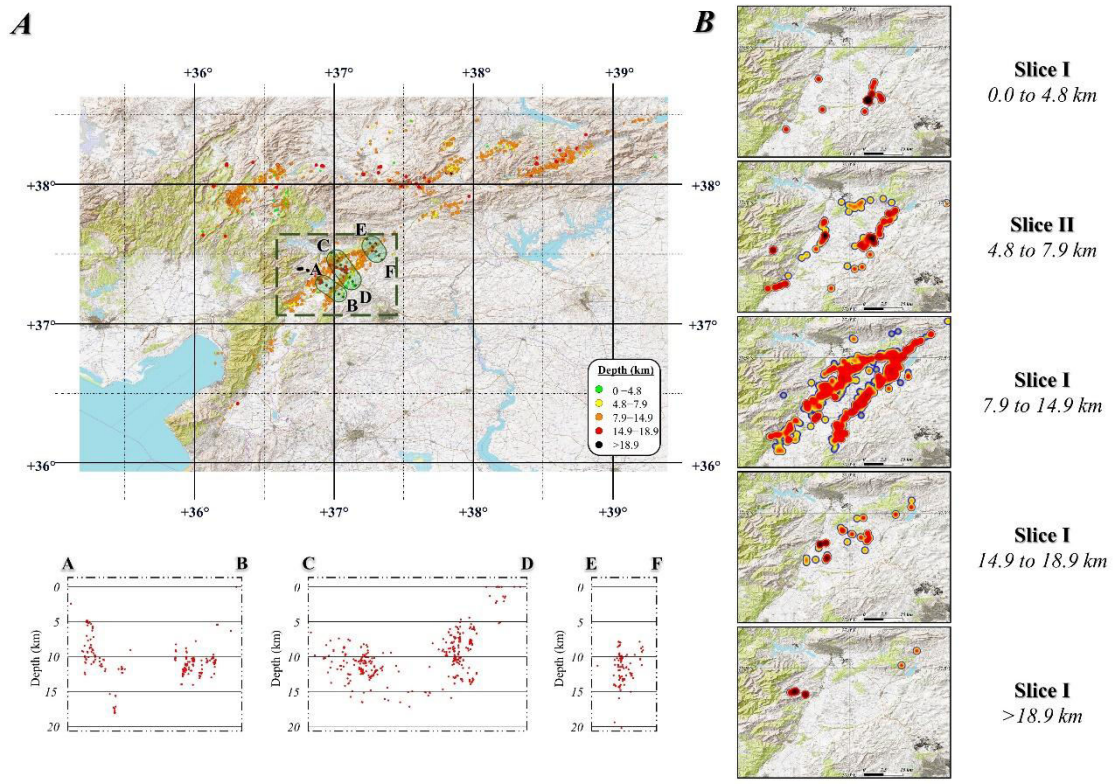

Figure 25. A seismicity profiles across the Main Strand of the EAFZ. From south to north: profiles *A-B*, *C-D*, and *E-F*, located in the region where the first large-magnitude earthquake occurred, to represent the 3-D architecture of the fault. Only point-cloud profiles are shown due to the low number of earthquakes, making kernel density estimation unnecessary. The area of interest in *B* is highlighted with a rectangle in *A*. B. Detailed kernel density maps of the highlighted area for each seismic slice defined in **Figure 22**.

The transect perpendicular to the Main Strand and SMFS (Profile *5-6*) shows four seismic foci: two within the SMFS, which seem isolated, while the two in the Main Strand appear to converge at depth. The maxima corresponding to the Main Strand in Profile *5-6* appear to define two principal planes that outline the three-dimensional structure of the EAFZ. The eastern maxima, exhibiting a curved shape, dip approximately 70–80ºN at greater depths, gradually flattening to around 20ºN at shallower levels. Güvercin et al. (2022) identified clusters within this region dipping between 65º and 40ºN below 7.5 km. In contrast, the western maxima are bounded by planes dipping around 40-50ºS— a feature not previously documented in the literature. These two nuclei converge below the zone of maximum seismic concentration, highlighting a complex structural geometry. In the northeastern part of the EAFZ (profile *G-H*), the elongate maxima dip at roughly 40ºN.

In the SMFS, the structure appears more symmetric, with dips for both planes ranging from 50 to 60ºN and S, although this symmetry is less clear due to the lower earthquake count. However, surface traces of these planes outline regions with significant topographic relief.

Figure *25* highlights the region where the largest earthquakes occurred along the Main Strand of the EAFZ on February 6, prompting the development of three additional profiles to examine fault morphology in greater detail. As noted earlier, fault morphology varies along its trace.

Southern profile (*A-B*): This profile reveals two fault zones. One, located to the NW, has a subvertical orientation, steeply dipping to the southeast, while the second, located at the SE, shows a lower inclination of approximately 45ºNW. The dip of this second fault zone rapidly increases below 10 km steepening into a subvertical structure, forming a stepped, flat-ramp-like morphology. Other subvertical parallel structures are visible to the south (near B point), indicating further complexity in the fault zone.

Central profile (*C-D*): The observed morphology aligns with that described in the southern profile, revealing a southeastward-dipping fault strand, to the NW, with an inclination of approximately 50–60ºS and a more vertically oriented northwestward-dipping strand, to the SE. This structure was previously suggested by the kernel density profile 5–6, indicating a continuation of structural variability along the fault with notable lateral variations in dip angles. Both branches converge at depth along a band of diffuse seismicity at a depth of ca. 15 km.

Northern profile (*E-F*): This profile shows two subvertical and parallel structures that converge at depth between 10 and 15 km depth.

The convergence of these two fault zones is consistent across the three profiles and is reflected in the detailed kernel maps (on the right side of **Figure *25***). In these maps, the seismic nuclei shift downward towards the center of the zone, moving away from the surface trace of the fault. The kernel maps help to visualize the deep structural changes, indicating how the fault's physical morphology may evolve with depth and how seismicity is distributed along these varying fault planes. Both fault zones correspond to the Main Strand of the EAFZ (the northwestern branch) and the Narli or Nurdağı-Pazarcık Fault (the southeastern branch).

Three distinct zones are identifiable along the EAFZ based on the kernel density maps and the analysis of the focal mechanism (**Figure *23*** to **Figure *26***). The westernmost section (EAFZ and SMFS) exhibits transtensional behavior, characterized by a significant prevalence of normal fault focal mechanisms. In contrast, the central region of the Main Strand primarily displays strike-slip mechanisms, while the central segment of the SMFS

is marked by a high concentration of reverse fault mechanisms, indicating a more transpressional character. The elongation of the kernel density maxima and one of the nodal planes associated with the strike-slip focal mechanisms align closely with the primary fault traces. Likewise, in the first zone, the nodal planes of normal fault mechanisms, and in the third zone, those of reverse fault mechanisms, align nearly parallel to the average strike of the main fault, closely matching the kernel density maxima.

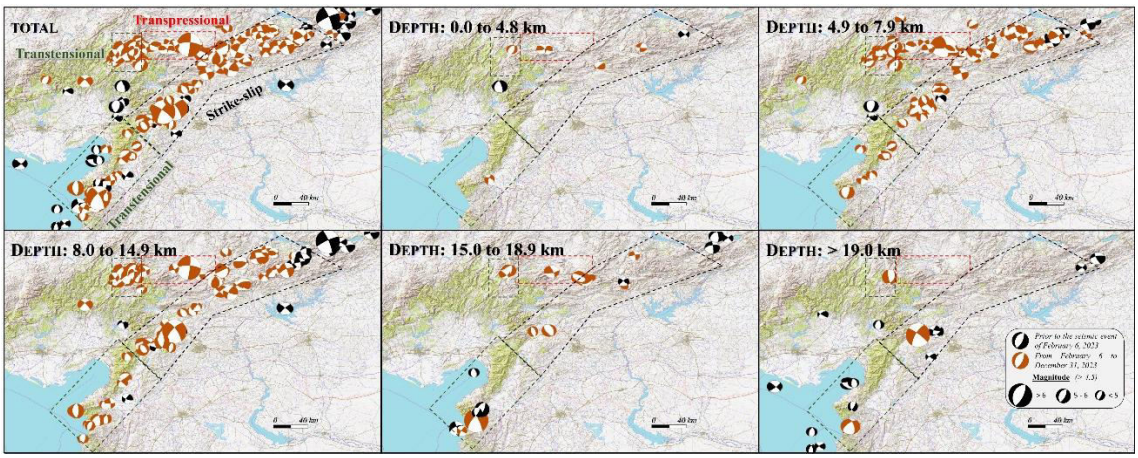

Figure 26. Focal mechanisms from the AFAD, GCMT, KOERI, and USGS catalogs, as well as those compiled by Över et al. (2023), filtered for M>4.5, are plotted on Digital Elevation Maps (DEM, OpenTopoMap, 2024 and OpenStreetMap, 2024) for the five distinct seismic layers. The colors of the focal mechanisms correspond to the age of the earthquake: black for events before 2023, and orange for events occurring during or after the February 6th, 2023 event (up to the end of December 2023). The relative size of the focal mechanisms represents their magnitude: large (>6), medium (5 to 6), and small (4.5 to 5).

5.2.5.2. Rheological layering

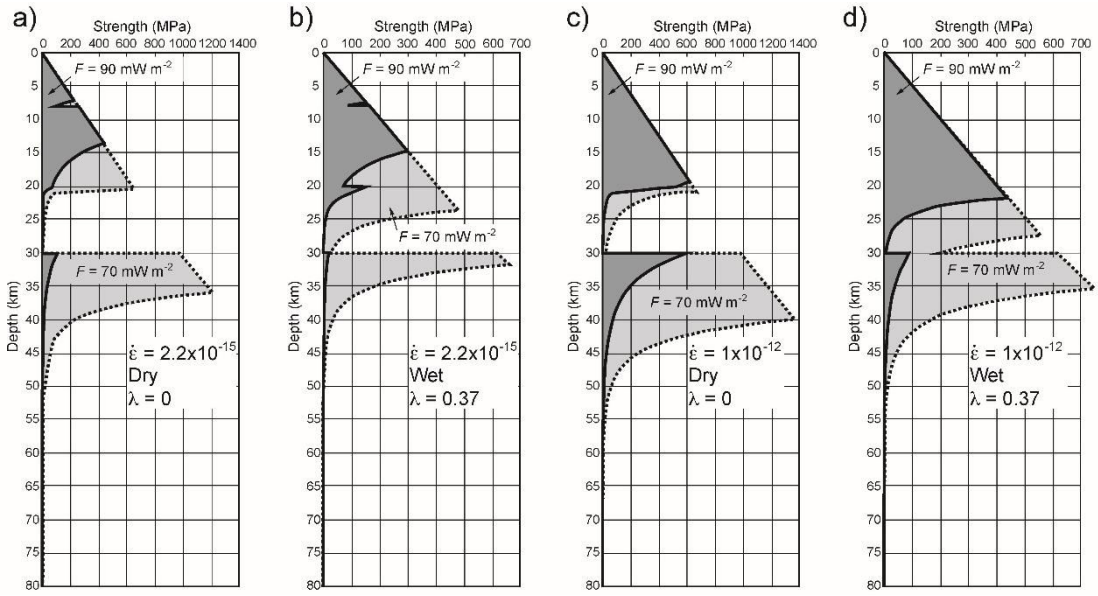

Figure 27. Strength profiles calculated for the studied area considering a strike-slip tectonic regime and dry rheologies with λ=0.37. (a) and (b), strain rate of $2.2 \cdot 10^{-15} s^{-1}$ and dry and wet rheologies, respectively. (c) and (d), strain rate of

$1 \cdot 10^{-12} s^{-1}$and dry and wet rheologies, respectively. See the main text and **Table 1** for a description of the distinguished lithosphere compositional layers, the methodology followed, and the values of the parameters involved.

A selection of rheological profiles for the studied area, assuming a predominant strike-slip regime, is shown in **Figure *27***. The brittle behavior of both the sediments and the sedimentary and metamorphic rocks of the upper crust characterize the upper half of the profile. However, both the depth of the brittle-ductile transition and the presence of a brittle layer at the top of the lithosphere mantle is highly dependent on surface heat flow, the fluid pressure, and the "dry" or "wet" rheological behavior throughout the lithosphere, and the strain rate. In this sense, a surface heat flow of 70 mW m-2 implies that the brittle-ductile transition in the crust would not be reached until a depth of between 20 and 27 km, that is, up to almost 10 km more than for a surface heat flow of 90 mW m-2 (**Figure *27***). Peak strengths in the crust range from more than 600 MPa (70 mW m^{-2}, "dry" materials, and no fluid pressure) to around 300 MPa (90 mW m^{-2}, "wet" materials, and high fluid pressure). Higher values of surface heat flow (e.g., 120 mW m^{-2}) could lower the brittle-ductile transition down to 5-7 km depth, with a maximum strength of around 100 MPa. A very thin (< 1 km) ductile band appears at the base of the upper crust (depths of 7-8 km) for relatively high values of surface heat flow (90 mW m^{-2}) and slow strain rates ($2.2x10^{-15}$ s^{-1}). Besides, a brittle layer up to 10 km thick is predicted in the uppermost lithosphere mantle only for low surface heat flow (70 mW m^{-2}). Finally, the Moho coincides with a rheological change (minimum strength), which may allow a mechanical decoupling between the crust and the mantle.

5.2.5.3. Horizontal and vertical distribution of P and T axes (focal mechanisms)

As outlined in **Figure *21*b**, the study area is segmented into six zones: the first three zones correspond to the EAFZ, from south to north, and the last three correspond to the SMFS, from east to west. According to **Figure *28*** and **Table 3**, zones 1 and 6 exhibit a sub-vertical average P-axis, which is characteristic of normal faulting. This orientation remains relatively stable with depth across the various seismogenic layers analyzed. In contrast, zones 3, 4, and 5 display similar patterns, likely due to the parallel alignment of faults within these segments: P-axes in these zones are sub-horizontal, oriented approximately N016º-022ºE, with minimal variation in orientation with depth. In zone 5, minor sub-horizontal, E-W, and even sub-vertical maxima are observed. Zone 2 shows a range of P-axis orientations, transitioning from horizontal to nearly vertical, likely reflecting its

position as a transitional zone between the transtensional characteristics of zone 1 and the strike-slip nature of zone 3.

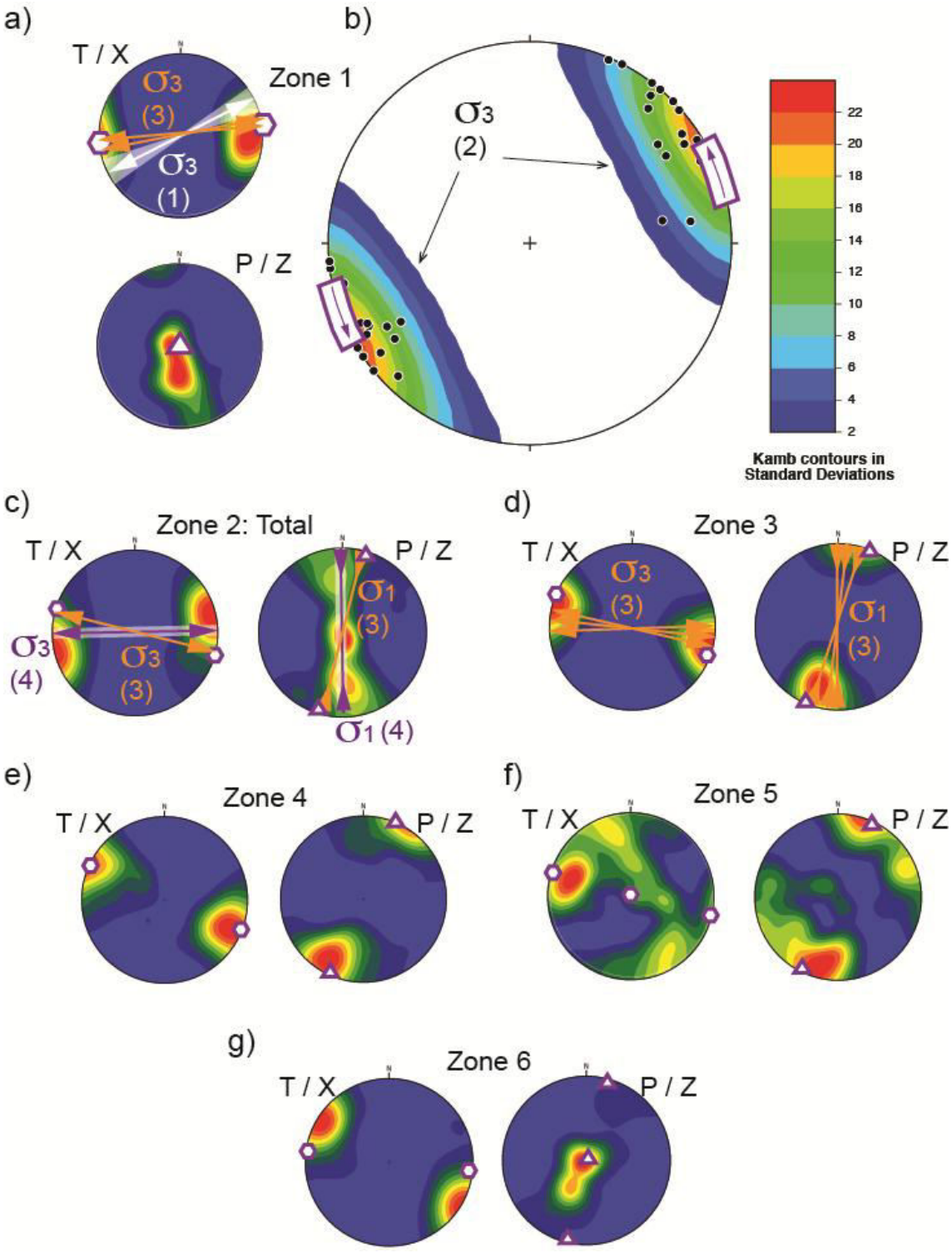

Figure 28. Equal-area, lower hemisphere, density plots of *T* and *P* axes from the focal mechanisms of zones 1 (*a* and *b*), and 2 to 6 (*c* to *g*) compared with the predictions of the kinematic model used in this work and with estimation of principal stress axes from field data. *X* (hexagonal with purple border), and *Z* (triangles with purple border) indicate the long and short axes of infinitesimal strain ellipsoid obtained from the transpression/transtension kinematic model, respectively (**Table 2**). For zone 1 only, the largest stereoplot on the right (*b*), polygons with purple border and white background mark the range of orientations of the *Z* axis of the finite strain ellipsoid according to the results of the kinematic model. The small purple arrows point to the progressive reorientation of the *Z* axis with the increasing finite

strain. Results of fault-slip analyses: The double headed white arrows (1) correspond to the orientation of the least principal stress axis (σ_3) according to Lyberis et al. (1992) for zones 1. In (b): Density plot (equal-area, lower hemisphere) of the σ_3 axes for zone 1 determined by Över et al. (2004a) (2). The double-headed orange arrows (3) mark σ_1 and σ_3 according to Güvercin et al. (2022) for zones 1 to 3. The double-headed purple arrows (4) correspond to the orientation of σ_3 (left plot) and σ_1 (right plot) for zone 2 according to Yilmaz et al. (2006).

Table 3. Statistical mean estimation of the plunge (δ) and trend (φ) of the *P* and *T* axes for each zone and slice of the EAFZ analyzed in this study. Seismic moment tensor calculations were performed for each focal mechanism with M>4.5, using data sourced from AFAD, GCMT, KOERI, and USGS catalogs and compiled by Över et al. (2023). FaultKin v8.1 software (Marrett & Allmendinger, 1990; Allmendinger et al., 2012) was used for the analysis.

T axis

Zone	Total			Slice I			Slice II			Slice III			Slice IV			Slice V		
	δ°	φ°	N	δ°	φ°	N	δ°	φ°	N	δ°	φ°	N	δ°	φ°	N	δ°	φ°	N
1	10.83	88.42	48	0.70	247.20	1	0.24	78.93	7	14.08	91.05	19	13.22	95.05	11	9.09	82.36	10
2	2.60	82.31	46	No data		0	6.55	82.60	15	0.45	266.90	20	10.55	259.30	3	8.07	78.11	8
3	5.35	104.10	64	19.24	126.50	3	0.01	285.30	18	5.66	103.50	29	13.31	111.90	8	3.84	90.13	6
4	0.44	114.20	34	No data		0	1.30	114.90	16	23.19	302.90	10	23.19	309.90	4	7.14	107.20	4
5	16.32	319.10	36	54.60	304.90	1	35.42	344.40	18	6.97	129.90	11	41.09	80.63	4	4.72	124.60	2
6	3.19	296.80	68	2.00	109.50	1	3.14	295.90	30	1.18	298.60	25	8.94	298.30	7	8.94	298.30	5

P axis

Zone	Total			Slice I			Slice II			Slice III			Slice IV			Slice V		
	δ°	φ°	N	δ°	φ°	N	δ°	φ°	N	δ°	φ°	N	δ°	φ°	N	δ°	φ°	N
1	64.65	188.80	48	32.80	156.80	1	62.76	169.30	7	65.34	194.20	19	67.27	208.60	11	63.73	176.00	10
2	52.62	177.10	46	No data		0	56.13	178.50	15	82.10	341.30	20	66.84	26.15	3	17.87	172.20	8
3	16.69	196.00	64	18.95	20.80	3	11.41	197.30	18	18.41	194.80	29	19.92	206.40	8	25.60	182.20	6
4	10.99	202.40	34	No data		0	9.10	207.60	16	8.56	192.70	10	10.69	203.40	4	21.05	199.90	4
5	12.93	216.70	36	17.50	188.50	1	15.86	222.10	18	5.05	214.50	11	20.78	216.00	4	6.86	213.90	2
6	74.51	210.30	68	85.90	228.90	1	82.48	204.40	30	65.71	212.20	25	80.89	218.10	7	42.46	207.30	5

Regarding the *T*-axes (see also **Figure *28*** and **Table 3**), zones 1 and 6 display notable differences. In zone 1, the T-axes are predominantly oriented E-W, while in zone 6, they exhibit a NW-SE trend. This orientation remains consistent with depth in zone 6, while in zone 1, a slight shift from E-W to ENE-WSW is observed in the shallow layers (above 7.9 km). Zones 3 and 4 are similar, with predominantly stable, sub-horizontal E-W to WNW-ESE trends. Zone 2 resembles zones 3 and 4 but maintains a nearly constant sub-horizontal ENE-WSW trend. Finally, zone 5 exhibits greater complexity, with the primary maximum of T-axes predominantly horizontal and trending WNW-ESE. Additionally, minor maxima are arranged along a NW-SE striking great circle, dipping steeply to the NE.

5.2.5.4. Kinematic models

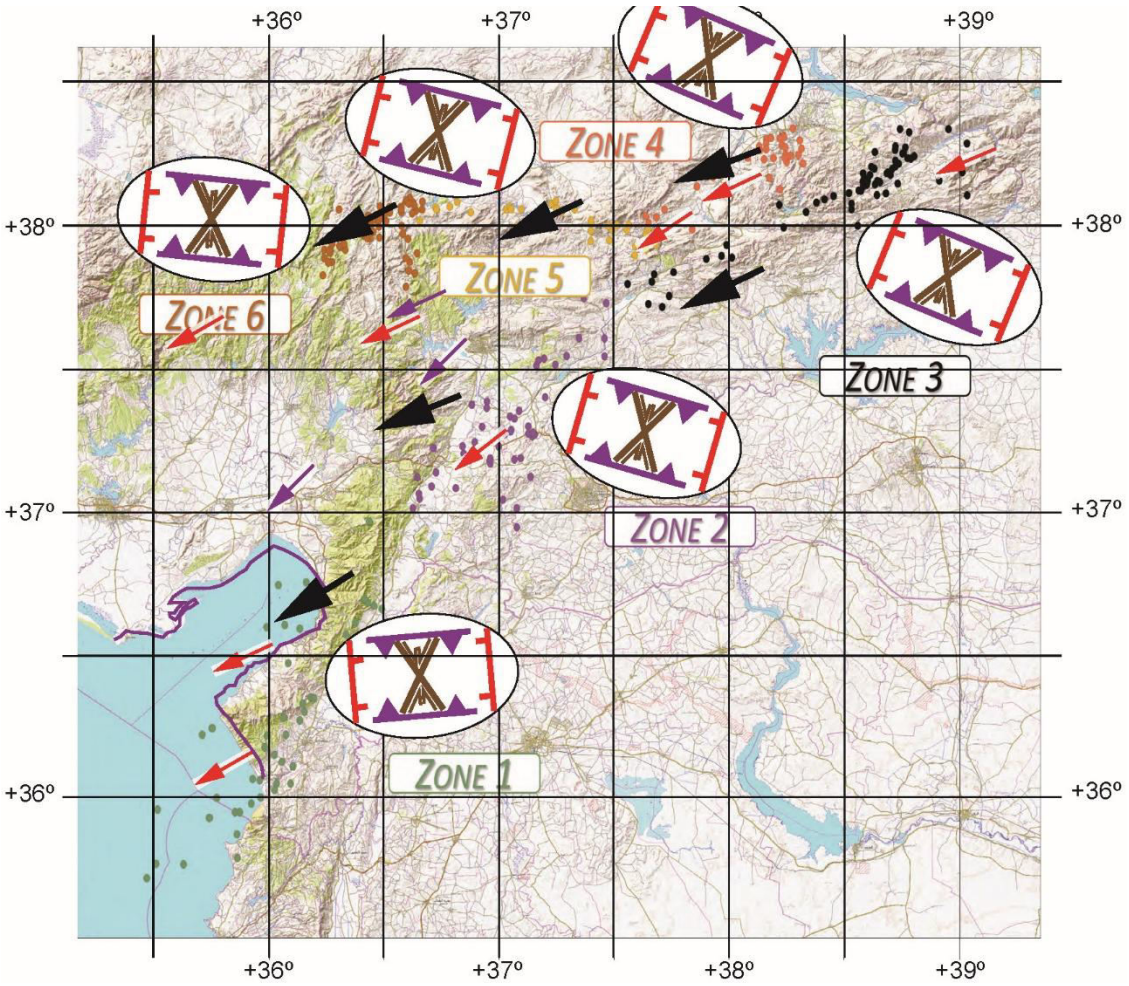

Figure 29. Results of the determination of the orientation of the relative velocity vector of Anatolia with respect to Arabia (black arrows), and its comparison with displacement vectors determined directly with GPS in nearby areas (red arrows, according to Reilinger et al., 2006 and Reilinger & McClusky, 2011; purple arrows according to Özkan et al., 2023). In each zone of the EAFZ sketches have been drawn showing the average theoretical orientation of minor structures (red, normal faults or tension joints; purple: reverse faults or fold traces; brown: strike-slip conjugate system).

The linear velocity vectors of Anatolia relative to Arabia are directed towards the SW, with orientations that vary between N238ºE and N249ºE (**Figure *29***). The resulting vectors virtually match GPS data determined in the area by, among others, Reilinger et al. (2006), Reilinger & McClusky (2011), and Özkan et al. (2023). As a result, and considering the variable orientation of the main structures in each zone according to the maps by Duman & Emre (2013), based on the kernel density maps and the analysis of the focal mechanism (**Figure *23*** to **Figure *26***), the angle α is clearly negative (oblique divergence, transtension) in zones 1 and 6 (**Table 2**). Zones 3 and 4 show low values of α with slight variations in their sign, indicating the predominance of almost pure strike-slip kinematics, with minor transtensional or transpressional segments depending on the local strike of the EAFZ. Zone 2 is predominantly of oblique divergence in its southwestern and central region and transcurrent in its northeastern area, in transition with zone 3 (**Table 2**). Finally, zone 5 is dominated by oblique convergence, although there are locally small segments of strike-slip displacement or even oblique divergence.

Vorticity values (**Table 2**) are high in zones 2, 3, and, 4, where simple shear dominates ($W_k > 0.84$). Lower values are obtained where oblique divergence is the rule (zone 1 and, partly, in zone 6), with $W_k < 0.81$, i.e., in the field of pure-shear-dominated transtension (Fossen et al., 1994). Zone 5 is mostly in the file of pure-shear dominated transpression (with W_k as low as 0.55), although more simple-shear-dominated segments are also present there ($W_k = 0.94$). The monoclinic transpression/transtension kinematic model allows obtaining the orientation of the X, Y, and Z axes of the ellipsoid of infinitesimal deformation. These orientations are shown in **Table 2**, and X and Z axes are plotted in **Figure *28***, where it is possible to appreciate a certain variability from one zone to another, and within each zone. In any case, the ellipsoid long axis (X) is mostly horizontal, and its trend deviates only slightly from the E-W direction.

5.2.6. Discussion

5.2.6.1. Seismicity and geology of the EAFZ

The seismic activity during the February 2023 earthquake shows a clear correlation with the geological features of the study area (**Figure *21***). Most epicenters align with the primary directions of the Main Strand of the EAFZ and the SMFS, with a significant concentration of events along the Savrun segment (N60ºE, Zone 6 in **Figure *21***). Significant activity is also observed at the connection between the Amanos (N40ºE) and

Pazarcık (N70ºE) segments and the Narli or Nurdağı-Pazarcık Fault (N40ºE), where the largest earthquake of the February 2023 event occurred (Zone 2).

Interestingly, the Çardak segment, where the second-largest earthquake of the event occurred, exhibits limited seismicity. This may be attributed to the strict filtering applied during the analysis. Seismicity also aligns well with specific geological formations. In the southwestern segment of the Main Strand, earthquakes are concentrated over Quaternary deposits and ophiolites. This ophiolitic suture, marking the boundary between the Anatolian and Arabian plates, is sharply defined by the seismic activity of February 2023.

Conversely, along the SMFS, seismic activity predominantly follows the boundaries of elongated blocks composed of metamorphic rocks of varying ages, from Precambrian to Cretaceous. These blocks run parallel to the main trace of the SMFS. Notably, despite their proximity to active faults, Paleozoic volcanic and sedimentary rocks, as well as plutonic formations, exhibit virtually no seismic activity.

As previously noted, seismic activity along the SMFS had been minimal in recent years, with only limited events occurring in the southwestern segment of the Main Strand. However, the February 2023 earthquake reactivated seismicity across these areas. Despite Malatya's historical susceptibility to earthquakes, no significant increase in seismic activity was observed near the city during this event. This lack of activity could potentially be attributed to a decoupling effect along the East Anatolian Fault Zone (EAFZ), like what could be occurring in the Pütürge segment and the northern portions of the EAFZ, which appear to have remained unaffected by this seismic event.

The depth distribution of seismicity indicates the presence of steeply dipping to sub-vertical fractures converging at depth along the East Anatolian Fault Zone (EAFZ), consistent with previous studies (e.g., Dolmaz et al., 2008). While the surface structure spans a broad area, seismicity at depths greater than 15 km is concentrated within high-seismicity cores (see also: Dolmaz et al., 2008; Balkan & Erkan, 2019; Amador Luna et al., 2024a, or section 5.2.5.4 and **Figure *18***). Güvercin et al. (2022) inferred a northward dip for this high-seismicity zone, occurring between depths of approximately 7 and 20 km (see also Profile G-H in **Figure *24***).

This configuration resembles a palm-shaped structure extending toward the surface, like in smaller-scale strike-slip faults documented in other regions worldwide (e.g., Harding & Lowell, 1979; Sylvester, 1988). However, a more intricate scenario is indicated by the

three-dimensional funnel-like geometry of the seismicity distribution, together with morphological variations along the fault. This funnel-like structure becomes more apparent when analyzing non-filtered data, as shown by Amador Luna et al. (2024a), or sections 5.2.5.3 and 5.2.5.4, as **Figure *17*** and **Figure *18***.

Along the EAFZ, locked segments, which rupture during major seismic events and generate the observed funnel geometries, alternate with segments exhibiting more continuous displacement (creep). Türkoğlu et al. (2015) highlighted spatial and temporal variations in fluid content and composition as a potential explanation for these contrasting behaviors.

The six zones into which the East Anatolian Fault Zone (EAFZ) are divided in this work (**Figure *21*b**) partially correspond to the segments identified by Duman & Emre (2013). According to **Figure *21*** and **Figure *23*** to **Figure *29***, zone 1 aligns with the terminal trace of the Amanos Fault, where its orientation closely corresponds to the seismic distribution and the kinematic model's predictions for a transtensional regime under these conditions. A similar situation is observed in Zone 6, which correlates with the Savrun segment.

Zones 3 and 4, corresponding to the Erkenek and Sürgü segments, respectively, show a good agreement with the kinematic model's expectations for a pure strike-slip regime. Zone 5, associated with the Çardak segment, presents a highly complex context, complicating a definitive identification of the primary orientation of the *P*-*T* axes. This complexity may be related to the Nurhac Fault Complexity, where the Sürgü, Çardak, and Malatya segments converge. Nevertheless, a transpressive regime is evident in this area, as indicated by the increased occurrence of reverse fault focal mechanisms, consistent with the kinematic model's predictions.

Finally, Zone 2 exhibits a "transitional" character, likely due to the inclusion of seismic events from both the Amanos and Pazarcık segments. Its proximity to Türkoğlu, where a notable change in the segment orientation of the EAFZ occurs, may explain these transitional characteristics.

5.2.6.2. The tectonic and kinematic conditions of the EAFZ

The theoretical orientation of the principal axes of the infinitesimal deformation in each zone, obtained from the monoclinic transpression/transtension model (**Table 2**), can be used to predict the initial orientation of the minor structures associated with the EAFZ.

An average position of those structures has been plotted in **Figure *29***, together with the relative motion vectors of Anatolia with respect to Arabia. The maps showing the structural complexities of the different segments of the EAFZ (e.g., Muehlberger & Gordon, 1987; Lyberis et al., 1992; Yilmaz et al., 2006; Aksoy et al., 2007; Duman & Emre, 2013; Köküm & İnceöz, 2018) broadly agree with the predictions of the kinematic model in **Figure *29***. Thus, normal faults are usually oriented in NNE-SSW direction in the central part of the EAFZ (zones 2 to 6), while they turn towards more northerly positions, or even NNW-SSE, in the southwestern part (zone 1). The traces of the thrust faults, on the other hand, tend to be E-W (in the western part) and WNW-ESE (central part). The synthetic strike-slip faults are arranged at a low angle to the general layout of the EAFZ, while the antithetical ones show NW-SE strikes. Similar conclusions, although based on a simpler model, only considering simple-shear kinematics for the EAFZ was advanced by Bulut et al. (2012).

This congruence between the predictions of the kinematic models and the large- and small-scale structure of the EAFZ can be confirmed by comparing these kinematic results with information from seismicity (focal mechanisms) and the inversion of fault-slip field data (**Figure *28***). Our statistical study on the average orientation of the *T* and *P* axes deduced from the focal mechanisms determined in each zone shows, in general, a good compatibility with the predictions of the transpression/transtension model (*X* and *Z* principal axes of the strain ellipsoid, respectively). Thus, for zone 1, the *T* and *P* axes are virtually coincident with the orientation of the long (*X*) and short (*Z*) axes of the infinitesimal strain ellipsoid, respectively (**Figure *28*a**). This coincidence is also excellent for the orientation of the principal stress axes obtained from stress inversion of focal mechanisms by Güvercin et al. (2022). The orientation of σ_3 (minimum principal stress axis) obtained by fault-slip inversion techniques by Lyberis et al. (1992) and Över et al. (2004a) is slightly oblique with respect to those obtained using focal mechanisms or the kinematic model. The instantaneous stretching axes are commonly interpreted as reflecting the principal stress axes (see e.g., discussion in Davis & Titus, 2011). However, in a non-coaxial shear zone (like the EAFZ), minor structures are necessarily rotated (for a recent review see Fernández & Díaz-Azpiroz, 2022) and the results of fault-slip inversion should deviate from the principal axes of the infinitesimal deformation. Instead, when finite deformation is considered, the agreement between the results of the fault-slip inversion and the transpression/transtension kinematic model is greater (**Figure *28*b**). In

line with what was indicated by previous authors (e.g., Över et al., 2004a, b), the EAFZ in zone 1 can be described as a kinematically transtensional structure with a predominance of the pure-shear component ($W_k < 0.81$).

In zone 2, the analysis of the focal mechanisms yielded similar results as the orientations of σ_1 and σ_3 (maximum and minimum principal stress axes, respectively) obtained by Yilmaz et al. (2006), also based on the study of focal mechanisms in the area between Türkoğlu and Celikhan (**Figure *28*c**). On the other hand, the orientation of the *X* and *Z* axes of the infinitesimal deformation predicted by the kinematic model deviate about 20º clockwise from the maximum of *P* or *T* axes obtained by analyzing the focal mechanisms. Note, however, that a good coincidence is still observed between the results of the kinematic model and the orientation of the principal stress axes obtained by Güvercin et al. (2022). The difference highlighted above may be due to the complexity of zone 2, characterized by the lateral change from a region of transtension (zone 1) to another where strike-slip displacements predominate (zone 3).

It is in zones 3 and 4 where the greatest similarity is observed between the results of the seismicity study (our own analysis of focal mechanisms or that of Güvercin et al., 2022) and those of the transpression/transtension model (**Figure *28*c**, **d**). These results also fully coincide with those obtained by structural analysis and fault-slip inversion by Köküm & İnceöz (2018) for the eastern part of the EAFZ. It can be concluded that in zones 3 and 4 the EAFZ (and associated structures like the Malatya Fault) behaves from the kinematic point of view as a purely transcurrent structure, although with a highly varied set of associated minor structures such as folds, normal, reverse, and strike-slip faults, and local releasing and restraining bends.

Zone 5 is the most complex from a kinematic point of view. In zone 5, the oblique convergence between the blocks separated by the fault (**Table 2**) takes place. The physical experiments of Cooke et al. (2020) have shown that, in the initial stages of evolution of fault systems subjected to oblique convergence, reverse faults, en-échelon extensional structures, and strike-slip faults develop, all of them with simultaneous activity. This type of slip partitioning under oblique convergence seems characteristic of zone 5, giving rise to several contrasted orientation maxima in the *T* and *P* axes of the focal mechanisms (**Figure *28*f**). Nevertheless, the comparison between the orientation of the infinitesimal deformation axes obtained from the kinematic study, and that of the maxima of the *P* and *T* axes from the analysis of earthquake focal mechanisms offers a reasonable fit.

Finally, in zone 6 there is an acceptable coincidence between the kinematic model and the focal mechanisms. The *T* and *P* axes show the typical pattern of normal faults (with the *P* axis vertical). However, the kinematic model predicts both vertical and horizontal orientations of the *Z* axes (**Figure *28*g**), which has not been observed so far in the analysis of focal mechanisms. This can be explained by the fact that zone 6 is the western continuation of zone 5, and has a curved geometry, implying a lateral transition between a strike-slip and a transtension regime.

5.2.6.3. Contributions on the rheological behavior of the EAFZ at depth

Before entering the comparison between the strength profile estimated for the area studied and the distribution of seismicity with depth, it is convenient to analyze the differences that reasonable changes in the value of the parameters used would produce in the strength profile. The effect of surface temperature variation (between, say 273 K and 293 K) is practically indistinguishable in the profiles. The same can be said when reasonable variations in the density of the different crustal layers are considered. The influence of the surface heat flow is crucial (**Figure *27***). The maps of Artemieva & Shulgin (2019) (their Figure 7**Figure *26***) indicate that the EAFZ would have values of heat flow ranging between 60 and 100 mW m^{-2}. Here intermediate reasonable values of 70 and 90 mW m-2 have been considered. The main effect on the strength envelopes of taking surface heat flows close to or larger than 90 mW m^{-2} is that the thickness of the brittle segments of the upper half of the crust and the strength of the upper mantle strongly decrease.

In this sense, it is tempting to suggest that the thermal state of the lithosphere along the EAFZ could have a decisive influence on its seismic response, so that zones with a thermal flow $\geq$ 100 mW m^{-2} would show a tendency to aseismic behavior, with a seismicity concentrated in the highest part of the crust and shallow blocking depths. On the contrary, the coldest zones (surface heat flow of 70 mW m^{-2} or less), with greater strength, would present deepest blocking depths, showing strong elastic deformations in the upper crust (and even in the upper mantle) which can cause large earthquakes. Differences in heat flow along the EAFZ could explain, together with temporal and spatial changes in crustal fluid content (Türkoğlu et al., 2015), the observed variation in seismicity, with the generation of the funnel-type structures that have been described in this work (**Figure *24***). This proposal is in line with the finding of Dolmaz et al. (2008) that the seismic gap zones of the EAFZ are in places whose Curie point depth (CPD) is

shallow, while the areas of steep lateral gradient in the CPD coincide with a dense concentration of earthquakes. Unfortunately, knowledge of the surface heat flow distribution along the EAFZ is still poor, so a quantitative comparison, segment by segment, of the mechanical structure of the lithosphere with the depth distribution of earthquakes is not yet possible.

However, it is feasible to make a general comparison of the strength profiles with the distribution of seismicity with depth in the entire area studied, which reveals an interesting correlation (**Figure *20***). Seismicity below 25 km has hardly been observed for the 2023 seismic events. The comparison has therefore been limited to the crust. On the other hand, the strength profiles for fast strain rates ($1 \cdot 10^{-12}$ s^{-1}) show a lithosphere with thick levels of high strength, which do not correspond to the depth distribution of the foci of the seismic events analyzed. Comparison of the rheological profiles for 90 mW m^{-2} with the distribution of seismicity at depth shows several similarities. Firstly, the minor maximum of earthquakes at around 8-9 km depth coincides with the contact between the upper and middle crust. In this zone, a thin zone with plastic behavior is observed at around 8 km depth, separating two brittle blocks. Most of the seismicity is concentrated in a prominent maximum located between 10 and 12 km depth, coinciding with the brittle part of the middle crust, with the main strength peak of the lithosphere for a strain rate of $2.2 \cdot 10^{-15}$ s^{-1}, and a surface heat flow of 90 mW m^{-2}. The highest part of the lower crust, in its contact with the middle crust (at a depth of 20 km), implies a contrast of strengths, marked by a small maximum in the seismicity distribution profile.

A possible explanation for the less abundant, although existent seismic activity located at depths where rheological profiles predict plastic behavior is found in the complex interactions between the brittle and plastic parts of large faults, especially in a structure as complex as the EAFZ. The segmentation, irregularities, and the presence of broad fracture bands in the EAFZ (e.g., Duman & Emre, 2013), characteristic of a still immature structure (e.g., Dewey et al., 1986; Muehlberger & Gordon, 1997; Yilmaz et al., 2006; Bayrak et al., 2015; Türkoğlu et al., 2015; Abgarmi et al., 2017), can trigger interaction mechanisms between plastic and brittle segments of adjacent structures (Cowie et al., 2013; Mildon et al., 2022). A detailed study of the seismicity depth distribution of each of the main structures associated with the EAFZ would be necessary to elucidate this possibility.

Another point highlighted by **Figure *30*** is the possibility for the EAFZ of a thick brittle-to-ductile transition, as has been suggested for large faults by Thom & Kirkpatrik (2023). In this sense, it would be essential to analyze the characteristics of the low-frequency events and the seismic tremor in the EAFZ area. A comparison of these data with the mechanical structure of the lithosphere (such as that shown in **Figure *30***) would be an important step to check the presence and width of transient creep zones in this large structure, and would also serve to understand the meaning of the determinations of locking depths in the EAFZ, such as those obtained by Aktug et al. (2016), which present thick uncertainty zones (larger than ± 6 km).

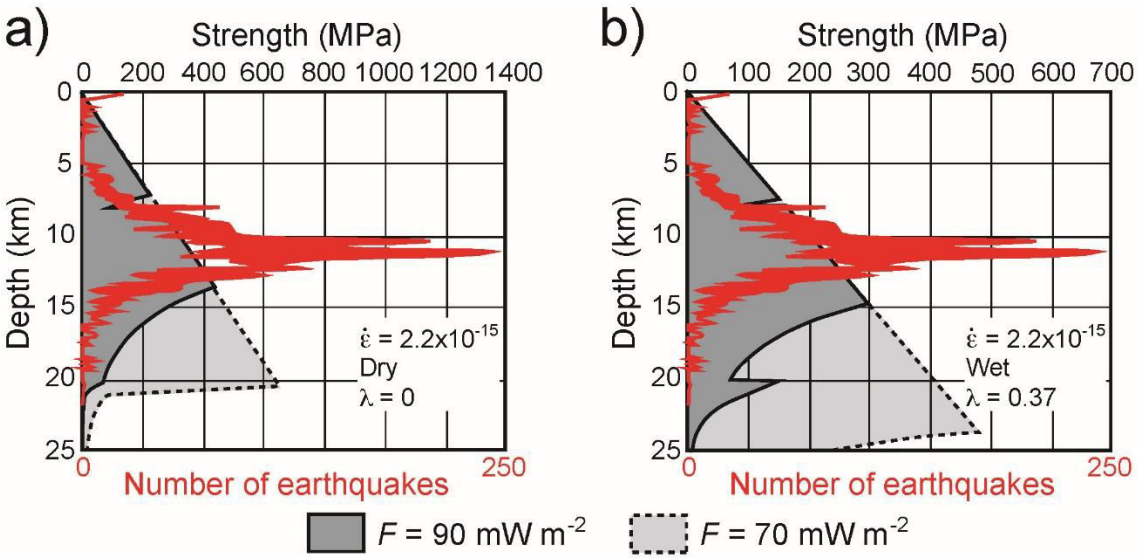

Figure 30. Comparison of the strength profiles calculated: a) for dry conditions, b) for wet conditions, with the earthquake depth distribution.

In summary, with all the limitations that the elaboration of a rheological profile entails, this tool allows us to understand the distribution of seismicity with depth. Thus, for example, most of the hypocenters of the main earthquakes of the February 2023 seismic series are located between 5 and 15 km deep (Okuwaki et al., 2023; Delouis et al., 2023), which coincides with the maximum lithospheric strength predicted by the rheological profiles (for $2.2 \cdot 10^{-15}$ s^{-1} and surface heat flow of 90 mW m^{-2}). However, much work remains to be done to gain a more precise and detailed understanding of the mechanical structure of the lithosphere along the EAFZ. For this, it would be necessary to have more detailed information on the distribution of surface heat flow in the different segments of the EAFZ and a more exhaustive knowledge of the structure and composition of the crust in each of these segments. It is also necessary to consider the limitations of the rheological profiles, which handle average values of depth and composition with a single dominant

rheology in each layer. Also, the variability of the parameters that govern the mechanical response of each layer is a factor to consider, albeit reasonable ranges of variation can be envisaged, as previously discussed in this work.

The different rupture episodes of the devastating dual earthquakes of February 6, 2023, have shown the presence of rupture barriers or asperities (Delouis et al., 2023). It is possible to explain these mechanical irregularities because of the complex structural geometry of the EAFZ (Duman & Emre, 2013; Okuwaki et al., 2023). Another possible explanation, not incompatible with the previous one, is the presence of zones or segments with different mechanical behavior, because of changes in the crustal composition (**Figure *20***), thermal flow (Dolmaz et al., 2008) or the presence of fluids at depth (Türkoğlu et al., 2015). In this sense, **Figure *27*** and **Figure *30*** show how variations along the EAFZ of the factors that condition the mechanical response of the crust could explain in part the changes in the velocity of lateral propagation of the rupture surface during a large earthquake. A better control of these variables would be desirable in the future to allow an exhaustive characterization of the rheological behavior of the lithosphere and, therefore, achieve a more reliable understanding of the level of seismic risk of the different segments of the EAFZ.

5.2.6.4. 3D architectural style of the EAFZ in the Kahramanmaras region

The tentative 3D architectural fault morphology of the EAFZ and associated faults in zone 2 is illustrated in **Figure *31***. The cross-section of zone 2 (**Figure *25***) reveals significant changes in the distribution of earthquakes with depth and along the trace of the EAFZ. The three cross-sections show that the southeastern fault zone (the Narli or Nurdağı-Pazarcık Fault), previously considered a secondary splay zone, exhibits a convergence of seismicity with the Main Strand of the EAFZ at about 15 km depth, suggesting that the two traces are part of the same Anatolian-Arabian boundary. Below a depth of 20 km, the virtual absence of seismicity indicates a plastic accommodation of displacements, while a brittle regime predominates at shallower depths.

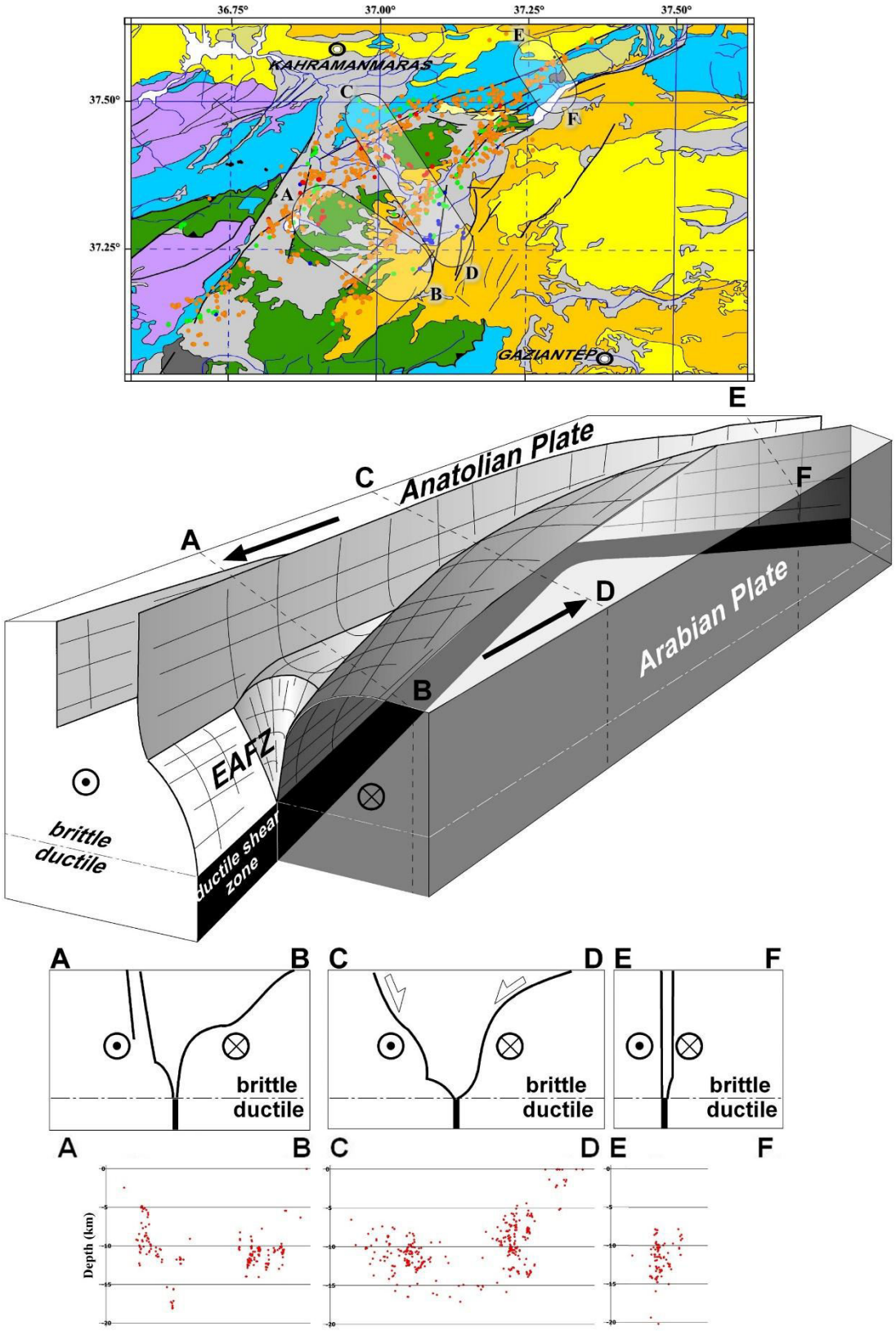

Figure 31. Seismicity over the geological map of the detailed area (where the first large earthquake occurred), showing the location of the three perpendicular profiles to the Main Strand of the EAFZ. At the bottom, the point-cloud profiles from **Figure 25** are displayed, along with their interpretations. In the center of the figure, an interpretative scheme of the 3-D architecture of the fault is presented.

The alignment of seismicity maxima reveals morphological variations along the fault trace above 20 km depth. In the southwestern part of the EAFZ (zone 2), the structure is highly asymmetric (**Figure *25***): To the southwest, it shows an extremely vertical branch dipping to the southeast and a less vertical structure dipping to the northwest. The central part of zone 2 displays a western branch dipping 50–60º to the south, while the eastern branch shows a variable dip, transitioning from 50º to the north at shallower depths to a vertical orientation at greater depths. In contrast, the northeastern part of zone 2, close to zone 3, features a more symmetrical configuration characterized by two parallel, vertical branches. This three-dimensional structure aligns well with the morphology of the Quaternary basin surrounding Türkoğlu. The accommodation of the strike-slip component and the change in fault trace orientations appear to generate a depression (graben) where sediments accumulate. This negative flower structure could explain the sigmoidal shape of the basin in plan view and the convergence of earthquakes at depth.

On the other side, zones 3 and 4 of the Main Strand of the EAFZ show a more symmetrical configuration, with a wide fault zone dipping around 40º to the NNW (profile G-H in **Figure *24***).

5.2.7. Conclusions

The distribution of seismicity in the central and southwestern part of the EAFZ has been studied. The profile of the number of earthquakes with depth has allowed to establish five different slices (I to V), characterized by peaks of seismic activity (they are interpreted as relatively high-strength blocks) and separated from each other by zones of relative seismicity minima (zones of lower relative strength). The distribution of the kernel density in these slices provides a three-dimensional image of the seismicity associated with the EAFZ and allows us to analyze the close relationship between the main geological and structural features of each segment or zone of the EAFZ and the observed seismicity. The highly variable morphology of the boundary between the Anatolian and Arabian plates became evident, revealing two branches: a main strand inclined at 50-60º S and the Narli or Nurdağı-Pazarcık Fault at approximately 70º N inclination, which other authors have considered a secondary splay fault. These two branches converge at depth with a steep northward dip to the north that becomes more inclined northward above the Anatolian plate.

On the other hand, a kinematic study of the entire region has been carried out, making it possible to explain, in terms of plate tectonics, the geological context and dominant structures of each zone or segment of the EAFZ. Finally, several rheological profiles of the lithosphere affected by the EAFZ are presented, which provide a mechanical explanation for some of the most characteristic features of the seismicity of the area, such as the presence of seismic peaks at different depths, the weak coupling of the structure in general, and the local presence of areas with greater coupling. This study will serve for a better seismotectonic knowledge of the EAFZ and can be used as a guide for carrying out in the future more detailed studies of the local relationship between the thermal and mechanical structure of the lithosphere and the seismic activity along the EAFZ.

5.3. Analysis of the Recent Seismicity at the Internal-External Zones Boundary of the Betic System Beneath the Granada Basin Using the Slice Method

5.3.1. Abstract

The Granada Basin, located in the Intrabetic Trough within the Betic Cordillera, covers the boundary between the Internal and External Zones of the orogen. Exhibits high seismic activity due to the collision between the Nubian and Iberian plates. Between 2020 and 2023, three seismic swarms were recorded.

This study applied the slice method to a seismic record from the IGN catalog (1997–2023), combined with geological and geophysical data, to analyze the lithospheric structure of the basin. In total, more than 6000 earthquakes were used. Four seismogenic levels (slices) were identified: I (0–9 km), II (10–18 km), III (19–29 km), and IV (>30 km). Although deep seismicity is lower in magnitude, it remains significant, with over 200 recorded earthquakes.

Seismicity correlates with surface faults and lithological contacts, aligning along NW-SE and NE-SW directions. The highest concentrations occur in Quaternary and Mio-Pliocene deposits, forming high-seismicity corridors. In the Sierra de Loja, seismic activity follows an N-S pattern with a southward dip.

The 3D analysis suggests a basal detachment at 10–15 km depth, gently dipping WSW, linked to the extensional regime associated with Nubia-Eurasia convergence. This detachment exhibits a south-southwestward displacement and appears to be abruptly truncated east and west of the basin.

5.3. Analysis of the Recent Seismicity at the Internal-External Zones Boundary of the Betic System Beneath the Granada Basin Using the Slice Method.

Debido a restricciones relacionadas con los derechos de autor, el apartado 5.3, correspondiente al artículo *"Analysis of the Recent Seismicity at the Internal-External Zones Boundary of the Betic System Beneath the Granada Basin Using the Slice Method"*, actualmente en proceso de publicación, ha sido retirado de esta tesis. En su lugar, se presenta un breve resumen de los contenidos principales de dicho artículo.

RESUMEN:

The Granada Basin, located in the Intrabetic Trough within the Betic Cordillera, covers the boundary between the Internal and External Zones of the orogen. Exhibits high seismic activity due to the collision between the Nubian and Iberian plates. Between 2020 and 2023, three seismic swarms were recorded.

This study applied the slice method to a seismic record from the IGN catalog (1997–2023), combined with geological and geophysical data, to analyze the lithospheric structure of the basin. In total, more than 6000 earthquakes were used. Four seismogenic levels (slices) were identified: I (0–9 km), II (10–18 km), III (19–29 km), and IV (>30 km). Although deep seismicity is lower in magnitude, it remains significant, with over 200 recorded earthquakes.

Seismicity correlates with surface faults and lithological contacts, aligning along NW-SE and NE-SW directions. The highest concentrations occur in Quaternary and Mio-Pliocene deposits, forming high-seismicity corridors. In the Sierra de Loja, seismic activity follows an N-S pattern with a southward dip.

The 3D analysis suggests a basal detachment at 10–15 km depth, gently dipping WSW, linked to the extensional regime associated with Nubia-Eurasia convergence. This detachment exhibits a south-southwestward displacement and appears to be abruptly truncated east and west of the basin.

At depths exceeding 40 km, beneath Sierra Tejeda, seismicity is disconnected from shallower structures and strongly inclined southward, possibly related to the local inclination of the Gibraltar slab. The estimated orientation (~N105E/62SW) aligns with the boundary between internal and external zones, suggesting compressional stresses consistent with the regional tectonic framework.

the boundary between the internal and external zones. This WNW-ESE direction may be associated with compressional stresses compatible with the regional tectonic setting.

5.4. Three-Dimensional Architecture of Foreland Basins from Seismic Noise Recording: Tectonic Implications for the Western End of the Guadalquivir Basin

5.4.1. Abstract

The Guadalquivir Basin is characterized by Neogene and Quaternary sediments covering a non-outcropping Paleozoic and Mesozoic basement. In this study, the subsurface of the western end of the Guadalquivir Basin was explored using the HVSR method, recording seismic noise at 319 stations located between the parallels of Ayamonte and Villamanrique de la Condesa. The fundamental frequency and mechanical basement were recorded, leading to the estimation of an empirical formula for basement depth in the area: $h = 80.16 \cdot f_0^{-1.48}$.

Five types of response were obtained: (a) low-frequency and high-amplitude peaks (deep substratum areas); (b) high-frequency and high-amplitude peaks (shallow substratum areas); (c) broad peaks, which could indicate critical zones (3D-2D effects); (d) double peaks (marshlands); and (e) no peaks (almost outcropping bedrock). The fundamental frequencies obtained vary between 0.23 and 18 Hz. Bedrock depth ranges from 1–5 meters in the northwestern zone to more than 600 meters in the southeastern areas. The slope of transects, which approximates the actual dip, is calculated at around 1–3º towards the SE. However, abrupt changes (5–7º) are observed along narrow bands with lateral continuity.

Borehole data exhibit strong correlation with passive seismic results, showing small discrepancies of 30–100 meters, possibly due to the presence of calcarenites acting as a mechanical basement. Additionally, geomorphological data corroborate these interpretations.

Although the possibility of ancient fluvial terraces of the Guadalquivir River contributing to abrupt slope changes is considered, the singularity of the records —particularly H/V spectra with broad peaks— suggests that these features are associated with fault zones.

The interpreted basement morphology reveals a horst and graben system, with structural highs corresponding to elevated areas (e.g., the Cabezos de Huelva) and depressions

associated with river marshes. These features likely result from deformation accommodation within the forebulge region of the Betic orogen.

5.4.2. Introduction

Passive seismic techniques based on the analysis and interpretation of seismic noise recorded by triaxial seismometers have proven to be valuable tools for studying the mechanical properties of soil. The Horizontal-to-Vertical Spectral Ratio (HVSR), also known as the H/V Spectral Ratio, is a passive seismic technique used to determine the fundamental frequency of soil by computing the Fourier spectral ratio between the horizontal and vertical components of seismic noise at a given location. The analysis of this phenomenon enables the estimation of the fundamental frequency (f_0), a parameter closely related to the thickness of sedimentary layers covering a basin and, consequently, to the depth of the underlying bedrock.

This approach was first proposed by Nogoshi & Igarashi (1970, 1971), but was later popularized by Nakamura (1989) for site-effect investigations. Due to its simplicity, it quickly gained popularity. Lermo & Chávez-García (1993) applied this method to S-wave seismic records and developed the theoretical foundation for the numerical inversion of SV-waves. A few years later, Ibs-von Seht & Wohlenberg (1999) identified a correlation between the fundamental frequency of a soil, measured through seismic noise, and the thickness of sedimentary layers. Their findings concluded that the Nakamura method is a powerful tool for estimating sediment thickness. Later, Yamazaki and Ansary (2008) expanded this approach to include site characterization, terrain classification, and other applications.

In Europe, the SESAME Project (Site EffectS assessment using AMbient Excitations) played a crucial role in assessing the reliability of the H/V and array techniques for site-effect estimation and seismic risk mitigation in urban areas. The project ultimately led to the development of guidelines for applying this technique (Bard et al., 2004).

In recent years, the H/V Spectral Ratio method has been extensively used for characterizing the seismic properties of the subsurface, including site classification, site-effect analysis, and velocity structure inversion, among others (e.g., Atakan et al., 2004a, b; Harinarayan & Kumar, 2017; Ji et al., 2017; Macau et al., 2015; Pinzón et al., 2019; Putti & Satyam, 2020; Xu & Wang, 2021). In the Guadalquivir Basin, the H/V spectral

ratio technique has proven particularly effective for subsurface studies (e.g., ICGC, 2016; Macau et al., 2016; Alonso-Chaves et al., 2019, 2020b; Amador Luna et al., 2023b, 2024b), enabling the identification of structures that influence the basin bedrock and shape its geomorphology.

The Guadalquivir Basin is a subtriangular basin, currently crossed by the the river of the same name from east to west, with an approximately main direction of N070ºE, open towards the Gulf of Cádiz in the southwestern Iberian Peninsula. It represents one of the three major geological domains of Andalusia: to the north, the Variscan Iberian Massif (southern parts of the Central Iberian, Ossa-Morena and South Portuguese Zones); to the southeast, the Alpine Betic Cordillera; and between these, the Guadalquivir Basin. In the westernmost region of the basin, rivers display abrupt changes in orientation, shifting to approximately N-S directions. This pattern is evident in the Guadalquivir River, its tributary the Guadiamar, and the Tinto, Odiel, and Piedras rivers. These sudden changes, along with the asymmetry in riverbank morphology and the absence of meandering forms, contrast sharply with the overall smoothness and low gradient of the basin's relief (1–2° southeastward).

These features may be influenced by blind faults affecting both the basin's bedrock and its overlying sediments, thereby conditioning its geomorphology, as suggested by Viguier (1977) and Alonso-Chaves et al., (2020b). However, the region's surface geology, dominated by Neogene and Quaternary sediments derived from the dismantling of the Variscan basement to the north and the Alpine orogenic front to the east and southeast, can obscure these structures, making their identification highly challenging.

In this context, passive seismic techniques, such as the H/V spectral ratio method, are crucial for identifying the soil's fundamental frequency, which is closely linked to the depth of the contact between materials with high mechanical contrast, such as soft sediments and hard bedrock. In the Guadalquivir Basin, Miocene and Pliocene sediments overlie a Paleozoic basement, with localized Mesozoic outcrops in Niebla and Ayamonte. The basin's basal unit, known as the Niebla Formation (Civis et al., 1987; Baceta & Pendón, 1999), is composed of calcarenitic sediments identified in deep boreholes (Alonso-Chaves et al., 2019). This formation also acts as a mechanically rigid substrate (though not corresponding to the geological basement), with an estimated thickness of 10–20 meters that slightly increases toward the basin interior (Baceta & Pendón, 1999).

This study aims to achieve two primary objectives. First, it seeks to determine the soil's fundamental frequency through passive seismic methods, specifically the H/V spectral ratio technique, to estimate the depth of the mechanical bedrock. Second, it analyzes the western margin of the Guadalquivir Basin by integrating seismic interpretations with surface geological information and borehole data to identify the tectonic structures conditioning the landscape and to construct a three-dimensional model of the underlying bedrock. Ultimately, the study aims to provide a tectonic perspective on the geodynamic evolution of the forebulge zone of the Betic orogen and to explore how strain partitioning may explain the presence of extensional structures in a region adjacent to an orogenic front within a plate convergence context.

5.4.3. Geographical and geological setting

Geologically, the study area is located on the northern margin of the westernmost sector of the Guadalquivir Basin, where the basin widens before being covered by the waters of the Atlantic Ocean. It lies between 37.10º and 37.50º latitude and -7.4º and -6.18º longitude (see **Figure *38***). The area extends from the vicinity of Aznalcóllar (Seville) in the northeast to the city of Ayamonte in the southwest, encompassing the southern region of Huelva province and the southwestern portion of Seville province.

The Guadalquivir Basin is a large Neogene depression located in the foreland of the Betic orogenic front. The most prominent geological feature in the study area is the discordance between the basin infill and the Variscan basement to the north. This discordance exhibits a primary N070ºE orientation (parallel to the northern boundary of the basin), dipping gently to the southeast. (see **Figure *38***)

The basement rocks of the study area crop out in the northern and northwestern sectors and belong to the South Portuguese Zone, the southernmost geological province of the Iberian Massif. These rocks include:

- Phyllite-Quartzite Group (PQ Group) Upper Devonian in age (e. g., Schermerhorn, 1971; Moreno et al., 1996): Located in the northeasternmost portion of the area (colored in greyish blue in **Figure *38***).

- Volcano-Sedimentary Complex ranging in age from the Upper Devonian to the Lower Carboniferous (e. g., Oliveira, 1990): Notable for its significant massive sulfide deposits (brownish in **Figure *38***).

- Synorogenic Unit of Culm Facies, a Carboniferous unit: Paleozoic shales and greywackes deposited on the Paleozoic seafloor (e.g., Schermerhorn, 1971; Moreno, 1993), which cover the largest area of the study region (greyish green in **Figure *38***)

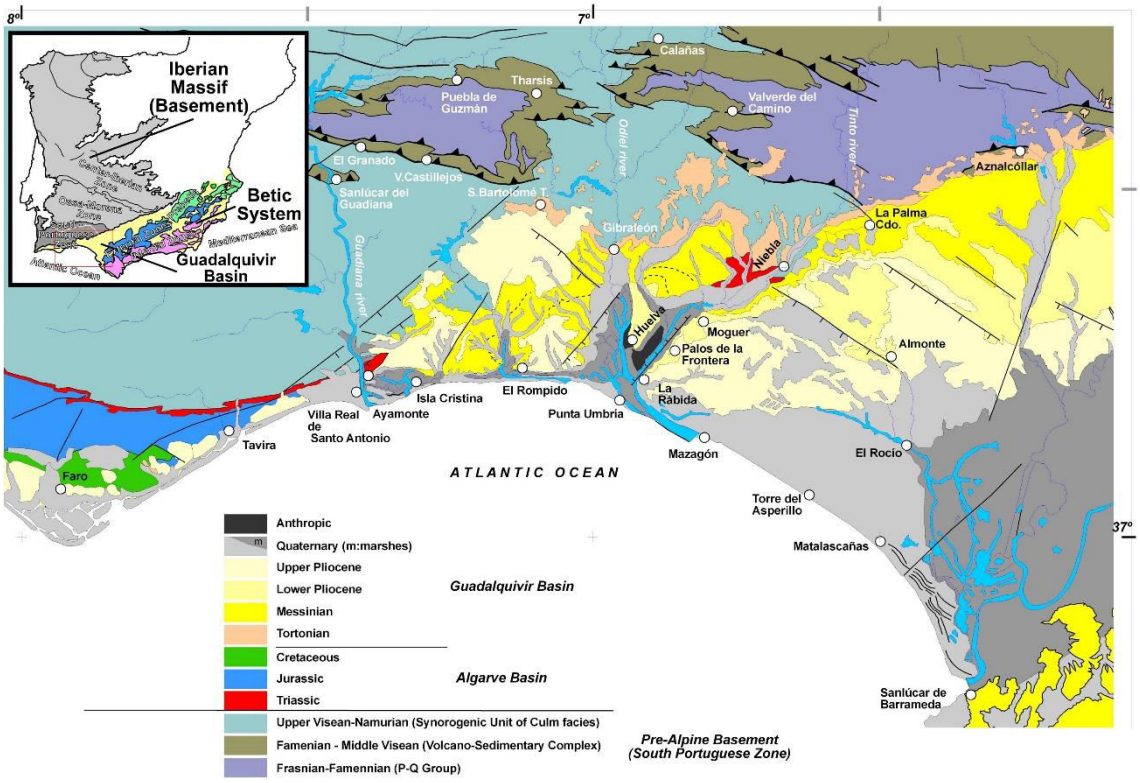

Figure 38. Geological map of the southwestern part of Iberia. In the upper left, a schematic representation of the three main domains in the southern Iberian region is shown: the Iberian Massif, the Guadalquivir Basin, and the Betic System. The red square highlights the area depicted in the detailed map.

These units, ranging from the Middle Devonian to the Upper Carboniferous, were affected by the Variscan Orogeny, and their main tectonic structures and fabrics show a predominant NW-SE strike. Locally, these basement rocks are overlain by Triassic deposits (red in **Figure *38***), including sandstones, carbonates, and volcanosedimentary rocks, which outcrop near Ayamonte and Niebla.

On the other hand, the filling of the Neogene-Quaternary basin:

- Niebla Formation (Tortonian): Calcarenitic sediments constituting the basal transgressive complex of the basin (Coullaut Sáenz de Sicilia et al., 1975) (light rose in **Figure *38***). This unit has been identified in boreholes located far from Niebla within the basin (Alonso-Chaves et al., 2019). These calcarenitic sediments act as a mechanical, not geological, basement (Alonso-Chaves et al., 2020b; Amador Luna, 2023b; 2024b). The geological (Variscan, Mesozoic) bedrock has to be found a few meters below this mechanical basement.

- Gibraleón Clays and Blue Marls Formation (Upper Tortonian–Lower Pliocene): Composed of clays and marls with some silt and sand levels. These layers exhibit glauconite-rich horizons and thicknesses ranging from 30–35 m near the Guadiamar River to over 2000 m southeast of Villamanrique de la Condesa (e. g., Civis et al., 1987; Leyva Cabello & Ramírez Capeiro del Villar, 1973; Sierro, 1984) (yellow in **Figure *38***).

- Huelva Sands Formation (Lower Pliocene): Silty sands with glauconite-rich basal levels, reaching a thickness of ~30 m (Civis et al., 1987; Mayoral & Pendón, 1986) (intermediate yellow in **Figure *38***).

- Bonares Sands Formation (Upper Pliocene): Fine-grained sands with a maximum thickness slightly greater than 20 m (Civis et al., 1987; Mayoral & Pendón, 1986) (light yellow in **Figure *38***).

- Pleistocene Conglomerates (Conquero Continental Unit, Pleistocene): Characterized by reddish gravel and coarse-grained sand layers with a maximum thickness of ~25 m (Bosch-Montoro et al., 2006).

- Quaternary Deposits: Fluvial sediments (conglomerates, sandstones, gravels, and sands) associated with terraces and low-elevation deposits, as well as marine-fluvial deposits and marsh clays and silts (light and dark grey in **Figure *38***)

All these Neogene units exhibit a gentle homocline structure with dips generally below 5º toward the southeast.

Data from boreholes drilled by the IGME (Spanish Geological Survey) and various oil companies along with seismic profiles (Martínez del Olmo, 2019) reveal the presence of olistostromic complexes in nearby areas. These complexes may exhibit mechanical contrasts resembling a geological basement. However, given the location and depth of these olistostromic units, their presence in the study area is unlikely to be detected with the methodology used in this work.

In the western Guadalquivir Basin, river systems display a pronounced reorientation to a N-S direction. Notably, the Guadalquivir River changes its course near Seville, shifting from an overall N070ºE trend to a southward flow towards the Gulf of Cádiz. This behavior is especially evident in the segment between the meridians of Aznalcóllar and Villamanrique de la Condesa. The river margins exhibit notable asymmetry, with the western margin presenting a slope gradient below 5%, while the eastern margin exceeds

30%. The tributary networks further highlight this contrast: the western tributaries are characterized by longer courses and more hierarchical drainage systems, whereas the eastern side lacks major tributaries, instead comprising short, first-order streams.

A similar pattern is observed in the Guadiamar River, a tributary of the Guadalquivir. Originating in the Sierra de Aracena (Huelva), the Guadiamar flows NW-SE before reorienting to a NNE-SSW direction near Aznalcóllar (Seville). In this segment, between Aznalcóllar and Villamanrique de la Condesa, the western margin features a hierarchical drainage network with a slope gradient below 10%, while the eastern margin comprises short, first-order tributaries with gradients exceeding 30%.

This asymmetry is also apparent in other rivers within the Guadalquivir Basin, including the Tinto, Odiel, and Piedras Rivers. For example, the Tinto River flows sinuously through Huelva province, transitioning to a pronounced N045ºE orientation near Moguer, northeast of Huelva, before discharging into the Ría de Huelva, the estuarine zone where it converges with the Odiel River. Its eastern margin exhibits steep slopes exceeding 30%, while the western margin consists of extensive marshlands with gradients below 5% (to get an idea of the slope of these river margins, refer to **Figure *39***).

Similarly, the Odiel River originates in the Sierra de Aracena and Picos de Aroche Natural Park (Huelva), flowing NW-SE through a narrow and steep valley until reaching the water reservoir “Embalse del Sancho”, located north of Gibraleón. From this point, the river adopts a N-S orientation, transitioning into an expansive marshland more than 4 km wide (designated as the Natural Area “Marismas del Odiel”) with gradients below 1% (see again **Figure *39***). The eastern margin of the Odiel is marked by prominent relief (up to 50 meters, known locally as "los cabezos de Huelva") with slopes occasionally exceeding 50%, while the western margin exhibits more subdued topography with elevations around 20 meters and slopes exceeding 10%.

Although less pronounced, the Piedras River also displays a reorientation in its final segment, adopting a well-defined NNE-SSW orientation over its last 12 km near the town of Lepe.

Special mention should be made of the numerous anthropogenic deposits and fills that cover the surface of the study area. Notably, immediately east of the city of Huelva, there is a massive phosphogypsum pond located directly on the marshlands, with dimensions

nearly comparable to those of the city itself. Additionally, the entire study area has been extensively used for agricultural purposes.

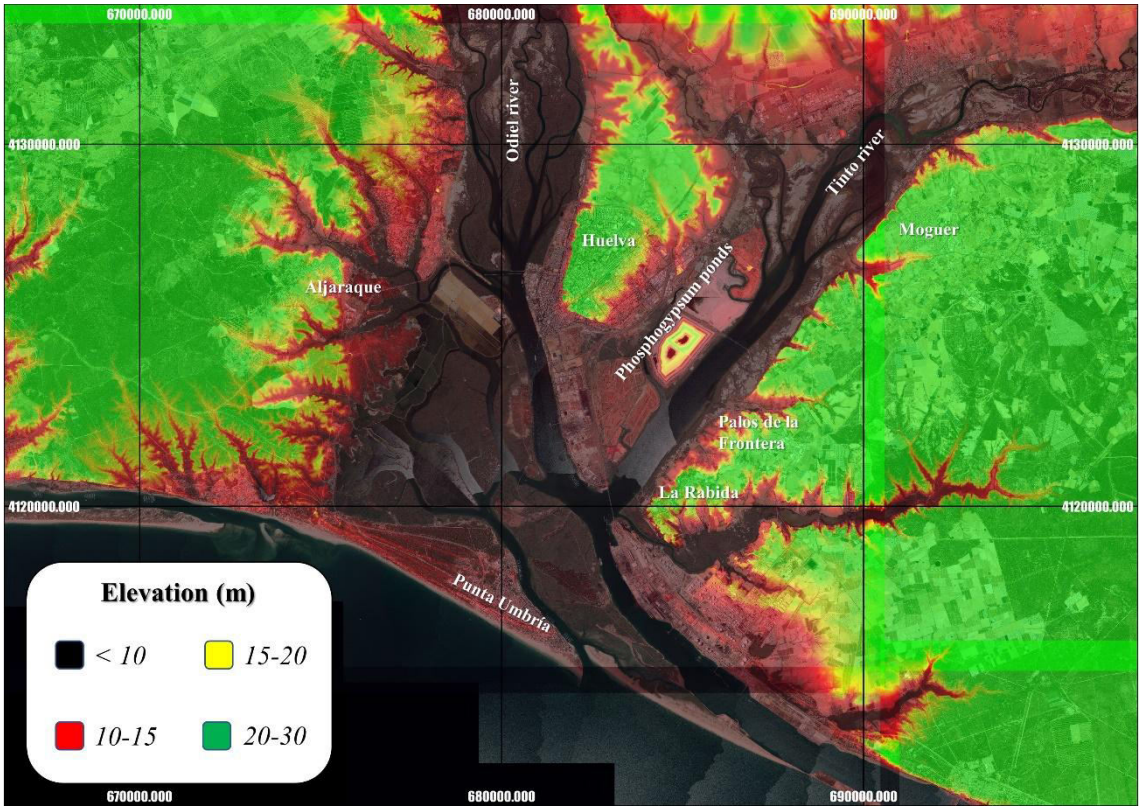

Figure 39. Elevation map over orthophotography (provided by the IGN), color-coded by range to highlight the slope on both margins of the two rivers.

5.4.4. Methodology

The seismic noise recording in the Guadalquivir Basin was conducted in order to apply the Horizontal to Vertical Spectral Ratio (HVSR) method, which facilitates the identification of the soil fundamental frequency. This parameter is closely linked to the thickness of the sedimentary cover overlying a hard rock basement. The depth (h) of the mechanical discontinuity between the crystalline basement and the "soft" sedimentary cover is strongly correlated with the soil fundamental frequency (f_0) and the shear wave velocity (V_S) (Bard, 1985). By applying an empirical equation, which relates the depth of the rock basement (not necessarily the geological Variscan basement) to the soil fundamental frequency, a three-dimensional map of the basin's basement can be constructed.

Seismic noise measurements were carried out at a total of 319 discrete sampling points, many of which were integrated into profiles. Most of these profiles are oriented

approximately NW-SE, following the general slope of the basement-cover contact (see **Figure *40***), with variable lengths ranging from 2 km to over 35 km. Additionally, orthogonal NE-SW profiles were designed to delineate potential structural features affecting the area.

The primary limitations encountered during this study were related to restricted access to protected areas, such as the "Marismas del Odiel" Natural Area (Huelva) and the Guadiamar Green Corridor (Seville), which limited vehicle entry and access to certain zones. However, efforts were made to maintain a sufficiently dense sampling grid in these areas to mitigate data gaps. Additional challenges included intense agricultural, industrial, and urban land use, which further restricted access to specific sites. Sampling efforts were consequently adapted to public areas, such as forest roads, walking paths, and other accessible zones.

Figure 40. Location of seismic noise sampling points in the western Guadalquivir basin.

This study includes seismic noise recordings acquired during the development of the ALERTES-RIM project, focusing on the central sampling area, specifically the city of Huelva and nearby industrial zones. Within this region, 5 seismic arrays were deployed in the city of Huelva to determine S-wave velocities (V_S), and 45 H/V sampling points were recorded, the results of which were previously published by the research team (Macau et al., 2016; Alonso-Chaves et al., 2020b).

Additionally, this work incorporates data collected during subsequent campaigns outside the scope of the ALERTES-RIM project, including the following (the acronyms refer to the names given to the different profiles and measurement points):

- June 2021: HVAME profiles to the east and west of Huelva, as well as *CEP* profiles covering the western region of Huelva (Corrales, Aljaraque), southern Huelva

(Isla Saltés and Punta Umbría), and specific points such as *HU* and *ARNO* to the southeast of Huelva. 70 sample points were recorded.

- October–December 2021: *RIN* and *GO* profiles in areas of interest where the sampling grid was densified. With 44 sample points.

- June 2022: *PAT* and *AZN* profiles located northeast of the study area (26 points in total).

- August 2023: *SLM*, *HVA*, and *PiAz* profiles, along with *AYA* sampling points. 23 sample points were registered.

- May–June 2024: *DAN* and *VL* profiles and *QUI* sampling points.

Through these campaigns, a total area exceeding 2,700 km² was covered (see location in **Figure *40***).

The profiles were designed to ensure continuity in the seismic noise data, spanning from the boundary of the basin, where the Variscan basement (geological substratum) outcrops, towards the interior of the basin. This design facilitates the development of both surface and basement topographic profiles.

Some sampling points were positioned directly above historical deep exploratory boreholes, enabling the derivation of empirical relationships for calculating the depth of the basement rock (Macau et al., 2016; ICGC, 2016). Additional details on sampling, locations, recording times, and other relevant information are provided in **Table A1** of the annexes.

Seismic noise measurements were made with a SARA SL06 digitizer and a Lennartz LE 3D/5s triaxial seismometer, with a natural frequency of 0.2 Hz. Exceptionally, Lennartz LE-3D/20s, with natural frequency of 0.05 Hz were employed in areas presumed to have greater basement depths (southeastern portion of the study area). The equipment simultaneously recorded both time (UTC) and location through an integrated GPS device. The measurements used a sampling frequency of 200.

The minimum recording time was approximately 25–30 minutes, with a standard duration of 45 minutes per sampling session. Exceptionally, longer recording times (up to 90 minutes) were used in areas with adverse conditions, such as high background noise from vehicular traffic or greater substrate depths.

The recorded signal was processed using Geopsy (v. 3.4.2) (Whatelet et al., 2020), which generates graphs that relate the Fourier spectra of the horizontal components (N and E) to the vertical component (Z). This process yields an H/V vs. frequency graph from which the soil's fundamental frequency (f_0) is determined. Between 7 and 19 calculation windows, each approximately 300 seconds long, were utilized for this analysis.

In most cases, the highest amplitude and lowest frequency peak in these graphs corresponds to the soil fundamental frequency. The high amplitude and narrow width of the peaks allowed for a precise determination of f_0.

The interpolation maps of basement depth were generated using Surfer (v. 15.6.3), employing kriging interpolation. These maps were subsequently imported into QGIS (v. 3.32), where they were overlaid onto the surface geological map.

5.4.5. Results and interpretations

5.4.5.1. Empirical equation for the estimation of the basement depth from Vs and f_0 for the western Guadalquivir Basin

The soil's fundamental frequency (f_0) is related to the shear wave velocity in the soft soil layer (V_S) and the thickness of this layer (h) following the relationship proposed by Bard (1985) (1):

$$f_0 = \frac{V_S}{4h} \quad (1)$$

To calculate the depth of the bedrock (h), it is necessary to know the vertical profile of shear wave velocity (V_S) at each point where the fundamental frequency of the soil (f_0) has been measured. However, this information is often not available a priori. To address this issue, the vertical profile of V_S is parameterized using empirical relationships of the form $h=a \cdot f_0^b$, derived from mechanical borehole or geophysical exploration data (Ibs-von Seht & Wohlenberg, 1999; Delgado et al., 2000; Parolai et al., 2002). Evidently, the parameters *a* and *b* depend on the geomechanical characteristics of the materials constituting the soft soil layer.

A new empirical relationship has been developed (**Figure *41***) for the southwestern region of the Guadalquivir Basin by combining data from the H/V spectral ratio method, array techniques (5 datasets), reflection seismics (2 datasets), and mechanical boreholes (2 datasets) that reached the bedrock. This empirical relationship was calibrated using nine

data pairs, covering a frequency range from 0.27 to 0.89 Hz and a wide depth range from 120 to 650 meters. The correlation coefficient for this relationship is 97.44% (see **Figure *41***).

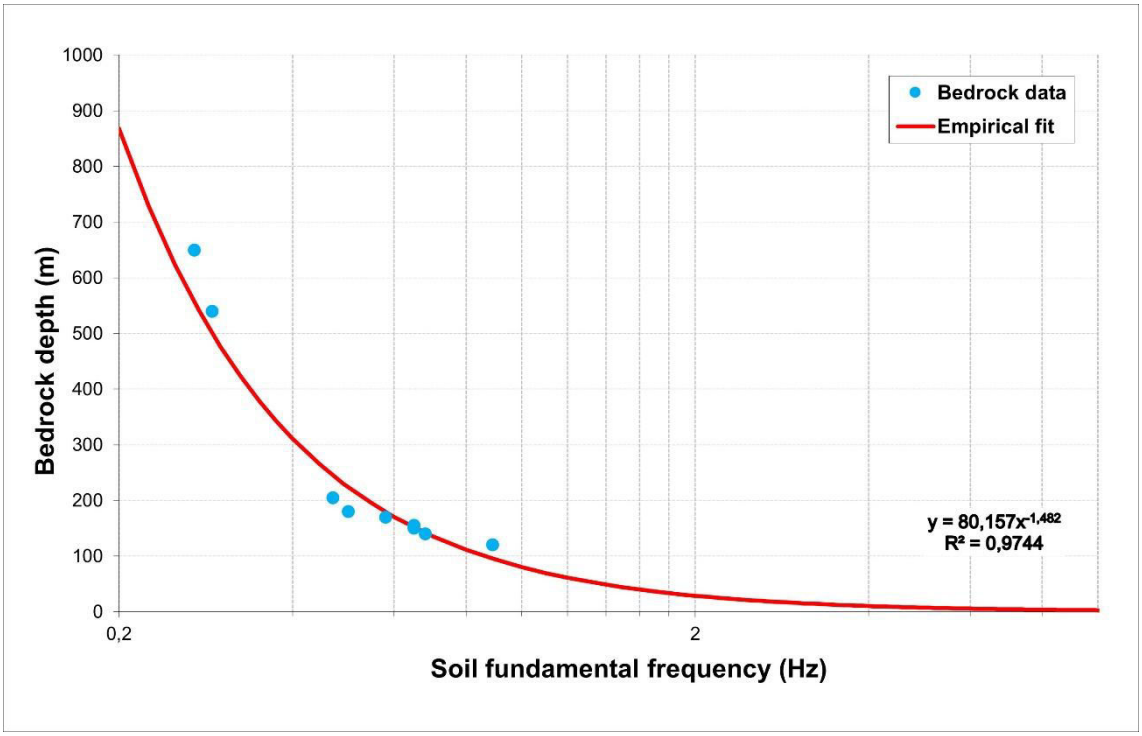

Figure 41. Empirical relationship for calculating the depth of the bedrock in the Guadalquivir Basin (near the city of Huelva) based on the fundamental frequency.

The equation used for estimating the depth is as follows (2):

$$h = 80.16 \cdot f_0^{-1.48} \quad (2)$$

This differs slightly from the equation used in Alonso-Chaves et al., 2020b.

5.4.5.2. H/V graphs, f_0 and estimated basement depth

The analysis of 319 seismic noise sampling points has led to the conclusion that most of the H/V spectral ratio graphs exhibit high amplitude and a sufficiently defined peak width for accurate peak identification, with at least one peak exceeding 2 H/V (a necessary criterion for considering it as f_0). Furthermore, five distinct response types have been identified in the H/V spectral ratio (see **Figure *42***):

a) High-frequency H/V peaks (>1 Hz): Characteristic of areas where the bedrock is closer to the surface.

b) Low-frequency H/V peaks (<1 Hz): Indicative of deep-seated bedrock.

c) Broad peaks: Potentially associated with irregular bedrock surfaces, such as fault zones, which are critical areas for further study.

d) Multiple peaks (at least two exceeding 2 H/V): Typically found in marshlands or areas with significant lithological contrast between unconsolidated Quaternary sediments and other type of Neogene sediments.

e) Flat response (no peaks exceeding 2 H/V): Classified as "rock", characteristic of shallow or exposed bedrock.

f) The fundamental frequency (f_0) estimated from these graphs ranges from 0.23 to 18 Hz, covering a wide spectrum of values (see **Figure *43***). The highest frequencies are systematically located near the basin margins (northern and northwestern areas), while lower frequencies dominate in the basin interior (southeastern areas). The f_0 values progressively decrease toward the SE, which correlates with the expected increase in sediment thickness and bedrock depth toward the basin interior (from NW to SE). Notably, the color bands representing different frequency ranges align closely with the structural boundary between the bedrock and sedimentary cover.

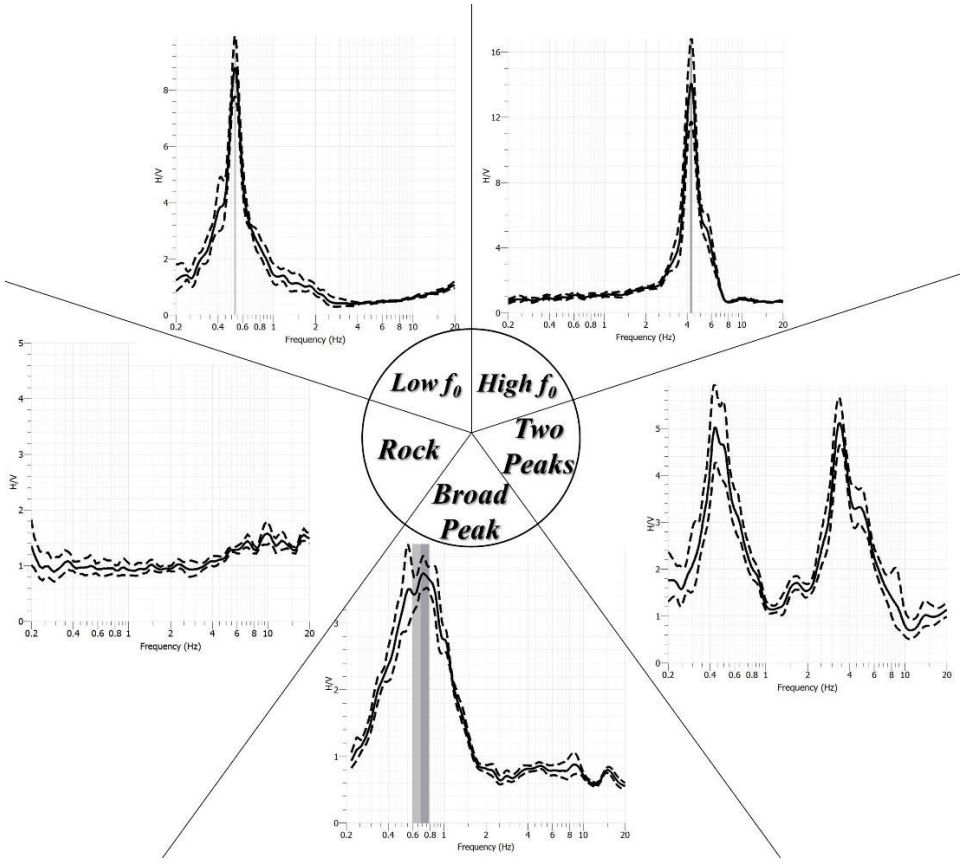

Figure 42. Example of the five different responses obtained during the study. Dashed lines represent the measurement error, while continuous lines represent the average. The gray bands correspond to the uncertainty range in the

calculation of f_0, where a wider band indicates greater indeterminacy in f_0. Finally, a peak is considered when its amplitude exceeds 2H/V.

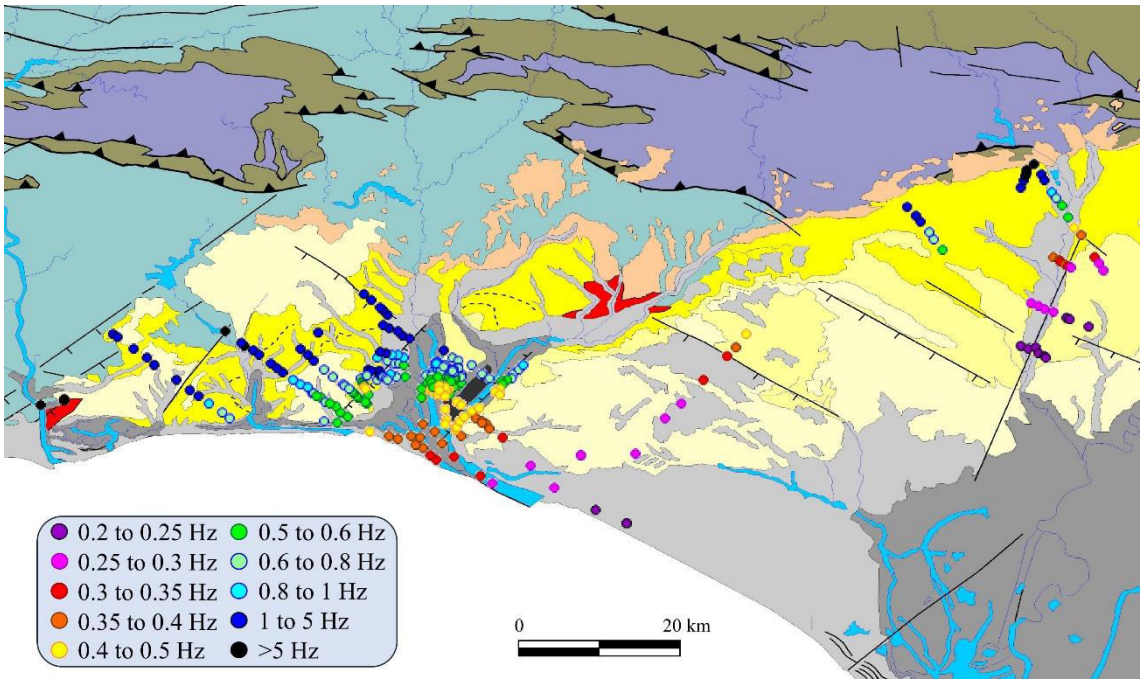

Figure 43. Fundamental frequency data measured with passive seismic over the same geological map of the study area (**Figure 38**). The colors represent different ranges of fundamental frequency: cold colors correspond to high frequencies, while warm colors indicate low fundamental frequencies.

Similarly, as shown in **Figure *44***, the flat response (rock-type, marked with a blue cross in the figure), observed at only one sampling point, is also located in the northwestern area, where the bedrock is either more exposed or even visible in certain sections.

Moreover, the areas where double-peak responses (green stars in **Figure *44***) are most concentrated are specifically located in marshlands and floodplains of various rivers. Wide peaks (yellow crosses in **Figure *44***) are systematically found along NE-SW oriented corridors near the Odiel River (on both the right and left banks) and NNE-SSW in the case of the Guadiamar River. As observed, these align with remarkable precision along fault traces identified through cartographic methods. However, no fault planes could be identified at the surface due to the unconsolidated nature of the overlying materials.

The basement depth is estimated to range from just a few meters below the surface level. (or even outcropping in some areas) in the northern and northwestern parts of the study area to depths exceeding 600 meters, reaching up to -667 meters above the sea level in the southeasternmost sector (**Figure *45***).

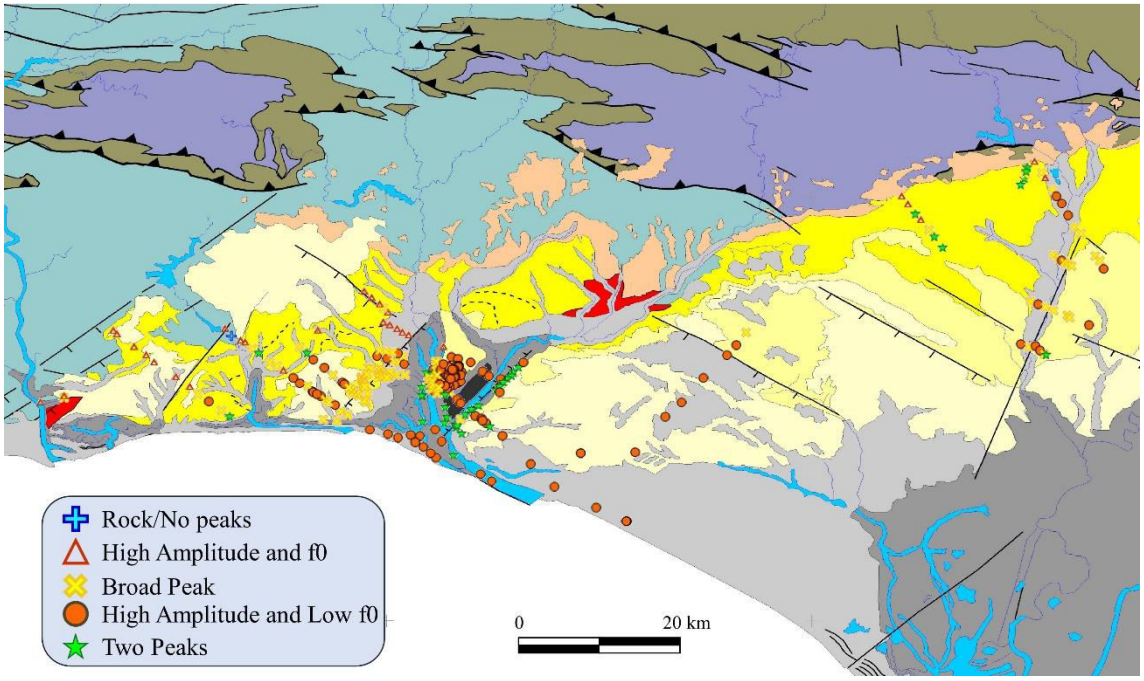

Figure 44. Location of the different types of H/V spectral ratio responses vs. f_0 (examples of each response type are shown in **Figure 42**) in the westernmost sector of the Guadalquivir Basin, overlaid on the geological map of the area (**Figure 38**).

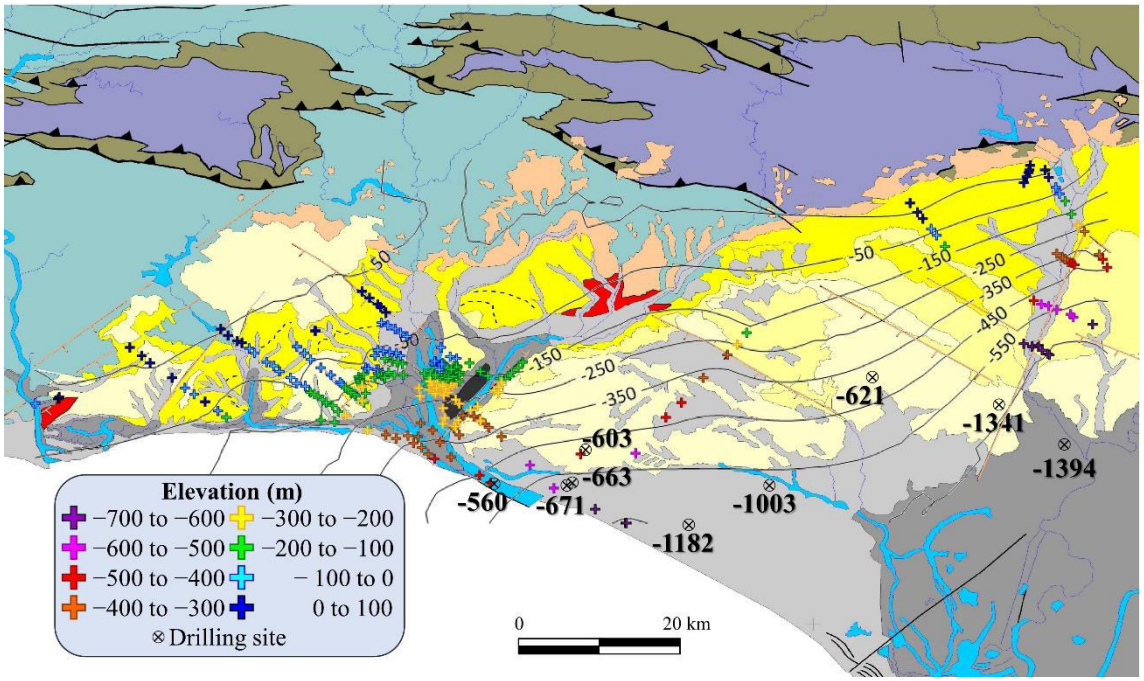

Figure 45. Map of basement depth (in meters above the sea level) estimated by kriging interpolation, based on depths obtained through the H/V method over the geological map (**Figure 38**). Faults in the study area have been smoothed to emphasize contour lines. Colored points represent depths derived from seismic noise measurements, while black points indicate depths obtained from borehole logging by IGME.

The isolines corresponding to the mechanical basement elevation follow a fairly consistent N70-80ºE direction, aligning well with the morphology and orientation of the Guadalquivir Basin. However, deviations in orientation are observed near the rivers

(Odiel, Tinto, and Guadiamar), where the isolines locally shift to an E-W direction, particularly beneath the city of Huelva, dipping southward. This pattern may be attributed to fractures affecting both the mechanical (and geological) basement and the overlying Neogene sediments.

5.4.5.3. Profiles

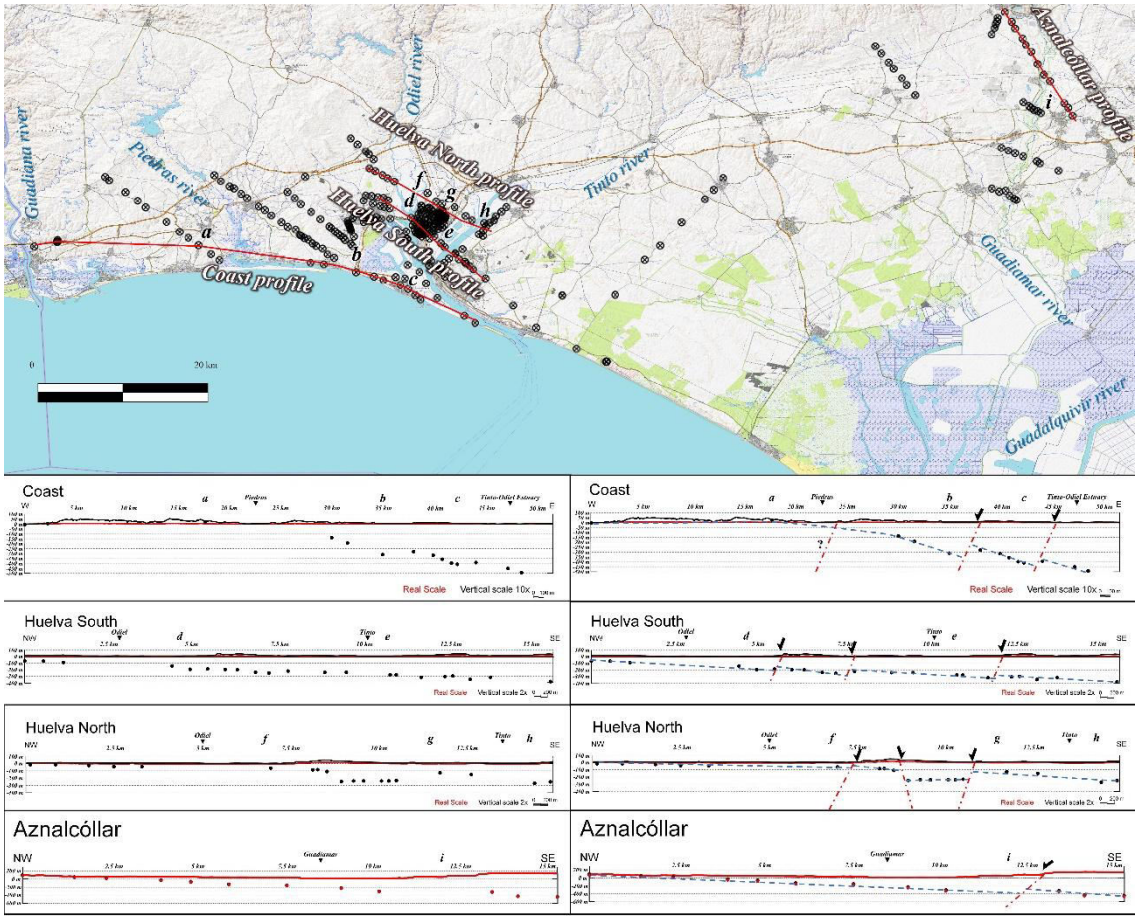

Figure 46. Map showing the location of sampling points used to establish topographic and mechanical basement depth profiles. The lower section displays the profiles for each transect, with the red line representing the true-scale profile and the black line showing the vertically exaggerated scale (the vertical exaggeration is indicated in the lower right corner of each profile). Black and red points represent the estimated depth. On the right, the same profiles are presented with interpreted data: the dashed blue line represents the mechanical (non-geological) basement, while the dashed red line marks faults that may explain slope discontinuities. Additionally, the locations of various rivers and specific points of interest (labeled with letters) are indicated.

Based on the transects conducted, most of which follow a NW-SE orientation and approximate the true dip of the mechanical basement, an average slope of approximately 1-3º dipping towards the SE has been estimated, with a standard deviation of around 1º. However, as seen in **Figure *46***, significant localized slope breaks of 5-7º have been identified. These slope discontinuities can be correlated across adjacent profiles (see

Figure *46*, also can be seen corresponding figures in Amador Luna et al., 2023b, 2024b). Notably, these ruptures tend to occur in areas near river channels.

In the Coast profile, two abrupt slope changes have been identified: one at the beginning of the Odiel marshes (on the western bank of the Odiel River, marked as *b* in **Figure *46***) and another at the confluence of the Odiel and Tinto rivers (*c* in the same figure). This subsurface morphology could explain the structural highs to the west and the depressed areas to the east (Odiel marshes and Huelva Estuary). The terraced morphology may be attributed to ancient river terraces on the western bank or to brittle structures (faults) that have downthrown the eastern sector.

In the Huelva profiles, slope changes correlate well with known structural highs identified in the topographic profile, such as the Cabezos de Huelva, east of the Odiel (point *d*), and the Cabezos de Moguer and Palos, east of the Tinto River (only slightly visible east of the Huelva North profile). A slight elevation, corresponding to the location of northern part of the current phosphogypsum deposits is also observed just east of the city (*g* in the Huelva North profile).

In the Aznalcóllar area, the slope change becomes evident beyond the Guadiamar River, coinciding at the surface with an increase in topographic elevation. This could be explained by the presence of a fault that relatively uplifts the eastern block. Although no fault planes have been identified at the surface, the significant basement offset and the corresponding change in the eastern riverbank slope suggest the existence of an uplifted block.

In all cases, these slope discontinuities can be attributed to faults affecting both the mechanical (and geological) basement and the sedimentary cover. These faults are high-angle structures, extending over 8 to 15 km, with vertical displacements between 50 and 100 m, and can be correlated across different profiles, following NE-SW to NNE-SSW orientations.

5.4.6. Discussion

5.4.6.1. Geology and passive seismic results

As shown in **Figure *43*** to **Figure *46***, the results from passive seismic methods are highly consistent with surface geology and the depth estimations inferred from it. High-

frequency signals (indicating shallower basement depths) are systematically located near the boundary between the basement and the sedimentary basin, progressively deepening toward the southeast, as expected. Conversely, low-frequency signals (indicating deeper basement levels) are concentrated in the southeastern areas (near to Mazagón or Villamanrique de la Condesa surroundings). The primary orientation of the isolines also exhibits a strong parallelism with this boundary, following an N60–80ºE trend. Changes in the basement slope direction coincide with the river channels and variations in surface topography, aligning with the mapped fault traces. However, no fault planes have been identified at the surface due to the high plasticity of the basin's sediments, which likely absorb deformation without leaving visible fault planes or striations.

The cross-sections reveal significant changes in the deep basement slope, which also correlate with geomorphological features and mapped fault traces. These slope offsets are estimated to range between 50 and 100 meters, affecting both the basement and its overlying cover, which may explain certain cartographic features. These slope variations can be correlated across different profiles, exhibiting an approximate N70–80ºE (or even NNE–SSW) orientation, once again coinciding with the basin's main structural trend.

Two main interpretations can be proposed for these slope changes: (i) they may correspond to ancient fluvial terraces of the Guadalquivir River, which has migrated eastward since the Miocene, leaving elevated terraces in the westernmost part of the basin; or (ii) they may be associated with fractures that control both surface relief and river courses. If the latter is the case, these fractures align well with the passive seismic records, where broad spectral peaks have been observed, typically associated with irregular basement structures such as fault zones. These alignments are consistent with previous studies (Alonso-Chaves, 2020a, b). Therefore, these slope discontinuities can be attributed to faults affecting both the mechanical (and geological) basement and the sedimentary cover. These faults are high-angle structures, extending over 8 to 15 km, with vertical displacements between 50 and 100 m, and can be correlated across different profiles NE-SW to NNE-SSW. A possible interpretation of these slope variations along the cross-sections as faults is illustrated in **Figure *46*** (right), where many of these fractures can be correlated across different profiles.

Three main fault zones have been identified in the western part: one at the easternmost end of the Odiel River, another at its western margin (coinciding with the relief of the cabezos de Huelva), and a third one along the western margin of the Tinto River near

Huelva. Additionally, another fault may be present along the western margin of the Guadiamar River to the east. However, other structures remain unidentified, possibly due to a lack of data or their truncation by orthogonal faults.

Figure *39* further reveals a sharp topographic break in southern Huelva. The orientation of this possible structure is also reflected in one of the western branches of the Odiel River, and if extended eastward, it coincides with the phosphogypsum deposits. This WNW–ESE-trending structure can also be identified in seismic records, where broad spectral peaks align in the same direction. Moreover, **Figure *39*** shows that the elevation of the phosphogypsum deposits in the northern sector (>30 m) is higher than in the southern sector (where maximum elevations range around 20 m), potentially indicating subsidence of the southern block (normal fault to the south). These observations are also consistent with previous studies by González (2022).

From a tectonic perspective, these fractures can be explained within the Iberia-Nubia framework where westward displacement of the orogenic front occurs due to the lateral escape of the Alboran microplate. The resultant load at the eastern end of the basin may induce uplift in the western sector, forming normal faults in the forebulge area to accommodate this deformation.

5.4.6.2. Boreholes

Some of the passive seismic measurements, as shown in **Figure *45***, were conducted directly above historical boreholes drilled by the IGME and oil companies in 1986. These measurements aimed to compare the depth estimates obtained through the passive seismic method with those derived from borehole data. A similar approach was later applied in the Aznalcóllar area using boreholes conducted by various companies operating in the area (see **Figure *47***).

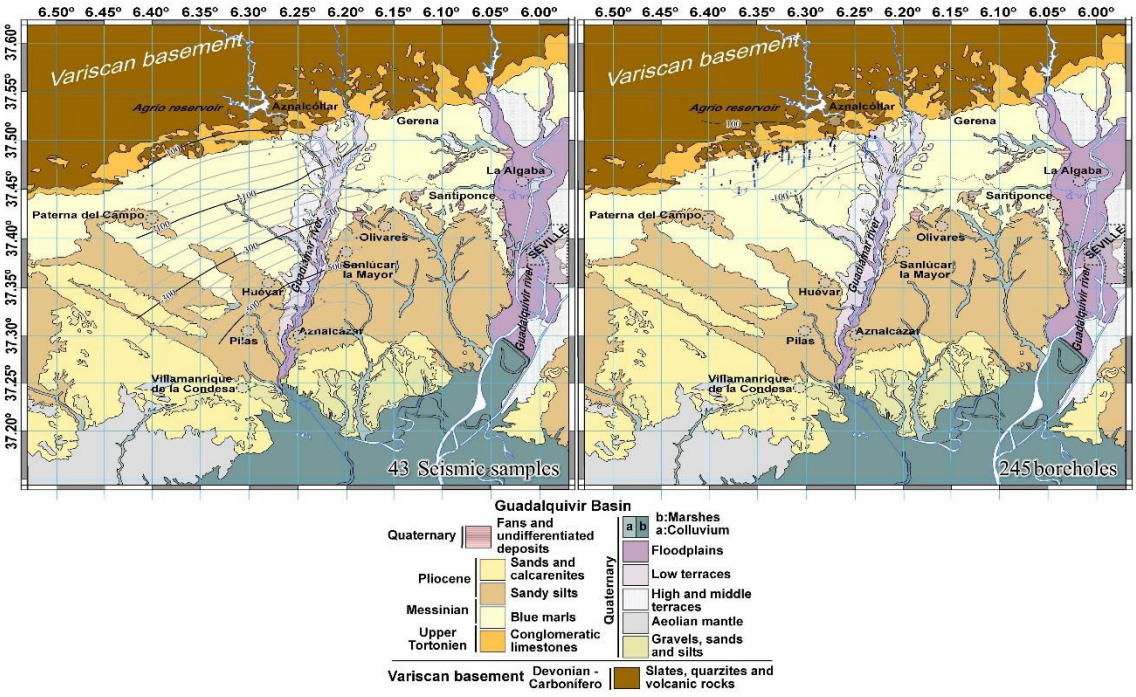

Figure 47. Comparison of depth maps (generated through kriging interpolation) between passive seismic data (left) and exploration borehole data (right).

Saltés-1, the easternmost borehole, reached the geological basement at an elevation of -560 m (meters above the sea level), while the passive seismic sampling point *HU42*, located vertically above it, estimated a mechanical basement depth of -494 m. In the case of *Huelva-1*, which reached -603 m for the geological basement, *HU41* estimated a depth of -500 m for the geological basement. Lastly, the *Moguer-1* and *Mazagón-1* boreholes reached the basement at -679 m, whereas *HVAME16* estimated a mechanical basement depth of -585 m. For the Aznalcóllar case, a similar pattern was observed, with an estimated depth discrepancy of approximately 30–50 meters above the actual geological basement depth (see **Figure *47***). As previously mentioned, this discrepancy may be attributed to the Niebla calcarenites, which outcrop in the northern part of the study area and have been confirmed to extend in depth through borehole data (Alonso-Chaves et al., 2019). This formation, although it is part of the basin filling, behaves as a mechanically rigid substrate, contrasting with the softer basin sediments. The observed 30-meter error in the northern zone and the approximately 100-meter discrepancy further into the basin could be related to the increasing thickness of this material toward the basin interior, with the actual geological basement lying between 30 and 100 meters below the estimated mechanical basement.

A separate discussion is warranted for boreholes located deeper within the basin, where geological basement depths exceed -1000 m. The passive seismic method typically operates at frequencies ranging from 0.2 to 20 Hz, corresponding to a maximum depth of approximately 850 meters (based on empirical formula). Thus, at such depths, the method could not reach the mechanical basement. However, in a nearby area, as shown in Figure 8, a well-defined depth of approximately -660 m has been identified (see *ARNO* in **Table A1** in appendix). This suggests the presence of a fault with significant throw toward the southeast, which could explain the substantial depth variation between these points.

Lastly, the Almonte-1 borehole, located further north, reached the geological basement at approximately -620 m—significantly deeper than the depth estimated by the seismic method. However, this borehole is situated between two fault systems identified in geological mapping, which correspond well with changes in the curvature of the depth isolines and are referenced by only a few nearby data points. This region is of particular interest, as borehole data indicate a former structural high (characterized by a thinner sedimentary cover compared to adjacent boreholes and the absence of certain units, such as the Guadalquivir sands). This elevated structure, along with those identified along the eastern margin of the Guadiamar and the western margin of the Guadalquivir, may represent active tectonic features that could have influenced the Guadalquivir River course and its progressive eastward migration. The presence of olistostrome bodies in boreholes further east from the study area (Villamanrique de la Condesa to the south) also suggests that the Miocene orogenic front was previously located further west, with the Guadalquivir Basin shifting over time. Future surveys should aim to increase data density in this area and extend measurements toward the Guadalquivir to enhance the depth model.

5.4.6.3. 3-D architecture

The morphology of the mechanical basement in the westernmost sector of the Guadalquivir Basin (considering that the Variscan basement should be located a few tens meters below it) is illustrated in **Figure *48***.

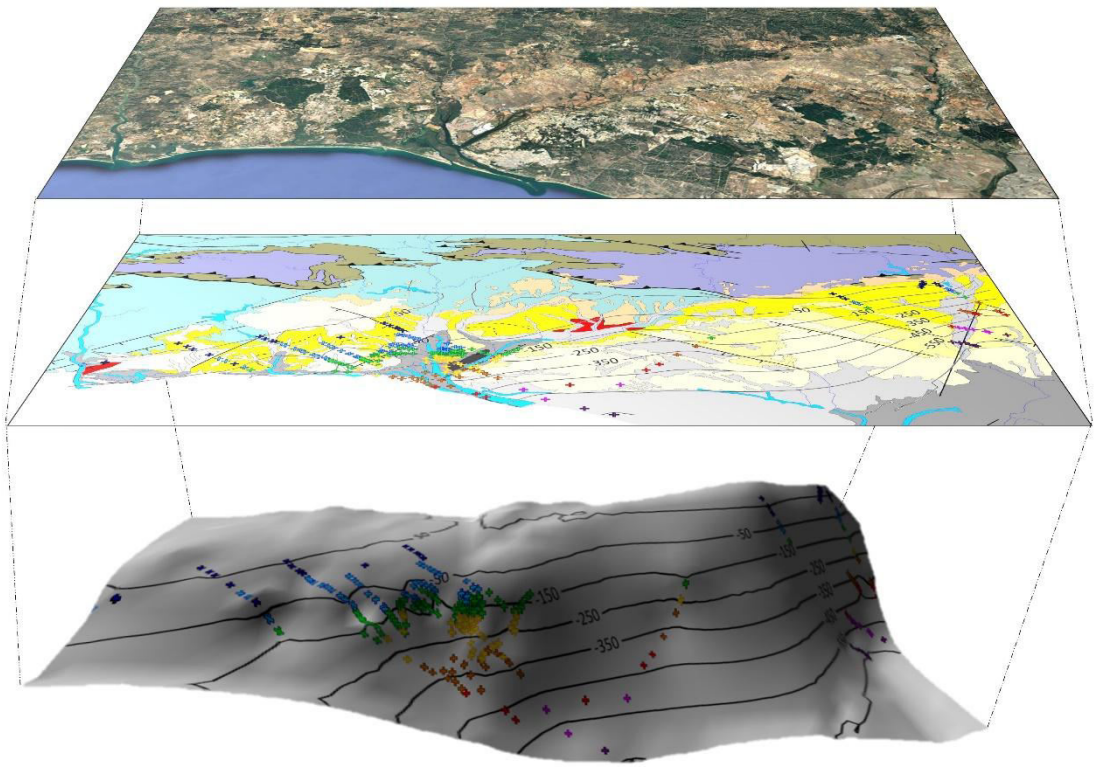

Figure 48. Composite figure of satellite image (top), geological map with data derived from interpolation of seismic noise measurements (**Figure 45**, middle), and 3D model derived from these data (bottom) of the westernmost sector of the Guadalquivir Basin.

As shown, the interpretations derived from all observations align well with the surface morphology and geology, presenting a general slope towards the southeast, from very shallow or even outcropping basement materials in the west, to deep basements in the east (depths greater than 600 m). Sudden changes in slope are systematically located along the riverbeds, aligning approximately in NE-SW directions (Piedras, Odiel, and Tinto rivers) or NNE-SSW directions (Guadiamar).

In summary, the relief of the western end of the Guadalquivir basin can be explained by the development of structures that create a horst and graben landscape, with the horsts located in areas such as the Cabezos de Huelva and other topographically higher zones (as can be also in the eastern end of the Guadiamar), and the grabens being associated with the river marshes. These structures could be explained by the accommodation of deformation caused by the advance of the Alpine orogenic front (the Betics) in the forebulge region, significantly distanced from the front itself.

5.4.7. Conclusions

Seismic noise measurements were conducted at 319 discrete sampling points in the southwestern end of the Guadalquivir Basin to apply the Horizontal-to-Vertical Spectral

Ratio (HVSR) method. Many of these sampling points were integrated into seismic profiles, predominantly oriented NW-SE, following the general dip of the basement-cover contact.

A new empirical relationship was developed for the southwestern Guadalquivir Basin by integrating data from the HVSR method, seismic array techniques (5 datasets), reflection seismics (2 datasets), and mechanical boreholes (2 datasets) that reached the bedrock. This relationship, expressed as $h=80.16 \cdot f_0^{-1.48}$, enabled the determination of the mechanical basement depth, the Tortonian paleotopography, and the presence of potential fractures influencing current topography.

The geological basement reaches depths exceeding 600 m near Mazagón and Villamanrique de la Condesa, located in the southeastern part of the study area. The estimated dip of the basement surface is approximately 1–3º southeastward, with slope breaks coinciding with fluvial courses. The main structural trend follows a N070ºE orientation, aligning with the basement-cover contact.

The HVSR spectral ratio method yielded five distinct response types: (i) high-frequency peaks or no response, associated with shallow or outcropping basement in the northwestern sector; (ii) low-frequency peaks in the southeastern sector, indicative of deep-seated basement; (iii) double peaks in marshland areas; and (iv) broad peaks, characteristic of irregular basement surfaces, potentially corresponding to fault zones.

Passive seismic results show strong consistency with surface geological observations and depth estimations. Borehole data validated these depth estimations, with minor discrepancies ranging from 30 to 100 m, likely due to the presence of mechanically rigid units such as the Niebla calcarenites.

Two main hypotheses are proposed to explain abrupt slope changes: (i) they may represent ancient fluvial terraces formed by the eastward migration of the Guadalquivir River since the Miocene, or (ii) they may be related to fault activity controlling surface relief and hydrological patterns. The alignment of broad seismic peaks with mapped fault zones supports the latter hypothesis, suggesting active or reactivated fault structures.

At depths greater than 800 m, the HVSR method presents limitations; however, the strong variations in basement depth suggest significant faulting in the southeastern sector of the study area.

The interpreted basement morphology reveals a horst and graben system, with structural highs corresponding to elevated areas (e.g., the Cabezos de Huelva) and depressions associated with river marshes. These features likely result from deformation accommodation within the forebulge region of the Betic orogen.

Given the structural complexity of the western Guadalquivir Basin, future research should focus on increasing data density, particularly in northeastern areas where borehole data indicate structural highs or anomalies. Additional passive seismic surveys, complemented by geophysical techniques and detailed geological mapping, will be essential to refine the depth model and improve understanding of the tectonic evolution of the region.

CONCLUSIONES GENERALES
GENERAL CONCLUSIONS

CONCLUSIONES GENERALES

La presente tesis tiene como objeto de estudio la sismicidad en contextos complejos de convergencia de placas. Se consideran como tales aquellas zonas donde confluyen distintos tipos de fallas activas (normales, inversas y/o de desgarre) o, en una escala mayor, donde convergen diversas placas tectónicas, dando origen a regiones de alta complejidad sismotectónica (por ejemplo, uniones triples). Además, se han seleccionado áreas de especial interés para el estudio y la elaboración de mapas de riesgo debido a su alta densidad de población o proximidad a zonas industriales.

El avance tecnológico y la mejora continua del registro sísmico han permitido el desarrollo de grandes catálogos sísmicos con una amplia cantidad de información (*big data*). En este estudio se han empleado diversos catálogos sísmicos (AFAD, KOERI, IGN, entre otros) para desarrollar un nuevo método de análisis: el "método de las lonchas". Este método permite delimitar diferentes niveles sismogenéticos (capas o “lonchas” con el mismo comportamiento mecánico), a partir de los cuales se generan mapas de densidad que facilitan la construcción de modelos tridimensionales de estructuras activas.

Se analizaron dos conjuntos de datos sísmicos correspondientes a los terremotos ocurridos en Turquía y Siria en 2023: uno sin procesar, con más de 60,000 eventos, y otro compuesto por terremotos relocalizados y filtrados con mayor fiabilidad. En ambos casos, se aplicó la misma técnica y se compararon los resultados, obteniéndose interpretaciones coincidentes. Este método ha demostrado ser altamente efectivo, especialmente con catálogos amplios, ya que el método kernel en sí mismo actúa como un filtro, proporcionando resultados equiparables. Aunque los catálogos relocalizados son más precisos, los datos sin filtrar permiten realizar análisis rápidos y eficaces. Este método ha resultado particularmente útil en las dos zonas estudiadas: la Zona de Falla del Este de Anatolia (*East Anatolian Fault Zone*) y la cuenca de Granada.

Aplicando este método, se han obtenido las siguientes conclusiones:

En la zona este de Anatolia se identificaron cinco niveles sismogenéticos (lonchas) y se elaboró una imagen tridimensional de la falla del este de Anatolia. Esto permitió reconocer zonas previamente inactivas que se reactivaron con el evento sísmico y visualizar una estructura en forma de palma a lo largo de la falla principal. Se identificaron diferencias en el comportamiento sismotectónico entre distintas zonas: una

región transtensiva al sur y oeste (zonas 1 y 6), una zona transpresiva al norte (zona 5) y una zona central con carácter de desgarre puro. La falla de Nurdagi-Pazarcik, anteriormente considerada una *splay fault*, parece ser, tras el análisis kernel, parte del brazo oriental de la falla principal, convergiendo en profundidad con la actualmente denominada *main fault*. Además, se realizó un estudio cinemático para explicar esta segmentación dentro del contexto de la tectónica de placas y se elaboraron perfiles reológicos para comprender la distribución de la sismicidad en profundidad.

En la cuenca de Granada, una región con alta actividad sísmica histórica y al menos tres enjambres sísmicos importantes en el periodo 2020-2022, se analizaron más de 6000 terremotos ocurridos entre 1997 y 2023. Se identificaron cuatro lonchas sísmicas, observándose patrones de sismicidad con direcciones NW-SE y NE-SW, en concordancia con estudios previos. En profundidad, estos patrones parecen converger hacia un despegue basal entre 10 y 15 km de profundidad, con un ligero buzamiento hacia el WSW, asociado a un régimen extensional producto de la acomodación de la deformación por la convergencia entre Nubia y Eurasia. Se identificaron fallas de alto y bajo ángulo a partir de los núcleos de densidad, las cuales convergen en dicho despegue. Todas estas observaciones, junto con los mecanismos focales, sugieren un desplazamiento hacia el SSW. El *detachment* parece truncarse al este por una estructura con orientación N-S y buzamiento al sur en la Sierra de Loja, y al oeste por una falla NW-SE en el extremo oriental de la cuenca. No se observa conexión aparente entre el despegue de Mecina (al este) y la Sierra de Loja (al oeste).

La sismicidad profunda bajo Sierra Tejeda no presenta conexión con estructuras superficiales de la cuenca ni de la Sierra de Loja. El buzamiento hacia el sur de este núcleo sísmico profundo podría estar relacionado con la inclinación local del *slab* de Gibraltar. La orientación estimada (N105ºE/62ºSW) coincide con la prolongación del límite entre las zonas interna y externa de las Béticas.

En un segundo bloque, se evaluó la eficacia del método HVSR (*Horizontal-to-Vertical Spectral Ratio*) en la cuenca del Guadalquivir, demostrando ser una técnica válida para el estudio del basamento de la cuenca. Se realizaron mediciones de ruido sísmico en 319 puntos del extremo occidental de la cuenca y se desarrolló una nueva relación empírica para la zona, integrando datos de HVSR, *arrays* sísmicos, sísmica de reflexión y sondeos mecánicos. La ecuación obtenida: $h = 80.16\ f_0^{-1.48}$ permitió determinar la profundidad del

basamento mecánico, la paleotopografía tortoniense y la presencia de posibles fracturas que influyen en la topografía actual.

Se logró identificar hasta cinco tipos distintos de respuesta: picos de alta frecuencia o sin respuesta en la zona noroccidental, indicando basamento somero o incluso aflorante; picos de baja frecuencia al suroeste, correspondientes a basamento profundo; doble pico en zonas de marisma; y picos anchos, representativos de basamentos irregulares (como fallas). El basamento mecánico alcanza profundidades superiores a 600 m cerca de Mazagón y Villamanrique de la Condesa, al sureste de la zona de estudio. La inclinación estimada de la superficie del basamento es de aproximadamente 1-3º hacia el sureste, con rupturas de la pendiente coincidentes con los cursos fluviales, alineadas también con las gráficas de pico ancho. La principal tendencia estructural sigue una orientación N070ºE, alineándose con el contacto basamento-cobertera.

Se observan ligeras discrepancias entre los sondeos y las estimaciones del método, probablemente debido a la presencia de unidades mecánicamente duras (calcarenitas de Niebla).

Se presentan dos posibles interpretaciones, destacando la actividad de fallas que controlan el relieve y la hidrografía. Se interpretan como sistemas de *horst* y *graben*, donde los altos estructurales coinciden con las zonas elevadas (como los Cabezos de Huelva) y las depresiones con áreas de marisma. Estas observaciones son congruentes con la partición de la deformación del antepaís del orógeno Bético.

En resumen, la presente tesis ha contribuido al desarrollo de una nueva técnica para el estudio de zonas sísmicamente activas, permitiendo la visualización tridimensional de las estructuras sismogénicas a partir de catálogos *big data* y la elaboración de mapas de riesgo tridimensionales de forma rápida y equiparable a los resultados obtenidos con terremotos relocalizados. Esta nueva técnica puede aplicarse en otros contextos, similares o diferentes. Asimismo, se ha contribuido al desarrollo de un modelo tridimensional del extremo occidental de la cuenca del Guadalquivir mediante técnicas de sísmica pasiva, que ha permitido el reconocimiento de fallas (¿ciegas?) que afectan tanto al basamento como a los sedimentos que lo recubren, condicionando la geomorfología de la superficie. Además, se ha favorecido el conocimiento sobre la afección de la partición de la deformación en zonas de *forebulge* (extremo occidental de la cuenca) de un orógeno

activo (las Béticas). Ambas técnicas abren un amplio abanico de futuras investigaciones en estos y otros contextos.

GENERAL CONCLUSIONS

This thesis focuses on the study of seismicity in complex plate convergence contexts. Such regions are defined as areas where different types of active faults (normal, reverse, and/or strike-slip) converge or, on a larger scale, where multiple tectonic plates meet, resulting in regions of high seismic-tectonic complexity (e.g., triple junctions). Areas of particular interest for the study and development of seismic hazard maps have been selected due to their high population density or proximity to industrial zones.

Technological advances and the continuous improvement of seismic recording have enabled the development of extensive seismic catalogs containing large amounts of data (big data). In this study, various seismic catalogs (AFAD, KOERI, IGN, among others) were used to develop a new analytical method: the "slice method." This method allows for the delimitation of different seismogenic levels (layers or “slices” with similar mechanical behavior), from which density maps are generated, facilitating the construction of three-dimensional models of active structures.

Two seismic datasets corresponding to the 2023 earthquakes in Turkey and Syria were analyzed: one unprocessed, with over 60,000 events, and another composed of relocated and more reliably filtered earthquakes. The same technique was applied to both datasets, and the results were compared, yielding consistent interpretations. This method has proven to be highly effective, particularly with large catalogs, as the kernel method itself acts as a filter, providing comparable results. While relocated catalogs are more accurate, unfiltered data allow for quick and effective analyses. This method has been especially useful in the two studied areas: the East Anatolian Fault Zone and the Granada basin.

By applying this method, the following conclusions were drawn:

In the eastern Anatolian region, five seismogenic levels (slices) were identified, and a three-dimensional image of the East Anatolian Fault was created. This enabled the recognition of previously inactive areas that were reactivated by the seismic event and the visualization of a palm-shaped structure along the main fault. Differences in the seismic-tectonic behavior were observed in different regions: a transtensive region to the south and west (zones 1 and 6), a transpressive region to the north (zone 5), and a central zone exhibiting pure strike-slip behavior. The Nurdagi-Pazarcik fault, previously considered a splay fault, appears, after kernel analysis, to be part of the eastern branch of the main fault, converging at depth with what is currently referred to as the main fault.

Additionally, a kinematic study was conducted to explain this segmentation within the context of plate tectonics, and rheological profiles were developed to understand the distribution of seismicity at depth.

In the Granada basin, a region with a high historical seismic activity and at least three significant seismic swarms between 2020 and 2022, over 6,000 earthquakes occurring between 1997 and 2023 were analyzed. Four seismic slices were identified, revealing seismicity patterns with NW-SE and NE-SW directions, consistent with previous studies. At depth, these patterns seem to converge toward a basal detachment between 10 and 15 km, with a slight dip toward the WSW, associated with an extensional regime resulting from the accommodation of deformation due to the convergence between Nubia and Eurasia. High- and low-angle faults were identified from the density kernels, which converge at this detachment. All these observations, together with focal mechanisms, suggest a displacement toward the SSW. The detachment appears to be truncated to the east by a north-south oriented structure with a southern dip in the Sierra de Loja and to the west by a NW-SE fault at the eastern end of the basin. No apparent connection is observed between the Mecina detachment (to the east) and the Sierra de Loja (to the west). The deep seismicity beneath Sierra Tejeda shows no connection with the surface structures of the basin or the Sierra de Loja. Its southward dip could be related to the local inclination of the Gibraltar slab. The estimated orientation of this deep seismicity nucleus (N105ºE/62ºSW) coincides with the prolongation of the boundary between the internal and external zones of the Betic range.

In a second section of this study, the effectiveness of the Horizontal-to-Vertical Spectral Ratio (HVSR) method was evaluated in the Guadalquivir Basin, demonstrating it to be a valid technique for studying the basement of the basin. Seismic noise measurements were taken at 319 points in the westernmost part of the basin, and a new empirical relationship for the region was developed by integrating HVSR data, seismic arrays, reflection seismics, and borehole data. The resulting equation: $h=80.16\ f_0^{-1.48}$ allowed the determination of the mechanical basement depth, the Tortonian paleotopography, and the presence of potential fractures influencing the current topography.

Up to five distinct response types were identified: high-frequency peaks or no response in the northwestern area, indicating shallow or outcropping basement; low-frequency peaks to the southwest, corresponding to deep basement; double peaks in marsh areas; and wide peaks, representative of irregular basements (such as faults). The mechanical

basement reaches depths exceeding 600 m near Mazagón and Villamanrique de la Condesa, southeast of the study area. The estimated inclination of the basement surface is approximately 1-3º to the southeast, with slope breaks coinciding with river courses, also aligned with the wide peak profiles. The main structural trend follows a N070ºE orientation, aligning with the basement-cover contact.

There are slight discrepancies between the borehole data and the method's estimates, likely due to the presence of mechanically hard units, such as the Niebla calcarenites.

Two possible interpretations are presented, emphasizing the activity of faults controlling the relief and hydrography. These are interpreted as horst and graben systems, where the structural highs coincide with elevated areas (such as the Cabezos de Huelva), and the depressions with marsh areas. These observations are consistent with the partitioning of deformation in the foreland of the Betic orogen.

In summary, this thesis has contributed to the development of a new technique for studying seismically active areas, enabling the three-dimensional visualization of seismogenic structures from big data catalogs and the rapid generation of three-dimensional seismic risk maps comparable to results obtained from relocated earthquakes. This new technique can be applied in other similar or different contexts. Additionally, a three-dimensional model of the westernmost part of the Guadalquivir Basin has been developed through passive seismic techniques, leading to the recognition of faults (possibly blind) affecting both the basement and the overlying sediments, thereby conditioning the surface geomorphology. Furthermore, the understanding of the partitioning of deformation in forebulge areas (western end of the basin) of an active orogen (the Betics) has been enhanced. Both techniques open up a broad range of future research opportunities in these and other contexts.

REFERENCES

REFERENCES

Abbas, M. A. & Abdelgowad, A. M. 2024. Application of seismic refraction and MASW geophysical techniques to characterize the subsoil structure under damaged buildings in Qeft city, Upper Egypt. *Model. Earth Syst. Environ.*, **10**, 3547–3557.

Abdelgowad, A. M., El-Haddad, A. E., Aglan M. I. & Hamed, A., 2025. Seismic refraction investigation of the shallow bedrock in New Qena City, Eastern Desert, Egypt. *Sci Rep.*, **15**, 2646.

Abgarmi, B., Delph, J. R., Ozacar, A., Beck, S. L., Zandt, G., Sandvol, E., Turkelli, N. & Biryol, C. B., 2017. Structure of the crust and African slab beneath the central Anatolia plateau from receiver functions: New insights on isostatic compensation and slab dynamics. *Geosphere*, **13**, 1774–1787.

AFAD (Disaster and Emergency Management Authority of Turkey). National Seismic Network of Türkiye (DDA). International Federation of Digital Seismograph Networks 2024. Available online: https://tdvm.afad.gov.tr/ (accessed on 27 May 2024).

Agnew, D. C., 2002. 1 – History of Seismology. In: Lee, W. H. K., Kanamori, H., Jennings, P. C., Kisslinger, C. International Geophysics. *Academic Press*, **81**, 3–11.

Aki, K., 1957. Space and time spectra of stationary stochastic waves, with special reference to microtremors. *Bulletin of the Earthquake Research Institute,* **35**, 415-456.

Akin, U., 2016. Investigation of the seismic velocity distribution and crustal structure of Turkey by means of gravity data. Bull. Miner. *Res. Explor.*, **153**, 185–202.

Aksoy, E., ˙Inceöz, M. & Koçyıgıt, A., 2007. Lake Hazar Basin: A negative flower structure on the East Anatolian Fault System (EAFS), SE Turkey. *Turk. J. Earth Sci*., **16**, 319–338.

Aktug, B., Ozener, H., Dogru, A., Sabuncu, A., Turgut, B., Halicioglu, K., Yilmaz, O. & Havazli, E., 2016. Slip rates and seismic potential on the East Anatolian Fault System using an improved GPS velocity field. *J. Geodyn.*, **94–95**, 1–12.

Al-Ahmadi, K., Al-Amri, A. & See, L., 2014. A spatial statistical analysis of the occurrence of earthquakes along the Red Sea floor spreading: Clusters of seismicity. *Arab. J. Geosci.*, **7**, 2893–2904.

Alavi, S. H.; Bahrami, A.; Mashayekhi, M.; Zolfaghari, M., 2024. Optimizing Interpolation Methods and Point Distances for Accurate Earthquake Hazard Mapping. *Buildings*, **14**, 1823.

Aldaya, F., Álvarez, F., Galindo-Zaldivar, J., González Lodeiro, F., Jabaloy, A. & Navarro-Vila, F., 1991. The Malaguide-Alpujárride contact (Betic Cordilleras, Spain): a brittle extensional detachment. C. R. Acad. Sci. Paris, 313, 1447-1453.

Aldaya, F., Campos, J., García-Dueñas, V., González Lodeiro, F. & Orozco, M., 1984. El contacto Alpujárrides-Nevado Filábrides en la vertiente meridional de Sierra Nevada. Implicaciones tectónicas. In: *El borde Mediterráneo español: evolución del orógeno bético y geodinámica de las depresiones neógenas (López Ruiz, J, Ed.), CSIC- Univ. Granada*, 18-20.

Alfaro, A. J., Navarro, B. M., Sánchez, F. J. & Pujades, L., 1997a. Microzonificación sísmica de Barcelona utilizando el método Nakamura: ventajas y limitaciones. *XII Jornadas Estructurales de la Ingeniería de Colombia*, Bogotá. 10-13 septiembre 1997, 198-220.

Alfaro, A., Gutierrez, F., Sugagna, T., Figueras, S., Goula, X. & Pujades, L., 1997b. Measurements of microtremors in Barcelona: a tool forseismic microzonation. Proceedings of IAMG'97. Barcelona, Spain.

Alfaro, A., Pujades, L., Goula, X., Susagna, T., Navarro, B. M., Sanchez, F.J. & Canas, J.A., 2001. Preliminary map of soil'spredominant periods in Barcelona using microtremors. *Pure and Applied Geophysics,* **158** (12), 2499–2511.

Alfaro, P., Delgado, J., Sanz De Galdeano, C., Galindo- Zaldivar, J., García-Tortosa, F.J., López-Garrido, A.C., López-Casado, C., Marín-Lechado, A., Gil, A. & Borque, M.J., 2008. The Baza Fault: a major active extensional fault in the central Betic Cordillera (south Spain). *International Journal of Earth Sciences*, **97**, 1353-1365.

Alguacil, G. & Martín Dávila, J., 2003. Stations and seismological networks in the Iberian Peninsula: State of the art. *Física de la Tierra*, **15**, 29–48.

Allen, C. R., 1969. Active Faulting in Northern Turkey; Rep. 1577; Division of Geological Sciences, California Institute of Technology: Pasadena, CA, USA; 32p.

Allen, T. I., 2010. The influence of attenuation in earthquake ground-motion and magnitude estimation: Implications for Australian earthquake hazard. In Proceedings of the Australian Earthquake Engineering Society 2010 Conference, Perth, WA, Australia, 26–28 November 2010.

Allmendinger, R. W., Cardozo, N. C. & Fisher, D., 2012. Structural Geology Algorithms: Vectors & Tensors. Cambridge University Press, Cambridge, UK, 289 p.

Alonso-Chaves, F. M., García-Dueñas, V. & Orozco, M., 1993. Fallas de despegue extensional miocenas en el área de Sierra Tejeda (Béticas centrales). *Geogaceta*, **14**, 116-118.

Alonso-Chaves, F. M. & Orozco, M., 1998. El sistema de fallas extensionales de La Axarquía (Sierras de Tejeda y La Almijara, Cordilleras Béticas). *Geogaceta*, **14**, 116-118.

Alonso-Chaves, F. M., Macau, A., Figueras, S., Benjumea, B., Gabàs, A., Roca, A., Puig, R. & Sedano, J., 2019. Fractures and paleogeography during the Tortonian in the northern border of the Guadalquivir basin inferred from deep wells and passive and active seismicity techniques. In: Workshop "Earthquakes and Tsunamis in Iberia (50th Years of the 1969 Saint Vincent Earthquake, M=8.0)", Madrid.

Alonso-Chaves, F. M., García-Navarro, E., Fernández, C. & Mayoral E., 2020a. Tectónica extensional durante el Triásico Superior en el extremo oriental de la cuenca del Algarve (Ayamonte, España) y la reactivación de fallas durante el Plioceno-Cuaternario. *Geogaceta*, **67**: 19–22.

Alonso-Chaves, F. M., Macau, A., Figueras, S., Benjumea, S., Gabàs, A., Roca, A., García-Navarro, E., Puig, R. & Sedano, J., 2020b. Fracturación cortical inferida a partir de técnicas de sismicidad activa y pasiva: extensión neógena en el forebulge de la Cuenca del Guadalquivir. *Geogaceta*, **67**, 15–18.

Amador Luna, D., Fernández, C. & Alonso-Chaves, F. M., 2023a. Análisis de la sismicidad en la Cuenca de Granada a partir de mapas de Estimación de Densidad Kernel. In: 10ª Asamblea Hispano-Portuguesa de Geodesia y Geofísica, Toledo, Spain, 304-313.

Amador Luna, D., Macau, A., Bellmunt Traver, F., García-Navarro, E., Expósito, I., Jiménez-Bonilla, A., Díaz-Azpiroz, M., Cruzado Zarza, D. & Alonso-Chaves, F. M., 2023b. Imagen 3D del basamento mecánico de la Cuenca del Guadalquivir en la provincia de Huelva. In: *10ª Asamblea hispanoportuguesa de geodesia y geofísica,* 231–239.

Amador Luna, D., Alonso-Chaves, F. M. & Fernández, C., 2024a. Kernel Density Estimation for the Interpretation of Seismic Big Data in Tectonics Using QGIS: The Türkiye–Syria Earthquakes (2023). *Remote Sensing,* **16**(20): 3849.

Amador Luna, D., Macau, A., Alonso-Landaeta, M. A., Berman Díaz, S. & Alonso-Chaves, F. M., 2024b. Determinación del basamento mecánico y geológico mediante técnicas de sísmica pasiva en el entorno del río Guadiamar: Implicaciones tectónicas. *Geo-Temas,* **20**, 565–568.

Ammon, C.J.; Lay. T. & Simpson, D.W., 2010. Great earthquakes and global seismic networks. *Seismological Research Letters*, **81**, 965–971.

Anduaga, A., 2004. Earthquakes, damage, and prediction: The Spanish Seismological Service, 1898–1930. *Earth Sciences History*, **23**, 175–207.

Anduaga, A., 2009. Geofísica, economía y sociedad en la España contemporánea. Consejo Superior de Investigaciones Científicas, Madrid, Spain, 379 pp.

Ansary, M.A., Yamazaki, F., Fuse, M. & Katayama, T., 1995. Use of microtremors for the estimation of ground vibration characteristics. *Third International Conference on Recent Advances in Geotechnical Earthquake Engineering and Soil Dynamics*. St. Louis, Missouri.

Aristotelis, 1887. Opera Omnia Graece et Latine. Paris: Ed. A. Firmin-Didot, 590-596.

Arpat, E. & Saroglu, F., 1972. The East Anatolian Fault system; thoughts on its development. *Bull. Miner. Res. Explor. Inst. Turk.*, **78**, 33–39.

Arpat, E. & Şaroğlu, F., 1975. Türkiye'deki bazı önemli genç tektonik olaylar: *Türkiye Jeol. Kur.Bült.*, **18**(1). 91–101. Ankara: MTA.

Artemieva, I. & Shulgin, A., 2019. Geodynamics of Anatolia: Lithosphere thermal structure and thickness. *Tectonics*, **38**, 4465–4487.

Asaly, S., Gottlieb, L. A., Inbar, N. & Reuveni, Y., 2022. Using Support Vector Machine (SVM) with GPS Ionospheric TEC Estimations to Potentially Predict Earthquake Events. *Remote Sens.*, **14**, 2822.

Atakan K., P.-Y. Bard, F. Kind, B. Moreno, P. Roquette, A. Tento & SESAME-Team, 2004a. JSESAME: a standardized software solution for the H/V spectral ration technique.

Proceedings of the 13th World Conference on Earthquake Engineering, Vancouver, August 2004, **Paper #2270**.

Atakan K., A.-M. Duval, N. Theodulidis, B. Guillier, J.-L. Chatelain, P. -Y. Bard & SESAME-Team, 2004b. The H/V spectral ratio technique: experimental conditions, data processing and empirical reliability assessment. *Proceedings of the 13th World Conference on Earthquake Engineering*, Vancouver, August 2004, **Paper # 2268**.

Baceta, J. I. & Pendón, J. G., 1999. Estratigrafía y arquitectura de facies de la Formación Niebla, neógeno superior, sector occidental de la cuenca del Guadalquivir. *Revista de la Sociedad Geológica de España*, **12** (3-4), 419-438.

Badji, R., Charvis, P., Bracene, R., Galve, A., Badsi, M., Ribodetti, A., Benaissa, Z., Klingelhoefer, F., Medaouri, M., & Beslier, M. -O., 2015. Geophysical evidence for a transform margin offshore Western Algeria: a witness of a subduction transform edge propagator? *Geophys. J. Int.*, **200**, 1029–1045.

Balanyá, J.C., 1991. Estructura del dominio de Alborán en la parte norte del arco de Gibraltar. Doctoral thesis, Univ. Granada. 232 pp. (Unedited).

Balanyá, J. C., García-Dueñas, V., Azañón, J. M., Sánchez-Gómez, M., 1997. Alternating Contractional and Extensional Events in the Alpujarride Nappes of the Alboran Domain (Betics, Gibraltar Arc). *Tectonics*, **16**, 226-238.

Balkan, E. & Erkan, K., 2019. Temperature-depth curves and heat flow in central part of Anatolia, Turkey. *Tectonophysics*, **757**, 24–34.

Bard, P. Y., 1985. Les effets de site d'origine structural: principaux resultants expérimentaux et théoriques. Genie Parasismique. París, 223-238.

Bard, P. Y., 1999. Microtremor measurements: A tool for site effect estimation. In: *Irikura, K., Kudo, K., Okada, H. & Sasatani, T. (Eds). The Effects of Surface Geology on Seismic Motion. Balkema, Rotterdam*, **3**, 1251-1279.

Bard P. Y. & SESAME-Team, 2004. Guidelines for the implementation of the H/V spectral ratio technique on ambient vibrations-measurements, processing and interpretations, *SESAME European research project EVG1-CT-2000-00026*, deliverable D23.12, http://www.sesame-fp5.obs.ujf-grenoble.fr.

Barka, A. A. & Kadinsky-Cade, K., 1988. Strike-slip fault geometry in Turkey and its influence on earthquake activity. *Tectonics*, **7**, 663–684.

Barrier, E. & Vrielynck, B., 2008. MEBE Atlas of Paleotectonic maps of the Middle East. Commission of the Geological Map of the World.

Batlló, J., 2004. Catálogo inventario de sismógrafos antiguos españoles. Instituto Geográfico Nacional, Madrid, Spain, 413 pp.

Batlló, J., 2014. Historical Seismometer. *Encyclopedia of Earthquake Engineering*, 1-31.

Batlló, J. & Bormann, P., 2000. A catalog of old Spanish seismographs. *Seismological Research Letters*, **71**, 570–582.

Bayrak, E., Yilmaz, ¸S., Softa, M., Türker, T. & Bayrak, Y., 2015. Earthquake hazard analysis for East Anatolian Fault Zone, Turkey. *Nat. Hazards*, **76**, 1063–1077.

Bektaş, Ö, Ravat, D., Büyüksaraç, A., Bilim, F., Ateş, A., 2007. Regional geothermal characterization of East Anatolia from aeromagnetic, heat flow and gravity data. *Pure and Applied Geophysics*, **164**, 975–998.

Benioff, H., 1935. A linear Strain Seismograph. *Bulletin of the Seismological Society of America*, **25** (4), 283-309.

Benjumea, B., Macau, A., Gabàs, A., Bellmunt, F., Figueras, S. & Cirés J., 2011, Integrated geophysical profiles and H/V microtremor measurements for subsoil characterization. *Near Surface Geophysics*, **9** (5), 413-425.

Benson, R., Lindholm, C. D., Ludwin, R. & Qamar, A., 1992. A method for identifying explosions contaminating earthquake catalogs: Application to the Washington Regional Earthquake Catalog. *Seismological Research Letters*, **63**, 533–539

Bilal, M. A., Wang, Y., Ji, Y., Akhter, M. P. & Liu, H., 2023. Earthquake Detection Using Stacked Normalized Recurrent Neural Network (SNRNN). *Appl. Sci.*, **13**, 8121.

Bletery, Q., Cavalié, O., Nocquet, J. M. & Ragon, T., 2020. Distribution of interseismic coupling along the north and east Anatolian faults inferred from InSAR and GPS data. *Geophys. Res. Lett.*, **47**, e2020GL087775.

Blumenthal, M., 1927. Versuch einer tektonischen Gliederung der Betischen Kordilleren von Central and Sùdwest Andalusien. *Eclogae Geol. Helv.*, **20**, 487-592.

Boloix Carlos-Roca, R., 1998. Aportaciones del Real Instituto y Observatorio de la Armada a la ciencia en España. 100 años de registros sísmicos. *Boletín del Real Observatorio de la Armada*, **5** (99), 3-10.

Bonnefoy-Claudet, S., Bard, P. -Y. & Cotton, F., 2003. Nature of noise wavefield. Deliverable D13.08, Part I. *European Project No. EVG1-CT-2000-00026 SESAME*, 2003, http://sesamefp5.obs.ujf-grenoble.fr .

Bonnefoy-Claudet, S., Cornou, C., Kristek, J., Ohrnberger, M., Wathelet, M., Bard, P. -Y., Fäh, D., Moczo, P. & Cotton, F., 2004. Simulation of seismic ambient noise: I H/V and array techniques on canonical models. *Proceedings of the 13th World Conference on Earthquake Engineering*, Vancouver, Canada, August 2004, **Paper # 1120**.

Bonnefoy-Claudet, S., Baize, S., Bonilla, L. F., Berge-Thierry, C., Pasten, C., Campos, J., Volant, P. & Verdugo, R., 2009. Site effect evaluation in the basin of Santiago de Chile using ambient noise measurements. *Geophys. J. Int.*, **176**, 925-937.

Booth-Rea, G., Azañón, J. M., García-Dueñas, V., Augier, R. & Sánchez-Gómez, M., 2003. A "core-complex like structure" formed by superimposed extension, folding and high angle faulting, The Sancti Petri dome (Western Betics, Spain). *C. R. Geoscience*, **335**, 857-865.

Bos, B. & Spiers, C. J., 2002. Frictional-viscous flow of phyllosilicate-bearing fault rock: microphysical model and implications for crustal strength profiles. *Journal of Geophysical Research* **107**.

Bosch-Montoro, A., Camacho, M. A., García-Navarro, E. & Alonso-Chaves, F. M., 2006. Características geotécnicas de los suelos de la ciudad de Huelva: parámetros de identificación y ensayos de consolidación. *Geogaceta*, **39**, 79-82.

Bouillin, J. -P., Durand-Delga, M., & Olivier, P., 1986. Betic-Rifian and Tyrrhenian Arcs: Distinctive Features, Genesis and Development Stages. The Origin of Arcs, 281–304. Campos, J., García-Dueñas, V., González-Lodeiro, F. & Aldaya, F., 1984. Direcciones de traslación y apilamiento de unidades en los mantos Alpujárrides centrales y orientales. In: El Borde Mediterráneo español: evolución del Orógeno Bético y geodinámica de las depresiones neógenas; ed. López Ruiz, 15-17. Granada.

Buforn Peiró, E., & Udías Vallina, A., 2022. El proyecto geodinámico internacional y los primeros perfiles sísmicos profundos en España. Revista Española de Física, **36** (1), 21-25.

Bulut, F., Bohnhoff, M., Eken, T., Janssen, C., Kılıç, T. & Dresen, G., 2012. The East Anatolian Fault Zone: Seismotectonic setting and spatiotemporal characteristics of seismicity based on precise earthquake locations. *J. Geophys. Res.*, **117**, B07304.

Büyüksaraç, A., Bektaş, Ö., Yilmaz, H. & Arisoy, M. Ö., 2013. Preliminary seismic microzonation of Sivas city (Turkey) using microtremor and refraction microtremor (ReMi) measurements. *J. Seismol.*, **17** (2), 425-435.

Cano, G., 2004. Modificaciones antrópicas de los regímenes del Guadalquivir y sus tributarios. In Gil Olcina, Alteración de los regímenes fluviales peninsulares, Cajamurcia.

Cano, G, 2016. La gestión de la cuenca del Guadalquivir. In: Libro jubilar en homenaje al profesor Antonio Gil Olcina. Ed. Ampliada. Publicaciones Universidad de Alicante, 289–306.

Capon, J., 1969. High-resolution frequency-wavenumber spectrum analysis. *Proc. IEEE*, **57** (8), 1408-1418.

Caristan, Y., 1982. The transition from high temperature creep to fracture in Maryland diabase. *Journal of Geophysical Research*, **87**, 6781– 6790.

Carreño, E.; Galán, J. & Sánchez, M., 1991a. Microseismicity studies in Southern Spain. In: Seismicity, Seismotectonics and Seismic Risk of the Ibero-Maghrebian Region, Mezcua, J. & Udías, A. (Eds.), 79–86. Monografía 8, Instituto Geográfico Nacional, Madrid, Spain.

Carreño, E., Rueda, J., López Casado, C., Galán, J. & Peláez, J. A., 1991b. Spanish national strong motion network. Recording of the Huelva earthquake of 20 December, 1989. *Pure and Applied Geophysics*, **136**, 395–404.

Caselles, J. O., Pérez-Gracia, V., Franklin, R., Pujades, L. G., Navarro, M., Clapes, J., Canas, J. A. & García, F., 2010. Applying the H/V method to dense cities. A case study of Valencia City. *Journal of Earthquake Engineering,* **14** (2), 192-210.

Castellaro, S. & Mulargia F, 2009. The effect of velocity inversion on H/V. *Pure appl Geophys*, **166**, 567–592

Catita, C., Teves-Costa, M. P., Matias, L. & Batlló, J., 2019. Spatial distribution of feltintensities for Portugal earthquakes. Int. Arch. Photogramm. *Remote Sens. Spat. Inf. Sci.*, **XLII-3/W8**, 87–92.

Ceccarelli, M., 2007. Zhang Heng's Seismoscope. In: Reconstruction Designs of Lost Ancient Chinese Machinery. History Of Mechanism And Machine Science, vol 3. Springer, Dordrecht, 119-161.

Čejka, F., Zahradník, J., Turhan, F., Sokos, E. & Gallovic, F., 2023. Long-period directivity pulses of strong ground motion during the 2023 Mw7.8 Kahramanmaras earthquake. *Commun. Earth Environ.*, **4**, 413.

Chávez-García, F. J., Rodríguez, M. & Stephenson, W. R., 2005. An alternative approach to the SPAC analysis of microtremors: Exploiting stationarity of noise. *Bull.Seismol. Soc. Am.*, **95**, 277-293.

Chávez-García, F. J., Rodríguez, M. & Stephenson, W. R., 2006. Subsoil structure using SPAC measurements along a line. *Bull. Seismol. Soc. Am.*, **96**, 729-736.

Cheddadi, A., 2001. Caracterización sísmica del suelo de la ciudad de Granada mediante análisis espectrales del ruido de fondo sísmico. Doctoral thesis. Universidad de Granada.

Choubert, G., & Faure-Muret, A., 1984. Moroccan Rif. In: *Mesozoic- Cenozoic Orogenic Belts*, Edinburgh, 37-46.

Christensen, N. I., 1965. Compressional wave velocities in metamorphic rocks at pressures to 10 kbar. *J. Geophys. Res.*, **70**, 6147–6164.

Christensen, N. I., 1974. Compressional wave velocities in possible mantle rocks to pressures of 30 kbar. *J. Geophys. Res.*, **79**, 407–412.

Christensen, N. I., 1979. Compressional wave velocities in rocks at high temperatures and pressures, critical thermal gradients, and crustal low velocity zones. *J. Geophys. Res.*, **84**, 6849–6857.

Christensen, N. I., 1982. Seismic velocities, Handbook of Physical Properties of Rocks, 2 R. S. Carmichael, 1–228, CRC Press, Boca Raton, Fla.

Christensen, N. I., 1985. Measurements of dynamic properties of rock at elevated pressures and temperatures, Measurement of Rock Properties at Elevated Pressures and

Temperatures H. J. Pincus, E. R. Hoskins, 93–107, *American Society for Testing and Materials*, Philadelphia, Pa.

Christensen, N. I., 1989. Reflectivity and seismic properties of the deep continental crust. *J. Geophys. Res.*, **94**, 17793–17804.

Christensen, N. I. & Fountain, D. M., 1975. Constitution of the lower continental crust based on experimental studies of seismic velocities in granulite. *Geol. Soc. Am. Bull.*, **86**, 227–236.

Christensen, N. I. & Salisbury M. H., 1975. Structure and constitution of the lower oceanic crust. *Rev. Geophys.*, **13**, 57–86.

Christensen, N. I. & Shaw, G. H. 1970. Elasticity of mafic rocks from the Mid-Atlantic Ridge. *Geophys. J. R. Astron. Soc.*, **20**, 271–284.

Civis, J., Sierro, F., González, J., Flores, J., Andrés, I., Porta, J. & Valle M., 1987. El Neógeno marino de la provincia de Huelva: Antecedentes y definición de las unidades litoestratigráficas. In: Paleontología del Neógeno de Huelva, (J. Civis, Ed). Univ. Salamanca, 9-21.

Confederación Hidrográfica del Guadalquivir, 2015. Plan Hidrológico de la Demarcación Hidrográfica del Guadalquivir. Segundo ciclo de planificación: 2016 - 2021. Anejo Nº 2. Descripción general de la Demarcación. Gobierno de España. Ministerio de Agricultura, Alimentación y Medio Ambiente. Confederación Hidrográfica del Guadalquivir.

Cooke, M. L., Toeneboehn, K. & Hatch, J. L., 2020. Onset of slip partitioning under oblique convergence within scaled physical experiments. Geosphere **16**, 875–889.

Coullaut Sáenz de Sicilia, J. L., Soler Sampere. M. & Portero García, J. M., 1978. Mapa Geológico de España, E.:1:50.000 and Memoria, Hoja 961 (11-39) “Aznalcóllar”, IGME. 45 pp.

Cowie, P. A., Scholz, C. H., Roberts, G. P., Faure Walker, J. P. & Steer, P., 2013. Viscous roots of active seismogenic faults revealed by geologic slip rate variations. *Nature Geoscience*, **6**, 1036–1040.

Cox, A. & Hart, R. H., 1986. Plate Tectonics. How It Works. Blackwell Sci. Pub., Palo Alto, CA, pp. 392.

Cuevas, J., Navarro-Vilá, F. & Tubía, J. M., 2001. Evolución structural poliorogénica del Complejo Maláguide (Cordilleras Béricas). *Bol. Geol. Min.*, **112**, 47-57.

d'Acremont, E., Lafosse, M., Rabaute, A., Teurquety, G., Couto, D. D., Ercilla, G., Juan, C., Lépinay, B. M., Lafuerza, S., Galindo Zaldivar, J., Estrada, F., Vazquez, J. T., Leroy, S., Poort, J., Ammar, A., & Gorini, C., 2020. Polyphase Tectonic Evolution of ForeArc Basin Related to STEP Fault as Revealed by Seismic Ref lection Data From the Alboran Sea (W-Mediterranean). *Tectonics*, **39**, e2019TC00588.

Dana, J. D., 1862. Manual of geology: treating of the principles of the science with special reference to American geological history. American Book Co. 1088 pp.

Davis, J. R. & Titus. S. J., 2011. Homogeneous steady deformation: a review of computational techniques. *Journal of Structural Geology,* **33**, 1046–1062.

Davison, C., 1921. Founders of Seismology. —I. John Michell. *Geological Magazine*, **58** (3), 98-107.

del Barco, A. J., 1756. Cartas del Doctor, Catedrático de Philosophia y Viario de la villa de Huelva, a Don N. satisfaciendo algunas preguntas curiosas sobre el terremoto de primeros de Noviembre de 1755. In: Discursos Mercuriales, XIV (565-606). In Juan Enrique Graef. Hurtado Simó, R., 2015. El terremoto de Lisboa de 1755 en el pensamiento de Feijoo y del Barco. Tales, Revista de Filosofía, 5, (115-124).

del Barco, A. J., 1996. Sobre el terremoto de primero de noviembre de 1755. Ed. Fombuena Filpo, V. Universidad de Huelva, 160 pp.

Delgado, J., López Casado, C., Estévez, A., Giner, J., Cuenca, A. & Molina, S., 2000. Mapping soft soils in the Segura River valley (SE Spain): a case study of microtremors as an exploration tool. *Journal of Applied Geophysics*, **45**, 19-32

Delgado, J., Alfaro, P., Galindo-Zaldivar, J., Jabaloy, S., López Garrido, A.C. & Sanz de Galdeano, C., 2002. Structure of the Padul-Nigüelas basin (S Spain) from H/V ratios of ambient noise: application of the method to study peat and coarse sediments. *Pure and Applied Geophysics*, **159** (11–12), 2733–2749.

Delouis, B, van den Ende, M. & Ampuero, J. P., 2023. Kinematic rupture model of the February 6th 2023 Mw7.8 Turkey earthquake from a large set of near-source motion

records combined by GNSS offsets reveals intermittent supershear rupture. Authorea. April 30, 2023.

Delouis, B., van den Ende, M. & Ampuero, J.P., 2024. Kinematic rupture model of the February 6th 2023 Mw7.8 Turkey earthquake from a large set of near-source strong-motion records combined with GNSS offsets reveals intermittent supershear rupture. *Bull. Geol. Soc. Am.*, **114**, 726–740.

DeMets, C., Gordon, R. G., Argus, D. F., & Stein, S., 1994. Effect of recent revisions to the geomagnetic reversal time scale on estimate of current plate motions. *Geophys. Res. Lett.*, **21** (20), 2191-2194.

DeMets, C., Iaffaldano, G. & Merkouriev, S., 2015. High-resolution Neogene and Quaternary estimates of Nubia-Eurasia-North America Plate motion. *Geophys. J. Int.*, **203** (1), 416–427.

Dercourt, J., Zonenshain, L. P., Ricou, L. -E., Kazmin, V. G., Le Pichon, X., Knipper, A. L., Grandjacquet, C., Sbortshikov, I. M., Geyssant, J., Lepvrier, C., Pechersky, D. H., Boulin, J., Sibuet, J. -C., Savostin, L. A., Sorokhtin, O., Westphal, M., Bazhenov, M. L., Lauer, J. P. & Biju-Duval, B., 1986. Geological evolution of the Tethys belt from the Atlantic to the pamirs since the Lias. *Tectonophysics*, **123**(1-4), 241–315.

Dercourt, J., Ricou, L. E. & Vrielynck, B., 1993. Atlas Tethys Palaeoenvironment Maps, 14 maps.

de Rubeis, V., Tosi, P., Gasparini, G. & Solipaca, A., 2005. Application of Kriging technique to seismic intensity data. *Bull. Seism. Soc. Am.*, **95**, 540–548.

Dewey, J. F., Hempton, M. R., Kidd, W. S. F., Sarogly, F. & Şengör, A. M. C., 1986. Shortening of continental lithosphere: the neotectonics of Eastern Anatolia – a young collision zone. In: Coward, M. P.; Ries, A. C. (Eds.), *Collision Tectonics, Special Publications,* **19**. Geological Society, London, 3–36.

Dewey, J. F., Pitman, W. C., Ryan, W. B. F. & Bonnin, J., 1973. Plate tectonics and the evolution of the Alpine system. *Geol. Soc. Am. Bull.*, **84**, 3137–3180.

Dilig, I. J. A. & San Juan, W. I. M., 2019. Geostatistical and Cluster Analysis of Earthquakes in the Philippines. Int. Arch. Photogramm. *Remote Sens. Spat. Inf. Sci.*, **42**, 185–192.

Dolmaz, M. N., Elitok, Ö. & Kalyoncuoglu, U. Y., 2008. Interpretation of low seismicity in the Eastern Anatolian Collisional Zone using geophysical (seismicity and aeromagnetic) and geological data. *Pure Appl. Geophys.*, **165**, 311–330.

Dou, S., Lindsey, N., Wagner, A.M., Wagner, A. M., Daley, T. M., Freifeld, B., Robertson, M., Peterson, J., Ulrich, C., Martin, E. R. & Ajo-Franklin, J. B., 2017. Distributed Acoustic Sensing for Seismic Monitoring of The Near Surface: A Traffic-Noise Interferometry Case Study. *Scientific Reports*, **7**, 11620.

Duman, T. Y. & Emre, Ö., 2013. The East Anatolian Fault: Geometry, Segmentation and Jog Characteristics. *Geol. Soc. Lond. Spec. Publ.,* **372**, 495–529.

Duval, A.-M., Méneroud, J.-P., Vidal, S. & Singer, A., 1998. Relation between curves obtained from microtremor and site effects observed after Caracas 1967 earthquake. *Proceedings of the 11th European Conference on Earthquake Engineering*. Paris, France

Duval, A. -M., Bard, P. -Y. & Lebrun, B., Lacave-Lachet, C., Riepl, J. & Hatzfeld, D., 2001a. H/V technique for site response analysis. Synthesis of data from various surveys. *Bollettino Di GeofisicaTeorica ed Applicata*, **42** (3–4), 267–280.

Duval, A. -M., Vidal, S., Méneroud, J.-P., Singer, A., De Santis, F., Ramos, C., Romero, G., Rodriguez, R., Pernia, A., Reyes, N & Griman, C., 2001b. Caracas, Venezuela, site effect determination with micro-tremor. *Pure and Applied Geophysics*, **158** (12), 2513–2523.

Duval, A. -M., Chatelain, J. -L., Guillier, B. & SESAME Project WP02 Team, 2004. Influence of experimental conditions on H/V determination using ambient vibrations (noise). *Proceedings of the 13th World Conference on Earthquake Engineering,* Vancouver, August 2004, **Paper # 306**.

Dziewonski, A. M., Chou, T. -A. & Woodhouse, J. H., 1981. Determination of earthquake source parameters from waveform data for studies of global and regional seismicity. *J. Geophys. Res.*, **86**, 2825–2852.

Egeler, C. G. & Bodenhausen, J. W. A., 1964. District phases of Alpine overthristing and subsequent thrusting in the eastern part of the Betic Zone of Spain. *Geol. Mijnbouw,* **43**, 316-320.

Eker, A. M., Akgün, H. & Koçkar, M. K., 2012. Local site characterization and seismic zonation study by utilizing active and passive surface wave methods: A case study for the northern side of Ankara, Turkey. *Engineering Geology*, **151** (0), 64-81.

Ekström, G., Nettles, M. & Dziewonski, A. M., 2012. The global CMT project 2004-2010: Centroid-moment tensors for 13,017 earthquakes, *Phys. Earth Planet. Inter*., 200-201.

Enomoto, T., Kuriyama, K., Navarro, M. & Iwatate, T., 2002. Site-effects evaluation by H/V spectra comparing microtremor with strong motion records observed at ground surface and basement using borehole. *12th European Conference on Earthquake Engineering*, paper 593, London.

Faccenna, C., Piromalli, C., Crespo-Blanc, A., Jolivet, L. & Rossetti, F., 2004. Lateral slab deformation and the origin of the western Mediterranean arcs. *Tectonics*, **23**, TC1012.

Frasca, G., Gueydan, F. & Brun, J. P., 2015. Structural record of lower miocene westward Alboran domain motion in the western Betics (southern Spain). Tectonophysics, 657, 1–20.

Fäh, D., Kind, F. & Giardini, D., 2001. A theoretical investigation of average H/V ratios. *Geophysical Journal International*, **145** (2), 535–549.

Fallot, P., 1948. Les Cordillères Bétiques. *Estudios geol.,* **IV** (7-8), 259-279.

Farias, P., Gallastegui, G., González Lodeiro, F., Marquínez, J., Martín-Parra, L. M., Martínez Catalán, J. R., Pablo Maciá, J. G. de y Rodríguez-Fernández, L. R., 1987. Aportaciones al conocimiento de la litoestratigrafía y estructura de Galicia Central. *Mem. Museo e Lab. Miner. Geol. Fac. Ciências, Univ. Porto*, **1**, 411-431.

Fernández, C. & Díaz-Azpiroz, M., 2009. Triclinic transpression zones with inclined extrusion. *Journal of Structural Geology,* **31**, 1255–1269.

Fernández, C. & Díaz-Azpiroz, M., 2022. Extension structures as kinematic indicators in monoclinic transpression and transtension zones. *Journal of Structural Geology,* **161**.

Fernández-Fraile, J., Mattesini, M. & Buforn, E, 2024. Re-Evaluation of the Earthquake Catalog for Spain Using the EMS-98 Scale for the Period 1900–1962. *Pure Appl. Geophys*.

Field, E. H., Clement, A. C., Jacob, S. M., Aharonian, V., Hough, S. E., Friberg, P.A., Babaian, T. O., Karapetian, S. S., Hovanessian, S. M. & Abramian, H. A., 1995. Earthquake site-response study in Giumri (formely Leninakan), Armenia, using ambient noise observations. *Bulletin of the Seismological Society of America,* **85** (1), 349–353.

Fossen, H & Tikoff, B, 1998. Extended models of transpression and transtension, and application to tectonic settings. In: Holdsworth, R. E., Strachan, R. A. & Dewey, J. F. (Eds.), *Continental Transpressional and Transtensional Tectonics, Special Publications,* **135**. Geological Society, London, 15–33.

Fossen, H., Tikoff, B. & Teyssier, C. T., 1994. Strain modeling of transpressional and transtensional deformation. *Norsk Geologisk Tidsskrift*, **74**, 134–145.

Foulger, G. & Natlad J. H., 2003. Geology. Is "hotspot" volcanism a consequence of plate tectonics? *Science*, **300**, 921–922.

Galindo-Zaldivar, J., González Lodeiro, F., & Jabaloy, A., 1989. Progressive extensional shear structures in a detachment contact in Western Sierra Nevada (Betic Cordillera, Spain). *Geodinamica Acta*, **3**, 73-85.

Galindo Zaldivar, J., González Lodeiro, F. & Jabaloy, A., 1993. Stress and paleostress in the Betic-Rif Cordilleras (Miocene to present-day). *Tectonophysics*, **227**, 105-126.

Galindo-Zaldivar, J., Jabaloy, A., González-Lodeiro, F., 1996. Reactivation Du Detachement Extensif de Mecina Dans Le Secteur Occidental de La Sierra Nevada (Cordilleres Betiques, SE de l'Espagne). *Comptes Rendus L'Acad. Sci. Ser. IIA-Sci. Terre Planetes*, **323**, 615–622.

Galindo-Zaldivar, J., Jabaloy, A, Serrano, I., Morales, J., González-Lodeiro, F. & Torcal, F., 1999. Recent and present-day stresses in the Granada Basin (Betic Cordilleras): Example of a late Miocene-present-day extensional basin in a convergence plate boundary. *Tectonics*, **18** (4), 686-702.

Galindo-Zaldivar, J., Ruano, P., Jabaloy, A., López-Chicano, M., 2000. Kinematics of Faults between Subbetic Units during the Miocene (Central Sector of the Betic Cordillera). *Comptes Rendus L'Acad. Sci. Ser. IIA-Earth Planet. Sci.*, **331**, 811-816.

Galindo-Zaldivar, J., Gil, A. J., Borque Arancón, M. J., González-Lodeiro, F., Jabaloy, A., Marín-Lechado, C., Ruano, P. & Sanz de Galdeano, C., 2003. Active faulting in the

internal zones of the central Betic Cordilleras (SE, Spain). *Journal of Geodynamics*, **36** (1-2), 239-250.

Galindo-Zaldivar, J., Gil, A. J., Tendero-Salmerón, V., Borque, M. J., Ercilla, G., González-Castillo, L., Sánchez-Alzola, A., Lacy, M. C., Estrada, F., Avilés, M., Alfaro, P., Madarieta-Txurruka, A. & Chacón, F., 2022. The Campo de Dalias GNSS Network Unveils the Interaction between Roll-Back and Indentation Tectonics in the Gibraltar Arc. *Sensors*, **22** (6), 2128.

Galitzin, B. B., 1902. Ueber Seismometrische Beobachtungen. Acad. Imp. Sciences. St. Petersburg. *Comptes Rendus Commission Sismique Permanente,* Liv. 1, 101-183.

Galitzin, B. B., 1903. Zur Methodik der Seismometrischen Beobachtungen. *Comptes Rendus Commission Sismique Permanente*, T. I. Liv. 3, 1-112.

Galitzin, B. B., 1905. Uber die Methode zur Beobachtungen von Neigungswellen. *Comptes Rendus Commission Sismique Permanente*, T. II. Liv. 2, 1-144.

Galitzin, B. B., 1907. Die Electromagnetische Registrirmethode. *Comptes Rendus Commission Sismique Permanente*, T. III. Liv. 1, 1-106.

García-Dueñas, V. & Balanyá, J. C., 1986. Estructura y naturaleza del arco de Gibraltar. *Maleo, Bol. Inf. Soc. Geol. Portugal*, **2**, 23.

García-Dueñas, V., Balanyá, J. C. & Martínez-Martínez, J. M. 1992. Miocene extensional detachments in the outcropping basement of the northern Alboran Basin and their tectonic implications. *Geo-Mar. Letters*, **12**, 88-95

García-Dueñas, V., Balanyá, J. C., Martínez-Martínez, J. M., Muñoz, M., Azañón, J. M., Crespo-Blanc, A., Orozco, M., Soto, J. I., Alonso-Chaves, F. M. & Sánchez-Gómez, M., 1993. Kinematic of the Miocene extensión detachment faults and shear zones in the Betics and Rif chains. *Docum. BRGM*, **219**, 76-77.

García Hernández, M., López Garrido, A. C., Rivas, P., Sanz de Galdeano, C. & Vera, J. A., 1980. Mesozoic paleogeographic evolution the External Zones of the Betic Cordillera. *Geol. Mijnbouw*, **59**, 155-168.

Garfunkel, Z., 2004. Origin of the Eastern Mediterranean basin: a reevaluation. *Tectonophysics*, **391**, 11-34.

Glassmeier, K. -H., 2020. Karl Friedrich Almstedt – scientist, teacher, andco-founder of the German Geophysical Society. *Hist. Geo Space Sci*., **11**, 71–80.

Göncüoğlu, M. C., 2010. Introduction to the geology ofTurkey: Geodynamic evolution of the Pre-Alpine and Alpineterrains. *General Directorate of Mineral Research and Exploration Monography Series*, **5**, 1–66.

Gong, Z., Li, H., Zhang, H., Kuterdem, K., Wang, S., Si, J., Xheng, Y., Liang, P., Li, C., Li, C., Ren, Z., Yu, J., Zhou, X., Xu, Y., Ma, Z., Li, J. & Tang, F., 2024. The 2023 Mw7.7 Pazarcik earthquake caused a reversal in vertical motion along the SW branch of the East Anatolian fault. *Journal of Structural Geology*, **184**, 105172.

Görür, N., 1988. Timing of opening of the Black Sea basin. *Tectonophysics*, **147**, 247-262.

González, A., 2017. The Spanish national earthquake catalogue: Evolution, precision and completeness. *Journal of Seismology*, **21** (3), 435-471.

González, F., 2022. InSAR-based mapping of ground deformation caused by industrial waste disposals: the case study of the Huelva phosphogypsum stack, SW Spain. *Bull. Eng. Geol. Environ.*, **81**, 304.

Govers, R. & Wortel, M. J. R., 2005. Lithosphere tearing at STEP faults: response to edges of subduction zones. *Earth Planet. Sc. Lett.*, **236**, 505–523.

Gülerce, Z., Shah, S. T., Menekşe, A., Özacar, A. A., Kaymakci, N. & Çetin, K. O., 2017. Probabilistic seismic-hazard assessment for East Anatolian Fault zone using planar fault source models. *Bulletin of the Seismological Society of America*, **107**, 2353–2366.

Günay, Y., Fourcade, E., Dercdurt, J., Azema, J., Kozlu, H., Bellier, J. P., Cordey, F., Cross, P., Wever, P., De-Enay, R., Lover, J. P., & Vrielynck, B. (1990). Güneydoğu Türkiye'de Arap Platformunun Kuzey Kenan ve Bu Kenarın Mesozoyik'te Bir Tetis Okyanusal Alanına Geçişi: Stratigrafi-Paleocografya: Türkiye 8. *Petrol Kongresi Bildirileri*, 403-434.

Gutenberg, B., 1914a. Zur Besprechung von M. P. Rudzki Über Erdbebenwellen V und VI: Lassen sich aus den Beobachtungen der Amplituden der Erdbebenwellen Schlüsse auf das Erdinnere ziehen? *Gerlands Beiträge zur Geophysik,* **13**, *Kleine Mitteilungen*, 198-203.

Gutenberg, B., 1914b. Über Erdbebenwellen VII A. Beobachtungen an Registrierungen von Fernbeben in Göttingen und Folgerungen über die Konstitution des Erdkörpers *Nachrichten von der Königlichen Gesellschaft der Wissenschaften zu Göttingen, mathematisch-physikalische Klasse*, 125-176.

Gutenberg, B. & Richter, C. F., 1936. Magnitude and Energy of Earthquakes. *Science*, **83** (2147), 183-185.

Gutenberg, B. & Richter, C. F., 1941. Seismicity of the Earth, *Geological Society of America*.

Gutenberg, B. & Richter, C. F., 1944. Frequency of earthquakes in California. *Bull. Seismol. Soc. Am.*, **34**, 185–188.

Gutenberg, B. & Richter, C. F., 1956. Earthquake magnitude. Intensity, energy, and acceleration. *Bull. Seismol. Soc. Am.*, **46**, 105–145.

Gutscher, M. -A., Malod, J. A., Réhault, J. -P., Contrucci, I., Klingelhoefer, F., Spakman, W. & x SISMAR scientific team, 2002. Evidence for active subduction beneath Gibraltar. *Geology*, **30**, 1071-1074.

Gutscher, M. -A, Domínguez, S., Westbrook, G. K., Le Roy, P., Rosas, F., Duarte, J. C., Terrinha, P., Miranda, J. M., Graindorge, D., Gailler, A., Sallares, V. & Bartolome, 2012. The Gibraltar subduction: A decade of new geophysical data. *Tectonophysics*, **574-575**, 72-92.

Güvercin, S. E., Karabulut, H., Konca, A. Ö., Dogan, U. & Ergintav, S., 2022. Active seismotectonics of the East Anatolian Fault. *Geophys. J. Int.*, **230**, 50–69.

Haines, S. S. & Ellefsen, K.J., 2010. Shear-wave seismic reflection studies of unconsolidated sediments in the near surface. *Geophysics*, **75** (2), 1MA-Z39.

Hall, R., 1976. Ophiolite emplacement and the evolution of the Taurus suture zone, southeastern Turkey. *Geol. Soc. Am. Bull.*, **87**, 1078-1088.

Hamed, A., Fat-Helbary, R. E. S., Mohamed, A. M., El-Faragawy, K. O., Gaber, A. A. E., & Meneisy, A. M., 2024. Application of seismic refraction and MASW methods for investigating the Spillway Fault trace along the western side of the Aswan High Dam, Egypt. *Acta Geodaetica et Geophysica*, **59** (1), 27-50.

Han, F., Zhang, H., Guo, Q., Wei, K., Shang, Z., 2018. An integrated method for seismic velocity modeling based on collocated cokriging. *J. Geophys. Eng.*, **15**, 1389–1398.

Haney, M. M., Mikesell, T. D., van Wijk, K. & Nakahara, H., 2012. Extension of the spatial autocorrelation (SPAC) method to mixed-component correlations of surface waves. *Geophys. J. Int.*, **191** (1), 189–206.

Hanks, T. C. & Kanamori, H., 1979. A moment magnitude and energy of earthquakes. *Journal of Geophysical Research*, **84**, 23480-23500.

Harding, T. P. & Lowell, J. D., 1979. Structural styles, their plate tectonic habitats and hydrocarbon traps in petroleum provinces. *Bull. Am. Assoc. Pet. Geol.*, **83**, 1–24.

Harinarayan, N. H. & Kumar, A., 2017. Site classification of strong motion stations of Uttarakhand, India, based on standard spectral ratio, and horizontal-to-vertical spectral ratio methods. *Geohazards*, **281**, 141–149.

Hempton, M. R. & Dewey, J. F., 1981. Structure and tectonics of the Lake Hazar pull-apart basin, SE Turkey. *Transactions, American Geophysical Union, EOS*, **62**, 1033.

Herber-Gustar, L. K. & Nott, P. A., 1980. John Milne: Father of the Modern Seismology. Tenterden (UK): Paul Norbury.

Herece, E., 2008. Doğu Anadolu Fayı (DAF) Atlası. *General Directorate of Mineral Research and Exploration*, Special Publication, **13**.

Herece, E. & Akay, E. 1992. Karlıova-Çelikhan arasında Doğu Anadolu fayı (East Anatolian Fault between Karlıova and Çelikhan). Abstracts, *9th Petroleum Congress of Turkey*, 361–372.

Hoernes, R., 1893. Erdbebenkunde: Die Erscheinungen und Ursachen der Erdbeben, die Methoden ihrer Beobachtung. Leipzig: Veit & Co.

Hohn, M. E., 1999. Overview of geostatistics. In Geostatistics and Petroleum Geology; Springer: Dordrecht, The Netherlands.

Hopkins, W., 1838. Researches in physical geology. *Transactions of the Cambridge Philosophical Society*, **6**, 1–84.

Hopkins, W., 1839, 1840, 1842. Researches in physical geology. *Philosophical Transactions of the Royal Society of London,* **129**, 381–423; **130,** 193–208; **132**, 43–55.

Hopkins, W., 1842. On the elevation and denudation of the District of the Lakes of Cumberland and Westmorland. *Quarterly Journal of the Geological Society of London*, **4**, 70–98.

Hopkins, W., 1848. Report on the geological theories of elevation and earthquakes. *Report of the Seventeenth Meeting of the British Association for the Advancement of Science*,. London, 33–92.

Huang, H. -C., Yang, Y. -T. & Chiu, H. -C., 2002. Site response evaluation using the H/V ratio at the Yan–Liau station in Hualien, Taiwan. *Pure and Applied Geophysics*, **159** (11–12), 2715–2731.

Hüsing, S. K., Zachariasse, W. J., Van Hinsbergen, D. J., Krijgsman, W., Inceöz, M., Harzhauser, M., Mandic, O. & Kroh, A., 2009. Oligocene–Miocene basin evolution in SE Anatolia, Turkey: constraints on the closure of the eastern Tethys gateway. *Geological Society of London Special Publications*, **311**(1), 107–132.

Ibs-von Seht, M. & Wohlenberg, J., 1999. Microtremor measurements used to map thickness of soft sediments. *Bulletin of the Seismological Society of America*, **89** (1), 250-259.

Institut Cartogràfic i Geològic de Catalunya (ICGC). 2016. Caracterización geofísica y microzonificación sísmica de la ciudad de Huelva. *Informes técnicos de l'Institut Cartogràfic i Geológic de Catalunya,* Generalitat de Catalunya. **GA-010/16**, 69 p.

Instituto Geográfico Nacional (IGN). 2023. Catálogo de terremotos. (Accessed on December 2023).

Ivanov, J., Park, C. B., Miller, R. D. & Xia, J., 2000. Mapping Poissons's Ratio of unconsolidated materials from a joint analysis of surface-wave and refraction events. In: *Proceedings of the Sympsosium on the Application of Geophysics to Engineering and Environmental Problems (SAGEEP 2000)*, Arlington, Virginia. 1-14.

Ivanov, J., Park, C. B., Miller, R. D., Xia, J. & Overtone, R., 2001. Modal separation before dispersion curve extraction by MASW method. In: *Procedings of th SAGEEP 2001.* Denver, Colorado, SSM-3, 1.11.

Jabaloy, A., Galindo-Zaldivar J. & González Lodeiro, F., 1992. The Mecina extensional system: Its relation with the post-Aquitanian piggy-back basins and the paleostresses evolution (Betic Cordillera, Spain). *Geo-Mar. Letters*, **12**, 95-103.

Jang, J., So, B. D. & Yuen, D. A., 2023. A machine learning algorithm with random forest for recognizing hidden control factors from seismic fault distribution. *Geosci. J.*, **27**, 113–126.

Ji, K., Ren, Y. & Wen, R., 2017. Site classification for National Strong Motion Observation Network System (NSMONS) stations in China using an empirical H/V spectral ratio method. *Journal of Asian Earth Sciences*, **147**, 79–94.

Jia, K. & Zhou, S., 2024. Machine Learning Applications in Seismology. *Appl. Sci.*, **14**, 7857.

Jolivet, L., 2001. A comparison of geodetic and finite strain in the Aegean, geodynamic implications.*Earth and Planetary Science Letters*, **187**, 95-104.

Jolivet, L., Faccenna, C., Goffé, B., Burov, E. & Agar, P., 2003. Subduction tectonics and exhumation of high-pressure metamorphic rocks in the Mediterranean orogens. *A,. J. Sci.*, **303**(5), 353–409.

Juhlin, C., Palm, H., Müllern, C. -F. & Wållberg, B., 2000. High-resolution reflection seismics applied to detection of groundwater resources in glacial deposits, Sweden. *Geophys. Res. Lett*, **27**, 1575–1578.

Julivert, M., Fontboté, J. M., Ribeiro, A. & Nabais-Conde, L. E., 1972. Mapa tectónico de la Península Ibérica y Baleares a escala 1:1.000.000. IGME, Memoria explicativa, 113p.

Kanli, A. I., Tildy, P., Pronay, Z., Pinar, A. & Hermann, L., 2006. V_{S30} mapping and soil classification for seismic site effect evaluation in Dinar region, SW Turkey. *Geophysical Journal International*, **165** (1), 223-235.

Karabulut, H., Güvercin, S. E., Hollingsworth, J. & Konca, A. Ö., 2023. Long silence on the East Anatolian Fault Zone (Southern Turkey) ends with devastating double earthquakes (6 February 2023) over a seismic gap: implications for the seismic potential in the Eastern Mediterranean region. *Journal of the Geological Society*, **180**, jgs2023-021.

Karaburun, A. & Demirci, A., 2016. Spatio-temporal cluster analysis of the earthquake epicenters in Turkey and its surrounding area between 1900 and 2014. *Int. J. Res. Earth Environ. Sci.*, **4**, 14–29.

Kaviris, G., Zymvragakis, A., Bonatis, P., Kapetanidis, V., Spingos, I., Mavroulis, S., Kotsi, E., Lekkas, E. & Voulgaris, N. A., 2023. Logic-Tree Approach for Probabilistic Seismic Hazard Assessment in the Administrative Region of Attica (Greece). *Appl. Sci.*, **13**, 7553.

Keller, E.A. & Pinter, N., 1996. Active Tectonics: Earthquakes, Uplift, and Landscape. Prentice Hall.

Ketin, İ., 1966. Tectonic units of Anatolia. *Mineral Research and Exploration Institute of Turkey (MTA) Bulletin*, **66**, 23–34.

Ketin, I., 1983. Turkiye Jeolojisine Genel Bil Bakis. I.T.U., Istanbul, 595 pp.

Kim, J., Han, J., Park, K. & Seok, S., 2022. Improved IDW Interpolation Application Using 3D Search Neighborhoods: Borehole Data-Based Seismic Liquefaction Hazard Assessment and Mapping. *Appl. Sci.*, **12**, 11652.

Kious, J. W. & Tilling, R. I., 1996. 5: Some unanswered questions. In: This Dynamic Earth: The Story of Plate Tectonics. USGS

Kiratzi, A.A., 1993. A study on the active crustal deformation of the North and East Anatolian Fault Zones. *Tectonophysics,* **225**, 191–203.

Kircher, A., 1664. Mundus subterraneus. In: XII libros digestus. Amsterdam: Joannem Janssonium Waesberghe.

Kirsch, R., 2006, Groundwater Geophysics A tool for hydrogeology: New York, Springer, 500 p.

Koç, A. & Kaymakcı, N., 2013. Kinematics of Sürgü Fault Zone (Malatya, Turkey): A remote sensing study. *J. Geodyn.*, **65**, 292–307.

Konno, K. & Ohmachi, T., 1998. Ground-motion characteristics estimated from spectral ratio between horizontal and vertical components of microtremor. *Bulletin of the Seismological Societyof America*, **88** (1), 228–241

Kandilli Observatory and Earthquake Research Institute (KOERI)—Istanbul, Turkey 2024. Available online: http://www.koeri.boun.edu.tr/ (accessed on 27 May 2024).

Köküm, M. & ˙Inceöz, M., 2018. Structural analysis of the northern part of the East Anatolian Fault System. *J. Struct. Geol.*, **114**, 55–63.

Kyprioti, A. P. & Taflanidis, A. A., 2021. Kriging metamodeling for seismic response distribution estimation. *Earthq. Eng. Struct. Dyn.*, **50**, 3550–3576.

Lacoss, R. T., Kelly, E. J. & Toksöz, M. N., 1969. Estimation of seismic noise structure using arrays. *Geophysics*, **34**, 21-38.

Lacombe, O. & Jolivet, L., 2005. Structural and kinematic relationships between Corsica and the Pyrenees-Provence domain at the time of the Pyrenean orogeny. *Tectonics*, **24**, TC1003.

Lankston, R. W., 1990. High-resolution refraction seismic data acquisition and interpretation. S. H. Ward, ed., *Geotechnical and Environmental Geophysics*, **1**, 45-73.

Larrey, M., Mouthereau, F., Do Couto, D., Masini, E., Jourdon, A., Calassou, S., Miegebielle, V., 2023. Oblique rifting triggered by slab tearing and back-arc extension: the case of the Alboran rift in the eastern Betics. *Solid Earth*, **14**, 1221-1244.

Lasocki, S., 2021. Kernel density estimation in seismology. In Statistical Methods and Modelling of Seismogenesis; Limnios, N., Papadimitriou, E., Tsaklidis, G., Eds.; ISTE Ltd.: London, UK; John Wiley & Sons, Inc.: Hoboken, NJ, USA; Chapter 1, 1–26.

Lay, T. & Wallace, T. C., 1995. Chapter 11 – Seismotectonics. *International Geophysics*, Academic Press, **58**, 434–495.

Lebrun, B., Hatzfeld, D. & Bard, P. -Y., 2001. Site effect study in urban area: experimental results in Grenoble (France). *Pure and Applied Geophysics,* **158** (12), 2543–2557.

Lehman, I., 1936. P'. Publications du Bureau Central Scientifiques, **14**, 87-115.

Leprêtre, R., Frizon de Lamotte, D., Combier, V., Gimeno-Vives, O., Mohn, G. & Eschard, R., 2018. The Tell-Rif orogenic system (Morocco, Algeria, Tunisia) and the structural heritage of the southern Tethys margin. BSGF – *Earth Sciences Bulletin*, **189**, 10.

Lermo, J. & Chavez-Garcia, F. J., 1993. Site effect evaluation using spectral ratios with only one station. *Bull. Seismol. Soc. Am.*, **83**, 1574–1594.

Leung, T. M., 1997. Evaluation of seismic refraction interpretation using first arrival raytracing. *Geol. Soc. London, Eng. Geol. Spec. Publ.*, **12**, 413–416.

Leyva Cabello, F. & Ramírez Copeiro del Villar, J., 1977. Mapa Geológico de España E.: 1:50.000 and Memoria, Hoja 983 (11-40) "Sanlúcar la Mayor", IGME. 18 pp.

Lithgow-Bertelloni, C., 2014. Driving Forces: Slab Pull, Ridge Push. In: Harff, J., Meschede, M., Petersen, S., Thiede, J. (eds) Encyclopedia of Marine Geosciences. *Springer*, Dordrecht.

Llácer, D., Otero, B., Tous, R., Monterrubio-Velasco, M., Carrasco-Jiménez, J. C. & Rojas, O., 2020. Random Forest parameterization for earthquake catalog generation. In Machine Learning, Optimization, and Data Science, Proceedings of the 6th International Conference, LOD 2020: Siena, Italy, July 19–23, 2020: *Revised Selected Papers, Part I; Springer: Berlin, Germany*, 233–243.

Lonergan, L. & Platt, J. P., 1995. The Malaguide-Alpujárride boundary: a major extensional contact in the Internal Zone of the eastern Betic Cordillera, SE Spain. *Jour. Struct. Geol.*, **17**, 1655-1671.

Lonergan, L., & White, N., 1997. Origin of the Betic-Rif mountain belt. *Tectonics*, **16** (3), 504-522.

Lomax, A., 2023. Precise, NLL-SSST-Coherence Hypocenter Catalog for the 2023 Mw 7.8 and Mw 7.6 SE Turkey Earthquake Sequence. 2023. Available online: https://zenodo.org/records/7699882 (accessed on 27 May 2024).

Lombardo, G., Coco, G., Corrao, M., Imposa, S., Azzara, R., Cara, F. & Rovelli, A., 2001. Results of microtremor measurements in theurban area of Catania, Italy. *Bollettino Di Geofisica Teorica ed'Applicata*, **42** (3–4), 317–334.

Lonergan, L. & Platt, J. P., 1995. The Malaguide-Alpujárride boundary: a major extensional contact in the Internal Zone of the eastern Betic Cordillera, SE Spain. *Jour. Struct. Geol.*, **17**, 1655-1671.

López, C. & Muñoz, D., 2003. Magnitude formulas in the Spanish bulletins and catalogues. *Física de la Tierra*, **15**, 49–71.

López Arroyo, A., Martín Martín, A.J. & Mézcua Rodríguez, J., 1981. El terremoto de Andalucía del 25 de diciembre de 1884. IGN, 5-94.

López Arroyo, A., & Udías, A., 1972. Aftershock sequence and focal parameters of the February 28, 1969 earthquake of the Azores-Gibraltar fracture zone. *Bulletin of the Seismological Society of America*, **62**, 99-720.

Lotze, F., 1945. Zur gliederung der Varisziden der Iberischen Meseta. *Geotekt. Forsch.*, **6**, 78-92.

Louie, J. N., 2001. Faster, better: Shear-wave velocity to 100 meters depth from refraction microtremor arrays. *Bulletin of the Seismologic Society of America*, **91** (2), 347-364.

Love, A. E. H., 1911. Some Problems of Geodynamics. *London Cambridge University Press*, 19-26.

Lozano, L., Cantavella, J., Gaite, B., Ruíz-Barajas, S., Antón. R. & Barco, J., 2022. Seismic Analysis of the 2020-2021 Santa Fe Seismic Sequence in the Granada Basin, Spain: Relocations and Focal Mechanisms. *Seismological Research Letters*, **93**(6): 3246-3265.

Lozano, L., Buforn, E., Cantavella, J., López-Sánchez, C., Manzanedo, M. V., Barco, J., Antón, R., Cabieces, R. & Mattesini, M., 2025. Relocation of Recent Shallow Seismic Activity in the Alboran Sea (Western Mediterranean Sea): The 2021–2024, 2016, and 2004 Seismic Series. *Bulletin of the Seismological Society of America*.

Lundberg, E., Malehmir, A., Juhlin, C., Bastani, M. & Andersson, M., 2014. High-resolution 3D reflection seismic investigation over a quick-clay landslide scar in southwest Sweden. *Geophysics*, **79** (2), B97–B107.

Lyberis, N., Yurur, T., Chorowicz, J., Kasapoglu, E. & Gundogdu, N., 1992. The East Anatolian Fault: an oblique collisional belt. *Tectonophysics*, **204**, 1–15.

Lyell, C., 1830. Principles of Geology. Londres: John Murray.

Lyell, C., 1847. Elementos de Geología (Traduction J. Ezquerra del Bayo). Madrid: Antonio Yenes.

Lyster, M., 1684. Three Papers of Dr. Martin Lyster, the First of the Nature of Earth-Quakes; More Particularly of the Origine of the Matter of Them, from the Pyrites Alone. *Philosophical Transactions of the Royal Society of London*, **14** (155-166), 512–515.

Macau, A., Benjumea, B., Gabàs, A., Figueras, S. & Vilà, M., 2015. The Effect of Shallow Quaternary Deposits on the Shape of the H/V Spectral Ratio. *Surveys in Geophysics*, **36** (1).

Macau, A., Figueras, S., Benjumea, B., Alonso-Chaves, F. M., Gabàs, P., Bellmunt, F., & Roca, A., 2016. Microzonificación sísmica de la ciudad de Huelva (ALERTES-RIM). In: *9ª Asamblea Hispano-Portuguesa de Geodesia y Geofísica*, Madrid, España.

Macpherson, J., 1885. Los terremotos de Andalucía. Madrid: Fortanet.

Maden, N., Aydin, A. & Kadirov, F., 2015. Determination of the crustal and thermal structure of the Erzurum-Horasan-Pasinler basins (Eastern Türkiye) using gravity and magnetic data. *Pure and Applied Geophysics,* **172**, 1599–1614.

Madarieta-Txurruka, A., González-Castillo, L., Peláez, J. A., Catalán, M., Henares, J., Gil, A. J., Lamas-Fernández, F. & Galindo-Zaldivar, J., 2022.The Role of Faults as Barriers in Confined Seismic Sequences: 2021 Seismicity in the Granada Basin (Betic Cordillera). *Tectonics*, **41**, e2022TC007481.

Madarieta-Txurruka, A., Peláez, J. A., González-Castillo, L., Gil, A. J., Catalán, M., Ruíz-Armenteros, A. M., Henares, J., Garrido-Carretero, M. S., Avilés, M., Lamas, F. & Galindo-Zaldivar, J., 2023a. Segmentación de la actividad tectónica en la zona central y oriental de la Cuenca de Granada. Análisis geológico, geofísico y geodésico. In: *10ª Asamblea Hispano-Portuguesa de Geodesia y Geofísica*, Toledo, España.

Madarieta-Txurruka, A., Peláez, J. A., González-Castillo, L., Gil, A. J. & Galindo-Zaldivar, J., 2023b. Active Collapse in the Central Betic Cordillera: Development of the Extensional System of the Granada Basin. *Appl. Sci.*, **13**, 9138.

Maecker, H., 1949. Quantitativer Nachweis von Grenzschichtwellen inder Optik. *Ann. Phys.*, **4**, 409–431.

Mahajan, A. K., Slob, S., Ranjan, R., Sporry, R., Champati ray, P. K. & van Westen, C., 2007. Seismic microzonation of Dehradun City using geophysical and geotechnical characteristics in the upper 30 m of soil column. *J. Seismol.,* **11** (4), 355-370.

Mahmoud Y., 2012. Caractérisation géodésique de la déformation active du point triple d'Hatay (Syrie-Turquie). Earth Sciences. Université de Strasbourg. English. NNT: 2012STRAH006.tel-00871982.

Mahmoud, Y., Masson, F., Meghraoui, M., Cakir, Z., Alchalbi, A., Yavasoglu, H., Yönlü, O., Daoud, M., Ergintav, S. & Inan, S., 2013. Kinematic study at the junction of the East Anatolian Fault and the Dead Sea fault from GPS measurements. *J. Geodyn.*, **67**, 30–39.

Mallet, R., 1848. On the dynamics of earthquakes; being an attempt to reduce their observed phenomena to the known laws of wave motion in solids and fluids. *The Transactions of the Royal Irish Academy,* **21,** 51–105.

Mallet, R., 1851. First report on the facts of earthquake phaenomena. *Report of the Twentieth Meeting of the British Association for the Advancement of Science*; London, 1–89.

Mallet, R., 1852. Second report on the facts of earthquake phaenomena. *Report of the Twenty-first Meeting of the British Association for the Advancement of Science*, London, 272–320.

Mallet, R., 1855. Third report on the facts of earthquake phaenomena. *Report of the Twenty-third Meeting of the British Association for the Advancement of Science*. London, 117–177.

Mallet, R., 1859. [Fourth report] on the facts and theory of earthquake phenomena. *Report of the Twenty-eighth Meeting of the British Association for the Advancement of Science*. London, 1–137.

Mallet, R., 1862. The Great Neapolitan Earthquake of 1657: The First Principles of Observational Seismology as Developed in the Report to the Royal Society of the Expedition to Investigate the Circumstances of the Great Earthquake of December 1857. 2 volumes. London: Chapman & Hall.

Mancilla, F. de L., Booth-Rea, G., Stich, D., Pérez-Peña, J. V., Morales, J., Azañón, J. M., Martin, R. & Giaconia, F., 2015. Slab rupture and delamination under the Betics and Rif constrained from receiver functions. *Tectonophysics*, **663**, 225–237.

Mancilla, F. de L., Heit, B., Morales, J., Yuan, X., Stich, D., Molina-Aguilera, A., Azañon, J. M. & Martín, R. A., 2018. STEP fault in Central Betics, associated with lateral

lithospheric tearing at the northern edge of the Gibraltar arc subduction system. *Earth Planet. Sc. Lett.*, **486**, 32–40.

Marrett, R. A. & Allmendinger, R. W., 1990. Kinematic analysis of fault-slip data. *Journal of Structural Geology*, **12**, 973–986.

Martín, R., Stich, D., Morales, J. & Mancilla, F., 2015. Moment tensor solutions for the Iberian-Maghreb region during the IberArray deployment (2009-2013). *Tectonophysics*, **663**, 261-274.,

Martín Algarra, A., 2022. Evolución geológica alpina del contacto entre las zonas internas y las zonas externas de la Cordillera Bética. Granada: Universidad de Granada.

Martín-Algarra, A., Alonso-Chaves, F. M, Andreo, B., Balanyá, J. C., Estévez, A., González-Lodeiro, F, Jabaloy, A., López Garrido, A. C., Martín-Martín, M., O'Dogherty, L., Orozco, M., Rodríguez Cañero, R., Ruíz-Cruz, M. D., Sanchez-Navas, A. & Sanz de Galdeano, C., 2004. 4.4.2. Complejo Maláguide. In: Vera, J. A., 2004. Geología de España. Sociedad Geológica de España, Madrid, 884 pp.

Martín-Rojas, I., Alfaro, P., Galindo-Zaldivar, J., Borque-Arancón, M. J., García-Tortosa, F. J., Sanz de Galdeano, C., Avilés, M., Sánchez-Alzola, A., González-Castillo, L., Ruano, P., Medina-Cascales, I., Tendero-Salmerón, V., Madarieta-Txurruka, A., Pedrosa-González, M. T. & Gil-Cruz, A. J., 2023. Insights of Active Extension Within a Collisional Orogen From GNSS (Central Betic Cordillera, S Spain). *Tectonics*, **42**, e2022TC007723.

Martinez, K. & Mendoza, J. A. 2011. Urban seismic site investigations for a new metro in central Copenhagen: Near surface imaging using reflection, refraction and VSP methods. *Physics and Chemistry of the Earth*, **36**, 1228– 1236

Martínez del Olmo, W., 2019. El complejo olistostrómico del Mioceno de la Cuenca del Río Guadalquivir (SO de España). *Revista de la Sociedad Geológica de España*, **32** (2), 3–16.

Martínez-Pagán, P., Navarro, P., Pérez.Cuevas, J., García-Jerez, A., Alcalá, F. J., Sandoval-Castaño, S. & Alhama, I., 2012. Comparative study of SPAC and MASW methods to obtain the V_{S30} for seismic site effect evaluation in Lorca town, SE Spain. *Near Surface Geoscience 2012-18th European Meeting of environmental and Engineering Geophysics*. Paris, France, 3-5 september, P61.

Marínez-Pagán, P., Navarro, P., Pérez.Cuevas, J., Alcalá, F. J., García-Jerez, A. & Sandoval-Castaño, S. 2014. Shear-wave velocity based seismic microzonation of Lorca city (SE Spain) from MASW analysis. *Near Surface Geophysics,* **12**, 739-749.

Martínez Solares, J. M., 1992. Optimización de parámetros de localización para distintos tipos de redes sísmicas. Aplicación a la Península Ibérica. PhD Thesis, Universidad Complutense de Madrid, 257 p.

Martínez Solares, J. M., 1995. Métodos de localización epicentral mediante el procesamiento de señales de dispositivos sísmicos. In: Redes sísmicas regionales, Mezcua, J. (Ed.), 113–144. Monografía 11, Instituto Geográfico Nacional, Madrid (Spain).

Martínez Solares, J. M., 2001. Los efectos en España del terremoto de Lisboa. **Monografía 19,** *Dirección General del Instituto Geográfico Nacional*, Madrid. 756 pp.

Martínez-Solares, J. M., 2003. Historical seismicity of the Iberian Peninsula. *Física de la Tierra*, **15**, 13–28.

Mayoral, E. & Pendón, J. G.,1986. Icnofacies y Sedimentación en Zona Costera. Plioceno Superior (?), Litoral de Huelva. *Acta Geológica Hispánica*, **21-22**, 507-513.

McClusky, S., Balassanian, S., Barka, A., Demir, C., Ergintav, S., Georgiev, I. & Veis, G. (2000). Global Positioning System constraints on plate kinematics and dynamics in the eastern Mediterranean and Caucasus. *Journal of Geophysical Research: Solid Earth*, **105**(B3), 5695–5719.

McKenzie, D., 1972. Active tectonics of the Mediterranean region. *Geophys. J. Int.*, **30**, 109–185.

McKenzie, D. P., 1978. Active tectonics of the Alpine-Himalayan belt: The Aegean Sea and surrounding regions. *Geophys. J. R. Astron. Soc.*, **55**, 217–254.

Medaouri, M., Déverchère, J., Graindorge, D., Bracene, R., Badji, R., Ouabadi, A., Yelles-Chaouche, K. & Bendiab, F., 2014. The transition from Alboran to Algerian basins (Western Mediterranean Sea): Chronostratigraphy, deep crustal structure and tectonic evolution at the rear of a narrow slab rollback system. *Journal of Geodynamics*, **77**, 186-205.

Medina-Cascales, I., Martín-Rojas, I., García-Tortosa, F.J., Peláez, J.A. Y Alfaro, P., 2020. Geometry and kinematics of the Baza Fault (central Betic Cordillera, South Spain): insights into its seismic potential. *Geologica Acta*, **18** (11), 1-25.

Meghan, H. E., Brink, U. T. & Pulliam, J., 2013. Slab tears and intermediate-depth seismicity. *Geophysical Research Letters*, **40** (16), 4244-4248.

Meghraoui M., Cakir Z., Masson F., Mahmoud Y., Ergintav S., Alchalbi A., Inan S., Daoud M., Yonlu O. & Altunel E., 2011. Kinematic modelling at the triple junction between the Anatolian, Arabian, African plates (NW Syria and in SE Turkey). *Geophys. Res. Abstr.*, **13**, 12599.

Menant, A., Jolivet, L. & Vryelynck, B., 2016. Kinematic reconstructions and magmatic evolution illuminating crustal and mantle dynamics of the eastern Mediterranean region since the Late Cretaceous. *Tectonophysics*, **675**, 103–140.

Memiş, C., Göğüş, O. H., Uluocak, E. B., Pysklywec, R., Keskin, M., Şengör, A. M. C. & Topuz, G., 2020. Long wavelength progressive plateau uplift in Eastern Anatolia since 20 Ma: implications for the role of slab peel-back and break-off. *Geochemistry, Geophysics, Geosystems*, **21**, e2019GC008726.

Mezcua, J.; Rueda, J. & García Blanco, R. M., 2004. Reevaluation of historic earthquakes in Spain. *Seismological Research Letters*, **75**, 75–81.

Michard, A., Chalouan, A., Feinberg, H., Goffé, B. & Montigny, R., 2002. How does the Alpine belt end between Spain and Morocco? *Bull. geol. Soc. France*, **173**, 3–15.

Michell, J., 1760. Conjectures concerning the Cause and Observations upon the Phaenomena of Earthquakes. *Philosophical Transactions*. London

Mier y Miura, E., 1910. Organización del Servicio Sismológico en España. Madrid: Memorial de Ingenieros del Ejército.

Mildon, Z. K., Roberts, G. P., Faure Walker, J. P., Beck, J., Papanikolaou, I., Michetti, A. M., Toda, S., Iezzi, F., Campbell, L., McCaffrey, K. J. W., Shanks, R., Sgambato, C., Robertson, J., Meschis, M. & Vittori, E., 2022. Surface faulting earthquake clustering controlled by fault and shear-zone interactions. *Nature Communications.* **13**.

Miller, R. D., Xia, J. & Park, C. B., 1999. Using MASW to map bedrock in Olathe, Kansas. *Open file report-Kansas survey*, 99-9.

Miller, R. D., Anderson, T. S., Ivanov, J., David, J. C., Olea, R., Park, C. B., Steeples, D. W., Moran, M. L. & Xia, J., 2003. 3-D Characterization of Seismic Properties at the Smart Weapons Test Range, YPG. In: *SEG Technical Program Expanded Abstracts 2003.* Society of Exploration Geophysicists, 1195-1198.

Mintrop, L., 1941. Geophysikalische Verfahren zur Erforschung vonGebirgsschichten und Lagerstätten, in: Die technische Entwick-elung des deutschen Steinkohlenbergbaues seit der Jahrhunder-twende, edited by: Verein für bergbauliche Interessen, VerlagGlückauf, Essen.

Mintrop, L., 1947. 100 Jahre physikalische Erdbebenforschung undSprengseismik*Die Naturwissenschaften*, **10**, 289–295.

Miyakoshi, K., Kagawa, T. & Kinoshita, S., 1998. Estimation of geological structures Ander the Kobe area using the array recordings of microtremors. In: *Irikura, K., Kudo, K., Okada, H. & Sasatani, T. (Eds.) The effects of surface geology on seismic motion, recent progress and new horizon in ESG study*, **2**, 691696, Balkema.

Mohorovičić, A., 1910. Das Beben vom 8.X.1909: Jahrbuch des Meteorologischen Observatoriums in Zagreb (Agram), *fuer das Jahr*, 1909, **9** (4-1), 1–63.

Morales, J., Vidal, F., De Miguel, F., Alguacil, G., Posadas, A. M., Ibáñez, J. M., Guzmán, A. & Guirrao, J. M., 1990. Basement structure of the Granada basin, Betic Cordilleras, southern Spain. *Tectonophysics*, **177** (4), 337–348.

Moreno, C., 1993. Postvolcanic Paleozoic of the Iberian pyrite belt; an example of basin morphologic control on sediment distribution in a turbidite basin. *Journal of Sedimentary Research*, **63** (6), 1118-1128

Moreno, C., Sierra, S., & Sáez, R., 1996. Evidence for catastrophism at the Famennian-Dinantian boundary in the Iberian Pyrite Belt. *Geological Society, London, Special Publications*, **107** (1), 153-162.

Moustafa, S. S. R., Yassien, M. H., Metwaly, M., Faried, A. M. & Elsaka, B., 2024. Applying Geostatistics to Understand Seismic Activity Patterns in the Northern Red Sea Boundary Zone. *Appl. Sci.*, **14**, 1455.

Muehlberger, W. R. & Gordon, M. B., 1987. Observations on the complexity of the East Anatolian Fault, Turkey. *Journal of Structural Geology*, **9**, 899–903.

Mussett, A. E. & Khan, M. A., 2000. Looking into The Earth: An Introduction to Geological Geophysics. New York, Cambridge University Press, 470 p.

Nakamura, Y., 1989. A Method for Dynamic Characteristics Estimation of Subsurface using Microtremor on the Ground Surface. *Quarterly Report of Railway Technical Research Institute (RTRI)*, **30** (1), 25-33.

Navarro, M., Enomoto, T., Sánchez, F. J., Matsuda, I., Iwawate, T., Posadas, A. M., Luzón, F., Vidal, F. & Seo, K., 2002. Surface Soil Effects Study Using Short-period Microtremor Observations in Almería City, Southern Spain. *Earthquake microzoning*. Roca, A. & Oliveira, C. (Eds.), Birkhäuser Verlag, Switzerland, 2481-2497.

Navarro, M., Vidal, F., Enomoto, T., Alcalá, F. J., García-Jerez, A., Sánchez, F. J. & Abeki, N., 2007. Analysis of the weightiness of site effects on reinforced concrete (RC) building seismic behaviour: The Adra town example (SE Spain). *Earthquake Engng. Struct. Dyn*., **36** (10), 1363-1383.

Navarro, M., García-Jerez, A., Alcalá, F. J., Vidal, F. & Enomoto, T., 2014. Local site effect microzonation of Lorca town (Southern Spain). *Bulletin of Earthquake Engineering*, **12**, 1933-1959.

Nguyen, F., Van Rompaey, G., Teerlynck, H., Van Camp, M.,Jongmans, D. & Camelbeeck, T., 2004. Use of microtremormeasurement for assessing site effects in Northern Belgium—interpretation of the observed intensity during the Ms = 5.0 June 111938 earthquake. *Journal of Seismology*, **8** (1), 41–56.

Nieto, J. M., Puga, E., Monié, P., Díaz de Federico, A. & Jagoutz, E., 1997. High pressure metamorphism from the Mulhacén Complex (Betic Cordillera, Spain). *Terra Nova*, **1**, 22-23.

Nogoshi, M. & Igarashi, T., 1970. On the propagation characteristics ofmicrotremors, *J. Seismol. Soc. JPN*, **23**, 264–280.

Nogoshi, M., & T. Igarashi, 1971. On the amplitude characteristics of microtremor (Part 2). *Jour. seism. Soc. Japan*, **24**, 26-40.

Ogden, C. S. & Bastow, I. D., 2022. The crustal structure of the Anatolian Plate from receiver functions and implications for the uplift of the central and eastern Anatolian plateaus. *Geophysical Journal International*, **229**, 1041–1062.

Okada, H. & Matsushima, K., 1989. An exploration method using microtremors (1) –A theory to identify Love waves in microtremors. *Proceedings of the 81st SEGJ Conference*, 15-18.

Okay, A. I., 2008. Geology of Turkey: A Synopsis. *Anschnitt*, **21**, 19–42.

Okay, A. I. & Şahintürk, Ö., 1997. Geology of the Eastern Pontides. In: A. Robinson (Ed.) *Regional and Petroleum Geology of the Black Sea and Surrounding Regions*, American Association of Petroleum Geologists, **Memoir 68**, 291-311.

Okuwaki, R., Yagi, Y., Taymaz, T. & Hicks, S. P., 2023. Multi-scale rupture growth with alternating directions in a complex fault network during the 2023 south-eastern Türkiye and Syria earthquake doublet. *Geophys. Res. Lett.*, **50**, e2023GL103480.

Oldham, R. D., 1899. Report of the Great Earthquake of 12th June, 1897. Chapter 25, The unfelt earthquake. *Memoirs of the Geological Survey India*, **29**, 226-256.

Oldham, R. D., 1906. The Constitution of the Interior of the Earth, as Revealed by Earthqueakes. *Quarterly Journal of the Geological Society*, **62** (1-4), 456-475.

Oldham, R. D., 1919. The interior of the earth. *Geol. Mag*, **6**, 18-27.

Oldroyd, D., Amador, F., Kozák, J., Carneiro, A. & Pinto, M., 2007. The study of earthquakes in the hundred years following the Lisbon earthquake of 1755. *Earth Sciences History*, **26** (2), 321-370.

Oliveira, J. T., 1990. Stratigraphy and synsedimentary tectonism. Pre-mesozoic geology of Iberia. 334-347.

OpenTopoMap, "OpenTopoMap – Topographic maps online", accessed November, 20, 2024. Available from: https://www.opentopomap.org.

OpenStreetMap contributors, "OpenStreetMap", accessed November, 20, 2025. Available from: https://www.openstreetmap.org.

Orozco, M., Alonso-Chaves, F. M. & Platt, J. P., 2017. Late extensional shear zones and associated recumbent folds in the Alpujarride subduction complex, Betic Cordillera, southern Spain. *Geologica Acta*, **15** (1), 51-66.

Oruç, B., Gomez-Ortiz, D. & Petit, C., 2017. Lithosphere flexural strength and effective elastic thickness of the Eastern Anatolia (Turkey) and surrounding region. *Journal of Asian Earth Sciences*, **150**, 1–13.

Oruç, B., Ulutaş, E., Pamakçu, O., Selim, H. H. & Sönmez, T., 2019. Rheological stratification and spatial variations in the effective elastic thickness of the lithosphere underneath the central Anatolian region, Turkey. *Journal of Asian Earth Sciences*, **176**, 1–7.

Orueta y Duarte, D., de, 1885. Informe sobre los terremotos ocurridos en el sur de España en diciembre de 1884 y enero de 1885. Málaga: Typography of Fausto Muñoz.

Ostrowski, S., Rybak-Ostrowska, B. & Lasocki, M., 2016. Fault zone imaging with seismic refraction tomography. In: *Near Surface Geoscience 2016 - 22nd European Meeting of Environmental and Engineering Geophysics*, **2016** (6). European Association of Geoscientists & Engineers.

Över, S., Özden, S. & Yilmaz, H., 2004a. Late Cenozoic stress evolution along the Karasu Valley, SE Turkey. *Tectonophysics*, **380**, 43–68.

Över, S., Özden, S., Unlugenc, U. C. & Yilmaz, H. A., 2004b. A synthesis: Late Cenozoic stress field distribution at northeastern corner of the Eastern Mediterranean, SE Turkey. *Comptes Rendus Geosci.*, **336**, 93–103.

Ozer, C., Ozyazicioglu, M., Gok, E. & Polat, O., 2019. Imaging the crustal structure throughout the East Anatolian Fault Zone, Turkey, by local earthquake tomography. *Pure Appl. Geophys.*, **176**, 2235–2261.

Özkan, A., Yavasoglu, H. H. & Masson, F., 2023. Present-day strain accumulations and fault kinematics at the Hatay Triple Junction using new geodetic constraints. *Tectonophysics*, **854**, 229819.

Pakiser, L. C. & Black, R. A., 1957. Exploring for ancient channels with the refraction seismograph. *Geophysics*, **22** (1), 32-47.

Panou, A. A., Theodulidis, N. P., Hatzidimitriou, P. M., Stylianidis, K. & Papazachos, C. B., 2005. Ambient noise horizontal-to-vertical spectral ratio in site effects estimation and correlation with seismic damage distribution in urban environment: the case of the city of

Thessaloniki (Northern Greece). *Soil Dynamics and Earthquake Engineering,* **25**, 261–274.

Park, C. B. & Miller, R. D., 2008. Roadside passive multichannel analysis of surface waves (MASW). *Journal of Environmental & Engineering Geophysics*, **13**, 1-11.

Park, C. B., Miller, R. D. & Xia, J., 1999. Multichannel analysis of surface waves. *Geophysics*, **64**, 800–808.

Park, C., B., Miller, R. D., Xia, J. & Ivanov, J., 2007. Multichannel analysis of surface waves (MASW)-active and passive methods. *The Leading Edge*, **26** (1), 60-64

Parolai, S., Bormann & P., Milkereit, C., 2002. New Relationship between Vs, Thickness of Sediments, and Resonance Frequency Calculated by the H/V Ratio of Seismic Noise for the Cologne Area (Germany). *Bulletin of the Seismological Society of America*, **92** (6), 2521-2527.

Passchier, C. W., 1998. Monoclinic model shear zones. *Journal of Structural Geology*, **20**, 1121–1137.

Payo Subiza, G., & Gómez-Menor, R., 1998. Historia del Observatorio Geofísico de Toledo. Madrid: Instituto Geográfico Nacional.

Platt, J., Behr, W., Johanesen, K., Williams, J., 2013. The Betic-Rif Arc and Its Orogenic Hinterland: A Review. *Annu. Rev. Earth Planet. Sci.*, **41**, 313–357.

Platt, J. P. & Vissers, R. L. M, 1980. Extensional structures in anisotropic rocks. *Jur. Struct. Geol.*, **2**, 397-410.

Pearce, J. A., Bender, J. F., De Long, S. E., Kidd, W. S. F., Low, P. J., Güner, Y., Şaroğlu, F., Yilmaz, Y., Moorbath, S., Mitchell, J. J., 1990. Genesis of collision volcanism in Eastern Anatolia Turkey. *J. Volcanol. Geotherm. Res.*, **44**, 189-229.

Perrey, A., 1847. Sur les tremblements de Terre de la péninsule Ibérique. Annales des Sciences Physiques et Naturelles d'Agriculture et d'Industrie, Tome X. Lyon: Barret.

Peterson, J. & Hutt, C. R., 2014. World-Wide Standardized Seismograph Network: A Data Users Guide. *U.S. Geological Survey* Open-File Report 2014U″ 1218, Reston (Virginia, U.S.A.), 74 p.

Petrescu, L. & Moldovan, I. -A., 2022. Prospective Neural Network Model for Seismic Precursory Signal Detection in Geomagnetic Field Records. *Mach. Learn. Knowl. Extr.*, **4**, 912–923.

Piip, V. B., 2009. Inversion of refraction traveltimes by homogeneous function method is analogue of CDP reflection method. In: *71st EAGE Conference & Exhibition*, 8–11.

Piip, V. B. & Efimova, E. A. 1996. Investigation of deep structure of the Eastern European Platform using seismic refraction data. In: *Oil and Gas in Alpidic Thrustbelts and Basins of Central and Eastern Europe,* eds. Wessely, G. & Leibl, W, 283–288.

Pinzon, L. A., Pujades, L. G., Macau, A., Carreño, E. & Alcalde, J. M., 2019. Seismic site classification from the horizontal-to-vertical response spectral ratio: use of the Spanish strong-motion database. *Geosciences*, **9** (7), 294.

Piquer, A., 1745. Física Moderna Racional y Experimental. Valencia: Pascual García.

Ponce de León, J., 1806. Memoria sobre los terremotos y aplicación de su doctrina a los que dan en Granada. Granada: Herederas de Nicolás Moreno.

Pugin, A. J. -M., Pullan, S. E. & Duchesne, M. J., 2013. Regional hydrostratigraphy and insights into fluid flow through a clay aquitard from shallow seismic reflection data. *The Leading Edge*, **32** (7), 725-856.

Putti, S. P. & Satyam, N., 2020. Evaluation of site effects using HVSR microtremor measurements in Vishakhapatnam. *Earth Systems and Environment*, **4**(2), 439–454.

Ramanna, C. K. & Dodagoudar, G. R., 2012. Seismic Hazard Analysis Using the Adaptive Kernel Density Estimation Technique for Chennai City. *Pure Appl. Geophys*., **169**, 55–69.

Ranalli, G., 1995. Rheology of the Earth (2nd ed). Chapman & Hall, London, 413 pp.

Ranalli, G., 1997. Rheology of the lithosphere in space and time. In: Burg, J.P., Ford, M. (eds) Orogeny Through Time. *Geological Society, London, Special Publications*, **121**, 19–37.

Ranalli, G. & Murphy, D. C., 1987. Rheological stratification of the lithosphere. *Tectonophysics*, **132**, 281–295.

Rebeur-Paschwitz, E., 1889. The earthquake of Tokyo. *Nature*, **40**, 294–295

Reilinger, R. & McClusky, S., 2011. Nubia-Arabia-Eurasia plate motions and the dynamics of Mediterranean and Middle East tectonics. *Geophys. J. Int.*, **186**, 971–979.

Reilinger, R., McClusky, S., Vernant, P., Lawrence, S., Engintav, S., Cakmak, R., Ozener, H., Kadirov, F., Guliev, I., Stepanyan, R., Nadariya, M., Hahubia, G., Mahmoud, S., Sakr, K., ArRajehi. A., Paradissis, D., Al-Aydrus, A., Prilepin, M., Guseva, T., Evren, E., Dmitrotsa, A., Filikov, S.V., Gomez, F., Al-Ghazzi, R., Karam, G., 2006. GPS constraints on continental deformation in the Africa-Arabia-Eurasia continental collision zone and implications for the dynamics of plate interactions. *Journal of Geophysical Research*, **111**, B05411.

Renner, J., Evans, B. & Siddiqi, G., 2002. Dislocation creep of calcite. *Journal of Geophysical Research*, **107**(B12), 2364.

Richter, C. F., 1935. An instrumental earthquake magnitude scale. *Bulletin of the Seismological Society of America*, **25** (1), 1-32.

Robertson, A H. F. & Aktaş, A. H. F., 1984. The Maden complex, SE Turkey: evolution of a neotethyan active margin. *The Geological Evolution of the Eastern Mediterranean. Blackwell*, Oxford, 375-402.

Robertson, A. H. F., Ustaömer, T., Pickett, E., Collins, A., Andrew, T. & Dixon, J. E., 2004. Testing models of Late Paleozoic-Early Meoszoic orogeny in Western Turkey: support for an evolving open-Tethys model. *Journal of the Geological Society, London*, **161**, 501-511.

Rodríguez de la Torre, F., 1989. Management and interpretation of hemerographical sources concerning research about historical Iberian seismicity. In: *Proceedings of the Workshop on Historical Earthquakes in the Ibero-Maghrebian Region. Methodological Approach and Case Studies*. Lisbon, Portugal, 15-17 November 1989. **IV**, 23–94.

Rodríguez de la Torre, F., 2004. Iberian seismic catalogue. A complete revision of all the 19th century. In: Papers of the European Seismological Commission General Assembly, Potsdam.

Rodríguez Domingo, J. M., 2006. Terra tremuit et quievit: El terremoto de Lisboa de 1755 en la diócesis de Guadix. Boletín Centro de Estudios Pedro Suárez, 19, (111-150). Aparicio Florido, J. A., 2017. 1755 El terremoto que viene. Cádiz: Q-book.

Rodríguez-Fernández, J. & Sanz de Galdeano, C., 2006. Late orogenic intramontane basin development: The Granada basin, Betics (southern Spain). *Basin Research*, **18** (1), 85–102.

Romagny, A., Jolivet, L., Menant, A., Bessière, E., Maillard, A., Canva, A., Gorini, C. & Augier, R., 2020. Detailed tectonic reconstructions of the Western Mediterranean region for the last 35 Ma, insights on driving mechanisms. *Bulletin de la Société Géologique de France.*, **191** (1), 37.

Rosenbaum, G., Lister, G. S. & Duboz, C., 2002. Reconstruction of the tectonic evolution of the Western Mediterranean since the Oligocene. In: Rosenbaum G, Lister GS, eds. Reconstruction of the Evolution of the Alpine-Himalayan Orogen. *Journal of the Virtual Explorer*, **8**, 107–126.

Ruano, P., 2003. Estructuras Tectónicas Recientes En La Transversal Central de Las Cordilleras Béticas. Doctoral Thesis, University of Granada, Granada, Spain.

Ruano, P., Galindo-Zaldivar, J., & Jabaloy, A., 2004. Recent tectonic structures in a transect of the Central Betic Cordillera. *Pure and Applied Geophysics*, **161** (3), 541–563.

Rucker, M. L., 2002. Seismic refraction interpretation with velocity gradient and depth of investigation. In: *The 2nd Annual Conference on the Application of Geophysical and NDT Methodologies to Transportation Facilities and Infrastructure*, **11**.

Sánchez-Roldán, J. L., Martínez-Díaz, J. J., Cantavella, J. V., Álvarez-Gómez, J. A. & Morales, J., 2021. Relocation of Seismicity in the Guadalentín Tectonic Vallet, Eastern Betics Shear Zone (Southeast Iberia). *Seismological Society of America*, **92** (5), 3046-3064.

Sanz De Galdeano, C., 1983. Los accidentes y fracturas principales de las Cordilleras Béticas. *Estud. Geol. Madrid*, **39**, 157-165.

Sanz de Galdeano, C. & Vera, J. A., 1991. Una propuesta de clasificación de las cuencas neógenas béticas. *Acta Geológica Hispánica*, **26**, 205-228.

Sanz de Galdeano, C., García-Tortosa, F., Peláez, J.A., Alfaro, P., Azañón, J.M., Galindo-Zaldivar, J., Lopéz Casado, C., López Garrido, A., Rodríguez-Fernández, J., Ruano, P., 2012. Main Active Faults in the Granada and Guadix-Baza Basins (Betic Cordillera). *J. Iber. Geol.*, **38**, 209–223.

Sanz de Galdeano, C., Azañón, J. M., Cabral, J., Ruano, P., Alfaro, P., Canora Catalán, C., Ferrater, M., García-Tortosa, F. J., García- Mayordomo, J., Gràcia, E, Insúa Arévalo, J. M., Jiménez-Bonilla, A., Gilles Lacan, P., Marín-Lechado, C., Martín-Banda, R., Martín-González, F., Martín-Rojas, I., Martínez-Díaz, J. J., Masana, E., Ortuño, M., Pedrera Parias, A., Perea, H. & Simón Gómez, J. L., 2020. Active Faults in Iberia. In: The Geology of Iberia: A Geodynamic Approach, Active Processes: Seismicity, Active Faulting and Relief, C. Quesada y J. T. Oliveira (Ed.), 5, Springer Nature, Cham, Switzerland.

Saroglu, F., Emre, Ö. & Kusçu, I., 1992. Active Fault Map of Turkey; General Directorate of Mineral Research and Exploration: Ankara, Turkey.

Schenková, Z., Schenk, V., Kalogeras, I., Pichl, R., Kottnauer, P., Papatsimba, C. & Panopoulou, G., 2007. Isoseismal maps drawing by the kriging method. *J Seismol.*, **11**, 345–353.

Schermerhorn, L., 1971. An outline stratigraphy of the Iberian Pyrite Belt. *Boletin Geológico y Minero*, **82**, 238–268.

Schorlemmer, D., Mele, F. & Marzocchi, W., 2010. A completeness analysis of the national seismic network of Italy. *Journal of Geophysical Research*, **115**, B04308.

Scudero, S., Marcocci, C. & D'Alessandro, A., 2021. Insights on the Italian seismic network from location uncertainties. *J. Seismol.*, **25**, 1061–1076.

Sheehan, J. R., Doll, W. E., Watson, D. B. & Mandell, W., 2005. Application of Seismic Refraction Tomography to Karst Cavities.

Séneca, L. A.,1929. Liber Sextus, De terrae motu. In: Quaestiones Naturales (Text and traduction P. Oltramare), 247-293.

Séneca, L. A., 1966. Book VI. De los temblores de tierra. In: Obras Completas (traduction and notes Lorenzo Riber), 883-904.

Şengör, A. M. C., Özeren, M. S., Keskin, M., Sakınç, M., Özbakır, A. D. & Kayan, I., 2008. Eastern Turkish high plateau as a small Turkic-typeorogen: implications for post-collisional crust-forming processes in Turkic-type orogens. *Earth-Sci Rev*, **90** (1–2), 1–48.

Şengör, A. M. C., & Yilmaz, Y., 1981. Tethyan evolution of Turkey: A plate tectonic approach. *Tectonophysics*, **75**, 181–241.

Shearer, P. M., 1999. Introduction to Seismology. *Cambridge University Press*, Cambridge, 272 pp.

Shelton, G. & Tullis, J., 1981. Experimental flow laws for crustal rocks. *Eos Transactions. AGU*, **62**, 396.

Sierro, F. J., 1984. Foraminíferos Planctónicos y Bioestratigrafía del Mioceno superior-Plioceno del Borde Occidental de la Cuenca del Guadalquivir (S.O. de España). Doctoral Thesis, Univ. Salamanca, 391 pp.

Silverman, B.W., 1986. Density Estimation for Statistics and Data Analysis; Chapman and Hall: London, UK.

Simão, N. M., Nalbant, S. S., Sunbul, F. & Mutlu, A. K., 2016. Central and eastern Anatolian crustal deformation rate and velocity fields from GPS and earthquake data. *Earth and Planetary Science Letters*, **433**, 89–98.

Smith-Konter, B., Sandwell, D. & Shearer, P., 2011. Locking depths estimated from geodesy and seismology along the San Andreas Fault System: Implications for seismic moment release. *J. Geophys. Res.*, **116**, B06401.

Socco, L. V., Foti, S. & Boeiro, D., 2010. Surface-wave analysis for building near-surface velocity models, established approaches and new perspectives. *Geophysics*, **75** (5), 75A83-75A102.

Sparacino, F., Palano, M., Peláez, J. A., Fernández, J., 2020. Geodetic Deformation versus Seismic Crustal Moment-Rates: Insights from the Ibero-Maghrebian Region. *Remote Sens.*, **12**, 952.

Stampfli, G. M., 2000. Tethyan oceans. *Geol. Soc. Lond. Spec. Publ.*, **173**, 1–23.

Stampfli, G. M., Hochard, 2009. Plate tectonics of the Alpine realm. *Spec. Publ. – Geol. Soc. London*, **327**(1), 89–111.

Stern, R. J., 2004. Subduction initiation: spontaneous and induced. *Earth and Planetary Science Letters*, **226**, 275–292

Stich, D., Serpelloni, E., Mancilla, F. de L. & Morales, J., 2006. Kinematics of the Iberia-Maghreb Plate Contact from Seismic Moment Tensors and GPS Observations. *Tectonophysics*, **426**, 295–317.

Stich, D., Morales, J., López-Comino, J. A., Araque-Pérez, C., Azañón, J. M., Dengra, M. A., Ruiz, M. & Weber, M., 2024. Seismogenic structures and active creep in the Granada Basin (S-Spain). *Tectonophysics*, **882**, 230368.

Sun, R., Kaslilar, A. & Juhlin, C., 2022. High resolution seismic reflection PP and PS imaging of the bedrock surface below glacial deposits in Marsta, Sweden. *Journal of Applied Geophysics*, **198**, 104572.

Sylvester, A. G., 1988. Strike-slip faults. *Geol. Soc. Am. Bull.*, **100**, 1666–1703.

Takagi, R., Nakahara, H., Kono, T. & Okada, T., 2014. Separating body and Rayleigh waves with cross terms of the cross-correlation tensor of ambient noise. *J. geophys. Res.*, **119**, 2005–2018

Tallavó, F., Cascante, G. & Pandey, M., 2009. Experimental and numerical analysis of MASW tests for detection of buried timber trestles. *Soil Dynamics and Earthquake Enginreering,* **29** (1), 91-102.

Tang, L., Zhang, M. & Wen, L., 2019. Support Vector Machine Classification of Seismic Events in the Tianshan Orogenic Belt. *J. Geophys. Res. Solid Earth.*, **125**, e2019JB018132.

Tatar, O., Poyraz, F., Gürsoy, H., Cakir, Z., Ergintav, S., Akpınar, Z., Koçbulut, F., Sezen, F., Türk, T., Hastaoglu, K.Ö., et al., 2012. Crustal deformation and kinematics of the Eastern Part of the North Anatolian Fault Zone (Turkey) from GPS measurements. *Tectonophysics*, **518–521**, 55–62.

Taymaz, T., Eyidoğan, H. & Jackson, J., 1991. Source parameters of large earthquakes in the East Anatolian Fault Zone (Turkey). *Geophysical Journal International,* **106**, 537-550.

Tejero, R. & Ruiz, J., 2002. Thermal and mechanical structure of the central Iberian Peninsula lithosphere. *Tectonophysics*, **350**, 49-62.

Theodulidis, N.P. & Bard, P. -Y., 1995. Horizontal to vertical spectral ratio and geological conditions: an analysis of strong motion data from Greece and Taiwan (SMART-1). *Soil Dynamics and Earthquake Engineering*, **14** (3), 177–197

Thom, C.A. & Kirkpatrick, J.D., 2023. A mechanism for transient creep in crustal shear zones. *Geology*, **51**, 642-646.

Tikoff, B. & Fossen, H., 1993. Simultaneous pure and simple shear: the unified deformation matrix. *Tectonophysics*, **217**, 267–283.

Topuz, G., Altherr, R., Schwartz, W. H., Dokuz, A. & Meyer, H. -P., 2007. Variscan amphibolites-facies rocks from the Kurtoğlumetamorphic complex (Gümüşhane area, Eastern Pontides, Turkey). *International Journal of Earth Sciences*, **96**, 861-873.

Torcal, F., Posadas, A.M., Chica, M. & Serrano, I., 1999. Application of conditional geostatistical simulation to calculate the probability of occurrence of earthquakes belonging to a seismic series. *Geophys. J. Int.*, **139**, 703–725.

Tormann, T., Wiemer, S. & Hauksson, E., 2010. Changes of reporting rates in the Southern California earthquake catalog, introduced by a new definition of ML. *Bulletin of the Seismological Society of America*, **100**, 1733–1742.

Tormann, T., Wiemer, S. & Hardebeck, J. L., 2012. Earthquake recurrence models fail when earthquakes fail to reset the stress field. *Geophysical Research Letters*, **39**, L18310.

Truesdell, C., 1953. Two measures of vorticity. *Journal of Rational Mechanics and Analysis*, **2**, 173-217.

Turcotte, D & Schubert, G., 2014. Geodynamics (3rd ed). Cambridge University Press, Cambridge, UK, 626 pp.

Türkoglu, E., Unsworth, M., Bulut, F. & Çaglar, ˙I., 2015. Crustal structure of the North Anatolian and East Anatolian Fault Systems from magnetotelluric data. *Phys. Earth Planet. Inter.,* **241**, 1–14.

Udías, A., 1967. The focal mechanism of earthquakes in the southern coast of the Iberian Peninsula. *Tectonophysics*, **4**, 229-234.

Udías, A., 1977. Perfiles sísmicos profundos en España (1974-1975). Comisión española del Proyecto Geodinámico. Madrid: Instituto Geográfico Nacional.

Udías, A., 2013. Development of seismology in Spain in the context of the three large earthquakes of 1755, 1884, and 1954. *Earth Science History*, **32**, 186-203.

Udías, A., 2024. Historia de la Sismología en España. *O. A. Centro Nacional de Información Geográfica*, Madrid, Spain, 132 pp.

Udías, A. & Buforn, E., 1991. Regional stresses along the Euroasia-Africa plate boundary derived from local mechanisms of large earthquakes. *PAGEOPH*, **136**, 433-448.

Udías, A. & López Arroyo, A., 1972. Plate tectonics and the Azores-Gibraltar region. *Nature*, **237**, 67-69.

Udías, A. & López-Arroyo, A., 2009. The Lisbon earthquake of November 1, 1755. In Spanish contemporary authors. In: L.A. Mendez Victor, C.S. Sousa Oliveira, J.B. Acevedo & A. Ribeiro, The 1755 Lisbon earthquake revisited (7-24). Berlin: Springer.

Udías, A. & Stauder, W., 1996. The Jesuit contribution to seismology. *Seismological Research Letters*, **67**, 10–19.

U.S. Department of Defense. Advanced Research Projects Agency, 1961. ADDENDUM to: Proceedings of Symposium: Project Vela (1st ed.) (263145). Washington, DC: U.S. Government Printing Office

United States Geological Survey (USGS), 2023. The 2023 Kahramanmaras, Turkey, Earthquake Sequence. Preliminar Seismic Report. USGS Geologic Hazards Science Center and Collaborators.

United States Geological Survey (USGS), 2024. Earthquake Lists, Maps, and Statistics, at https://www.usgs.gov/natural-hazards/earthquake-hazards/lists-maps-and-statistics. (Accessed May 27, 2024).

Ustaömer, P. A., Mundil, R. & Renne, P. R., 2005. U/Pb and Pb/Pb zircon ages for arc-related intrusionsof the Bolu Massif (W Pontides, NW Turkey): evidence for Late Precambrian (Cadomian) age. *Terra Nova*, **17**, 215-223.

Ustaömer, T. & Robertson, A. H. F, 1994. Late Paleozoic marginal basin and subduction-accretion: the Paleotethyan Küre Complex, Central Pontides, northern Turkey. *Journal of the Geological Society London*, **151**, 291-305.

van Bemmelen, R. W., 1927. Bijdrage tot de geologie der Betisch Ketens in de provincie Granada. *Doctoral tesis*, Universidad de Delft, 176 pp.

van Hinsbergen, D. J. J., Vissers, R. L. M. & Spakman, W., 2014. Origin and consequences of western Mediterranean subduction, rollback, and slab segmentation. *Tectonics*, **33**, 393–419.

Vera, J. A., Ancochea, E., Barnolas, F., Bea, Calvo, J. P., Civis, J., De Vicente, G., Fernández-Gianotti, J., García-Cortés, A., Pérez-Estaún, A., Pujalte, V., Rodríguez-Fernández, L. R., Sopeña, A., & Tejero, R., 2004. Capítulo 1. Introducción. In: Vera, J. A., 2004. Geología de España. *Sociedad Geologica de España*, Madrid, 884 pp.

Vergés, J. & Fernàndez, M., 2012. Tethys-Atlantic interaction along the Iberia-Africa plate boundary: The Betic-Rif orogenic system. *Tectonophysics*, **579**, 144–172

Viguier, C., 1977. Les grands traits de la tectonique du Bassin neogene du Bas–Guadalquivir. In: *Instituto Geológico y Minero de España (Ed.), Boletín Geológico y minero*, **88** (1), 39-44.

Vilanova y Piera, J., 1860. Manual de Geología Aplicada a la Agricultura y a las Artes Industriales. Madrid: Imprenta Nacional.

Viltres, R., Jónsson, S., Alothman, A.O., Liu, S., Leroy, S., Masson, F., Doubre, C. & Reilinger, R., 2022. Present-day motion of the Arabian plate. *Tectonics*, **41** (3).

Vissers, R. L. M., Platt, J. P. & van der Wal, D., 1995. Late orogenix extension of the Betic Cordillera and the Alboran Domain: a lithospheric view. *Tectonics*, **14**, 1-154.

von Humboldt, A., 1848. Cosmos. Essai d'une description physique du monde. Paris: Gide et Baudry.

von Schmidt, O., 1938. Über Knallwellenausbreitung in Flüssigkeiten und festen Körpern, *Zeitschr. f. technische Physik*, **12**, 554–561.

von Schmidt, O., 1939. Über Kopfwellen in der Seismik. *Zeitschr. f. Geo-phys*., **15**, 141–148.

Walker, G. W., 1910. The Galitzin Seismograph. *Nature*, **84**, 218-219.

Wang, Z., Juhlin, C., Lü, Q., Ruan, X., Liu, Z., Yu, C. & Chen, M., 2025. High-resolution seismic reflection surveying to delineate shallow subsurface geological structures in the karst area of Shenzhen, China. Preprint.

Wasserman, L., 2006. All Nonparametric Statistics; Springer: New York, NY, USA; 268pp.

Wathelet, M., Chatelain, J.L., Cornou, C., Di Giulio, G., Guillier, B., Ohrnberger, M. & Savvaidis, A., 2020. Geopsy: A User-Friendly Open-Source Tool Set for Ambient Vibration Processing. *Seismological Research Letters*, **91** (3), 1878-1889.

Weglarczyk, S., 2018. Kernel density estimation and its application. ITM Web Conf., **23**, 00037.

Westaway, R. 1994. Present-day kinematics of the Middle East and eastern Mediterranean. *Journal of Geophysical Research*, **99**, 12071–12090.

Westaway, R. & Arger, J., 2001. Kinematics of the Malatya–Ovacık Fault Zone. *Geodin. Acta*, **14**, 103–131.

Wiechert, E., 1896. Ueber die Beschaffenheit des Erdinnern, *Silzher. Physik.-okonom. Ges. Konigsherg*, **37**, 4-5.

Wiechert, E., 1897. Ueber die Massenverteilung im Innern der Erde. *Nachr. Ges. Wiss. Gottingen Math. physik. K1*, 221-243.

Wiechert, E., 1904. Ein astatisches Pendel höher Empfindlichkeit zur mechanischen Registrierung von Erdbeben. *Beitr Geophys,* **6**, 435–450.

Wilsdorf, H. & Schmidt, P., 1981. Erdbebentheorien und Prodigia in der griechisssch-römischen Antike und einige Aspectekte ihre rezeption in späterer Zeit. *Geschichte der Seismologie Seismik und Ergezeitenforschug*, 199-220.

Woessner, J. & Wiemer, S., 2005. Assessing the quality of earthquake catalogues: Estimating the magnitude of completeness and its uncertainty. *Bulletin of the Seismological Society of America*, **95**, 684–698.

Woo, G., 1996. Kernel estimation methods for seismic hazard area source modeling. *Bull. Seismol. Soc. Am.*, **86**, 353–362.

Xia, J., Park, C. B., Hunter, J. A., Harris, J. B. & Ivanov, J., 2002. Comparing shear-wave velocity profiles from multichannel Analysis of surface wave with borehole measurement. *Soil Dynamics and Earthquake Engineering (SDEE)*, **22** (3), 181-190.

Xu, C. & Butt, S. D., 2006. Evaluation of MASW techniques to image steeply dipping cavities in laterally inhomogeneous terrain. *Journal of Applied Geophysics*, **59** (2), 106-116.

Xu, R. & Wang, L., 2021. The Horizontal-to-Vertical spectral ratio and its applications. *EURASIP Journal on Advances in Signal Processing*, **75**.

Yamamoto, H., 1998. An experiment for estimating Swave velocity structure from phase velocities of Love and Rayleigh waves in mocrotremors, In: *Irikura, K., Kudo, K., Okada, H. & Sasatani, T. (eds.) The effects os surface geology on seismic motion, recent progress and new horizon in ESG study*, **2**, 705-710, Balkema.

Yamazaki, F. & Ansary, M.A., 2008. Horizontal-to-vertical spectrum ratio of earthquake ground motion for site characterization. *Earthquake Engineering & Structural Dynamics*. **26** (7), 671–689.

Yan, H. -S. & Hsiao, K. -H., 2006. The Development of Ancient Earthquake Instruments. In: *Proceedings of the ASME 2006 International Design Engineering Technical Conferences and Computers and Information in Engineering Conference. Volume 2: 30th Annual Mechanisms and Robotics Conference, Parts A and B.* Philadelphia, Pennsylvania, USA. September 10–13. 275-279

Yan, H. -S. & Hsiao, K. -H., 2007. Reconstruction design of the lost seismoscope of ancient China. *Mechanism and Machine Theory*, **42**(12), 1601-1617.

Yang, W.; & Ben-Zion, Y., 2010. An algorithm for detecting clipped waveforms and suggested correction procedures. *Seismological Research Letters*, **81**, 53–62.

Yıldız, S. S., ÖZkan, A., Yavaşoğlu, H. H., Masson, F., Tyriakioğlu, I., Alkan, M. N. & Bilgi, S. (2020). Determination of recent tectonic deformations in the vicinity of Adana–Osmaniye–Hatay–Gaziantep triple junction region by half-space modelling. Comptes Rendus Géoscience — Sciences de la Planète. Académie des sciences, Paris. **352** (3), 223-232.

Yilmaz, H., Över, S. & Özden, S., 2006. Kinematics of the East Anatolian Fault Zone between Turkoglu (Kahramanmaras) and Celikhan (Adiyaman), eastern Turkey. *Earth Planets Space*, **58**, 1463–1473.

Yilmaz, Y., 1993. New evidence and model on the evolution of the southeast Anatolian orogen. *Geological Society of America Bulletin,* **105**, 252-271.

Yilmaz, Y., 2021. A model of the crust and upper mantle structures in Central Anatolia, Turkey, constrained by gravity and seismic data. Ms. Thesis, University of Alabama, 60 pp.

Yönlü, O., Altunel, E. & Karabacak, V., 2017. Geological and geomorphological evidence for the southwestern extension of the East Anatolian Fault Zone, Turkey. *Earth Planet. Sci. Lett.*, **469**, 1–14.

Zaragoza, J., 1675. Esphera en común, celeste y terráquea. Madrid: Juan Martín del Barrio.

Zeng, Y., Petersen, M. & Boyd, O., 2022. Lower Seismogenic Depth Model for Western U.S. Earthquakes. *Seismol. Res. Lett.*, **93**, 3186–3204.

Zhang, Y., 2011. Introduction to Geostatistics. Course Notes. Department of Geology and Geophysics, University of Wyoming, Laramie, WY, USA, Draft, 12 January 2011. Available online:
https://www.uwyo.edu/geolgeophys/people/faculty/yzhang/_files/geosta1.pdf (accessed on 10 August 2024).

APPENDIX

APPENDIX

Table A1. Resume table of the main parameters obtained from the seismic noise record in the westernmost Guadalquivir basin.

STATION	COORDINATES		TIME (min)	FUNDAMENTAL FREQUENCY (f_0) (Hz)	THICKNESS (m)	ELEVATION (m)	INTERPRETATION
	LAT (°)	*LONG (°)*					
HVAME2	37.2888	-6.9326	30-45	0.74	125	-84	LOW F_0 PEAK
HVAME3	37.2859	-6.9255	30-45	0.77	118	-79	LOW F_0 PEAK
HVAME4	37.2817	-6.9108	30-45	0.71	133	-106	LOW F_0 PEAK
HVAME10	37.2265	-6.9096	30-45	0.43	280	-276	TWO PEAKS
HVAME11	37.2202	-6.9057	30-45	0.38	336	-321	LOW F_0 PEAK
HVAME12	37.2171	-6.8987	30-45	0.37	349	-311	LOW F_0 PEAK
HVAME13	37.1654	-6.8418	30-45	0.28	527	-506	LOW F_0 PEAK
HVAME14	37.2121	-6.8932	30-45	0.36	364	-345	LOW F_0 PEAK
HVAME15	37.2151	-6.8977	30-45	0.38	336	-298	LOW F_0 PEAK
HVAME5	37.2714	-6.8980	30-45	0.7	136	-127	LOW F_0 PEAK
HVAME7	37.2391	-6.9268	30-45	0.47	245	-241	LOW F_0 PEAK
HVAME8	37.2347	-6.9225	30-45	0.46	253	-246	LOW F_0 PEAK
HVAME9	37.2472	-6.9346	30-45	0.5	224	-222	BROAD PEAK
HVAME16	37.1391	-6.8149	30-45	0.25	624	-585	LOW F_0 PEAK
HVAME17	37.1975	-6.8746	30-45	0.33	414	-382	LOW F_0 PEAK
HVAME18	37.2079	-6.8889	30-45	0.39	323	-319	TWO PEAKS
HVAME19	37.3162	-6.5948	30-45	0.44	270	-159	BROAD PEAK
HVAME20	37.3021	-6.6058	30-45	0.37	349	-246	LOW F_0 PEAK
HVAME21	37.2910	-6.6163	30-45	0.33	414	-316	LOW F_0 PEAK
HVAME22	37.2639	-6.6438	30-45	0.3	476	-376	LOW F_0 PEAK
HVAME23	37.2365	-6.6689	30-45	0.29	501	-413	LOW F_0 PEAK
HVAME24	37.2894	-7.0182	30-45	0.83	106	-74	LOW F_0 PEAK
HVAME25	37.2861	-7.0071	30-45	0.75	123	-114	LOW F_0 PEAK
HVAME26	37.2832	-6.9984	30-45	0.71	133	-120	BROAD PEAK
HVAME27	37.2820	-6.9937	30-45	0.62	163	-156	BROAD PEAK
HVAME28	37.1143	-6.7674	30-45	0.24	663	-619	LOW F_0 PEAK
HVAME29	37.1781	-6.7219	30-45	0.27	557	-512	LOW F_0 PEAK
HVAME30	37.2195	-6.6871	30-45	0.29	501	-429	LOW F_0 PEAK
HVAME31	37.2664	-7.0064	30-45	0.76	120	-116	BROAD PEAK
HVAME32	37.2737	-7.0145	30-45	0.89	95	-91	BROAD PEAK
HVAME33	37.2755	-7.0293	30-45	1.35	51	-46	BROAD PEAK
HVAME34	37.2640	-7.0180	30-45	0.68	142	-132	BROAD PEAK
HVAME35	37.2680	-6.9864	30-45	0.56	189	-187	BROAD PEAK
HVAME36	37.2679	-6.9968	30-45	0.69	139	-136	BROAD PEAK
HVAME37	37.2702	-7.0029	30-45	0.8	112	-109	BROAD PEAK
HVAME38	37.2804	-6.9873	30-45	0.58	180	-174	LOW F_0 PEAK
HVAME39	37.1533	-6.8994	30-45	0.31	454	-451	LOW F_0 PEAK
HVAME40	37.1746	-6.9311	30-45	0.34	396	-393	TWO PEAKS
HVAME41	37.2049	-6.9522	30-45	0.38	336	-331	LOW F_0 PEAK
HVAME42	37.1915	-6.9443	30-45	0.36	364	-361	LOW F_0 PEAK
HVAME43	37.2134	-6.9660	30-45	0.39	323	-320	TWO PEAKS
HVAME44	37.2530	-6.9677	30-45	0.52	211	-207	TWO PEAKS

HVAME45	37.2257	-7.0604	30-45	0.56	189	-159	BROAD PEAK
HVAME46	37.2218	-7.0524	30-45	0.5	224	-211	BROAD PEAK
HVAME47	37.1989	-6.9804	30-45	0.37	349	-345	LOW F_0 PEAK
HVAME48	37.1973	-6.9692	30-45	0.38	336	-331	LOW F_0 PEAK
HVAME49	37.1724	-6.9509	30-45	0.33	414	-410	LOW F_0 PEAK
HVAME50	37.1849	-6.9655	30-45	0.36	364	-359	LOW F_0 PEAK
HVAME51	37.2985	-6.9427	30-45	1.17	64	-62	HIGH F_0 PEAK
HVAME52	37.2329	-7.0664	30-45	0.58	180	-155	LOW F_0 PEAK
HVAME53	37.2434	-7.0832	30-45	0.55	194	-156	LOW F_0 PEAK
HVAME54	37.1952	-6.9947	30-45	0.39	323	-317	LOW F_0 PEAK
HVAME55	37.1897	-6.9749	30-45	0.36	364	-359	LOW F_0 PEAK
HVAME56	37.2584	-7.1073	30-45	0.93	89	-32	LOW F_0 PEAK
HVAME57	37.2640	-7.1146	30-45	0.83	106	-46	LOW F_0 PEAK
HVAME58	37.2046	-7.0267	30-45	0.42	289	-281	LOW F_0 PEAK
HVAME59	37.2719	-7.1266	30-45	1.38	50	-32	HIGH F_0 PEAK
HVAME60	37.2784	-7.1339	30-45	1.51	44	-20	BROAD PEAK
HVAME61	37.2975	-7.1619	30-45	1.69	37	-22	BROAD PEAK
HVAME62	37.3038	-7.1705	30-45	8.55	3	20	HIGH F_0 PEAK
HVAME63	37.3060	-7.1755	30-45	4.05	10	23	HIGH F_0 PEAK
HVAME64	37.3124	-7.1861	30-45	0	0	33	ROCK
HVAME65	37.3194	-7.1936	30-45	5.39	7	56	HIGH F_0 PEAK
HVAME66	37.3178	-7.0867	30-45	1.59	40	16	HIGH F_0 PEAK
HVAME67	37.2663	-6.8902	30-45	0.62	163	-152	LOW F_0 PEAK
HVAME68	37.2489	-7.0930	30-45	0.65	152	-120	LOW F_0 PEAK
HVAME69	37.2553	-7.0979	30-45	0.81	109	-69	BROAD PEAK
HVAME70	37.2824	-7.1416	30-45	1.5	44	-18	BROAD PEAK
HVAME71	37.2924	-7.1550	30-45	1.37	50	-25	TWO PEAKS
HU1	37.2746	-6.9403	30-45	0.62	163	-98	LOW F_0 PEAK
HU2	37.2725	-6.9404	30-45	0.6	171	-123	LOW F_0 PEAK
HU3	37.2779	-6.9464	30-45	0.77	118	-97	BROAD PEAK
HU4	37.2739	-6.9535	30-45	0.76	120	-117	LOW F_0 PEAK
HU5	37.2693	-6.9621	30-45	0.66	148	-146	TWO PEAKS
HU6	37.2502	-6.9436	30-45	0.5	224	-223	BROAD PEAK
HU7	37.2709	-6.9254	30-45	0.67	145	-125	LOW F_0 PEAK
HU8	37.2793	-6.9386	30-45	0.65	152	-102	INDETERMINED
HU9	37.2764	-6.9361	30-45	0.66	148	-108	LOW F_0 PEAK
HU10	37.2717	-6.9332	30-45	0.62	163	-132	LOW F_0 PEAK
HU11	37.2735	-6.9306	30-45	0.66	148	-119	LOW F_0 PEAK
HU12	37.2787	-6.9506	30-45	0.86	100	-95	BROAD PEAK
HU13	37.2758	-6.9498	30-45	0.81	109	-103	BROAD PEAK
HU14	37.2684	-6.9552	30-45	0.67	145	-141	TWO PEAKS
HU15	37.2602	-6.9601	30-45	0.55	194	-190	BROAD PEAK
HU16	37.2549	-6.9579	30-45	0.55	194	-190	TWO PEAKS
HU17	37.2607	-6.9272	30-45	0.54	200	-193	LOW F_0 PEAK
HU18	37.2577	-6.9253	30-45	0.52	211	-205	LOW F_0 PEAK
HU19	37.2605	-6.9227	30-45	0.55	194	-188	LOW F_0 PEAK
HU20	37.2561	-6.9302	30-45	0.5	224	-216	LOW F_0 PEAK
HU21	37.2535	-6.9351	30-45	0.47	245	-235	LOW F_0 PEAK
HU22	37.2522	-6.9380	30-45	0.46	253	-249	LOW F_0 PEAK
HU23	37.2583	-6.9358	30-45	0.48	238	-222	LOW F_0 PEAK

HU24	37.2599	-6.9385	30-45	0.48	238	-219	LOW F_0 PEAK
HU25	37.2664	-6.9390	30-45	0.53	205	-173	LOW F_0 PEAK
HU26	37.2639	-6.9393	30-45	0.5	224	-194	LOW F_0 PEAK
HU27	37.2693	-6.9302	30-45	0.61	167	-141	LOW F_0 PEAK
HU28	37.2674	-6.9462	30-45	0.53	205	-158	LOW F_0 PEAK
HU29	37.2742	-6.9454	30-45	0.61	167	-100	LOW F_0 PEAK
HU30	37.2649	-6.9512	30-45	0.53	205	-198	LOW F_0 PEAK
HU31	37.2624	-6.9457	30-45	0.5	224	-184	LOW F_0 PEAK
HU32	37.2605	-6.9452	30-45	0.49	230	-196	LOW F_0 PEAK
HU33	37.2513	-6.9567	30-45	0.48	238	-235	BROAD PEAK
HU34	37.2642	-6.9582	30-45	0.54	200	-197	BROAD PEAK
HU35	37.2811	-6.9412	30-45	0.71	133	-106	BROAD PEAK
HU36	37.2784	-6.9280	30-45	0.69	139	-106	LOW F_0 PEAK
HU37	37.2619	-6.9474	30-45	0.5	224	-191	LOW F_0 PEAK
HU38	37.2578	-6.9469	30-45	0.48	238	-199	BROAD PEAK
HU39	37.2578	-6.9489	30-45	0.48	238	-212	LOW F_0 PEAK
HU40	37.1774	-6.7842	30-45	0.27	557	-500	LOW F_0 PEAK
HU41	37.1774	-6.7842	30-45	0.27	557	-500	LOW F_0 PEAK
HU42	37.1446	-6.8867	30-45	0.29	501	-494	LOW F_0 PEAK
G9-10 HU3	37.2440	-6.9662	30-45	0.5	224	-222	TWO PEAKS
G25-26 HU3	37.2439	-6.9667	30-45	0.48	238	-236	TWO PEAKS
G40 HU3	37.2439	-6.9671	30-45	0.5	224	-222	TWO PEAKS
R0S1	37.2503	-6.9504	30-45	0.44	270	-266	TWO PEAKS
R1S2	37.2504	-6.9506	30-45	0.46	253	-249	TWO PEAKS
R1S3	37.2505	-6.9502	30-45	0.47	245	-241	TWO PEAKS
R1S4	37.2501	-6.9503	30-45	0.46	253	-249	TWO PEAKS
R2S5	37.2507	-6.9505	30-45	0.38	336	-331	LOW F_0 PEAK
R2S6	37.2502	-6.9498	30-45	0.47	245	-241	TWO PEAKS
R2S7	37.2500	-6.9507	30-45	0.47	245	-241	LOW F_0 PEAK
R3S2	37.2507	-6.9514	30-45	0.48	238	-234	LOW F_0 PEAK
R3S3	37.2509	-6.9495	30-45	0.46	253	-249	LOW F_0 PEAK
R3S4	37.2494	-6.9501	30-45	0.47	245	-240	LOW F_0 PEAK
R4S5	37.2523	-6.9514	30-45	0.49	230	-227	LOW F_0 PEAK
R4S6	37.2496	-6.9479	30-45	0.47	245	-241	LOW F_0 PEAK
R4S7	37.2488	-6.9528	30-45	0.48	238	-234	LOW F_0 PEAK
R5S2	37.2505	-6.9547	30-45	0.44	270	-266	BROAD PEAK
R5S3	37.2528	-6.9474	30-45	0.43	280	-275	BROAD PEAK
R5S4	37.2467	-6.9494	30-45	0.48	238	-234	BROAD PEAK
R0S1	37.2696	-6.9232	30-45	0.64	155	-140	LOW F_0 PEAK
R1S2	37.2696	-6.9230	30-45	0.65	152	-137	LOW F_0 PEAK
R1S3	37.2698	-6.9233	30-45	0.66	148	-133	LOW F_0 PEAK
R1S4	37.2695	-6.9235	30-45	0.66	148	-133	LOW F_0 PEAK
R2S5	37.2699	-6.9228	30-45	0.65	152	-137	LOW F_0 PEAK
R2S6	37.2697	-6.9238	30-45	0.64	155	-139	LOW F_0 PEAK
R2S7	37.2692	-6.9231	30-45	0.64	155	-140	LOW F_0 PEAK
R3S2	37.2694	-6.9221	30-45	0.64	155	-141	LOW F_0 PEAK
R3S3	37.2705	-6.9234	30-45	0.66	148	-132	LOW F_0 PEAK
R3S4	37.2691	-6.9241	30-45	0.64	155	-139	LOW F_0 PEAK
R4S5	37.2711	-6.9214	30-45	0.67	145	-131	LOW F_0 PEAK
R4S6	37.2703	-6.9259	30-45	0.64	155	-134	LOW F_0 PEAK

R4S7	37.2673	-6.9226	30-45	0.63	159	-146	LOW F_0 PEAK
R0S1	37.2659	-6.9295	30-45	0.58	180	-163	LOW F_0 PEAK
R1S2	37.2660	-6.9292	30-45	0.57	184	-167	LOW F_0 PEAK
R1S3	37.2661	-6.9297	30-45	0.58	180	-162	LOW F_0 PEAK
R1S4	37.2657	-6.9295	30-45	0.57	184	-168	LOW F_0 PEAK
R2S5	37.2664	-6.9294	30-45	0.58	180	-161	LOW F_0 PEAK
R2S6	37.2656	-6.9292	30-45	0.58	180	-164	LOW F_0 PEAK
R2S7	37.2658	-6.9300	30-45	0.58	180	-164	LOW F_0 PEAK
R3S2	37.2662	-6.9284	30-45	0.58	180	-163	LOW F_0 PEAK
R3S3	37.2665	-6.9303	30-45	0.58	180	-161	LOW F_0 PEAK
R3S4	37.2650	-6.9299	30-45	0.56	189	-175	LOW F_0 PEAK
R0S1	37.2775	-6.9251	30-45	0.68	142	-122	LOW F_0 PEAK
R1S2	37.2776	-6.9248	30-45	0.68	142	-122	LOW F_0 PEAK
R1S3	37.2776	-6.9253	30-45	0.68	142	-121	LOW F_0 PEAK
R1S4	37.2772	-6.9251	30-45	0.69	139	-119	LOW F_0 PEAK
R2S5	37.2779	-6.9250	30-45	0.68	142	-121	LOW F_0 PEAK
R2S6	37.2772	-6.9247	30-45	0.69	139	-120	LOW F_0 PEAK
R2S7	37.2773	-6.9257	30-45	0.68	142	-118	LOW F_0 PEAK
HU43	37.2898	-6.9889	30-45	0.83	106	-93	BROAD PEAK
HU44	37.2928	-6.9943	30-45	0.97	84	-68	LOW F_0 PEAK
HU46	37.2935	-7.0013	30-45	0.95	86	-68	BROAD PEAK
HU47	37.2951	-7.0085	30-45	1.06	74	-51	BROAD PEAK
HU48	37.2956	-7.0154	30-45	1	80	-67	BROAD PEAK
HU49	37.2680	-6.9497	30-45	0.55	194	-180	BROAD PEAK
HU50	37.2597	-6.9552	30-45	0.53	205	-202	BROAD PEAK
HU51	37.2629	-6.9345	30-45	0.52	211	-187	LOW F_0 PEAK
HU52	37.2562	-6.9539	30-45	0.5	224	-218	BROAD PEAK
HU53	37.2547	-6.9406	30-45	0.46	253	-239	LOW F_0 PEAK
HU54	37.2566	-6.9470	30-45	0.48	238	-228	LOW F_0 PEAK
Odiel1	37.2837	-6.9497	30-45	0.88	97	-95	BROAD PEAK/TWO PEAKS
Odiel2	37.2836	-6.9501	30-45	0.91	92	-90	BROAD PEAK/TWO PEAKS
Odiel3	37.2835	-6.9503	30-45	0.89	95	-93	BROAD PEAK/TWO PEAKS
R0S1	37.2738	-6.9306	30-45	0.65	152	-124	LOW F_0 PEAK
R1S2	37.2740	-6.9304	30-45	0.65	152	-124	LOW F_0 PEAK
R1S3	37.2735	-6.9306	30-45	0.65	152	-123	LOW F_0 PEAK
R1S4	37.2738	-6.9308	30-45	0.65	152	-123	LOW F_0 PEAK
R2S5	37.2742	-6.9309	30-45	0.65	152	-123	LOW F_0 PEAK
R2S6	37.2737	-6.9301	30-45	0.65	152	-124	LOW F_0 PEAK
R2S7	37.2734	-6.9311	30-45	0.64	155	-124	LOW F_0 PEAK
R3S2	37.2743	-6.9298	30-45	0.66	148	-121	LOW F_0 PEAK
R3S3	37.2729	-6.9305	30-45	0.65	152	-123	LOW F_0 PEAK
R3S4	37.2737	-6.9317	30-45	0.66	148	-117	LOW F_0 PEAK
ARNO-G12 (L1)	37.0991	-6.7319	30-45	0.23	706	-660	LOW F_0 PEAK
ARNO-G12 (L2)	37.0989	-6.7326	30-45	0.23	706	-661	LOW F_0 PEAK
ARNO-G2 (L1)	37.0988	-6.7321	30-45	0.24	663	-661	LOW F_0 PEAK
WALJ_09	37.2468	-7.0293	50	0.53	205	-188	BROAD PEAK
RIN_15	37.2360	-7.0309	37	0.51	220	-199	BROAD PEAK
RIN_14	37.2384	-7.0329	37	0.51	220	-211	BROAD PEAK

RIN_13	37.2430	-7.0400	40	0.57	183	-146	BROAD PEAK
RIN_07	37.2588	-7.0584	38	0.75	123	-88	LOW F_0 PEAK
RIN_08	37.2572	-7.0560	48	0.73	129	-96	LOW F_0 PEAK
WALJ_01	37.2652	-7.0370	31	0.66	148	-112	BROAD PEAK
WALJ_02	37.2628	-7.0362	30	0.53	203	-176	BROAD PEAK
WALJ_03	37.2611	-7.0354	30	0.52	211	-188	BROAD PEAK
WALJ_04	37.2594	-7.0346	35	0.56	187	-165	BROAD PEAK
WALJ_06	37.2565	-7.0336	30	0.51	217	-197	BROAD PEAK
WALJ_05	37.2574	-7.0340	33	0.51	217	-192	BROAD PEAK
WALJ_07	37.2552	-7.0333	30	0.48	241	-211	BROAD PEAK/TWO PEAKS
WALJ_08	37.2536	-7.0326	35	0.49	228	-212	BROAD PEAK/TWO PEAKS
EALJ_01.5	37.2743	-7.0167	29	1.10	70	-66	BROAD PEAK
EALJ_02.5	37.2695	-7.0156	33	1.01	79	-75	BROAD PEAK
EALJ_03	37.2681	-7.0120	42	0.78	116	-111	BROAD PEAK/TWO PEAKS
EALJ_03.5	37.2666	-7.0110	44	0.77	117	-112	BROAD PEAK/TWO PEAKS
EALJ_04	37.2656	-7.0078	38	0.75	122	-112	BROAD PEAK
EALJ_05	37.2644	-7.0067	38	0.74	126	-115	BROAD PEAK/TWO PEAKS
RIN_12	37.2455	-7.0419	65	0.52	212	-189	BROAD PEAK
RIN_11	37.2481	-7.0455	40	0.51	215	-188	BROAD PEAK
RIN_10	37.2507	-7.0483	34	0.57	185	-167	BROAD PEAK
RIN_01	37.2996	-7.1075	45	1.40	49	-4	BROAD PEAK
RIN_02	37.2924	-7.0990	50	1.14	66	-37	TWO PEAKS
RIN_03	37.2854	-7.0918	36	1.01	79	-40	LOW F_0 PEAK
RIN_04	37.2761	-7.0797	33	0.67	145	-78	LOW F_0 PEAK
RIN_05	37.2675	-7.0688	35	0.72	129	-84	BROAD PEAK
RIN_09	37.2531	-7.0514	40	0.60	171	-150	BROAD PEAK
CEP_13A	37.2480	-7.0916	32	0.63	157	-128	LOW F_0 PEAK
CEP_13B	37.2451	-7.0877	25	0.56	191	-150	LOW F_0 PEAK
CEP_14A	37.2391	-7.0782	31	0.62	163	-134	BROAD PEAK/TWO PEAKS
CEP_14B	37.2361	-7.0737	62	0.57	182	-160	BROAD PEAK/TWO PEAKS
GO_08.5	37.3120	-6.9817	40	1.48	45	-41	HIGH F_0 PEAK
GO_07.5	37.3157	-6.9894	41	1.50	44	-39	HIGH F_0 PEAK
GO_06.5	37.3196	-6.9956	40	1.78	34	-27	HIGH F_0 PEAK
GO_05.5	37.3243	-7.0043	45	2.20	25	-14	HIGH F_0 PEAK
GO_04.5	37.3275	-7.0111	35	2.10	27	-14	HIGH F_0 PEAK
GO_05	37.3384	-7.0061	80	1.99	29	11	HIGH F_0 PEAK
GO_04	37.3446	-7.0117	37	2.62	19	16	BROAD PEAK
GO_03	37.3478	-7.0155	38	2.27	24	21	HIGH F_0 PEAK
GO_02	37.3559	-7.0250	36	2.74	18	36	HIGH F_0 PEAK
GO_01	37.3630	-7.0330	32	4.85	8	40	HIGH F_0 PEAK
E_01	37.2685	-7.0305	68	0.71	134	-105	BROAD PEAK
E_02	37.2748	-7.0256	65	1.06	74	-68	BROAD PEAK
PAT_01	37.4722	-6.4158	36	17.99	1	111	HIGH F_0 PEAK/ALMOST ROCK
PAT_02	37.4635	-6.4087	40	3.80	11	83	HIGH F_0 PEAK
PAT_03	37.4531	-6.3999	39	1.82	33	47	TWO PEAKS

PAT_04	37.4456	-6.3941	64	1.31	54	25	HIGH F_0 PEAK
PAT_05	37.4345	-6.3845	50	0.78	116	-40	BROAD PEAK
PAT_06	37.4263	-6.3788	50	0.68	142	-66	TWO PEAKS
PAT_07	37.4144	-6.3688	53	0.53	205	-117	TWO PEAKS
AZN_01	37.5127	-6.2633	40	7.73	4	106	HIGH F_0 PEAK
AZN_02	37.5010	-6.2550	40	2.71	18	61	BROAD PEAK
AZN_03	37.4933	-6.2512	42	1.44	47	33	HIGH F_0 PEAK
AZN_04	37.4810	-6.2425	45	0.92	91	-17	BROAD PEAK
AZN_05	37.4736	-6.2385	45	0.72	130	-63	LOW F_0 PEAK
AZN_06	37.4654	-6.2320	50	0.58	180	-122	LOW F_0 PEAK
AZN_07	37.4513	-6.2248	23	0.53	205	-149	LOW F_0 PEAK
AZN_08	37.4386	-6.2175	40	0.47	245	-215	BROAD PEAK
AZN_09	37.4309	-6.2100	43	0.38	336	-304	BROAD PEAK
AZN_11	37.4047	-6.1933	40	0.30	476	-319	BROAD PEAK
AZN_12	37.3993	-6.1886	42	0.26	589	-425	BROAD PEAK
AZN_13A	37.3899	-6.1837	48	0.26	589	-441	LOW F_0 PEAK
E_03	37.2685	-7.0305	58	0.71	134	-105	BROAD PEAK
AZN_17	37.4861	-6.2789	45	1.77	34	36	TWO PEAKS
AZN_16	37.4936	-6.2754	51	2.77	18	52	TWO PEAKS
AZN_15	37.4982	-6.2740	51	5.68	6	70	BROAD PEAK
AZN_13B	37.5059	-6.2717	53	7.62	4	89	TWO PEAKS
AZN_14	37.5016	-6.2724	55	5.47	6	78	TWO PEAKS
SLM_01	37.4059	-6.2417	49	0.36	367	-326	BROAD PEAK
SLM_02	37.4014	-6.2350	42	0.36	370	-342	BROAD PEAK
SLM_03	37.3997	-6.2324	54	0.35	386	-363	LOW F_0 PEAK
SLM_04	37.3968	-6.2287	56	0.36	365	-343	BROAD PEAK
SLM_05	37.3957	-6.2249	52	0.32	427	-404	BROAD PEAK
SLM_06	37.3934	-6.2211	52	0.30	481	-447	BROAD PEAK
HVA_01	37.3520	-6.2674	53	0.28	536	-479	BROAD PEAK
HVA_02	37.3487	-6.2592	45	0.27	551	-515	LOW F_0 PEAK
HVA_03	37.3456	-6.2512	48	0.27	558	-531	BROAD PEAK
HVA_04	37.3418	-6.2418	54	0.27	567	-550	BROAD PEAK
HVA_06	37.3363	-6.2255	55	0.24	670	-564	BROAD PEAK
HVA_07	37.3337	-6.2223	50	0.23	694	-596	BROAD PEAK
HVA_08	37.3248	-6.2002	51	0.23	707	-620	LOW F_0 PEAK
PiAz_01	37.3036	-6.2786	52	0.24	647	-601	LOW F_0 PEAK
PiAz_02	37.3000	-6.2698	59	0.24	658	-638	BROAD PEAK
PiAz_03	37.3011	-6.2625	56	0.24	667	-653	LOW F_0 PEAK
PiAz_04	37.2954	-6.2576	55	0.24	653	-621	LOW F_0 PEAK
PiAz_05	37.2916	-6.2522	60	0.23	694	-658	BROAD PEAK
PiAz_06	37.2902	-6.2497	63	0.23	701	-672	TWO PEAKS
VL_01	37.3173	-7.3219	39	4.68	8	123	HIGH F_0 PEAK
VL_02	37.3132	-7.3176	42	4.17	10	103	HIGH F_0 PEAK
VL_03	37.2993	-7.2981	45	4.34	9	55	HIGH F_0 PEAK
VL_04	37.2893	-7.2837	40	4.29	9	59	HIGH F_0 PEAK
VL_05	37.2816	-7.2744	40	4.52	9	58	HIGH F_0 PEAK
VL_06	37.2642	-7.2499	45	2.97	16	29	HIGH F_0 PEAK
VL_08	37.2526	-7.2344	41	1.43	47	-3	HIGH F_0 PEAK
VL_10	37.2455	-7.2242	48	1.39	49	-8	BROAD PEAK
VL_12	37.2369	-7.2123	43	0.99	82	25	LOW F_0 PEAK

VL_14	37.2262	-7.1975	45	0.77	119	-89	BROAD PEAK
VL_16	37.2190	-7.1877	42	0.67	146	-144	TWO PEAKS
AYA_01	37.2406	-7.3789	57	7.73	4	16	HIGH F_0 PEAK/ALMOST ROCK
AYA_02	37.2409	-7.3782	24	13.22	2	11	BROAD PEAK/ALMOST ROCK
AYA_03	37.2426	-7.3782	43	10.36	3	41	HIGH F_0 PEAK/ALMOST ROCK
AYA_04	37.2354	-7.4055	43	6.34	5	-5	HIGH F_0 PEAK
DAN_01	37.1995	-6.9219	44	0.39	319	-318	TWO PEAKS
DAN_02	37.2064	-6.9281	41	0.40	311	-307	TWO PEAKS
DAN_03	37.2099	-6.9286	44	0.43	283	-279	TWO PEAKS
DAN_04	37.2092	-6.9266	40	0.43	277	-272	TWO PEAKS
DAN_05	37.2296	-6.9409	40	0.44	274	-268	TWO PEAKS
DAN_06	37.2180	-6.9386	42	0.45	266	-264	TWO PEAKS
DAN_07	37.2446	-6.9404	52	0.46	255	-252	TWO PEAKS
DAN_08	37.2124	-6.9409	41	0.44	275	-275	TWO PEAKS
DAN_09	37.2710	-6.8624	54	0.65	153	-150	TWO PEAKS
DAN_10	37.2764	-6.8557	49	0.70	137	-135	TWO PEAKS
DAN_11	37.2818	-6.8500	44	0.81	110	-107	LOW F_0 PEAK
DAN_12	37.2660	-6.8645	60	0.62	165	-160	TWO PEAKS
DAN_13	37.2633	-6.8694	51	0.59	174	-171	TWO PEAKS
DAN_14	37.2630	-6.8761	65	0.59	175	-173	LOW F_0 PEAK
DAN_15	37.2589	-6.8737	52	0.51	218	-215	TWO PEAKS
DAN_16	37.2541	-6.8772	46	0.49	230	-227	TWO PEAKS
DAN_17	37.2497	-6.8822	51	0.44	275	-273	TWO PEAKS
DAN_18	37.2477	-6.8775	51	0.44	271	-250	LOW F_0 PEAK
DAN_19	37.2159	-6.9230	51	0.43	284	-282	BROAD PEAK
DAN_20	37.2210	-6.9177	43	0.40	308	-306	TWO PEAKS
DAN_21	37.2275	-6.9101	45	0.43	280	-277	TWO PEAKS
DAN_22	37.2323	-6.9015	41	0.43	280	-277	TWO PEAKS
DAN_23	37.2526	-6.9480	48	0.44	273	-268	BROAD PEAK
QUI_01	37.1777	-6.9573	43	0.34	394	-387	LOW F0 PEAK
QUI_02	37.2158	-7.0803	41	0.62	163	-145	BROAD PEAK
QUI_03	37.2141	-7.0648	44	0.53	205	-195	BROAD PEAK
QUI_04	37.1995	-7.0056	34	0.39	319	-313	LOW F_0 PEAK
ZPC_01	37.2799	-6.9425	45	0.75	124	-86	LOW F_0 PEAK

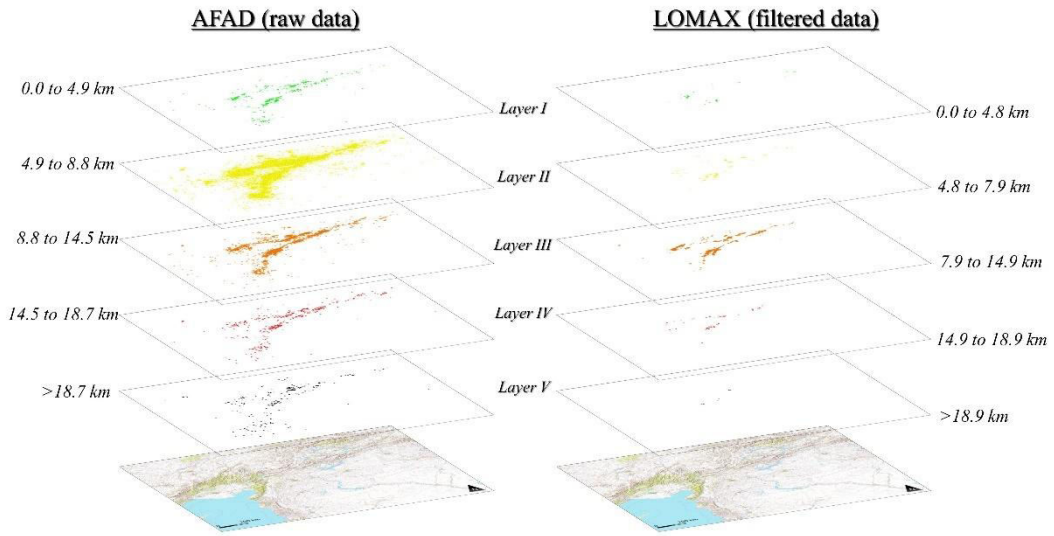

Figure A1. Comparison of stacked point cloud maps for the central and southwestern part of the EAFZ, represented at different depth ranges (seismological layers) identified by the seismic distribution profile, Layers I to V (**Figure 14**). Left: AFAD (raw data). Right: Lomax, 2023 (relocated-filtered data). This figure represents the same maps as in **Figure 16** but stacked to illustrate the 3D morphology of the patterns. For color codes see **Figure 16**.

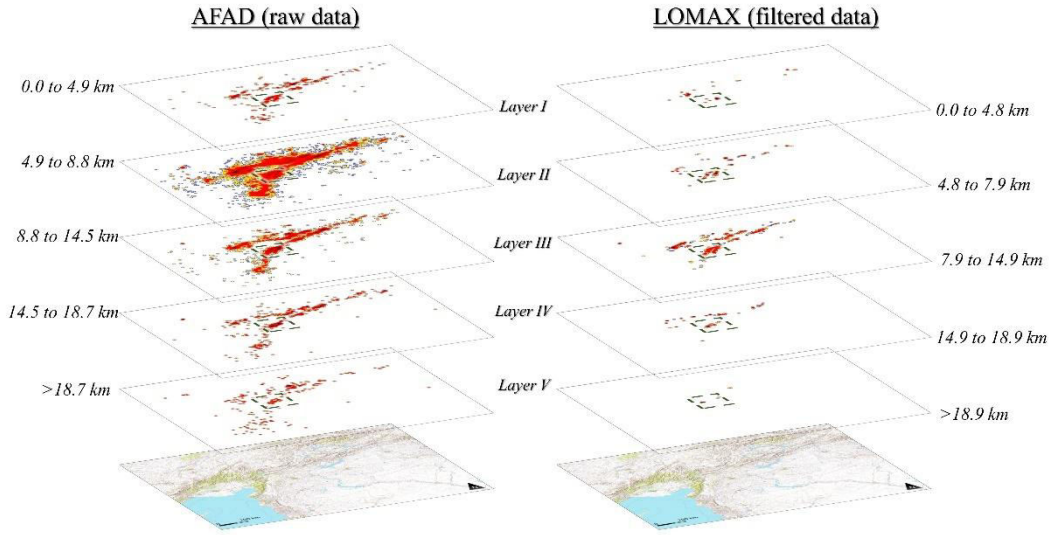

Figure A2. Comparison of stacked kernel maps of seismicity density for the central and southwestern part of the East Anatolian Fault Zone (EAFZ), represented at different depth ranges (seismological layers) identified by the seismic distribution profile, Layers I to V (**Figure 14**). Left: AFAD (raw data). Right: Lomax, 2023 (relocated-filtered data). The area where the converging nuclei from upper to lower layers is easily identifiable is highlighted by a rectangle. This figure represents the same maps as in **Figure 17** but stacked to illustrate the 3D morphology of the patterns. For color codes see **Figure 17**.